AD-A071 017 POLYTECHNIC INST OF NEW YORK FARMINGDALE DEPT OF ELE--ETC F/G 20/9
STUDIES ON THE INTERACTIONS BETWEEN ELECTROMAGNETIC FIELDS AND --ETC(U)
APR 79 B R CHEO, E E KUNHARDT, S P KUO AFOSR-74-2668

UNCLASSIFIED POLY-EE-79-053 AFOSR-TR-79-0752 NL

1 OF 4

AD A071017

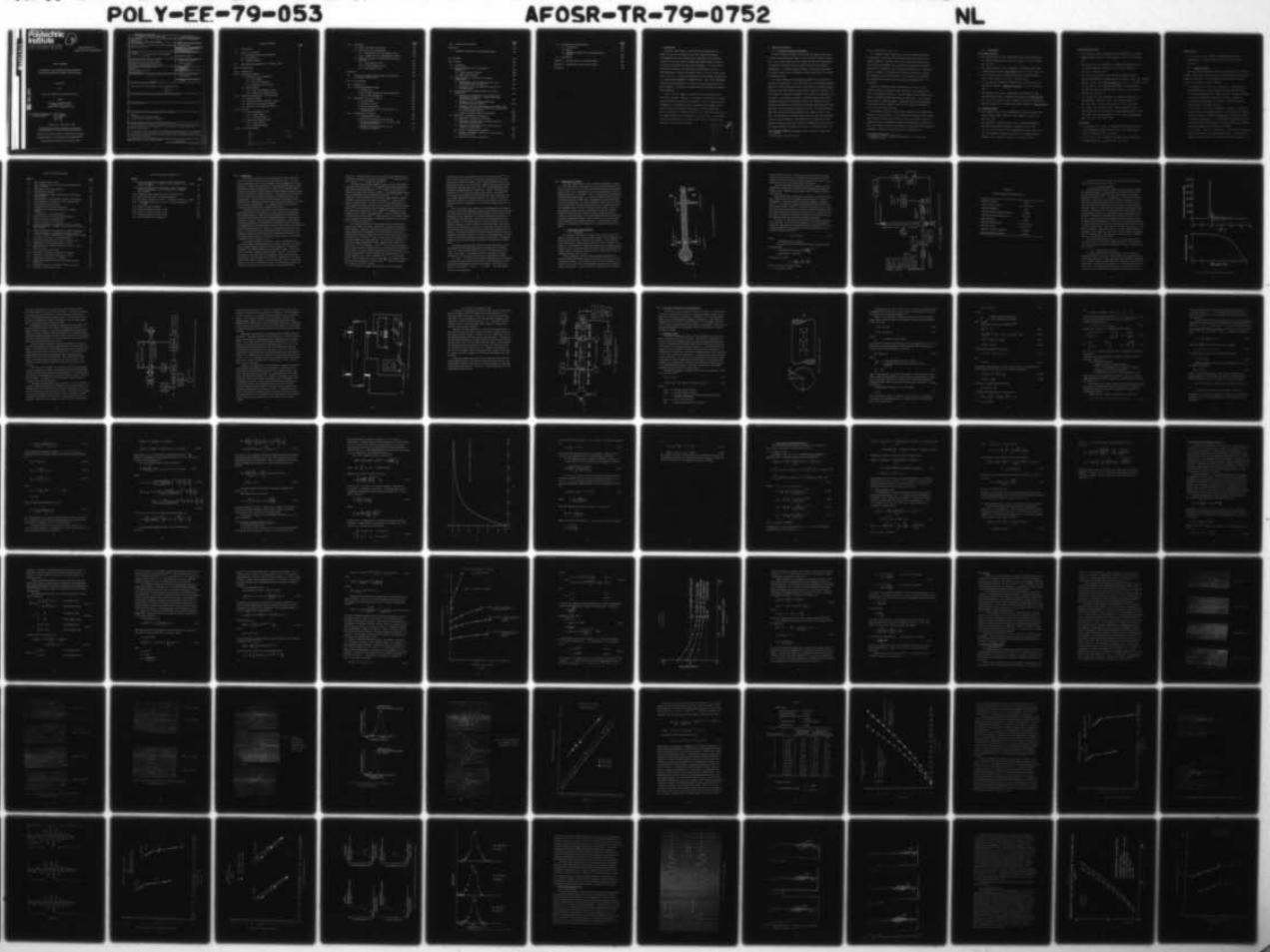

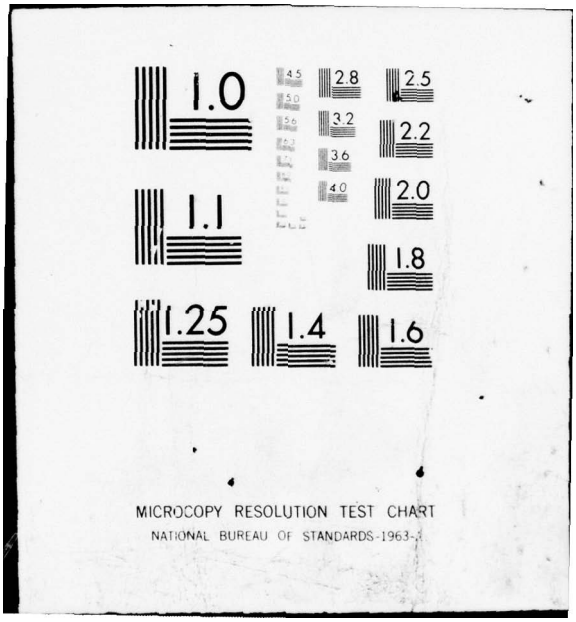
1.0
1.1
1.25
1.4
1.6
1.8
2.0
2.2
2.5
2.8
3.2
3.6
4.0
4.5
5.0
5.6
MICROCOPY RESOLUTION TEST CHART
NATIONAL BUREAU OF STANDARDS-1963-A

Polytechnic Institute of New York

DEPARTMENT OF
ELECTRICAL ENGINEERING

FINAL REPORT

STUDIES ON THE INTERACTIONS BETWEEN ELECTROMAGNETIC FIELDS AND PLASMAS

April 1979

for

Air Force Office of Scientific Research

under

Grant No. AFOSR-74-2668
Project No. 9751-03
(April 1974 - September 1978)

By: Principal Investigator: B.R-S Cheo
Co-Investigators: E.E. Kunhardt
S.P. Kuo
T.Q. Yip

Report No. POLY EE 79-053

DEPARTMENT OF ELECTRICAL ENGINEERING

POLYTECHNIC INSTITUTE OF NEW YORK

Unclassified

REPORT DOCUMENTATION PAGE

READ INSTRUCTIONS BEFORE COMPLETING FORM

1. REPORT NUMBER: AFOSR-TR- 79-0252	2. GOVT ACCESSION NO.
3. RECIPIENT'S CATALOG NUMBER	
4. TITLE (and Subtitle): Studies on the Interactions between Electromagnetic Fields and Plasmas	5. TYPE OF REPORT & PERIOD COVERED: Final Report, April 1974 - September 1978
6. PERFORMING ORG. REPORT NUMBER: POLY-EE-79-053	
7. AUTHOR(s): B.R-S Cheo, E.E. Kunhardt, S.P. Kuo and T.Q. Yip	8. CONTRACT OR GRANT NUMBER(s): AFOSR-74-2668
9. PERFORMING ORGANIZATION NAME AND ADDRESS: Polytechnic Institute of New York, Electrical Engineering Department, Route 110, Farmingdale, N.Y. 11735	10. PROGRAM ELEMENT, PROJECT, TASK AREA & WORK UNIT NUMBERS: Project 9751-03, 61102F
11. CONTROLLING OFFICE NAME AND ADDRESS: AFOSR/NP, Bolling AFB, Bldg.#410, Wash DC 20332	12. REPORT DATE: April 1979
	13. NUMBER OF PAGES: 315
14. MONITORING AGENCY NAME & ADDRESS(if different from Controlling Office)	15. SECURITY CLASS. (of this report): Unclassified
	15a. DECLASSIFICATION/ DOWNGRADING SCHEDULE

16. DISTRIBUTION STATEMENT (of this Report)

Approved for public release, distribution unlimited.

17. DISTRIBUTION STATEMENT (of the abstract entered in Block 20, if different from Report)

18. SUPPLEMENTARY NOTES

19. KEY WORDS (Continue on reverse side if necessary and identify by block number)

Plasma
Parametric Decay Instabilities
Non-Linear Phenomena in Plasmas

20. ABSTRACT (Continue on reverse side if necessary and identify by block number)

Final report on a variety of subjects in the non-linear interactions between electromagnetic fields and plasmas. Work includes both theoretical and experimental efforts.

Principal results are: 1) the first experimental verification of the existence of two distinct group velocities in a non-linear dispersive medium and 2) the development of a general vector theory of parametric excitation of plasma waves in a magnetized plasma.

DD FORM 1 JAN 73 1473 EDITION OF 1 NOV 65 IS OBSOLETE

Unclassified

SECURITY CLASSIFICATION OF THIS PAGE (When Data Entered)

TABLE OF CONTENTS

		Page
I.	Introduction	1
II.	Review of Activities	2
	2.1 Principal Scientific Achievements	2
	2.2 Publications	4
	2.3 Graduate Students	6
III.	High Amplitude Propagation in a Plasma Column	8
List of Illustrations		9
III-1.	Introduction	11
III-2.	Experimental Program	14
	2.1 Description of the Apparatus	14
	2.1.1 The Plasma	14
	2.1.2 The Pulse Generator	19
	2.1.3 Parallel Plate Structure	19
	2.2 The Experiment	21
	2.2.1 Zero Axial Magnetic Field	21
	2.2.2 Finite Axial Magnetic Field	27
III-3.	Analytical Formulation of the Experiment	29
	3.1 Analytical Model	29
	3.2 Functional Relation Between κ_α and ω	39
	3.3 Final Form of Amplitude Equation	44
	3.4 Analysis of the Amplitude Equation	48
III-4.	Results	60
	4.1 Zero Axial Magnetic Field	60
	4.1.1 Linear Regime	60
	4.1.2 Nonlinear Regime	78
	4.2 Finite Axial Magnetic Field	84
	4.2.1 Linear Regime	84
	4.2.2 Nonlinear Regime	88
III-5.	Concluding Remarks	100

		Page
III-6.	Appendices	102
	6.1 Formal Derivation of Operators	102
	6.2 Evaluation of the Eigenvectors	103
	6.2.1 Eigenvectors for Zero Magnetic Field	105
	6.2.2 Eigenvectors for Large Magnetic Fields	109
	6.3 Explicit Evaluation of Nonlinear and Collision Operators	113
	6.3.1 Zero Magnetic Field	113
	6.3.2 Infinite Magnetic Field	115
	6.3.3 Weak Magnetic Field	118
References		120
IV.	Evolution of Parametrically Excited Instabilities in a Magneto Plasma Column	124
List of Illustrations		125
IV-1.	Introduction	127
IV-2.	Plasma and Microwave Systems	137
	A- Plasma Device	137
	B- The Microwave System and Power Measurement	140
	C- Basic Plasma Parameters	144
IV-3.	Experimental Set-up and Results	152
	A- The Experiment	152
	B- Detection of Waves	154
	C- Typical Observations	157
	D- Decay and Growth of the Electrostatic Ion Cyclotron Wave	166
IV-4.	Interpretation of Results	176
	A- Phenomenological Model	176
	B- Calculation of Decay and Growth Rate	184
	C- Physical Significance of C_1, C_2 and C_3, and Saturation Mechanisms	193
	D- Derivation of Modes Involved in the Parametric Experiment	203

		Page
IV-5.	Summary and Conclusions	218
References		221
V.	Parametric Excitation of Coupled Plasma Waves	224
List of Figures		225
List of Tables		226
V-1.	Introduction	227
V-2.	General Formulation for the Parametric Excitation	232
	5.1 Overall Physical Features	232
	5.2 Hamiltonian Approach	232
V-3.	Kinetic Approach to Calculate the Coupling Coefficients	238
	3.1 Transformation of the Vlasov Equations to the Oscillating Frame of Reference	238
	3.2 Integration Along the Unperturbed Trajectory in the Phase Space	240
V-4.	Detailed Analysis of Threshold Power and Initial Growth Rate	249
	4.1 Conditions and Properties of the Instabilities Occurring on the Basis of a General Form of the Coupled Mode Equations	249
	4.2 Parametric Decay into Longitudinal Modes (Electrostatic Approximation)	252
	4.3 Parametric Decay into Electrostatic Ion Cyclotron Wave and Harmonics of Electron Cyclotron Wave (Hybrid Mode) in a Uniform Magneto Plasma	259
	4.4 Comparison Between Theory and Experiments	262
V-5.	Description of Experiment and Results	264
	5.1 Experimental Apparatus and Procedure	264
	5.2 Measurement of Growth and Decay Times of Electrostatic Ion Cyclotron Waves	269
	5.3 Frequency of Electrostatic Ion Cyclotron Wave as a Function of Pump Power	281
	5.4 Summary of Experimental Parameters	281
	5.5 Evidence of Parametric Excitation of Electrostatic Ion Cyclotron Wave	286
	5.6 Simplified Theoretical Explanation	287

	Page
V-6. Nonlinear Saturation Mechanism	292
6.1 Introduction	292
6.2 Theory	293
6.3 Comparison Between Theory and Experimental Results	299
V-7. Conclusions	301
Appendix A: Normalization of the Acoustic Modes	302
Appendix B: Normalization of the Optical Modes	306
References	309

I. Introduction

During the period between 1 April 1974 and 30 September 1978, a number of topics in the general area of the interactions between electromagnetic fields and plasmas were conducted at the Polytechnic Institute of New York, under the AFOSR grant AFOSR-74-2668. Basically, the topics are divided into two general categories: (a) the study of a nonlinear plasma wave excited along a glow discharge column by a high amplitude ($\approx$ 2 KV/cm) and extremely sharp ($\approx$ 0.2 ns) electric field pulse; and (b) the study of parametrically excited decay instabilities in a plasma column imbedded in a magnetic field. Most of the significant results have been published in a series of five journal papers with one more submitted. In addition, nine papers have been presented at APS and IEEE conferences.

In Sec. II of this report, a review of the activities during the period will be given. Section III is devoted to the details of the work on the high speed pulse excited plasma waves. Section IV describes the experiments on the parametric decay instabilities with emphasis on the time evolution of the growth and saturation of these instabilities. Section V consists of a theoretical analysis of a three wave decay process in a magneto plasma which is applicable to all wave types. This remains the only theory which has this general applicability. Experiments supporting the theory are also included.

II. Review of Activities

II-1. Principal Scientific Achievements

A number of topics have been studied under the support of the Grant. A listing of the publications given in II-2 shows the breadth of activities. Two of these topics represent efforts of particular significance: (1) first real life demonstration of group splitting of wave packets propagating in nonlinear dispersive media; and (2) the establishment of a general vector theory of parametric decay instabilities in a plasma with magnetic field.

(1) Group splitting, or wave packet bifurcation, was predicted by the theory of modulation*. It is predicted that in a nonlinear dispersive medium, if certain conditions are met, there would be two distinct group velocities with their difference proportional to the wave amplitude. If a wave packet is launched to propagate in the medium, it would split into two packets. The modulation theory is a general nonlinear wave theory developed heuristically and formally based on the assumptions of some conservation properties of the amplitude and phase characteristics of the wave packet and the nonlinear dispersion relation. The group splitting effect was the most astonishing prediction not known to exist at that time. The experiment by Kunhardt and Cheo was the first real-life demonstration of this phenomenon. This demonstration, together with some computer simulations, has thus provided the confidence in the validity of the modulation theory.** Details of this work are elaborated in Sec. III

---

* G.B. Whitham, "Linear and Nonlinear Waves", John Wiley & Sons, 1973; pp. 489-490

** G.B. Whitham, ibid, pp. 519-520

and in Publications (1), (2), (5).

(2) Parametric decay instabilities have been studied extensively for many years. Two recent review articles* have each cited over one hundred references. The basic form of the coupled mode equations was first derived by Nishikawa for a plasma with no magnetic field and the same theory is applicable to the ordinary mode excitation in a magnetized plasma. Because of the complexity of the modal structure in a plasma with magnetic field, previous efforts in this area are only limited to the longitudinal waves where the electrostatic approximation $\vec{E} = -\nabla\varphi$ is applied.

Because the parametric decay instabilities are thought to be an important process in rf plasma heating, and that in many applications such as in ionosphere heating or in various magnetic field confined plasma devices, interactions among hybrid waves do take place. A more general vector theory is therefore needed. The general vector theory developed by Kuo and Cheo [3] is capable to deal with these cases and remains to be the only such theory available.

The approach is based on Poisson bracket relations of the Hamiltonian densities of the decay waves. It is shown that the general vector coupled mode equations obtained can be reduced to those of the special cases obtained previously, and compared favorably with experiments. Section V of this report shows the detailed development of the theory and the supporting experiments. Essence of this work is given in Publication (3).

---

* M. Porkolab, Physica C 82, 86, 1976.
M. Porkolab and R.P.H. Chang, Rev. Modern Phys., vol. 50, #4, pp. 745-795, Oct. 1978.

II-2. Publications

(1) Journal Articles:

1. E.E. Kunhardt and B.R. Cheo, "Observation of Wave Packet Bifurcation in a Magneto-Plasma Column", Phys. Rev. Letters, vol. 37, 25, 1688; Dec. 20, 1976.
2. E.E. Kunhardt and B.R. Cheo, "Propagation of Nonlinear Waves Along a Magneto-Plasma Column", Phys. Fluids, vol. 20, 9, 1499; Sept. 1977.
3. S.P. Kuo and B.R. Cheo, "Parametric Excitation of Coupled Plasma Waves", Phys. Fluids, vol. 21, 10; 1753; Oct. 1978.
4. N.T. de Neef and C. Hechtman, "Numerical Study of the Flow due to a Cylindrical Implosion", Computers and Fluids; vol. 6, pp. 185-202; 1978.
5. E.E. Kunhardt and B.R. Cheo, "Experiments on Propagation of High Amplitude Surface Waves", accepted for publication by Plasma Physics.
6. T.Q. Yip, S.P. Kuo and B.R. Cheo, "Temporal Evolution of Parametrically Excited Instabilities in a Magnetized Plasma", submitted to Plasma Physics.

(2) Conference Papers:

1. E.E. Kunhardt and B.R. Cheo, "Propagation of Transient Surface Waves Along a Plasma Column", IEEE Intl. Conf. Plasma Sc., Austin, TX; May 24-26, 1976.
2. E.E. Kunhardt, J. Tardiff and B.R. Cheo, "The Bouncing Conductor Generator", Pulsed Power Conference, Lubbock, TX; Nov. 1976.
3. T.Q. Yip, S.P. Kuo and B.R. Cheo, "Experimental Study of Time Evolution of Parametrically Excited Instabilities in a Magneto-Plasma", IEEE Intl. Conf. Plasma Sc., Troy, N.Y.; May 23-25, 1977.

Conference Papers (cont.)

4. S.P. Kuo and B.R. Cheo, "Parametric Decay Instabilities in a Uniform Magneto-Plasma", IEEE Intl. Conf. Plasma Sc., Troy, N.Y.; May 23-25, 1977.
5. S.P. Kuo and B.R. Cheo, "Saturation of Parametric Instabilities due to Anomalous Diffusion Processes", IEEE Intl. Conf. Plasma Sc., Troy, N.Y.; May 23-25, 1977.
6. T.Q. Yip, S.P. Kuo and B.R. Cheo, "Evolution of Parametrically Excited Instabilities in a Magneto-Plasma", Plasma Div. Mtng., APS, Colorado Springs, CO; Nov. 1978; Bull. Am. Phys. Soc., vol. 23, 7, 799; Sept. 1978.
7. S.P. Kuo and B.R. Cheo, "Harmonic Generation of the Electrostatic Ion Cyclotron Wave in a Uniform Plasma", IEEE Intl. Conf. Plasma Sc., Monterey, CA; May 1978.
8. S.P. Kuo and B.R. Cheo, "Saturation of Parametric Instabilities by Heating Effect", Plasma Div. Mtng., APS, Colorado Springs, CO; Nov. 1978; Bull. Am. Phys. Soc., vol. 23, 7, 817; Sept. 1978.
9. H.M. Huang, S.P. Kuo and B.R. Cheo, "Harmonic Generation of the Electrostatic Ion Cyclotron Wave in a Uniform Magneto-Plasma", Plasma Div. Mtng., APS, Colorado Springs, CO; Nov. 1978; Bull. Am. Phys. Soc., vol. 23, 7, 818; Sept. 1978.

(3) Reports:

1. E.E. Kunhardt and B.R. Cheo, "An Experimental and Theoretical Study of the Propagation of High Amplitude Pulses in a Bounded Magneto-Plasma", Poly-EE/EP-76-011; June 1976.
2. S.P. Kuo and B.R. Cheo, "Studies of Parametric Decay Instabilities in Magneto-Plasmas", Poly-EE/EP-77-027; June 1977.

Reports (cont.)

3. T.Q. Yip and B.R. Cheo, "Evolution of Parametrically Excited Instabilities in a Magneto-Plasma Column", Poly-EE/EP-77-028; June 1977.

II-3. Graduate Students

There have been seven graduate students participating in the research program. Three have obtained their Ph.D. degrees and four are progressing toward this direction. All three graduates are presently successfully placed in the general scientific community.

1. E.E. Kunhardt, Ph.D., June 1976. Dissertation: "An Experimental and Theoretical Study of the Propagation of High Amplitude Pulses in a Bounded Magneto-Plasma". Present position: Assistant Professor of Electrical Engineering, Texas Tech. University, Lubbock, TX. Was elected the new professor of the year. Participated and initiated a number of research activities.
2. S.P. Kuo, Ph. D., June 1977. Dissertation: "Studies of Parametric Decay Instabilities in Magneto-Plasmas". Present position: Research Assistant Professor of Electrical Engineering, Polytechnic Institute of New York, Farmingdale, N.Y. Participated and generated activities in the new fields of MHD generation of electric power and ionospheric heating and modification. Worked on EBT at ORNL.
3. T.Q. Yip, Ph.D., June 1977. Dissertation: "Evolution of Parametrically Excited Instabilities in a Magneto-Plasma Column". Present position: Member of Technical Staff, Bell Telephone Laboratories, Holmdel, N.J.

Student Graduates (cont.)

Began a new career in communications. Continued to collaborate with the Poly group in plasma work (no compensation).

4. R. Faaland: A second year graduate student. Teaching fellow in the EE Department. Actively involved in the effort of building a new ECRH plasma station and electronics associated with the system.
5. C. Hechtman: An advanced graduate student. Passed qualifying examination. Currently research assistant in the program. Built the capacitor bank for the exploding tube experiment. Published a paper on the topic.
6. H.M. Huang: An advanced graduate student. Passed qualifying examination. Currently research fellow in the program. Working on the microwave generated and sustained beam plasma. Doing both theoretical and experimental work. Presented a paper at APS Plasma Division meeting.
7. B.R. Poole: A second year graduate student. Teaching fellow in the EE Department. Has been an active participant in the program for several years. Passed qualifying examination.

III

High Amplitude Propagation on a Plasma Column

LIST OF ILLUSTRATIONS

Figure		Page
2.1	Basic experimental set up	15
2.2	D.C. discharge tube, associated vacuum system and D.C. circuitry	17
2.3	BBG output and Fourier spectrum	20
2.4	Parallel plate structure	22
2.5	Block diagram of impulse generation, transmission and reception	24
2.6	Arrangement to record spatial profile of wavepackets	26
2.7	Block diagram of experiment, finite magnetic field	28
3.1	The magneto-plasma column	30
3.2	Computer plot of dispersion equation	41
3.3	Velocity of first peak of wavepacket vs. plasma frequency	55
3.4	α' parameter vs. plasma frequency	57
4.1	Effect of pressure on propagating wavepacket	62
4.2	Effect of polarity of exciting pulse	64
4.3	Evolution in space of initial pulse	65
4.4	Linear oscillograms for different receiver positions (positive pulse) f_p = 1.4GHz. a) z = 27 cm, b) z = 56 cm c) z = 90 cm	67
4.5	Fourier transform of wavepacket for different positions	68
4.6	Linear oscillograms for different plasma frequencies z = 27 cm. a) f_p = .76 GHz, b) f_p = .9 GHz, c) f_p = 1.4 GHz	69
4.7	Velocity of first peak vs. plasma frequency	70
4.8	Normalized time position of zeros of electric field	73
4.9	Amplitude of wavepacket envelope vs. time	75
4.10	Oscillograms for different plasma frequencies. Tube radius = .3 cm	76
4.11	Zero crossing for small tube.	77
4.12	Response as a function of input pulse strength	79
4.13	Amplitude of wavepacket envelope vs. time	80
4.14	Amplitude of wavepacket vs. distance	81
4.15	Linear and nonlinear spectrum for different plasma frequencies	82
4.16	Nonlinear spectrum for different receiver locations	83
4.17	Response to high negative pulse	85

LIST OF ILLUSTRATIONS (Con't.)

Figure		Page
4.18	Linear oscillograms for different plasma frequencies. Cyclotron frequency = .6 GHz. a) f_p = 1.4 GHz, b) f_p = 1.6 GHz c) f_p = 1.7 GHz	86
4.19	Linear oscillograms for different cyclotron frequencies. Cyclotron frequency a) f_c = .6 GHz, b) f_c = .84 GHz, c) f_c = 1 GHz	87
4.20	Normalized time position of zeros of electric field	89
4.21	Velocity of first peak vs. plasma frequency	90
4.22	Oscillogram taken at z = 56 cm. Cyclotron frequency = .6 GHz	91
4.22	a) Oscillogram taken at z = 34 cm. Cyclotron frequency = .6 GHz	92
4.23	Linear Fourier transform	93
4.24	Fourier transform of Fig. 4.22 b)	94
4.25	Fourier transform of Fig. 4.22 c)	95
4.26	Fourier transform of Fig. 4.22 d)	96
4.27	Time separation of wavepackets	98

III-1. Introduction

The general problem we are concerned with is that of the interaction of a plasma medium with an electromagnetic field. At linear level of excitation, the various problems of wave propagation have been explored at length and a fair amount of understanding has been reached. At nonlinear levels of excitation, due to the lack of a general method of attack, the analysis made to date are mostly ad hoc and under various forms of idealization and approximation. The purpose of this investigation is to study some of these interactions both theoretically and experimentally. The results have yielded new data and insight into the problem of the competition between dispersion and non-linearity in a number of plasma configurations. The comparison between theoretical result and experimental data is generally favorable.

Theoretical studies in the linear and weakly nonlinear regimes may be grouped into two categories, namely, analysis in unbounded and bounded plasmas. Experimental investigations on the other hand must be performed with plasmas of bounded geometry. There are experiments, however, where the pertinent dimensions are such that to a good approximation, the waves under consideration may be thought as propagating in an infinite medium and the results behave as predicted by unbounded plasma theory.[1] Studies in unbounded plasmas have been many, and several text books have been written on this subject. Comprehensive expositions have been done by Ginzburg[2] and Stix[3] for the linear regime; and for the weakly nonlinear regime by Tsytovich,[4] Davidson[5] and F. Einaudi et. al.[6].

The bounded geometry considered in this investigation are: a circular plasma column imbeded in an infinite dielectric (free space) and a circular magneto plasma column surrounded by a conducting waveguide of the same dimension as the plasma column. These structures are known to support numerous types of waves. The work in this study is concerned with the propagation of the slow mode whose characteristics do not depend on ion motion. These waves are sometimes called "space charge" or "electron plasma" waves. They differ from the "true" electron plasma waves in an infinite plasma since the boundary conditions posed by the system have altered the wave

structure. Practical interest in these modes are the possibilities of applications in laboratory plasma diagnostics[7, 8, 9], high gain microwave devices[10, 11], and plasma heating[12].

The basic experimental results of linear slow wave propagation have been well documented [13, 14] and good agreements with theoretical analysis have been obtained[15, 16]. However, the situation is different for the weakly nonlinear regime. Very few theoretical analysis of the boundary value problem have been done[17, 18, 19, 20]. The emphasis in most of these studies has been on the nonlinear coupling of waves, in particular three wave interaction[21]. This problem takes a variety of forms. Perulli, et. al. [22] studied the decay of a slow wave into two other slow waves with different azimuthal variation. Larsen[23] used the method of the averaged Lagrangian to analyze the interaction of three slow waves. Kuhn[24] formulated the same problem from a coupled mode formalism. Aside from experiments on surface wave echo (spatial)[25], experimental work has been confined to the mixing of two pump waves of different frequencies to produce a third at the beat frequency[26].

All of the theoretical and experimental efforts mentioned thus far have one feature in common: they are all concerned with steady state situations. Recently, transient techniques have been employed in the experimental investigation of wave propagation in plasmas. Voltage steps and pulses (base band and RF) have been used to excite transient waves. Schmitt[27] was one of the first experimentalists to use pulse excitation to study plasmas. He observed the dispersion of base band pulses propagating through a plasma filled coaxial line. Proni, et. al. [28] and Tregruis, et. al. [29] used microwave pulses to excite transient electron plasma waves in systems where the boundary had no effect. The only reported applications of base band pulses to study the propagation of space charge waves were by Anicin, et. al. [30] for the symetric mode, and by Demokan, et. al. [31] for the dipole mode. Recently Landt et. al. used various types of transient inputs to study the linear properties of these modes[32]. These experiments were limited to the linear regime.

In the nonlinear regime, pulse excitations and time domain

observations have been reported by Sindoris, Cheo and Grody[33] in a Tonks-Dattner type structure using a home developed device called a Bouncing Ball Generator (BBG), which produced baseband pulses 120 picosecond wide at 1.1 KV into 50 ohm. Other nonlinear transient work includes the observation by Ikezi et. al.[34] of the propagation of electron plasma waves excited by voltage steps, and the observation by K. Saeki et. al.[48] of electron plasma wave shocks. Manheimer[49] has studied the development of finite amplitude electron plasma waves in a bounded plasma with infinite magnetic field using the method of expansion in terms of a complete set of linear solutions. He did not include the effect of dispersion, but predicted the steepening observed in (48).

The work in this effort consists of a comprehensive investigation of linear and nonlinear phenomena affecting the propagation of very short base band pulses along a glow discharge magneto plasma column. The advantages of this approach over nonlinear steady state studies are: 1) by keeping the duty cycle low, heating of the background electrons (a major problem in CW experiments) need not be considered; 2) if the transient response is short compared to ionization times, background electron density changes will not occur; 3) the ability to observe short-lived phenomenon is greatly enhanced because of the expanded time resolution. The major advantage of transient studies both large and small amplitude excitations is that we can observe the development in time or in space of an initial disturbance produced at some point. Tremendous insight is gained into the competitive effects of dispersion and nonlinearity.

The source that was used to excite the transient waves is an improved version of the BBG mentioned in the experiment of Sindoris et. al.[33]. The new BBG produces a pulse 0.50 nanosecond wide at 3.2 KV into 50 ohm. This generator and the techniques developed presented us with the unique tools for such comprehensive studies.

In III-2. of this report the experimental program is presented. To analyze the experimental observations a nonlinear theory for wave propagation along plasma column was developed. This theoretical analysis is presented in III-3. In III-4. the experimental results are then analyzed.

III-2. Experimental Program

The basic experimental set up is shown schematically in figure 2.1, where the plasma is the positive column of a glow discharge confined in a glasss tube 175 cm long, with A and K the anode and cathode respectively. M-M' represents a set of coils providing an axial D.C. magnetic field up to 1.2K Gauss. WG is a removable conducting wall surrounding the plasma tube. L is a pair of parallel plates connected to the pulse generator (BBG) which establishes an impulse like electric field in the plasma. The wave evolution in space-time as a function of initial pulse strength is monitored by the receiving structure R on a sampling scope. The work was done in two stages. The first consisted of a comprehensive investigation of linear and nonlinear phenomena affecting the propagation of pulses along the positive column of a glow discharge. The second stage involved the addition of a uniform longitudinal magnetic field variable up to 1.2K Gauss and the surrounding of the plasma column by a conducting wall. Subsequently, a description of the experimental apparatus and procedure is given.

2.1 Description of the Apparatus

2.1.1 the plasma

For a plasma, the positive column of a hot cathode, glow discharge in argon is used. Fig. 2.2 shows a layout of the discharge tube and its associated vacuum and electrical systems. The discharge tube comprises two Western Electric mercury vapor cathodes contained in a round flask and connected by means of a quick glass to glass joints to a 175 cm long glass tube, the end of which is terminated with a hallow anode. Because of the quick coupler, glass tube sections of different diameter may be used.

It was necessary, due to the type (sampling technique) and amount of measurements that had to be performed, to provide a clean and stable discharge. By allowing Argon gas to flow through the discharge tube at a slow rate; contamination, due mainly to ion bombardment of the cathode, is reduced since such impurities are constantly

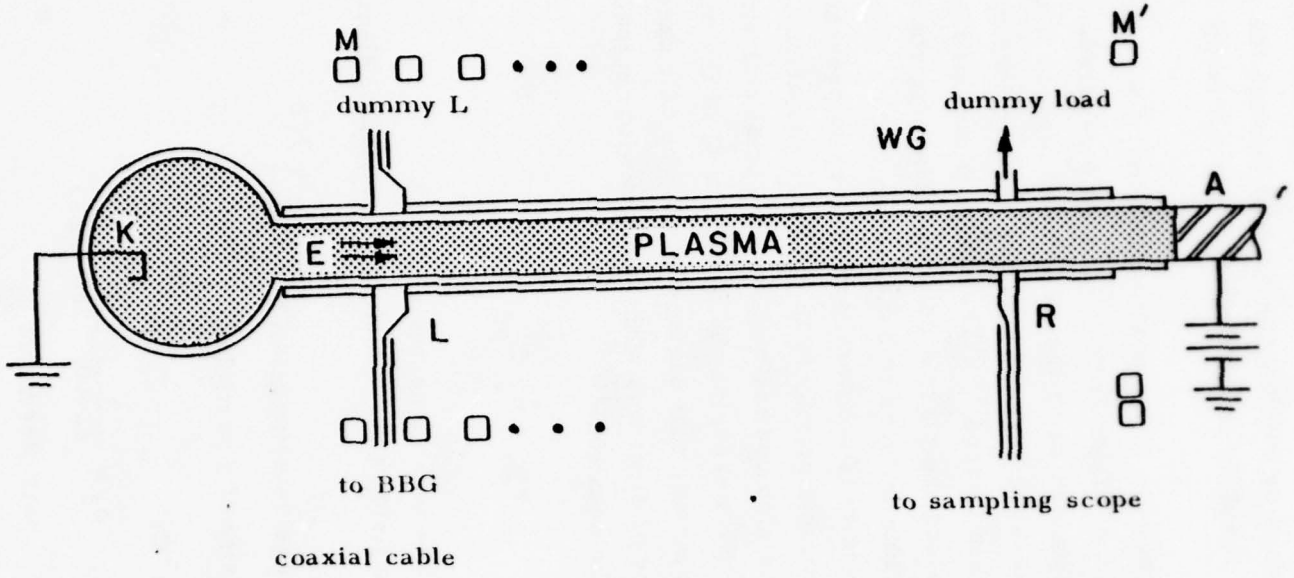

Fig. 2.1 Basic experimental set up

removed from the tube. To provide effective regulation of the gas pressure, the argon inflow is regulated by a flow meter valve and needle valve and the evacuation rate by a high vacuum valve. Adjustment of these valves provide the desired pressure.

Once the discharge is operating, the desired range of electron densities is obtained by varying the current through the pentode regulator circuit. Stability of the system, over all range considered, was excellent.

Basic parameters of the positive column, i.e. electron temperature, density, and collision frequency, were measured. Electron temperature is obtained using the well known method of Langmuir probe[35]. To measure average electron number density, the cavity perturbation method is used[9]. The cavity is mounted in a carriage which can move along the plasma column. The electron density variation along the column is found to be less than 0.5%. During the experiments, the density is constantly monitored to prevent drifts from the operating point, due primarily to pressure variations.

The cavity is also used to measure the total collision frequency of the electrons. By measuring the change in Q of the microwave cavity due to the plasma, this parameter may be calculated[36]. The collision frequency of electrons with ions and with neutrals is also calculated using the equation[37]

$$\nu_{e\beta} = n_\beta \, Q_{e\beta} \, v \qquad (2\text{-}1)$$

where

$\beta \equiv$ implies ions or neutrals

$Q_{e\beta} \equiv$ collision corssection for collision of electrons with β-type particles

$v \equiv$ average velocity given by $\left(\frac{8KT}{\Pi m}\right)^{1/2}$

$n_\beta \equiv$ density of β particles

For neutrals, at 20° C:

$$n_\beta = \frac{A}{22400} \; \frac{P}{760} \; \frac{273}{293}$$

where $A = 6.02 \times 10^{23}$ particles/mole

P = pressure in mm.

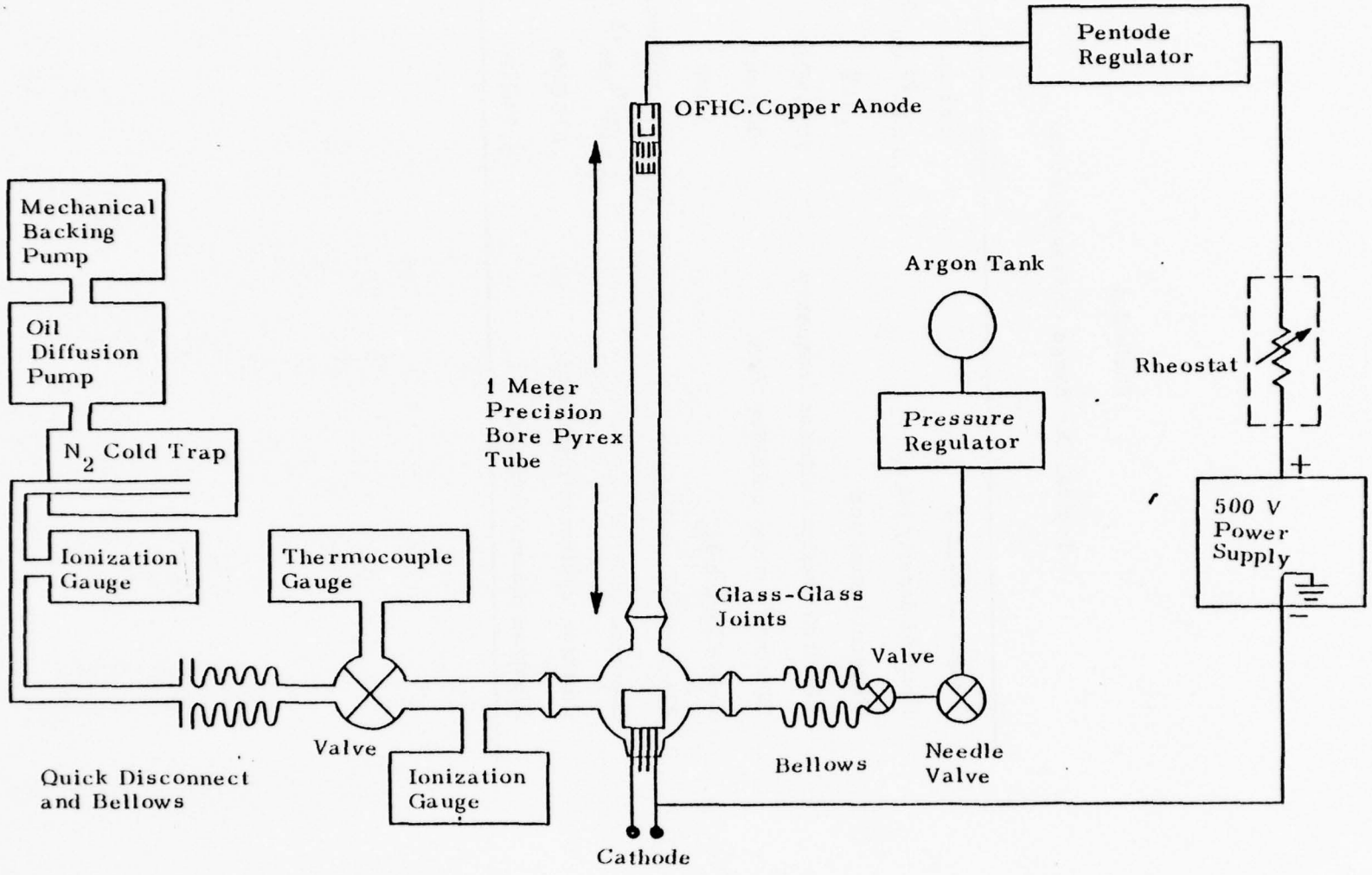

Fig. 2.2 D.C. discharge tube, associated vacuum system and D.C. circuitry

Table 2.1

Typical Discharge Characteristics

Radius of column	.66 cm
Neutral density (at 1μ)	3.3×10^{13} cm^{-3}
Percent ionization	.01%
Electron neutral collision frequency	17.2 MHz
Electron neutral collision time	100 n sec.
Debye length λ_D	1 mm
Electron thermal speed	1.5×10^{8} cm/sec.
Electron density	2×10^{10} cm^{-3}
Electron cyclotron frequency	.632 GHz
Electron plasma frequency	1.3 GHz

Typical parameters obtained using the experimental techniques mentioned above are shown in table 2.1.

2.1.2 The pulse generator

A Bouncing Ball Generator (BBG) is the source for the pulses used in the experiment. This generator has previously been used in time domain studies of EM precursors and in impulse stimulated emission from plasmas[33]. The generator, at the time of those experiments, produced base band pulses with peak voltage of 1.1 kilovolts and a risetime faster than 120 picoseconds. For this experiment, the BBG was modified and is now capable of producing pulses with peak voltage of 3.2 kilovolts with approximately 200 picoseconds rise time. The peak power into a 50 ohm line is 259 kilowatts. The average power, however, is 4 milliwatts because of the short pulse duration. The display of the BBG output pulse shown in Fig. 2.3 is an X-Y recorder plot of the oscillogram from the sampling scope. To obtain such an oscillogram, the pulse, after being attenuated 63 dB is applied to the scope through a 60 nanosecond delay cable (RG-9B/u) of 4.4 dB insertion loss. The output of the scope is then used to drive the X-Y recorder. Also shown in fig. 2.3 is the voltage spectrum of the pulse. This is obtained from Fourier analysis using a computer of the time domain signal. The spectrum is extremely wide, extending from D.C. and almost flat to 1 GHz.

To control the amplitude of the pulse, wide band attenuators (GR type 874-GL) are used at the output of the BBG. Also at the output, a pre-trigger pick off has been installed to obtain a trigger signal for the scope.

2.1.3 Parallel plate structure

To couple the BBG pulse to the plasma, a section of parallel plate transmission line is used. The parallel plate coupling structure consists of a wide band coaxial to parallel plate transition which opens up to a length of uniform transmission line, then tapers down again to a coaxial line. The line is then attenuated by 20 dB and terminated with a 50 Ω load. The dimensions of the structure are such as to keep a constant 50 ohms characteristic impedance along the structure over a

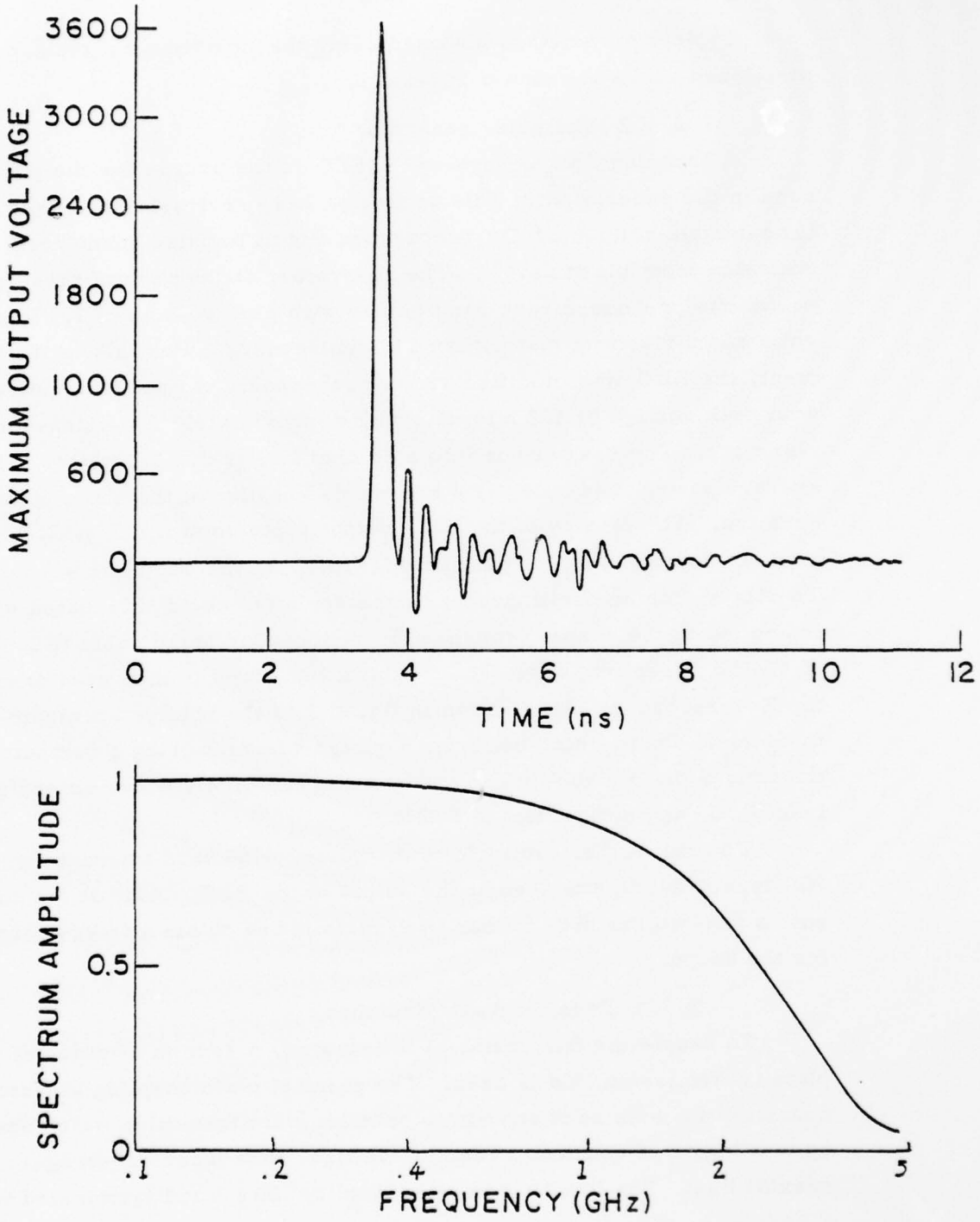

Fig. 2.3 BBG output and Fourier spectrum

wide range of frequencies. The plasma tube is inserted perpendicular to the plane of the plates through holes made at the center of the plates, as shown in fig. 2.4. The holes are made to fit tightly around the column.

The plate structure is a very good wide band coupler with an almost flat passband extending from 50 MHz to approximately 2 GHz. This feature of the structure made it a suitable coupler in the pulse experiments because of the wide bandwidth of the exciting pulse. A similar structure is also used to couple the propagating wavepacket to the sampling scope. The receiving plates are mounted on a carriage to allow for movement along the column.

2.1.4 Sampling scope and recorder

To observe the input pulse and the propagating wavepackets, a Tektronix 564 storage scope with sampling plug-ins is used. To facilitate further analysis, the observed oscillograms are also recorded using a Hewlet-Packard X-Y recorder connected to the output of the storage scope.

It must be remarked that the sampling technique for observing fast transient time phenomena requires that each experiment be identical. This in turn demands that the input pulse be identical for each experiment and that the plasma relaxes to its initial state before the following pulse arrives at the launcher. The last condition may be ascertained by comparing the width of the packet with respect to the pulse separation. However, considering that the BBG is an electromechanical device, it is remarkable that the pulses it produces are identical within a few percent of each other, to the extent that the technique was succesful.

2.2 The Experiment

2.2.1 Zero axial magnetic field

For the investigation, the apparatus described in section 2.1 was arranged as shown in fig. 2.5. The output pulse of the BBG, after attenuation to the desired voltage, is coupled to the plasma through the wide band parallel plate structure. A 60 nanosecond delay cable is used between the generator and the plates. For high amplitude pulses,

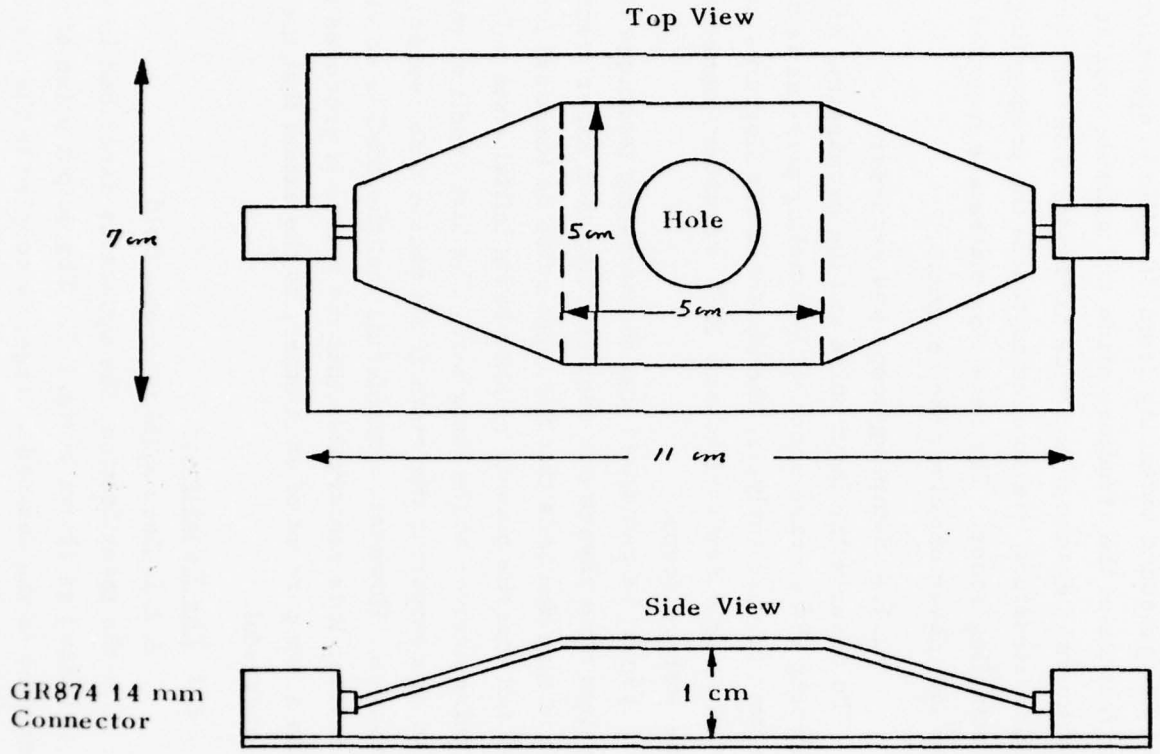

Fig. 2.4 Parallel plate structure

difficulty is encountered with reflections from the plates (due to a small mismatch), that travel back to the BBG. At the BBG, these are once again reflected (the BBG is an open transmission line) and return to the plates generating unwanted signals. By introducing the delay line, the reflection arrives at the plates 120 ns after the original pulse, long after the observations are made.

The plasma column is inserted perpendicular to the plane of the plates through the holes at the center. The holes are made to fit tightly around the column. As the pulse propagates along the parallel plates, the region of plasma within the plates (1 cm separation) feels uniformly around the column the effect of the electric field of the pulse. The field is directed parallel to the axis of the column, such that electrons are accelerated towards the anode.

With this mode of coupling, circularly symmetric waves are excited in the plasma and they propagate along the column towards the anode. To prevent waves from propagating towards the cathode, the section of plasma between cathode and launcher is surrounded with a copper sheet and no wave can propagate under those conditions. More will be said on this in chapter III. Since the tube is of finite length, wide band microwave absorbers are used at the end of the column to prevent possible reflections from the anode and into the receiver.

The receiver is mounted on a carriage and can be moved along the whole length of the column. These plates pick up the longitudinal electric field associated with the propagating wave. The field strength is displayed on the sampling scope and also plotted on paper using the X-Y recorder. A trigger pulse from the BBG is used to properly synchronize the time of sampling.

Two types of oscillograms were recorded. First, for a fixed position of the receiving plate, oscillograms in time were taken. The analog output of the scope drives the Y axis of the plotter, while the scope's time base is used to drive the X axis. In this manner, a replica of the trace that appears on the scope's screen is plotted. Secondly, the spatial distribution of the waves, for fixed sampling time, were obtained. The Y axis of the plotter is driven as in the time measure-

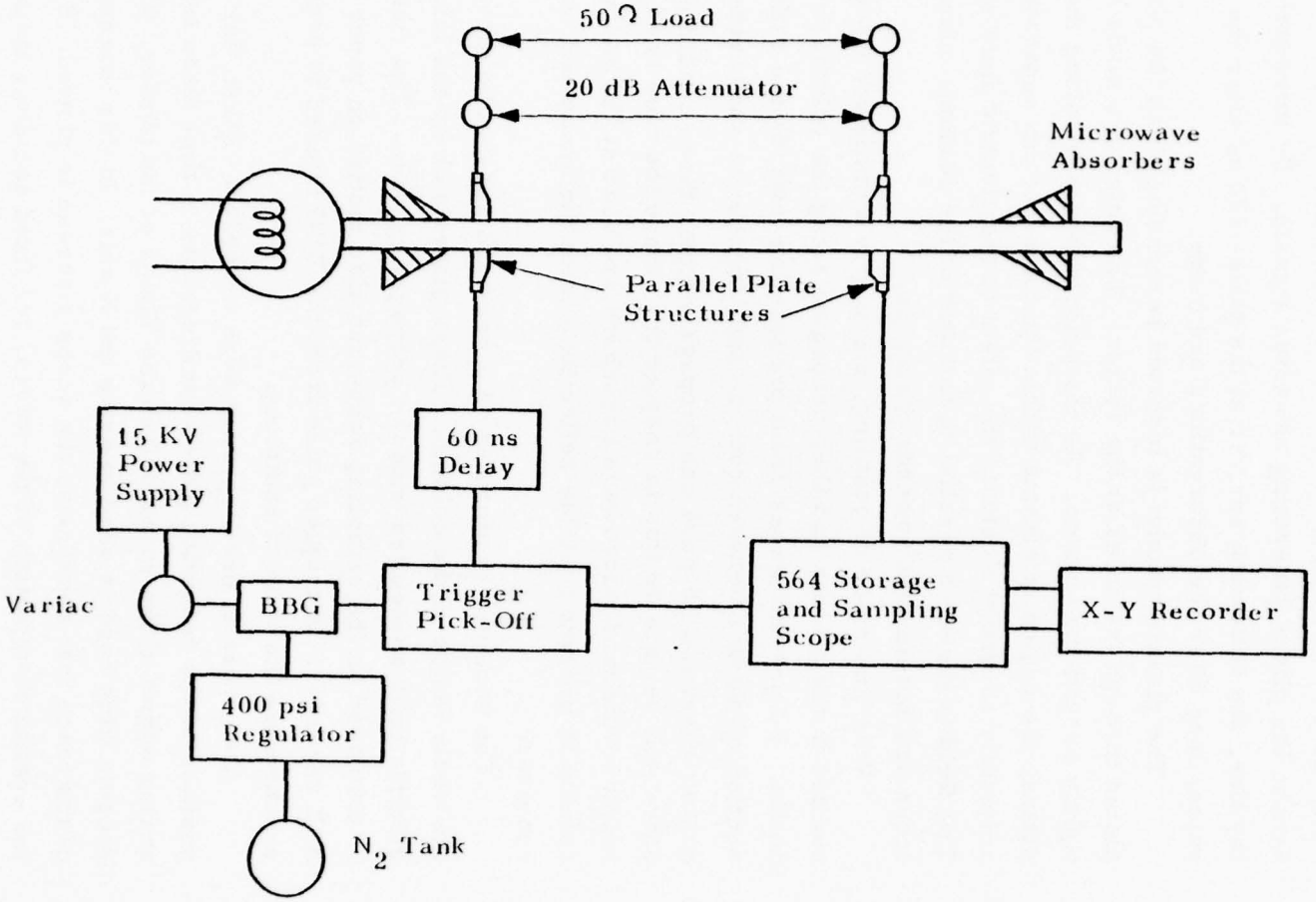

Fig. 2.5 Block diagram of impulse generation, transmission and reception

ments; the X axis however is driven by a voltage proportional to the position of the receiver with respect to the launcher. The arrangement is shown in fig. 2.6. A constant voltage is applied across the potentiometer. As the crank is turned to move the probe, the arm of the potentiometer rotates a distance proportional to the probe's motion along the axis of the column. Thus the voltage of the arm is equivalent to the distance of the probe with respect to the structure. This voltage increases continuously as the receiving structure moves away from the launcher.

Both types of oscillograms were taken under different operating conditions. The argon discharge was operated over a range of neutral gas pressure and D. C. discharge current. The pressure was varied from 1 to 10 μ Hg and the current between 20 and 300 mA. In this domain, the electron temperature ranged between 2.5 and 5 eV. (the high temperature corresponding to the lowest pressure), while the average electron densities were of the order of 10^{9}-10^{10} cm^{-3} (the low densities corresponding to the lowest pressures and discharge currents). The range of electron collision frequencies has been tabulated in sec. 2.1.1. To investigate the effect of column radius on the propagation of the waves, column section of diameters; .6 cm, .952 cm and 1.32 cm, were used.

Finally, the characteristic of the waves as a function of exciting pulse polarity and amplitude were investigated. A BBG was also constructed to produce negative pulses. For a negative pulse, ions are accelerated towards the anode. Since the amplitude of the BBG pulse (both positive and negative) is constant, attenuators are used to obtain the lowest desired level of excitation (this corresponded to approximately 100 volts). Then, the peak voltage of the exiting pulse (numerically equal to the longitudinal electric field the charged particles between the plates feel) is progressively increased (by reducing the attenuation) to its maximum value. In taking the oscillograms, each time the exciting pulse is increased, the received waves are attenuated by a corresponding value to keep the gain of the system fixed, allowing direct comparison of the profiles of the received signals.

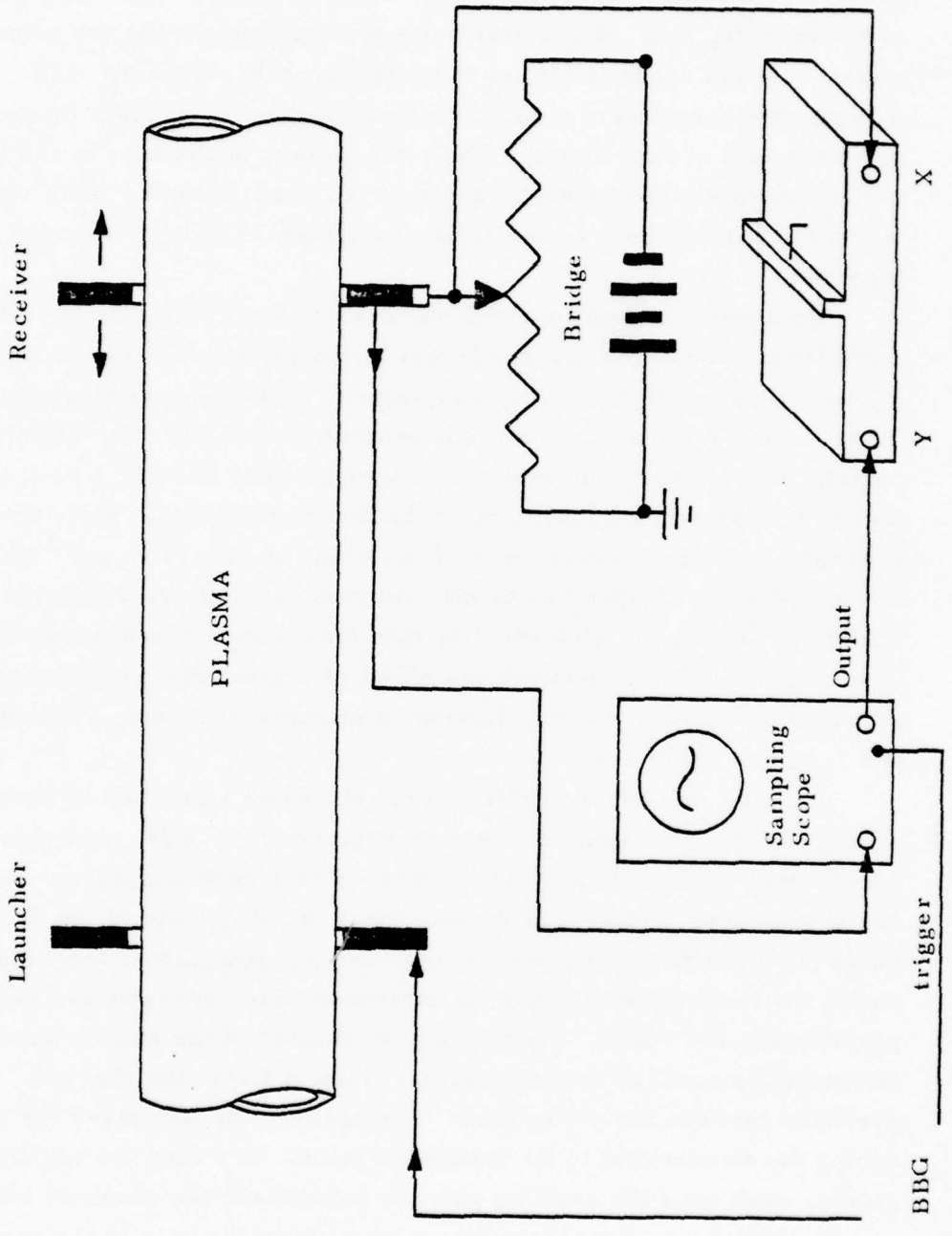

Fig. 2.6 Arrangement to record spatial profile of wavepackets

2.2.2 Finite axial magnetic field

To study the propagation of large amplitude pulses along magneto plasma columns, a uniform magnetic field of strength up to 1.2 K Gauss was added to the set-up of fig. 2.5. The field was produced by seven ESI 49 coils arranged in such a fashion that the magnetic field variation over the test region was only $\pm$ 1% . Moreover, the test section in fig. 2.5 was surrounded with a conductor, except at the launcher, and receiver locations.

Initially, the same method (i.e. tube inserted perpendicular to the plates through holes made in them) was used to couple the pulse to the magneto plasma column. It proved to be very inefficient in exciting propagating bulk waves due to great coupling losses. The tube section was then redesigned and copper rings were inserted such that the parallel plates were in direct contact with the plasma. This improved the coupling greatly and proved to be necessary to launch the waves. The modified set up is shown in fig. 2.7. Similar recordings as for the case of no magnetic field were obtained under different conditions of: plasma frequency, magnetic field strength and background neutral pressure.

Before presenting the results of the experiments (both with and without magnetic field), an analytical formulation and analysis of the experimental conditions will be given in the next chapter. In the light of knowledge acquired from such analysis experimental data will then be presented and analyzed.

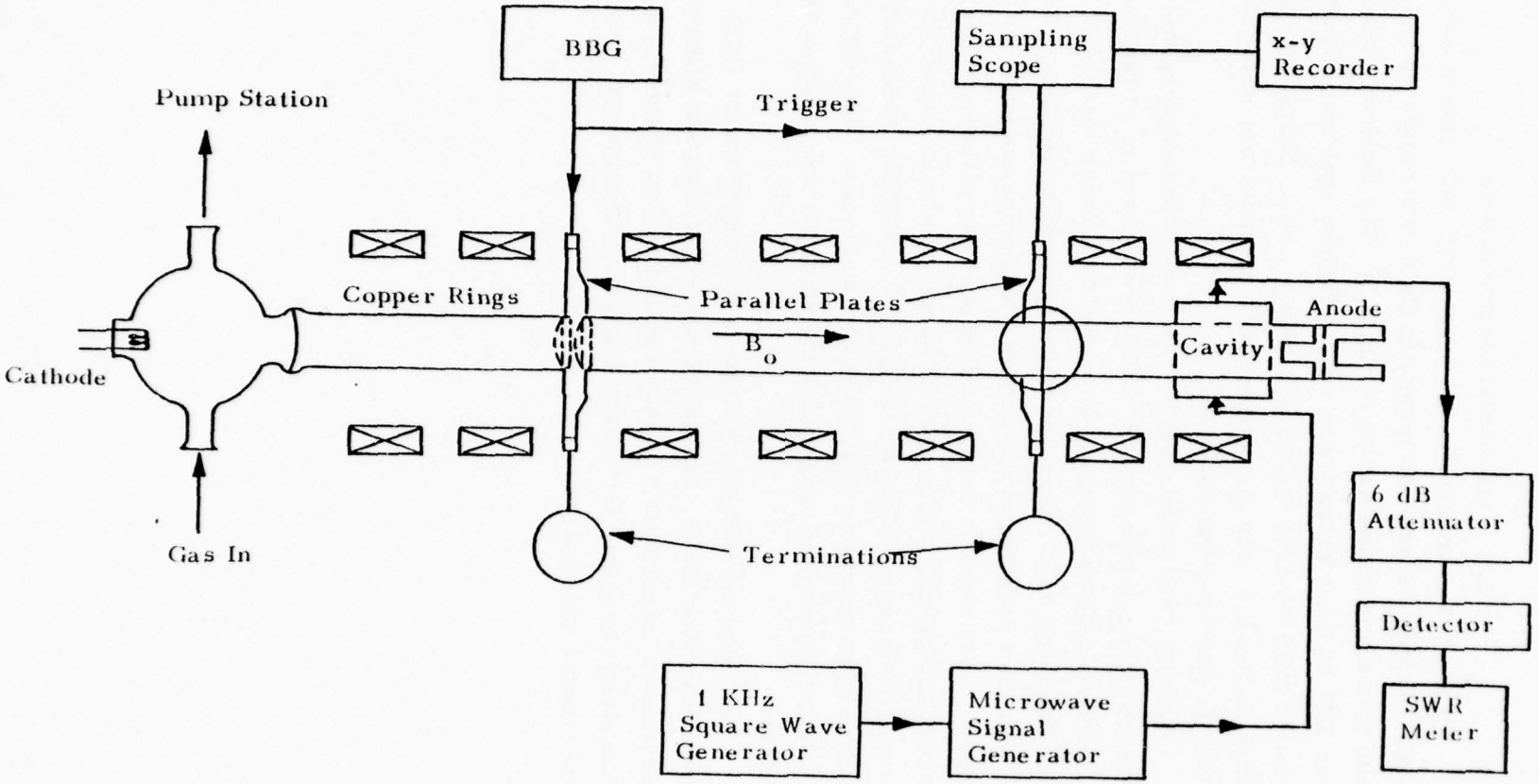

Fig. 2.7 Block diagram of experiment, finite magnetic field

III-3. Analytical Formulation of the Experiment

The problem posed by the experiment is as follows: a plasma column of circular cross-section of radius b, and infinite length, either in free space or surrounded by a conductor, is excited at z = 0 by a finite amplitude source of electromagnetic radiation. In general, a finite axial D. C. Magnetic field is present as shown in Figure 3.1. The spatial and temporal evolution of the excited bounded modes is investigated. This analysis involves the adoption of an appropriate idealized model which is mathematically tractable.

3.1 Analytical Model

Consider a homogeneous plasma column imbedded in the gas from which it is formed by partial ionization. The plasma is considered to be a cold electron gas moving through a stationary neutralizing background of ions. The dynamical interaction between electrons and the background is described by a constant collision frequency ν_c. The interaction is assumed to be such that there is no loss of electrons due to ionization, recombination or attachment. Since the percentage ionization of the discharge is low (.01%), it may be assumed that ν_c is basically the electron neutral collision frequency. The fact that the background density of the discharge is dependent on radius, undermines the assumption of a uniform plasma column, but a compromise is necessary if the finite amplitude analysis is to be mathematically tractable. The effects introduced by the inhomogeneity will be discussed at the proper place.

Quantitatively, Euler's equations will be used to describe the dynamics of the electrons[37]:

$$d_t n + \nabla \cdot n\underset{\sim}{v} = 0 \tag{3-1}$$

$$mnd_t\underset{\sim}{v} + mn\underset{\sim}{v} \cdot \nabla \underset{\sim}{v} + mn\nu_c\underset{\sim}{v} + en\underset{\sim}{E} + n\underset{\sim}{v} \times \mu_o \underset{\sim}{H}_o = 0 \tag{3-2}$$

where

$n(\underset{\sim}{r}, t)$ ≡ electron number density

$\underset{\sim}{v}(\underset{\sim}{r}, t)$ ≡ average electron velocity

ν_c ≡ collision frequency for momentum transfer between electrons and neutrals

$\underset{\sim}{E}(\underset{\sim}{r}, t)$ ≡ electric field intensity

$\underset{\sim}{H}_o$ ≡ background magnetic field intensity

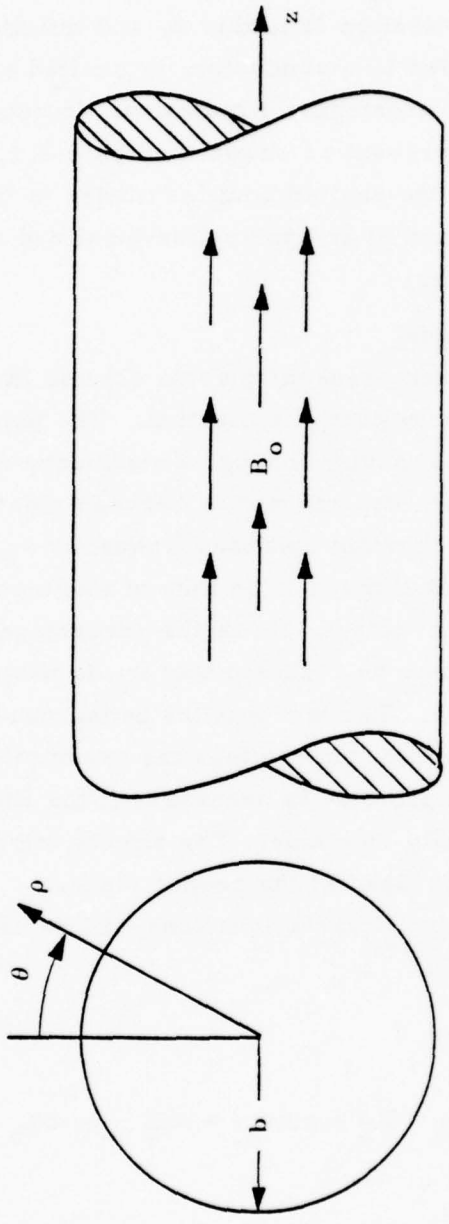

Fig. 3.1 The Magneto-Plasma Column

When stated in the form of (3-1)-(3-2), a series of assumptions must be appended to the exact Euler system. These assumptions may be found in a standard text on plasma dynamics[38].

Since it is our interest to study the interaction of the above plasma model with an electromagnetic field, Maxwell's equations must be added to (3-1) and (3-2):

$$\nabla \times \underset{\sim}{E} = -\mu_o \, d_t \, \underset{\sim}{H} \tag{3-3}$$

$$\nabla \times \underset{\sim}{H} = \epsilon_o \, d_t \, \underset{\sim}{E} + \underset{\sim}{J}_e \tag{3-4}$$

where

$\underset{\sim}{J}_e$ ≡ electric current source.

$\underset{\sim}{J}_e$ involves all electric current densities present, applied or induced. The interaction of plasma and EM field occurs through the quantities $\underset{\sim}{J}_e$ and ne $\underset{\sim}{E}$ in a self-consistent manner. Explicitly

$$\underset{\sim}{J}_e = \underset{\sim}{J}_{app} + \underset{\sim}{J}_c \tag{3-5}$$

where

$\underset{\sim}{J}_{app}$ ≡ externally applied electric current

$\underset{\sim}{J}_c$ ≡ electron convection current in plasma and is given by

$$\underset{\sim}{J}_c = - en\underset{\sim}{v} \tag{3-6}$$

Other contributions to $\underset{\sim}{J}_e$ (such as polarization, currents, drift currents due to plasma inhomogeneities, $\underset{\sim}{E} \times \underset{\sim}{H}$ drifts, etc; and conduction currents) will be neglected. Equations (3-1)-(3-6) form a determinate system of equations through which any interaction problem may be studied, once $\underset{\sim}{J}_{app}$ is specified.

Redefining the product $n\underset{\sim}{v}$ as a new variable:

$$\underset{\sim}{u} = n\underset{\sim}{v} \tag{3-7}$$

and considering n which is a function of space and time as composed of two parts: a time independent part or background and a time dependent part or fluctuating term:

$$n(\underset{\sim}{r}, t) = n_o + \tilde{n}(\underset{\sim}{r}, t) \tag{3-8}$$

where

$\underset{\sim}{n}_o$ ≡ background electron density

$\tilde{n}$ ≡ time varying electron density

and $n_o \gg \tilde{n}$.

The system (3-1)-(3-6) simplifies to[39]:

$$d_t \tilde{n} + \nabla \cdot \underset{\sim}{u} = 0 \tag{3-9}$$

$$m d_t \underset{\sim}{u} + \frac{m}{n_o} \nabla \cdot \underset{\sim}{u}\,\underset{\sim}{u} = -ne\,\underset{\sim}{E} - e\mu_o \underset{\sim}{u} \times \underset{\sim}{H}_o - m\nu_c \underset{\sim}{u} \tag{3-10}$$

$$\nabla \times \underset{\sim}{H} = \epsilon_o d_t \underset{\sim}{E} - e\underset{\sim}{u} + J_{app} \tag{3-11}$$

$$\nabla \times \underset{\sim}{E} = -\mu_o d_t \underset{\sim}{H} \tag{3-12}$$

To this set of equations, we also add

$$\epsilon_o \nabla \cdot \underset{\sim}{E} = -e(n - n_o) = -e\,\tilde{n} \tag{3-13}$$

and

$$\nabla \cdot \underset{\sim}{H} = 0 \tag{3-14}$$

Formally solving equations (3-10) to second order in $\underset{\sim}{u}$ (see Appendix 1) and using the results in eqs. 11; the system is reduced to:

$$\nabla \times \underset{\sim}{H} = \underset{\approx}{\epsilon} \cdot \underset{\sim}{E} + N(\underset{\sim}{E}) + J_{app} \tag{3-15a}$$

$$\nabla \times \underset{\sim}{E} = -\mu_o d_t \underset{\sim}{H} \tag{3-15b}$$

where $\underset{\approx}{\epsilon}$ is a linear operator given by:

$$\underset{\approx}{\epsilon} \rightarrow (\epsilon_o d_t \underset{\approx}{1} + e\,\underset{\approx}{\Pi})$$

and $N(\underset{\sim}{E})$ is a nonlinear term in $\underset{\sim}{E}$ given by:

$$N(\underset{\sim}{E}) \rightarrow \underset{\approx}{\Pi}\left(\frac{m}{n_o^2} \nabla \cdot \underset{\approx}{\Pi}\,\underset{\sim}{E}\,\underset{\approx}{\Pi}\,\underset{\sim}{E} - \frac{\epsilon_o}{n_o} \underset{\sim}{E} \nabla \cdot \underset{\sim}{E}\right)$$

with

$\underset{\approx}{1}$ ≡ unit dyad

and

$$\underset{\approx}{\Pi}\,(d_t, \underset{\sim}{H}, \nu_c) \equiv (m d_t \underset{=}{1} - e\mu_o \underset{\sim}{H}_o \times \underset{=}{1} - m\nu_c \underset{=}{1})^{-1} e n_o$$

Decomposing the gradient operator as $\nabla = \nabla_t + d_z \underset{\sim}{z}_o$, Eq 3-15 may be cast into a form appropriate for guided wave analysis[40]. Written in operator form:

$$(L + i d_z \Gamma)\psi = N(\psi) + i J_{app} \tag{3-16}$$

where, for $\rho < b$ (where b is the radius of the column)

$$L \rightarrow i \begin{pmatrix} -\epsilon_o d_t \underset{=}{1} - e\Pi & \nabla_t \times \underset{=}{1} \\ -\nabla_t \times 1 & -\mu_o d_t \underset{=}{1} \end{pmatrix} \quad \underset{\sim}{\psi}(\underset{\sim}{r}, t) \quad \begin{pmatrix} \underset{\sim}{E} \\ \underset{\sim}{H} \end{pmatrix} \tag{3-16a}$$

$$\Gamma \rightarrow \begin{pmatrix} 0 & -\underset{\sim}{z}_o \times \underset{=}{1} \\ \underset{\sim}{z}_o \times 1 & 0 \end{pmatrix} \qquad N(\psi) \rightarrow i \begin{pmatrix} N(\underset{\sim}{E}) \\ 0 \end{pmatrix} \tag{3-16b}$$

for $\rho > b$, $n_o \rightarrow 0$ and the equations reduce to Maxwell's equation in free space.

Along with these defining equations, boundary conditions must be specified. These are:

For a column in free space

a) plasma boundary is assumed sharp

b) at $\rho = b$, tangential $\underset{\sim}{E}$ and $\underset{\sim}{H}$ fields are continuous

c) solutions must be finite everywhere

d) conditions at the source will be deferred until later

When the column is surrounded by conductor, the above conditions apply except that b) must be restated as: Tangential $\underset{\sim}{E}$ and $\underset{\sim}{H}$ fields are zero @ $\rho = b$.

Now we proceed to obtain a solution to the above posed problem. As a matter of convenience, the source term in Eq. 3-16 will be dropped until the time it needs to be considered to interpret the experimental results.

Taking Fourier transform in time of 3-16, one obtains:

$$L(-i\omega, \nabla_t)\ \psi(\underset{\sim}{r}, \omega) + i\Gamma d_z \psi(\underset{\sim}{r}, \omega) = N[\psi(\underset{\sim}{r}, \omega)] \tag{3-17}$$

where the transformed operators are obtained from Equations 3-17 by recognizing that $d_t \rightarrow -i\omega$ in the transform domain and that the transform of a product is the convolution of the individual transform (see Appendix 1).

We shall seek solutions of the problem in the form of an expansion in terms of the eigenfunctions of the transverse, lossless operator L_0, where $L_0 = L\big|_{\nu_c = 0}$. Assume that $\psi(r, \omega)$ lies in the space spanned by the transverse, lossless eigenvectors; moreover, that the operators in Eq.(3-17) act on this space. Then $\psi(r, \omega)$ may be represented as:

$$\psi(r, \omega) = \sum_{\alpha} a_{\alpha}(z, \omega)\, \psi_{\alpha}(r, \omega) \tag{3-18}$$

where the eigenvalue problem for the ψ_{α} is defined:

$$L_o(-i\omega, \nabla_t)\, \psi_{\alpha} = \kappa_{\alpha}(\omega)\, \Gamma \psi_{\alpha} \tag{3-19}$$

the eigenvectors ψ_{α} possess the orthogonality property

$$(\psi_{\alpha}, \Gamma \psi_{\beta}) = \delta_{\alpha\beta} \tag{3-19a}$$

Using this property of the ψ_{α}'s, the amplitudes in Eq. (3-18) are found to be given by:

$$a_{\alpha} = (\psi, \Gamma \psi_{\alpha}) \tag{3-20}$$

where ψ is the actual nonlinear, lossy field. The equation for determining the co-efficients a_{α} may then be obtained as follows: Scalar multiply Eq (3-17) by ψ_{α} and (3-19) by ψ and subtract:

$$(\psi_{\alpha}, L\psi) - (\psi, L_o\psi_{\alpha}) + i\partial_z(\Gamma\psi, \psi_{\alpha}) + \kappa_{\alpha}(\omega)(\Gamma\psi_{\alpha}, \psi)\,[N(\psi), \psi_{\alpha}]$$

or

$$[\psi_{\alpha}(L - L_o)\psi] + i\partial_z(\psi, \Gamma\psi_{\alpha}) + \kappa_{\alpha}(\omega)\,(\psi, \Gamma\psi_{\alpha}) = [N(\psi), \psi_{\alpha}]$$

identifying $(L - L_o)$ as the loss operator ν, using Eq. (3-20) and then replacing $\psi(\rho, \omega)$ by the expansion Eq. (3-18), we obtain for the amplitudes:

$$i\partial_z \mathcal{A}_\alpha(z,\omega) + \kappa_\alpha(\omega)\mathcal{A}_\alpha(z,\omega) + i\gamma(\omega)\mathcal{A}_\alpha(z,\omega) = i[\underline{\Xi}_\alpha, N(\mathcal{A}_\alpha \underline{E})] \quad (3\text{-}21)$$

where $\gamma(\omega) \equiv (\psi_\alpha, \underline{\underline{\nu}}\, \psi_\alpha)$

Thus, the solution of the field problem is cast into a study of the evolution in z of the modal amplitudes. To arrive at an explicit form, we must evaluate the two inner products involved. To do this, an explicit form for the eigenvectors, ψ_α, must be obtained. Keeping in mind that the goal is in the analysis of the experimental results, we are interested in obtaining a set of eigenvectors to represent the guided field produced by an electric current source directed along $\underset{\sim}{z}_o$ and independent of θ. These are obtained in Appendix 2, for both $\underset{\sim}{H}_o \neq 0$, and $H_o = 0$. The results are summarized below:

For zero magnetic field, the discrete spectrum contains a single eigenvector and the corresponding eigenvalue, i.e., $\alpha = 1$. The properly normalized eigenvector, i.e., normalized as in Eq. (3-19a), is given in component form:

$$E_{\alpha\rho} = \begin{cases} (\kappa_\alpha(\omega)/\omega\epsilon_o)^{1/2}(1/2\beta)^{1/2} \dfrac{I_1(\kappa_{\perp 1}\rho)}{\kappa_{\perp 1}} & \rho < b \\ (\kappa_\alpha(\omega)/\omega\epsilon_o)^{1/2}(1/2\beta)^{1/2} \dfrac{I_0(\kappa_{\perp 1}b)}{K_0(\kappa_{\perp 2}b)} \dfrac{K_1(\kappa_{\perp 2}\rho)}{\kappa_{\perp 2}} & \rho > b \end{cases} \quad (3\text{-}22a)$$

$$H_{\alpha\theta} = \begin{cases} (\omega\epsilon_o/\kappa_\alpha(\omega))^{1/2}(1/2\beta)^{1/2}(1-\omega_p^2/\omega^2) \dfrac{I_1(\kappa_{\perp 1}\rho)}{\kappa_{\perp 1}} & \rho < b \\ (\omega\epsilon_o/\kappa_\alpha(\omega))^{1/2}(1/2\beta)^{1/2} \dfrac{I_0(\kappa_{\perp 1}b)}{K_0(\kappa_{\perp 2}b)} \dfrac{K_1(\kappa_{\perp 1}\rho)}{\kappa_{\perp 2}} & \rho > b \end{cases} \quad (3\text{-}22b)$$

$$E_{\alpha z} = \begin{cases} i(1/\omega\epsilon_o\kappa_\alpha(\omega))^{1/2}(1/2\beta)^{1/\alpha} I_0(\kappa_{\perp 1}\rho) & \rho < b \\ i(1/\omega\epsilon_o\kappa_\alpha(\omega))^{1/2}(1/2\beta)^{1/2} \dfrac{I_0(\kappa_{\perp 1}b)}{K_0(\kappa_{\perp 2}b)} K_0(\kappa_{\perp 2}\rho) & \rho > b \end{cases} \quad (3\text{-}22c)$$

I_1, I_0, K_0, K_1, are the modified Bessel functions of the given order, $\kappa_{\perp 1}$, $\kappa_{\perp 2}$ and the eigenvalue $\kappa(\omega)$ (the α may be dropped from the eigenvalue; however, it will be retained on the eigenvector so as to differentiate it from the total field) are related as follows:

$$\kappa_{\perp 1}^2 = \kappa^2 - (1 - \omega_p^2/\omega^2)\,\kappa_0^2 \tag{3-23a}$$

$$\kappa_{\perp 1}^2 = \kappa^2 - \kappa_0^2 \qquad \kappa_0^2 = \omega^2 \mu_o \epsilon_o \tag{3-23b}$$

$$(1 - \omega_p^2/\omega^2)\,\frac{I_1(\kappa_{\perp 1} b)}{\kappa_{\perp 1} I_o(\kappa_{\perp 1} b)} + \frac{K_1(\kappa_{\perp 2} b)}{\kappa_{\perp 2} K_o(\kappa_{\perp 2} b)} = 0 \tag{3-23c}$$

For low Magnetic fields ($\omega_c < \omega_p$), column surrounded by conductor, we make the assumption that the waves are slow and therefore are primarily of a TM type.[8] The exact eigenvectors are then approximated by the quasi-static eigenvectors:

$$E_{\alpha_z} = iAJ_o(\kappa_{\perp 1}\rho) \tag{3-24a}$$

$$E_{\alpha_\rho} = A\kappa_\alpha \frac{\epsilon_3}{\epsilon_1}\,\frac{J_1(\kappa_{\perp 1}\rho)}{\kappa_{\perp 1}} \tag{3-24b}$$

$$H_{\alpha_\theta} = A\omega\epsilon_o\epsilon_3\,\frac{J_1(\kappa_{\perp 1}\rho)}{\kappa_{\perp 1}} \tag{3-24c}$$

Where J_o, J_1 are the Bessel function of the first kind,

$$\epsilon_3 = \epsilon_o\left[1 - \frac{\omega_p^2}{\omega^2 - \omega_c^2}\right],\quad \epsilon_1 = 1 - \frac{\omega_p^2}{\omega^2},\quad \kappa_{\perp 1}^2 = -\kappa_2^2\,\frac{\epsilon_3}{\epsilon_1} \text{ and } \kappa_{\perp 1} b = p_n \tag{3-24d}$$

p_n is the nth zero of J_o. The normalization constant is given (from Eq. 3-19a) by:

$$A = \frac{\kappa_{\perp 1}}{(\omega \kappa_\alpha \epsilon_o / \epsilon_1)^{1/2} \epsilon_3 b J_1(\kappa_{\perp 1} b)} \tag{3-25}$$

In the limit of large magnetic fields; i. e. $\omega_c/\omega >> 1$, $\omega_c/\omega_p >> 1$; the eigenvectors are obtained from the exact equations and are given by:

$$E_{\alpha_z} = iA' J_o(\kappa_{\perp 1} \rho) \tag{3-26a}$$

$$E_{\alpha_\rho} = A' \frac{\kappa_\alpha \epsilon}{\kappa_{\perp 1}} J_1(\kappa_{\perp 1} \rho) \tag{3-26b}$$

$$H_{\alpha_\theta} = A' \frac{\omega \epsilon_o \epsilon}{\kappa_{\perp 1}} J_1(\kappa_{\perp 1} \rho) \tag{3-26c}$$

where

$$\kappa_{\perp 1}^2 = \epsilon(\omega^2 \mu_o \epsilon_o - \kappa_\alpha^2) \qquad \epsilon = 1 - \omega_p^2/\omega^2$$

$$\kappa_{\perp 1} b = p_n$$

and the normalization constant given by:

$$A' = \frac{\kappa_{\perp 1}}{(\omega \kappa_\alpha \epsilon_o)^{1/2} \epsilon b J_1(\kappa_{\perp 1} b)} \tag{3-27}$$

For completeness, the properly normalized eigenvectors for the case of a column in free space with an infinite magnetic field present are also derived in Appendix 2, but not reproduced here.

Using these eigenvectors, the various terms in equation 3-21 can be evaluated explicitly. Expanding the various inner product, the amplitude equation may be rewritten as:

$$id_z \mathcal{A}_\alpha(z,\omega) + \kappa_\alpha(\omega)\mathcal{A}_\alpha(z,\omega) + i\gamma(\omega)\mathcal{A}_\alpha(z,\omega)$$

$$= \int_{-\infty}^{\infty} \mathcal{L}(\omega,\omega_1,\omega_2)\,\mathcal{A}_\alpha(z,\omega_1)\;\mathcal{A}_\alpha(z,\omega_2)\,\delta(\omega-\omega_1-\omega_2)\,d\omega_1\,d\omega_2 \qquad (3\text{-}28)$$

where $\mathcal{L}(\omega,\omega_1,\omega_2)$ is the Kernel of the integral operator. The effects of collisions have been neglected in R.H.S. $\gamma(\omega)$ and $\mathcal{L}(\omega,\omega_1,\omega_2)$ are given by (see Appendix 3):

For zero magnetic field, column in free space,

$$\mathcal{L} \to \frac{e\epsilon_o}{m}\frac{\omega_p^2}{\omega_1\omega_2}\int_o^b [P(\omega,\omega_1,\omega_2,\rho) - W(\omega,\omega_1,\omega_2,\rho)]\,\rho\,d\rho \qquad (3\text{-}29)$$

where

$$P(\omega,\omega_1,\omega_2,\rho) = \left(\frac{\kappa(\omega_1)\kappa(\omega_2)\kappa(\omega)}{\omega_1\omega_2\omega\,\epsilon_0^3 2^3\beta^1\beta^2\beta^o}\right)^{1/2} \frac{I_1'^{(2)}}{\kappa_{\perp 1}^{(2)}}\,\frac{I_1'^{(0)}}{\kappa_{\perp 1}^{(2)}}\,\frac{I_1'^{(2)}}{\kappa_{\perp 1}^{(1)}} \qquad (3\text{-}29a)$$

$$W(\omega,\omega_1,\omega_2,\rho) = \kappa(\omega_1)\left(\frac{\kappa(\omega_1)\kappa(\omega)}{\kappa(\omega_2)\omega_1\omega_2\omega\,\epsilon_o^3 2^3\beta\,\beta^1\beta^2}\right)^{1/2} I_0^{(2)}\frac{I_1^{(0)}}{\kappa_{\perp 1}^{(0)}}\frac{I_1^{(1)}}{\kappa_{\perp 1}^{(0)}}$$

$$+\left(\frac{\kappa(\omega_2)}{\kappa(\omega_1)\kappa(\omega)\omega_1\omega_2\omega\,\epsilon_o^3 2^3\beta\,\beta^1\beta^2}\right)^{1/2}\left[I_0^{(1)}\,I_0^{(2)}\,I_0^{(0)} - \frac{I_1^{(2)}}{\kappa_{\perp 1}^{(2)}}\,I_0^{(0)}\right] \qquad (3\text{-}29b)$$

$f^{(i)} \to f(\omega_i)$ $i = 0, 1, 2$; $\omega_o \equiv \omega$, and the prime denotes $\frac{d}{d\rho}$ and

$$\gamma(\omega) = \frac{\omega_p^2\nu}{\omega^2+\nu^2}\,\frac{\kappa(\omega)}{\omega 2\beta}\left\{\int_o^b \frac{I_1^2(\kappa_{\perp 1}\rho)}{\kappa_{\perp 1}^2}\,\rho\,d\rho + \int_o^b \frac{I_o^2(\kappa_{\perp 1}\rho)}{\kappa_\alpha^2}\,\rho\,d\rho\right\}$$

For small axial magnetic fields, column surrounded by a conductor:

$$\mathcal{L} \to \frac{-e\epsilon_o}{m}\left[\left(2 - \frac{\omega_p^2}{\omega_p^2+\omega_c^2}\right)\frac{\omega_p^2}{\omega\,\omega_1\,\omega_2} + \frac{\omega_p^2\,\omega_c^2}{\omega\,\omega_1^2\,(\omega_p^2+\omega_c^2)}\right]$$

$$\kappa_\alpha(\omega_1)A(\omega_1)\,A(\omega_2)\,A(\omega)\int_o^b J_o^3(\kappa_{\perp 1}\rho)\,\rho\,d\,\rho \qquad (3\text{-}30)$$

this form of $\mathcal{L}$ is obtained by using the assumption that the maximum contribution to the nonlinear term is due to the coupling of the longitudinal component of the total field. This is consistent with the quasi-static assumption (see Appendix 3). When the axial field goes to infinity,

$$\mathcal{L} \to \frac{-e\epsilon_o}{m}\left[\frac{2\omega_p^2}{\omega\,\omega_1\,\omega_2} + \frac{\omega_p^2}{\omega\,\omega_1^2}\right]\kappa_\alpha(\omega_1)\,A'(\omega_1)\,A'(\omega)\,A'(\omega_\alpha)$$

$$\int_o^b J_o^3(\kappa_{\perp 1}\rho)\rho\,d\,\rho \qquad (3\text{-}31)$$

Note that equation 3-30 reduces to the above equation in the limit $\omega_c \to \infty$.

The collision term is given by:

$$\gamma(\omega) \to \int_o^b \left[A^2(\omega)\,J_o^2(\kappa_{\perp 1}\rho)\,\rho\,d\,\rho\right]\frac{\omega_p^2\nu\,\epsilon_o}{\omega^2+\nu^2} \qquad (3\text{-}32)$$

The above forms of $\mathcal{L}$ and γ apply for the column in free space, with an infinite axial magnetic field present. However the proper normalization $A(\omega)$ must be used (see Appendix 2).

To continue the analysis, the functional dependence of κ_α on ω must be obtained.

3.2 Functional relation between κ_α and ω

a) No axial magnetic field:

Since there is only one mode present, the functional relationship may be obtained from equations (2-23). This set of equations is

transcendental and an explicit solution for κ_α in terms of ω is impossible. Computer solution of these equations is shown in figure 3.2. In order to carry analytical methods further so as to gain insight into the phenomena, an approximate analytical function of ω will be used for κ_α. The approximation is derived from the behavior of κ_α in equations 2.23 for large and small ω.

For $\omega \to 0$, equation (2-23c) reduces to:[16]

$$-(\kappa_\alpha^2 b^2 - \kappa_o^2 b^2) \ln (\kappa_\alpha^2 b^2 - \kappa_o^2 b^2)^{1/2} = Kp \frac{I_o(Kp)}{I_1(Kp)} \frac{\omega^2}{\omega_p^2}$$

where $Kp = \dfrac{\omega_p b}{c}$ $\kappa_o = \dfrac{\omega}{c}$ $c \equiv$ speed of light.

Equation (2-23c) may be further reduced to

$$\kappa_\alpha = \left(Kp \frac{I_o(Kp)}{I_1(Kp)} + \frac{\omega_p^2 b^2}{2c^2} \right)^{1/2} \frac{\omega}{\omega_p} \tag{3-33}$$

thus for $\omega \to 0$, κ_α and ω are linearly related. Moreover, for $\omega \to \omega_p/\sqrt{2}$, a resonance is observed. The appropriate choice of approximate equation must take cognizance of these facts. Such a choice is given by:

$$\kappa_\alpha^2 = \frac{\omega^2}{v_o^2} \left(\frac{1}{1 - 2\ \omega^2/\omega_p^2} \right) \tag{3-34}$$

where

$$v_o^2 = \omega_p^2 b^2 \left(Kp \frac{I_o(Kp)}{I_1(Kp)} + \frac{\omega_p^2 b^2}{2c^2} \right)^{-1}$$

the values of κ_α obtained from (3-34) were compared with those obtained by computer solution of equations (3-23) and (3-34). The values of v_o obtained for a best fit were:

$$v_o = \begin{cases} (.5163422)\ \omega_p b & \text{for 14 point fit} \\ (.67165)\ \omega_p b & \text{for 21 point fit} \end{cases} \tag{3-34a}$$

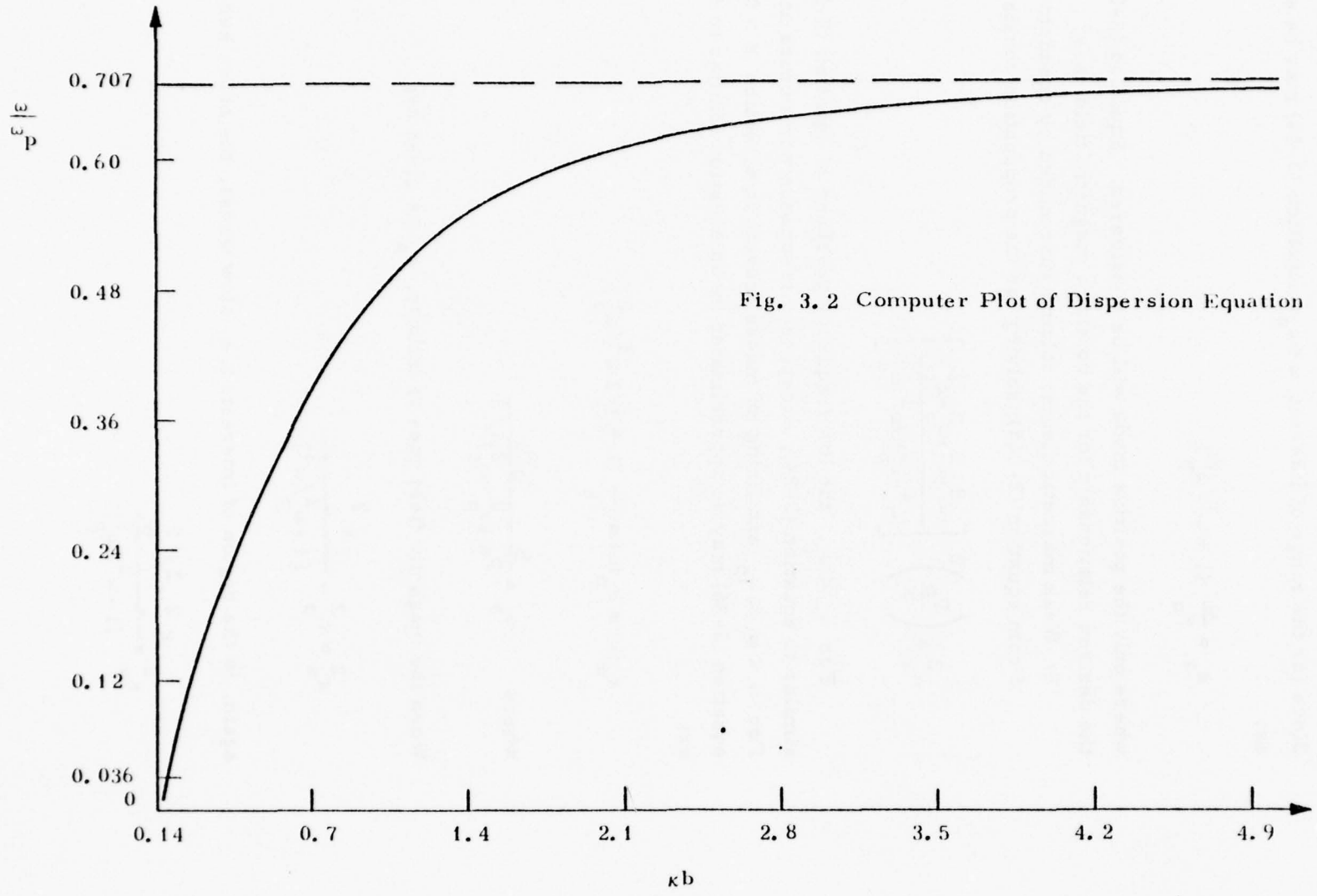

Fig. 3.2 Computer Plot of Dispersion Equation

Since for the range of interest $\omega < \omega_p$; equation (3-34) may be expanded as:

$$\kappa_\alpha = \frac{\omega}{v_o} \left(1 + \omega^2/\omega_p^2\right) \tag{3-35}$$

where only the positive mode will be considered. Equation (3-35) is the desired relationship for the no static magnetic field case.

b) Weak magnetic fields; column surrounded by conductor

From equation (2-24d); solving for the propagation constant[8]

$$\kappa_\alpha^2 = \left(\frac{p_n}{b}\right)^2 \left[\frac{-\omega^2(\omega^2-\omega_p^2-\omega_c^2)}{(\omega^2-\omega_p^2)(\omega^2-\omega_c^2)}\right] \tag{3-36}$$

For $\omega_c < \omega_p$, the low frequency passband of equation (3-36) is similar to equation (3-34), except that resonance now occurs at ω_c. For $\omega < \omega_c < \omega_p$ and fixing on modes moving in direction $z > 0$; equation (3-36) may be approximated by an equation similar to (3-35) as:

$$\kappa_\alpha(\omega) = \kappa_n(\omega) = \frac{\omega}{v_s} \left(1 + 1/2\, \omega^2/\omega_c^2\right) \tag{3-37}$$

where $$v_s = \frac{b}{p_n} \frac{\omega_p \omega_c}{(\omega_p^2+\omega_c^2)^{1/2}}$$

When the magnetic field goes to infinity, κ_α is given by:

$$\kappa_\alpha^2 = \kappa_o^2 - \frac{\kappa_\perp^2}{[1-\omega_p^2/\omega^2]}$$

again, in the region of interest, i.e. slow waves, the above becomes:

$$\kappa_\alpha^2 = \frac{\kappa_\perp^2 \omega^2/\omega_p^2}{(1-\omega^2/\omega_p^2)}$$

or

$$\kappa_\alpha = \kappa_n(\omega) = \frac{\omega}{v_\infty}\left(1 + 1/2\ \omega^2/\omega_p^2\right) \tag{3-38}$$

Where $v_\infty = \omega_p / \kappa_\perp$ and $\kappa_\perp = p_n / b$. (3-38a)

By equations (3-35), (3-37) and (3-38), the coefficients that appear in the amplitude equation (3-28) have been explicitly defined. In the next section the final form of the amplitude equation is obtained.

3.3 Final Form of Amplitude Equation

Using the approximate relations, derived in 3.2, between κ_α and ω; Eq. (3-28) may be written in its final form.

A. No Magnetic Field:

Using Eq. (3-35), Eq. (3-3a), and the results of Appendix 3 in Equation (3-28), we finally obtain for the modal amplitude:

$$i\,d_z a_\alpha(z,\omega) + \left(-\frac{\omega}{v_o} + \frac{\omega^3}{v_o \omega_p^2}\right) a_\alpha(z,\omega) + i\,\frac{\nu_c}{v_o}\, a_\alpha(z,\omega)$$

$$= C_1 \int_o^\Omega \omega_1 \omega_2 \omega\, a_\alpha(z,\omega_2)\, a_\alpha(z,\omega_1)\, d\lambda + C_2 \int_o^\Omega \omega_1^2 \omega\, a_\alpha(z,\omega_1)\, a_\alpha(z,\omega_2)\, d\lambda$$

$$+ C_3 \int_o^\Omega \omega_2 \omega_1^2\, a_\alpha(z,\omega_1)\, a_\alpha(z,\omega_2)\, d\lambda + C_4 \int_o^\Omega \omega_2\, a_\alpha(z,\omega_2)\, a_\alpha(z,\omega_1)\, d\lambda \tag{3-39}$$

where: $d\lambda \rightarrow \delta(\omega - \omega_1 - \omega_2)\, d\omega_1\, d\omega_2$

$$C_1 = \frac{e}{m}\,\frac{b}{2^5}\left\{\frac{1}{\omega_p^2 v_d^6 v_o^3 \epsilon_o}\right\}^{1/2} \tag{3-39a}$$

$$C_2 = -\frac{e}{m}\,\frac{b}{2^4}\left\{\frac{1}{\omega_p^6 v_d^6 v_o \epsilon_o}\right\}^{1/2} \tag{3-39b}$$

$$C_3 = +\frac{e}{m}\,\frac{b}{2^4}\left\{\frac{\omega_p^2}{\omega_p v_d^6 v_o^3 \epsilon_o}\right\}^{1/2} \tag{3-39c}$$

$$C_4 = -\frac{e}{m}\,\frac{1}{2b}\left\{\frac{v_o}{\omega_p^2 v_d^6 \epsilon_o}\right\}^{1/2} \tag{3-39d}$$

and v_d is given in appendix 3.

Multiplying by -i, and recognizing that $-i\omega \rightarrow \partial_t$, the above equation transforms to the time domain as,

$$d_z a_\alpha(z,t) + \frac{1}{v_o} d_t a_\alpha(z,t) - \frac{1}{v_o \omega_p^2} d_t^3 a_\alpha(z,t) + \frac{\nu_c}{v_o} a_\alpha(z,t) = C_1 \partial_t \left(d_t a_\alpha(z,t)\right)^2$$

$$+ C_2 d_t \left(a_\alpha d_t^2 a_\alpha\right) + C_3 d_t^2 a_\alpha(z,t)\, d_t a_\alpha(z,t) + C_4 a_\alpha(z,t)\, d_t a_\alpha(z,t).$$

Expanding the R. H. S. of the above and collecting terms:

$$d_z a_\alpha(z,t) + \frac{1}{v_o} d_t a_\alpha(z,t) - \frac{1}{v_o \omega_p^2} d_t^3 a_\alpha(z,t) + \frac{\nu_c}{v_o} a_\alpha(z,t)$$

$$= C_1' d_t a_\alpha(z,t)\, d_t^2 a_\alpha(z,t) + C_2 a_\alpha d_t^3 a_\alpha + C_4 a_\alpha d_t a_\alpha \qquad (3\text{-}40)$$

where $C_1' = 2C_1 + C_2 + C_3$

this equation is the final form of the amplitude equation. It holds for times such that $a_\alpha(z,\omega) = 0$ for $\omega > \Omega$. Moreover, the linear damping term must be modified for cases where $a_\alpha(z,\omega) \neq 0$ for $\omega \leq \nu_c$ These implications will be discussed in section 3.4.

B. Infinite Magnetic Field.

The final form of the modal amplitude equation for this case is obtained using equations (3-31), (3-38) and the results of appendix 3 in equation (3.28). Note that from Appendix 3, it has been assumed that only a single mode (the lowest order) is propagating i.e., the α's reduce to only one. For the case of a metal conductor surrounding the plasma column,

$$i d_z a_\alpha(z,\omega) + \left(\frac{\omega}{v_\infty} + \frac{\omega^3}{2 v_\infty \omega_p^2}\right) a_\alpha(z,\omega) + i C_c a_\alpha(z,\omega)$$

$$= C_4' \int_o^\Omega \omega_1\, a_\alpha(z,\omega_1)\, a_\alpha(z,\omega_2)\, d\lambda \qquad (3\text{-}41)$$

where $C_4' = \frac{3e}{m}\left(\frac{k_\perp}{b}\right)^3 \frac{1}{\omega_p^4} \sqrt{\frac{v_\infty}{\epsilon_o}} \quad \frac{\int_o^b J_o^3(k_\perp o)\, o\, do}{J_1^3(k_\perp b)}$

and C_c given in Appendix 3.

since $\int_0^b J_0^3(k_\perp \rho)\, d\rho = .72\, b^2/2\, J_1^2(kb)$

$$C_4' = 1.08\ \frac{e}{m}\ \frac{k_\perp^3}{b}\ \frac{1}{\omega_p^4}\ \sqrt{\frac{v_\infty}{\epsilon_0}}\ \frac{1}{J_1(k_\perp b)}$$

multiplying by -i and transforming into time domain:

$$d_z \mathcal{A}_\alpha(z,t) + \frac{1}{v_\infty}\, d_t \mathcal{A}_\alpha(z,t) - \frac{1}{2 v_\infty \omega_p^2}\, d_t^3 \mathcal{A}_\alpha(z,t) + C_c \mathcal{A}_\alpha(z,t)$$

$$= C_4^f\ {}_\alpha(z,t)\, d_t \mathcal{A}_\alpha(z,t) \qquad (3\text{-}42)$$

when there is no conducting wall present, the constant C_4^f above is given by:

$$C_4^f = \frac{3}{2}\ \frac{e}{m}\ \frac{}{\omega_p v_\infty^3 b}\ \sqrt{\frac{v_\infty}{\epsilon_0}} \qquad (3\text{-}43)$$

where v_∞ is given by: (3-38a)

Equation (3-28) is a Kortweg-de Vries equation with a damping term for the modal amplitude. It is valid only up to times when the frequency spectrum of $\mathcal{A}_\alpha(z,t)$ contain frequencies close to ω_p.

C. Weak Magnetic Field, column surrounded by a perfect waveguide.

The derivation follows the same fashion as that leading to equation (3-41) (see Appendix 3), with the exception that the constant coefficients are different. From eqs. (3-30), for the nonlinear term; equation (3-37) for the dispersion relation and (3-25) for the normalization constant, we have from appendix 3:

$$d_z \mathcal{A}_\alpha(z,t) + \frac{1}{v_s}\, d_t \mathcal{A}_\alpha(z,t) - \frac{1}{2 v_s \omega_c^2}\, d_t^3 \mathcal{A}_\alpha(z,t)$$

$$= C_4'' \mathcal{A}_\alpha(z,t)\, d_t \mathcal{A}_\alpha(z,t) \qquad (3\text{-}44)$$

where C_c = collision coefficient and is approximately given by (3-39)

$$C_4'' = \frac{e}{m}\left(\frac{k_\perp}{b}\right)^3 \frac{\sqrt{(\omega_p^2+\omega_c^2)^3}}{\omega_p^4\omega_c^3}\sqrt{\frac{v_s}{\epsilon_o}}\;\frac{\int_o^b J_o^3(k_\perp\rho)\,d_o}{J_1^3(k_\perp b)}$$

$$C_4'' = .36\,\frac{e}{m}\,\frac{k_\perp^3}{b}\,\frac{\omega_c}{\omega_p^4}\sqrt{\frac{v_s}{\epsilon_o}}\,\frac{1}{J_1(k_\perp b)}\,\frac{\sqrt{(\omega_p^2+\omega_c^2)^3}}{\omega_c^3}$$

Equation (3-44a) is also a Kortweg-de Vries equation for the model amplitude. For this case, it is valid up to times when the frequency spectrum of $\mathcal{A}_\alpha(z,t)$ contain frequencies close to the Cyclotron frequency, ω_c.

3.4 Analysis of the Amplitude Equation

Comparing the magnitude of the terms on the right hand side of equation (3-39), we find that the last term [the term whose coefficient is C_4] is the dominant one. From equation 6-37 of Appendix 3, observe that this term arises from the nonlinear coupling of the longitudinal electric field of waves of different frequencies. Since, from equations (2-21), the magnitude of the longitudinal field is greater than the transverse field, it is expected that the strongest nonlinearity would result from interactions involving only the longitudinal components of the field. Neglecting the other two terms in the R. H. S. of (3-39), the resulting equation has the same form as equation (3-42), i. e., Eq. (3-39) reduces to the K-de V equation.

Thus the evolution in z of the modal amplitudes is described by an equation of the K-de V type. This results in the recognition that propagation of large amplitude slow waves and surface waves along a plasma column belong to a very general class of nonlinear wave phenomena, i. e., nonlinear dispersive waves. It is important to note that the sign of the nonlinear term in (3-42) is opposite to the corresponding one in (3-39). This difference results in qualitatively different behavior of the solution which will be discussed in the next section.

Noting from Equation (3-18) that, since for each case we are only considering a single mode, the field solution is:

$$\psi(\underset{\sim}{\rho}, t; z) = \int_{-\infty}^{\infty} \mathcal{A}_\alpha(z, \omega)\, \psi_\alpha(\rho, \omega) e^{-i\omega t}\, \frac{d\omega}{2\pi}$$

where $\mathcal{A}_\alpha(z, \omega)$ and $\psi_\alpha(\rho, \omega)$ are given by Eqs. (3-39) and (3-22) respectively, for surface waves and by Eqs. (3-24) and (3-42) respectively for body waves. In particular, for the longitudinal electric field of the waves:

$$E_z(\rho, \omega; z) = \mathcal{A}_\alpha(z, \omega)\, E_\alpha(\rho, \omega)$$

Putting in the value for $E_\alpha(\rho, \omega)$ for either case, we find in the regime $\kappa_1 b < 1$

$$E_z(\rho, \omega; z) \sim \text{const} \cdot i\omega\, \mathcal{A}_\alpha(z, \omega) \qquad (3\text{-}45a)$$

or from inversion:

$$E_z(\rho, t; z) \sim - \text{const}\ \partial_t \mathcal{A}_\alpha(z, t). \tag{3-45b}$$

This result is very convenient since it allows the solution of Eqs. (3-42) or (3-39) to be immediately associated with the longitudinal electric field of the wave. Thus the Modal Amplitude acts as a potential whose time derivative is proportional to the longitudinal E field.

Rewriting equations (3-42) and (3-39) as

$$\partial_z \mathcal{A}_\alpha(z, t) + \frac{1}{v_i} \partial_t \mathcal{A}_\alpha(z, t) - C_d \partial_t^3 \mathcal{A}_\alpha(z, t) + C_c' \mathcal{A}_\alpha(z, t)$$
$$- C_4^m \mathcal{A}_\alpha(z, t)\, \partial_t \mathcal{A}_\alpha(z, t) = 0 \tag{3-46}$$

where

$$v_i = \begin{cases} v_o & \underset{\sim}{B}_o = 0 \\ v_\infty & \underset{\sim}{B}_o = \infty \\ v_s & \text{Weak } B_o \end{cases}$$

$$C_d = \begin{cases} 1/\omega_p^2 v_o & \text{No magnetic field} \\ 1/2\omega_p^2 v_\infty & \text{Infinite magnetic field} \\ 1/2 v_s \omega_c^2 & \text{Weak magnetic field} \end{cases}$$

$$C_c' = \begin{cases} \nu_c/v_o & \text{No magnetic field} \\ C_{c_1} \\ \\ C_{c_2} \end{cases} \quad \text{Infinite Magnetic field} \begin{cases} \text{column surrounded by perfect conductor} \\ \text{column in free space} \end{cases}$$
$$C_{c_3} \quad \text{Weak magnetic field}$$

$$C_4^{\pm} \begin{cases} -\frac{1}{2}\frac{e}{m}\sqrt{\frac{v_o}{\epsilon_o}}\,\frac{1}{v_d^3} & \text{No magnetic field} \\ \frac{3}{2}\frac{e}{m}\,\frac{1}{v_d^3}\sqrt{\frac{v_\infty}{\epsilon_o}} & \text{Infinite magnetic field; column in free space} \\ 1.08\,\frac{e}{m}\,\frac{k_\perp^3}{b}\,\frac{1}{\omega_p^4}\sqrt{\frac{v_\infty}{\epsilon_o}}\,\frac{1}{J_1(k_\perp b)} & \text{Infinite magnetic field; column surrounded by perfect conductor} \\ \frac{.36}{\omega_c^3}\,\frac{e}{m}\,\frac{k_\perp^3}{b}\,\frac{(\omega_p^2+\omega_c^2)^{3/2}}{\omega_p^3}\sqrt{\frac{v_s}{\epsilon_o}}\,\frac{1}{J_1(k_\perp b)} & \text{Weak magnetic field} \end{cases}$$

With the observation made in (3-45), Equation (3-46) may be used as the starting point for the study of pulse propagation, of limited band-width and finite amplitude, along a plasma column with infinite axial magnetic field, or with a weak magnetic field, respectively. Ikezey et al[34], using quasi-static approximation derived a K-de-V Equation for the evolution in time of the potential of an electron acoustic wave propagating in a cylindrical plasma column in an infinite magnetic field and surrounded by a perfect conductor.

The K-de-V equation can be obtained for other kinds of plasma waves, for example ion waves in a cold plasma for the case $\omega_{ce} >> \omega_{pe}$ [41] hydromagnetic waves[42], and for other wave phenomena[43]. For a comprehensive survey of K-de-V literature see [44].

As previously pointed out we could not operate the experiment in the regime $\omega_{ce} >> \omega_{pe}$. Results were obtained only for $\omega_{ce} = 0$ and $\omega_{ce} < \omega_{pe}$. Even though the dispersion relation for symmetric body waves in the regime $f_{ce} < f_{pe}$ can be approximated by an equation of the form (3-37), the structure of the properly normalized and exact eigenvectors is rather complex and is not amenable to analytical manipulation. The coupling coefficients in the equations for the modal amplitudes (more than one mode has to be considered[16]) would not be simple functions of frequency, and numerical solution would have been

inevitable. By properly approximating the exact eigenvectors, the coupling coefficients in the modal amplitude equations could be simplified, and the analytical result in the form of Equation (3-46) was then possible.

Since no attempt is made here to solve the K-de-V equation either analytically or numerically the equation for the modal amplitude will be subsequently normalized so that the results obtained by others[42] may be used to enable us to rephrase the results obtained in Chapter III.

Introducing new variables, and restricting ourselves to experimental conditions:

$$\hat{a}_\alpha(z,t) = \begin{cases} +\omega_p b \left| C_4^{m} \right| a_\alpha(z,t) & \text{No magnetic field} \\ -\omega_c b \left| C_4^{m} \right| a_\alpha(z,t) & \text{Weak magnetic field} \end{cases} \tag{3-47a}$$

$$z' = \begin{cases} \dfrac{z}{b} & \text{No magnetic field} \\ \dfrac{z}{b} & \text{Weak magnetic field} \end{cases} \tag{3-47b}$$

$$t' = \begin{cases} \omega_p(t - z/v_o) & \text{No magnetic field} \\ \omega_c(t - z/v_s) & \text{Weak magnetic field} \end{cases} \tag{3-47c}$$

We obtain from (3-46) and (3-47):

$$\partial_{z'} \hat{a}_\alpha(z',t') + b C_c' \hat{a}_\alpha(z',t') \partial_{t'} \hat{a}_\alpha(z',t') - \alpha' \partial_{t'}^3 \hat{a}_\alpha(z',t') = 0 \tag{3-48}$$

where $\alpha' = \begin{cases} \omega_p b / v_o & \text{No magnetic field} \\ \omega_c b / 2 v_s & \text{Weak magnetic field} \end{cases}$

Equation (3-48) is in the "standard form" (neglecting the collision term) discussed by Berezin and Karpman [42]. They investigated the evolution, for different values of α', of a disturbance at $z = 0$, radiated for a bounded time interval Δ, i.e., given $\hat{a}_\alpha(0, t') \sim \phi(t'/\Delta)$. How does $\hat{a}_\alpha(z', t')$ depend on Δ and α, if $\hat{a}_\alpha(z', t')$ evolves as in (3-48).

The boundary condition for (3-48) may be obtained from the experiment as follows: from figure 2-7, as the BBG pulse propagates in the parallel plate structure, part of its energy is coupled to a radiation field, part to a plasma guided field and the rest is dissipated by the termination. The amount of energy that goes into each type depends on how well the parallel plate couples to that mode. Even though we measured the coupling of energy by the parallel plate structure to the guided field as a function of frequency, an absolute measurement on the percentage of energy of the initial pulse that goes into the guided field could not be done. The unnormalized modal amplitude at $z = 0$, i.e., $a_\alpha(0, t)$ is related to the longitudinal electric field component of guided field, excited by the pulse, by equation (3-45a), and therefore from equation (3-45b):

a) No magnetic field:

$$\partial_{t'} \hat{a}_\alpha(0, t') = -\frac{1}{2}\left(\frac{e}{m}\frac{b}{v_o^2}\right) E_z(b, 0, t') \tag{3-49}$$

Note that the factor in parenthesis has the dimensions of $(\text{coul-sec}^2)/(\text{kg-cm})$ or of $(\text{electric field})^{-1}$ as it should. Since

$v_o = \omega_p b(.67165)$:

$$\partial_{t'} \hat{a}_\alpha(0, t') = -1.9503 \times 10^{\text{n}} \frac{1}{\omega_p^2 b} E_z(b, 0, t') \tag{3-50}$$

with

ω_p in sec^{-1}

b in cm

E_z in $\frac{\text{kg-cm}}{\text{Coul-sec}^2}$

$E_z(b, 0, t')$ is the longitudinal field, evaluated at the boundary of the column of the "already set up" guided field at $z = 0$. It is not the actual BBG pulse. However, since the field is applied for a finite amount of time, we expect that the guided field at $z = 0$ also possess this characteristic in time, but as mentioned before, its absolute strength is unknown.

b) Weak magnetic field

From (3-24), $E_z(\rho, 0, \omega) \sim \hat{E}_z(0, \omega)\, J_o(k_\perp \rho)$

$$\partial_{t'} \hat{a}_\alpha(0, t') = + (3.664 \times 10^{m}) \frac{\omega_p^2 + \omega_c^2}{\omega_p^2\, \omega_c^2\, b} \hat{E}_z(0, t') \tag{3-51}$$

Looking into the physical consequences of the above theory, let us first consider the linearized equation obtained from (3-48) when the nonlinear term, $\hat{a}_\alpha \partial_{t'} \hat{a}_\alpha$, is neglected. The resulting equation is the Airy equation with a damping term

$$\partial_{z'} \hat{a}_\alpha(z', t') + b\, C_c' \hat{a}_\alpha(z', t') - \alpha' \partial_{t'}^3 \hat{a}_\alpha(z', t') = 0$$

whose solution is:

$$\hat{a}_\alpha(z', t') = \int_{-\infty}^{\infty} \hat{a}_\alpha(\omega)\, e^{i(\kappa(\omega) z' - \omega t')} \frac{d\omega}{2\pi} \tag{3-52}$$

with

$$\kappa(\omega) = \alpha' \omega^3 - ib\, C_c'$$

and the normalized amplitude $\hat{A}_\alpha(\omega)$ is given in terms of the boundary condition (3-50) or (3-51):

$$\hat{A}_\alpha(\omega) = \frac{1}{(-i\omega)} \int_{-\infty}^{\infty} (\text{const})\, E_z(0, t)\, e^{i\omega t}\, dt$$

and from (3-45), we get for the actual guided field:

$$E_z(z', t') = \int_{-\infty}^{\infty} (\text{const})\, E_z(0, \omega)\, e^{i[\kappa(\omega) z' - \omega t']} \frac{d\omega}{2\pi}$$

or

$$E_z(z', t') = (\text{const})\, e^{-bC_c' z'} \int_{-\infty}^{\infty} G(z', t' - t'')\, E_z(0, t')\, dt'' \qquad (3\text{-}53)$$

with

$$G(z', t') = \frac{1}{(3\alpha' z')^{1/3}}\ \mathrm{Ai}\left(-\frac{-t'}{(3\alpha' z')^{1/3}}\right)$$

where

$$\mathrm{Ai}(x) = \frac{1}{2\pi} \int_{-\infty}^{\infty} e^{i(\tau^3/3 + x\tau)}\, d\tau$$

Since the initial width of the applied signal is sufficiently small, then for large z', $G(z', t')$ is a slow varying function, and the solution (3-53) of the linearized equation can be written in the following form[42]:

$$E_z(z', t') \sim (\text{const})\, \frac{e^{-bC_c' z'}}{(3\alpha' z')^{1/3}}\ \mathrm{Ai}\left(-\frac{t'}{(3\alpha' z')^{1/3}}\right) \quad \text{for large } z' \qquad (3\text{-}54)$$

E_z does not depend on the character of the initial radiation as long as its width is small. However, for small z', the solution depends strongly on the boundary condition. The solution (3-54) represents a wavepacket moving away from the launcher with the first peak moving with velocity v_o for $\underset{\sim}{B}_o = 0$, and v_s for $\underset{\sim}{B}_o \neq 0$. The packet spreads and its amplitude is reduced as it moves. Figure 3-3 shows a plot of the velocity of the first peak as a function of plasma parameters, i.e., ω_p and ω_c. The solution (3-54) is discussed further in Chapter III in relation to the experimental results.

Next, for the full nonlinear equation, the nonlinear parameter σ[42] provides a measure for the nonlinear effects. To compute σ for typical experimental conditions, assume the boundary conditions for Eq. (3-48) to be given at $z = 0 + \Delta z$, i.e., a few centimeters to the right of the launching plates. Placing the receiving plates close to the launcher, we observe a wave packet of four oscillations extended over an interval of time τ. Thus, take as the boundary condition for $\hat{\mathcal{A}}_\alpha(z', t')$ a function of the type:

$$\hat{\mathcal{A}}_\alpha(\Delta z', t') = +\mathcal{A}_o\, \phi(t'/\tau\omega_i) \qquad (3\text{-}55)$$

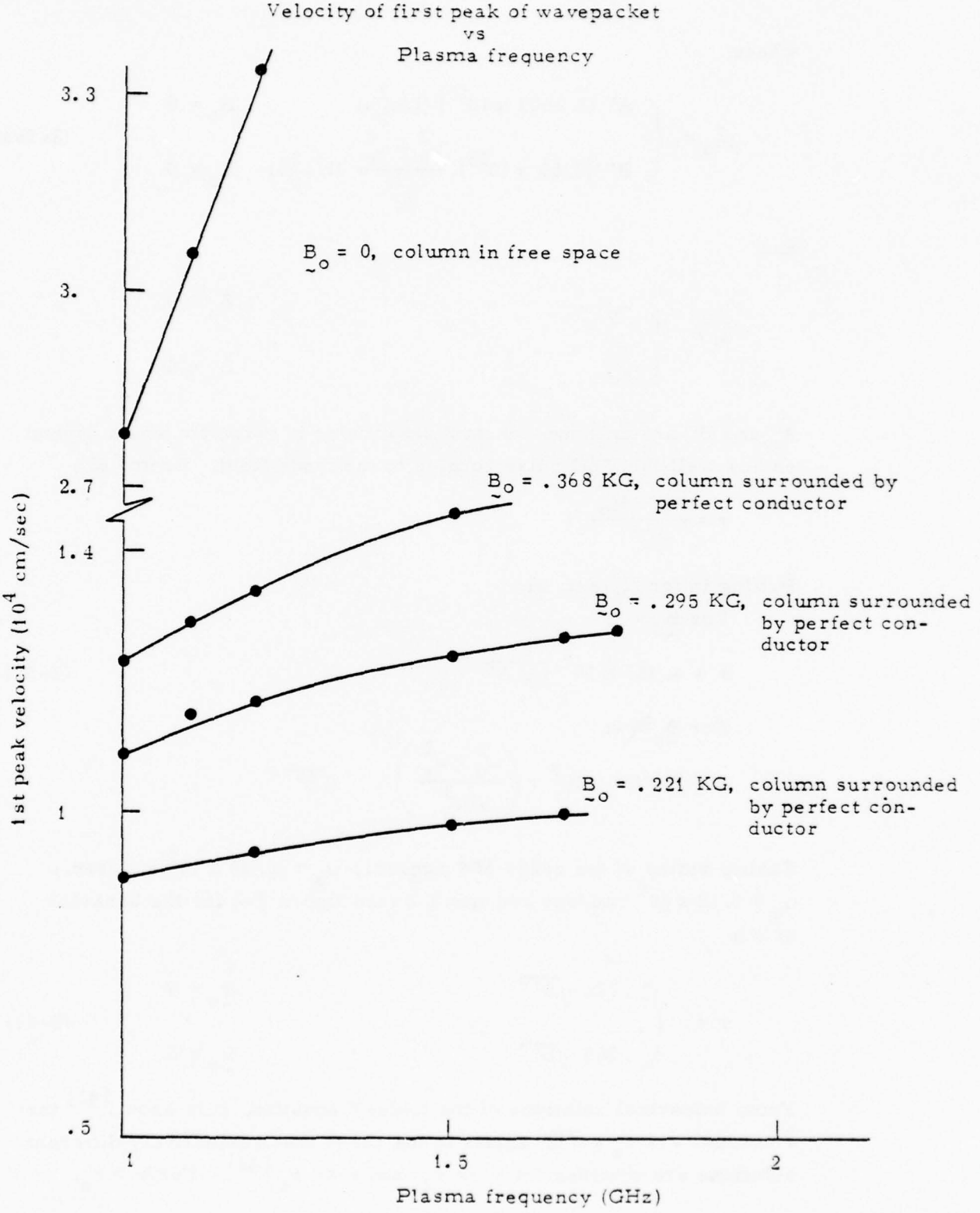
Velocity of first peak of wavepacket
vs
Plasma frequency
3.3
3.
2.7
1.4
1
.5
1st peak velocity (10^4 cm/sec)
B_o = 0, column in free space
B_o = .368 KG, column surrounded by perfect conductor
B_o = .295 KG, column surrounded by perfect conductor
B_o = .221 KG, column surrounded by perfect conductor
1
1.5
2
Plasma frequency (GHz)

Fig. 3.3

where

$$a_o = \begin{cases} A' \ (1.9503 \times 10^{15}) \ (1/\omega_p^2 b) & B_o = 0 \\ B' \ (3.66 \times 10^{15}) \ \dfrac{\omega_p^2 + \omega_c^2}{\omega_c^2} \ (1/\omega_p^2 b) & B_o \neq 0 \end{cases} \tag{3-56a}$$

and

$$\omega_i = \begin{cases} \omega_p & B_o = 0 \\ \omega_c & B_o \neq 0 \end{cases}$$

A' and B' are unknown constant amplitudes in volts/cm which depend on how well the BBG pulse couples to the mode field. From [42],

$$\sigma = \frac{\omega_i \tau \sqrt{a_o}}{\sqrt{\alpha}}$$

Putting in for a_o and α:

For $\underset{\sim}{B}_o = 0$:

$$\sigma = 4.455 \times 10^7 \ \tau \sqrt{A'} \tag{3-57}$$

For $\underset{\sim}{B}_o \neq 0$:

$$\sigma = 7.4467 \times 10^7 \ \tau \left(\frac{\omega_p^2 + \omega_c^2}{\alpha' \omega_p^2} \right)^{1/2} \sqrt{B'}$$

Taking widths of the order of 5 nonsec., $\omega_p \sim 10.49 \times 10^9$ rad/sec., $\omega_c \sim 5.18 \times 10^9$ rad/sec and $\alpha \sim 1.4$ (see figure 3-4 for the behavior of α):

$$\sigma = \begin{cases} .222 \sqrt{A'} & \underset{\sim}{B}_o = 0 \\ .365 \sqrt{B'} & \underset{\sim}{B}_o \neq 0 \end{cases} \tag{3-59}$$

From numerical solutions of the K-de-V equation, it is known[42] that a critical $\sigma = \sigma_c = \sqrt{12}$ exists in the sense that qualitatively different solutions are obtained for $\sigma >> \sigma_c$ and $\sigma << \sigma_c$ [42]. For $\sigma > \sigma_c$,

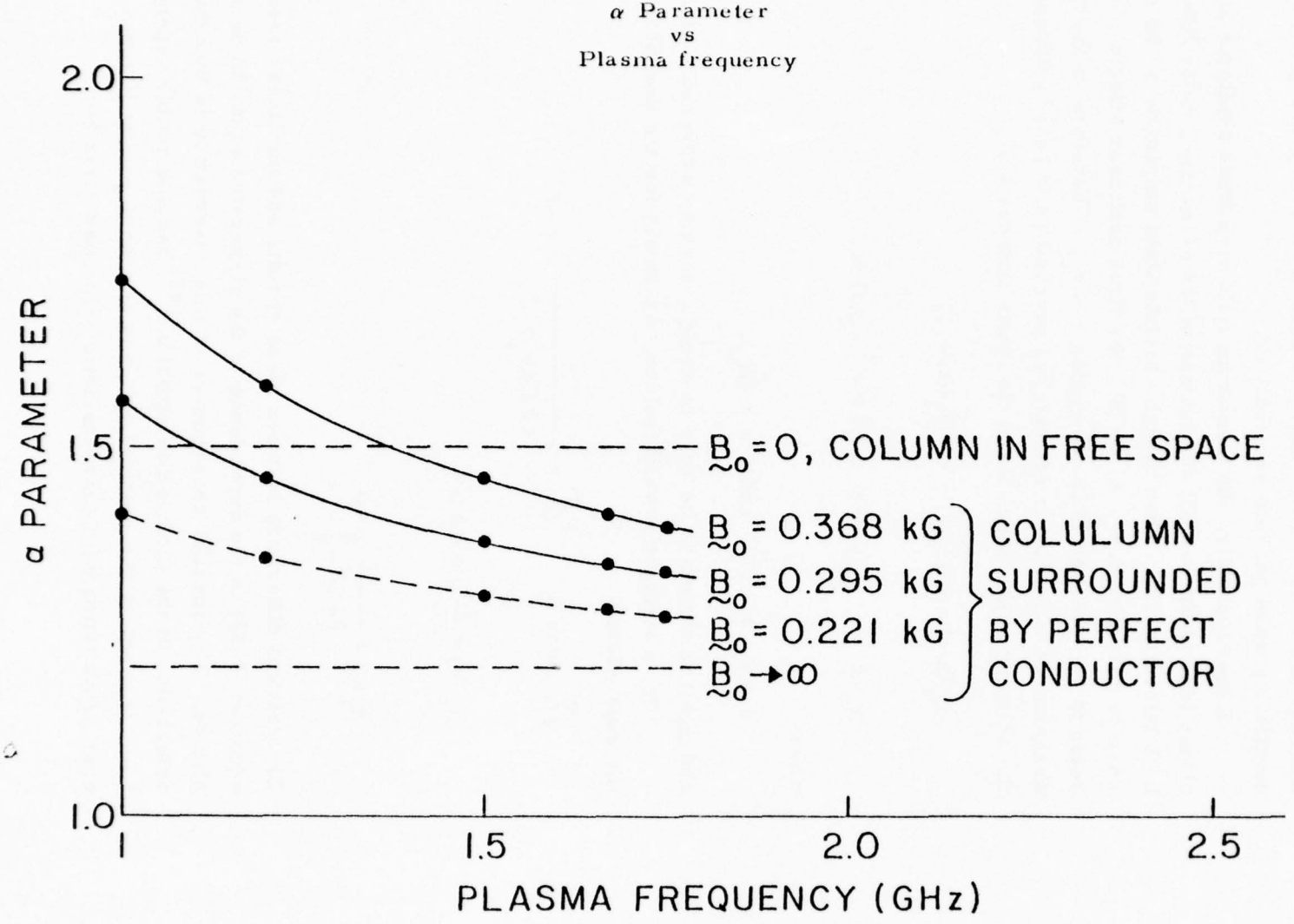
α Parameter
vs
Plasma frequency
2.0
1.5
1.0
α PARAMETER
B_o = 0, COLUMN IN FREE SPACE
B_o = 0.368 kG
B_o = 0.295 kG
B_o = 0.221 kG
$B_o \to \infty$
COLULUMN SURROUNDED BY PERFECT CONDUCTOR
1.5
2.0
2.5
PLASMA FREQUENCY (GHz)

Figure 3.4

nonlinear stationary solutions of the "solitary type" are permissible, whereas for $\sigma < \sigma_c$ "nonsolitary" solutions corresponding to rapidly-oscillating wave packets are obtained.

Experimentally, the maximum field amplitude available at the plates (due to the 4.4 dB attenuation of the 60 nansec. delay line) is 1.92 kilovolts/cm. Even though absolute field amplitude of the excited wave is unknown, i.e., A' or B', the first nonlinear effects which begin to be observed is in the region $\sigma < \sigma_c$. Therefore in the first assessment of nonlinear effects, we proceed as in [45] by expanding the solution of the K-de-V and the wave number as:

$$\hat{a}_\alpha(z, t) = \epsilon\, \hat{a}_1(\theta) + \epsilon^2\, \hat{a}_2(\theta) + \ldots \tag{3-60}$$

$$\kappa_\alpha(\omega) = \kappa_o(\omega) + \epsilon\, \kappa_1(\omega) + \epsilon^2\, \kappa_2(\omega) + \ldots$$

where

$$\theta = \kappa_\alpha\, z - \omega t \quad \text{and} \quad \epsilon = \epsilon\, (\hat{a}_\alpha).$$

and $\kappa_1(\omega)$ is chosen to be zero to avoid a secular expression of $\hat{a}_\alpha$.

In a straightforward fashion, we obtain for the coefficients of the expansion:

$$\hat{a}_1 = \cos\theta \qquad \hat{a}_2 = -\frac{1}{12\, Cd\, \omega_p\, b\, \omega^2} \cos 2\theta$$

$$\kappa_o(\omega) = \frac{1}{v_i}\,\omega + Cd\,\omega^3 \tag{3-61}$$

$$\kappa_2(\omega) = \frac{1}{24\, Cd\, \omega_p^2\, b^2\, \omega}$$

The critical difference between these results and the linear results in equation (3-52) is the dependence of the dispersion equation on the amplitude. The specific consequence of this observation is that the characteristics of the modulation equations[45] become doubly degenerate, i.e., it predicts the eventual splitting of a wave packet into two separate ones propagating with characteristic velocities given by:

$$C_+ = \frac{1}{\kappa_o'(\omega) + \frac{a_o}{2\omega_p b}} \qquad \text{for the slow wavepacket}$$

$$C_- = \frac{1}{\kappa_o'(\omega) - \frac{a_o}{2\omega_p b}} \qquad \text{for the fast wavepacket.} \tag{3-62}$$

where a_o is the normalized amplitude of the nonuniform wavetrain, and $\kappa_o'(\omega) = \frac{\omega}{d\omega}\kappa_o$. Using these velocities, we can get an upper estimate as to the distance away from the source at which this separation can be observed:[45]

$$z = \frac{C_+ \; C_-}{C_+ - C_-} \; \tau$$

or using (3-62):

$$z = \frac{\omega_c \, b \, \tau}{-2 a_o}$$

For weakly magnetic field, from equations (3-47) and (3-56a): Note that for surface waves we obtain a negative value for z. The consequence of this result is discussed in the next chapter.)

$$z = \frac{\omega_c^3 \, b^2}{3.66 \times 10^{15}} \; \frac{\omega_p^2}{\omega_p^2 + \omega_c^2} \; \frac{\tau}{2B'}$$

For the typical experimental parameter previously considered:

$$z = \frac{2.06 \times 10^3}{2B'} \; \tau \tag{3-63}$$

thus for a wavepacket of actual field strength of 50 volts/cm, separation of approximately 3 nansec. will result at 61 cm away from the boundary.

These results are used in the analysis of the experimental observations which are discussed next.

III-4. Results

In light of the analytical results derived in chapter III, the data obtained using the apparatus described in chapter II will be subsequently presented and analyzed. The results for the no anial magnetic field case are presented in section 4.1; and in section 4.2, the results for the weak axial magnetic field case are presented. As previously mentioned, there are two fundemental differences between these two cases:

1. Even though a Kortweg-de Vries type equation describes the evolution in space-time of a given disturbance, different qualitative results will be obtained in both cases for the same excitation. This is due to the fact that the signs of the nonlinear terms (or of the normalized initial distribution in Eq. 3-46) are opposite. In interpreting the results of this chapter, it is important to note that the Electric field at the launching plate points in the $-\hat{z}$ direction for what has been referred to as the positive pulse in the preciding chapters.

2. The coupling structures used for either case were different. The set up shown in Fig. 2-5 was used for the no magnetic field case, where as for the weak magnetic field, the set up is shown in Fig. 2-7. In the latter case, the addition of the brass rings allowed for the pulsed field to be directly coupled to the plasma, improving the launching efficiency for the body waves. For $\underline{B}o = O$, surface waves were strongly excited without the need of the brass rings. For these waves, the fields are concentrated at the plasma boundary.

Each of the above sections, i.e., 4.1 and 4.2, are divided into two subsections. The low amplitude or linear results are presented in the first subsection; while in the second subsection, we present the finite amplitude or nonlinear results.

4.1 Zero Axial Magnetic Field

4.1.1 Linear Regime

For experiments in this regime, the peak pulse electric field at the launching plates was kept below 192 Volts/cm. At these field levels, the integral solution, equation (3-53), obtained in section 3.4 is valid. From this equation, the mechanism that affects the propagation of the pulse is dispersion.

The vital experimentally controlled parameters which appear in the solution (3-53) are: the background neutral pressure (i.e. collision fre-

quency), initial pulse polarity, plasma frequency and plasma column radius. As a matter of organization, the effect of each of the above parameters on the propagation of the pulse will be sequentially presented and quantitatively compared to the solution (3-53).

Pressure effects had no particular quantitative interest to us except from the point of view of being able to launch the waves. Due to the increase with pressure of electron-neutral collision, it was difficult to launch the waves as illustrated in the sequence of Fig. 4.1. High attenuation, column striations, and loss of statistical sampling coherence are the factors responsible for this behavior. For the rest of the experiments, the pressure was kept at a point where collision related effects had the least influence on the wavepacket characteristics.

The effect, in this regime, of pulse polarity is trivial: it merely changes the sign of the solution (3-53). In Fig. (4.2a), we display oscillogram in time obtained at z = 56 cm for the "positive" pulse and in Fig. (4.2b) for the "negative" pulse. Figure 4.2b is just the negative of Fig. 4.2a. The polarity of the first oscillation is as predicted from the solution (3-54). Quantitative differences in the freguency of oscillation and amplitude are due to slight differences in plasma frequency and initial pulse characteristics. In Fig. a, the "positive" pulse generator produces, at the launching plates, an Electric field pulse in the negative z direction, its strength is approximately 192 volts/cm and its duration is approximately 1 nanosecond. The "negative" generator, in the other hand, produces a field in the positive z direction and its duration is approximately .5 nanosecond. The seemingly reverse naming comes from the fact that the labeling is appropriate for the voltage of the front plate with respect to the ground plate. The evolution in space of the initial disturbance is shown in Fig. 4.3. The a)sequence corresponds to the positive pulse whereas the b)sequence correspond to the negative pulse. This sequence is explained, in terms of equation (3-53) as follows: at z = o, the launcher position, a wave is radiated for a bounded time interval. As the pulse travels to the right, i.e., z > 0, it rapidly breaks into oscillations due to strong dispersive effects. Since the dispersion is negative, the long wavelength are observed to propagate at a higher speed.

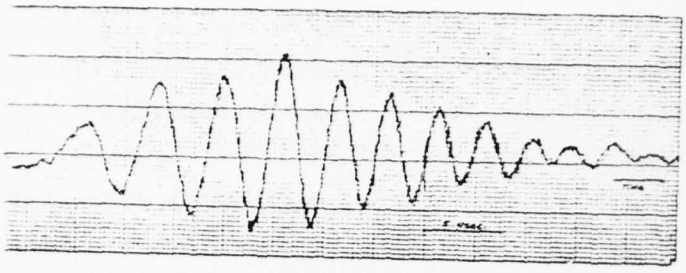

Pressure = 1 μ

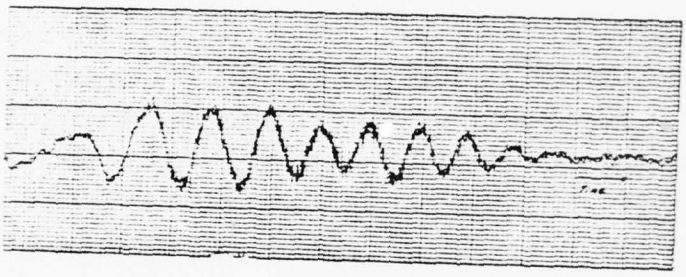

Pressure = 5 μ

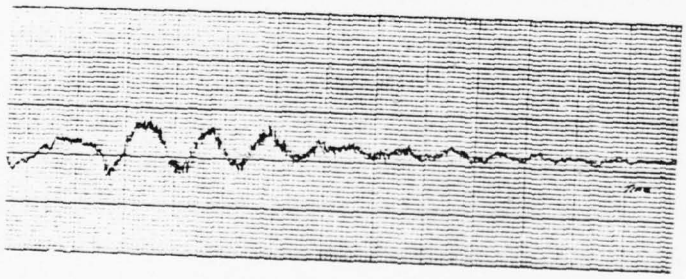

Pressure = 10 μ

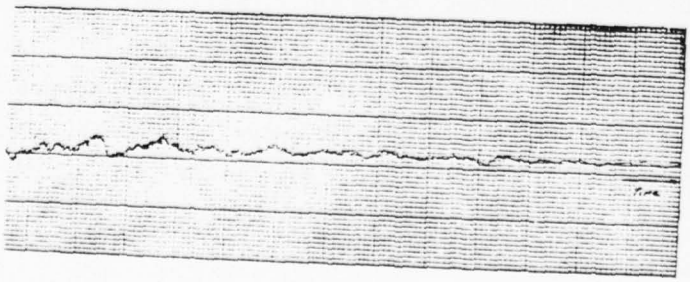

Pressure = 20 μ

Fig. 4.1 Effect of pressure

Figures 4.4 a, b, and c show oscillograms in time for different positions of the receiver. The part of the oscillogram marked with an A corresponds to free space electromagnetic radiation propagating at the speed of light. This radiation is observed even if the plasma were not present (see Fig. 4.2). From these curves, we again observe the negative dispessive properties of the system. This property is further displayed by fourier analyzing the wave forms of Fig. 4.4. From the relation

$$\Delta t \, \Delta\omega \sim 1$$

where Δt = spread of the wavepacket in time

$\Delta\omega$ = spread in frequency

Thus, as the packet propagates and spreads in time due to dispersion, its fourier transform becomes narrower. This is displayed in Fig. (4.5).

As the averaged plasma frequency is changed, the packet characteristics, are also observed to change. The speed of propagation, frequency of oscillation, width of the packet and the normalized amplitude increase as a function of f_p. Time oscillograms for various averaged plasma frequencies are shown in Figure (4.6). Figure (4.7) shows a plot of the velocity of the first peak of the wavepacket as a function of plasma frequency. Two different methods were used to calculate this velocity. The first uses the fact that the first observed disturbance corresponds to the free space electromagnetic radiation travelling at the speed of light. By comparing the time of arrival at the point of observation, of the first peak of the wavepacket with respect to the EM signal, the speed of propagation is obtained. The second method uses the time of flight of the first peak between two points. Also plotted in Figure (4.7) is equation (3-34a). As was pointed out in section 3.4, the speed of propagation of the first peak is given by v_o. The experimental values differ from the theoretical by 20%. This difference lies in the manner that v_o was obtained, i.e. by numerically fitting the solution of the dispersion relation to equation (3-34a). In Equation (3-34a), 14 points were used to determine the low frequency or linear slope of equation (3-34a), i.e., v_o. If fewer points are used, a large v_o is obtained (see equation (3-34b) for example) and a better approximation to the propagation speed.

NO PLASMA

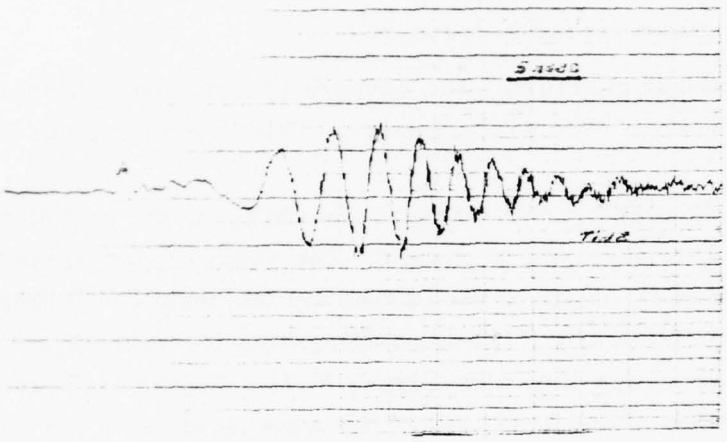

a) "positive" pulse

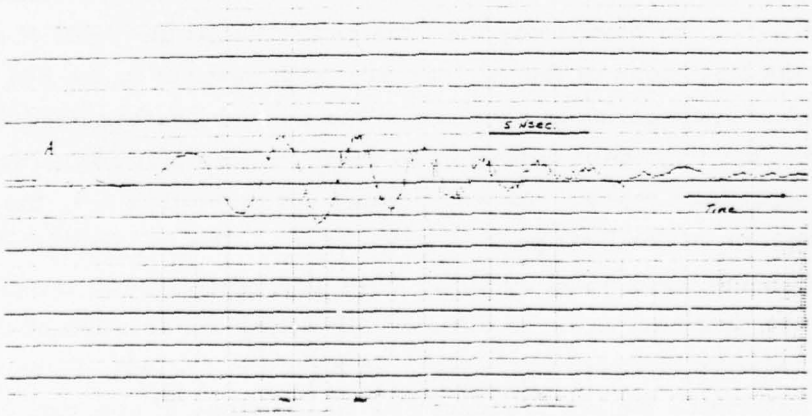

b) "negative" pulse

Fig. 4.2 Effect of polarity of input pulse

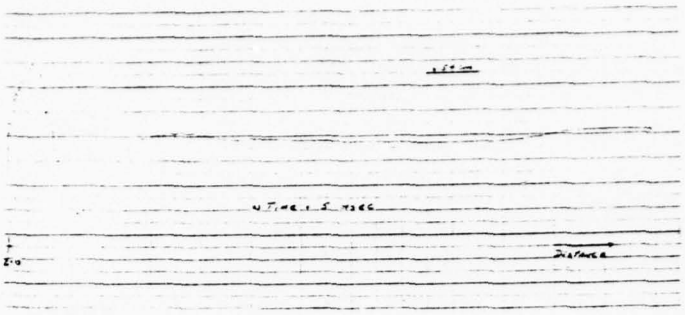

time = 5 nsec.

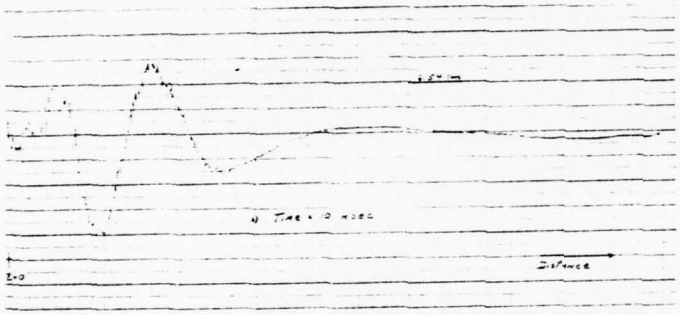

time = 10 nsec.

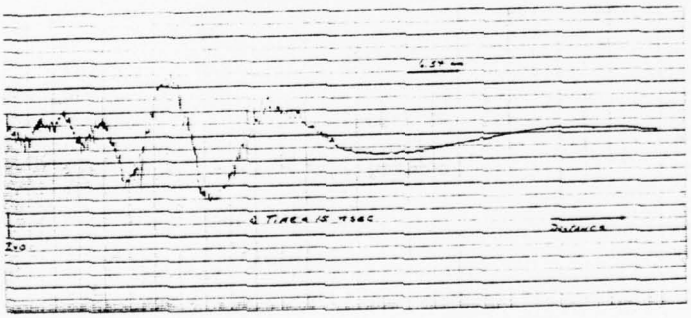

time = 15 nsec.

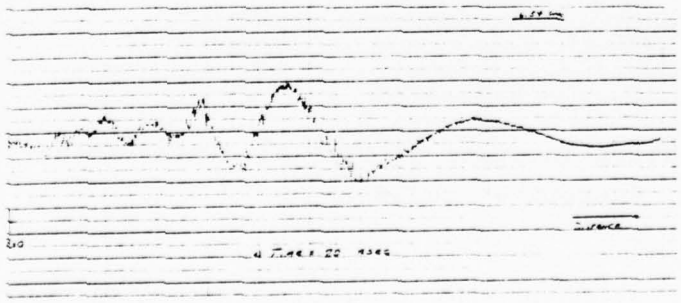

time = 20 nsec.

Fig. 4.3 Evolution in space of initial disturbance
a) "positive" pulse

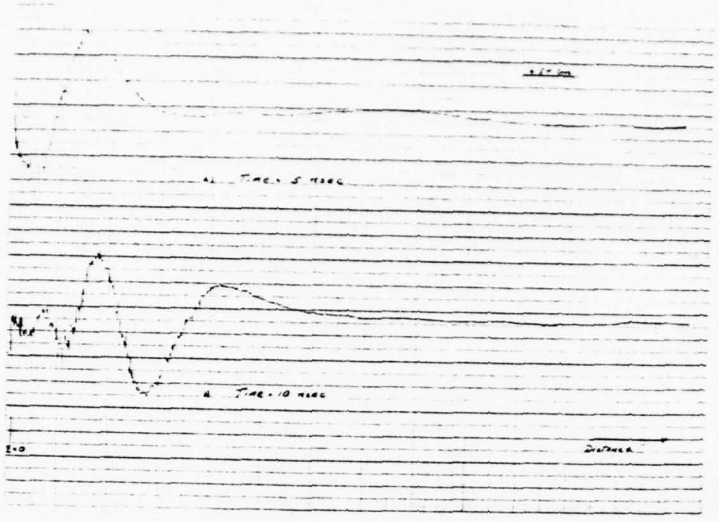

time = 5 nsec

time = 10 nsec

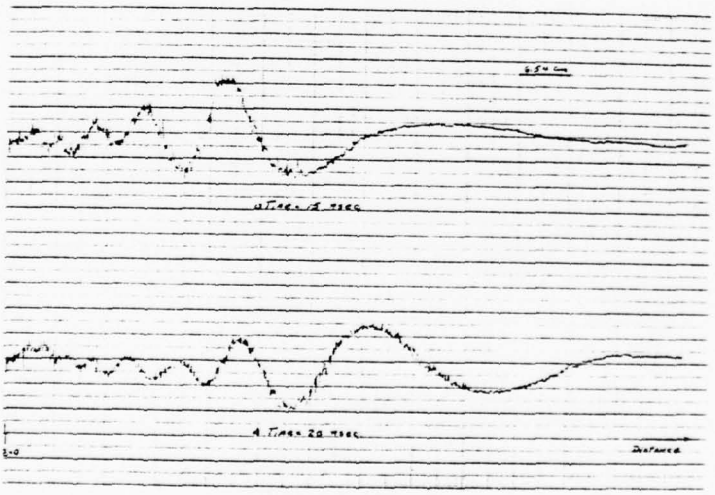

time = 15 nsec

time = 20 nsec

Fig. 4.3 Evolution in space of initial disturbance
b) "negative" pulse

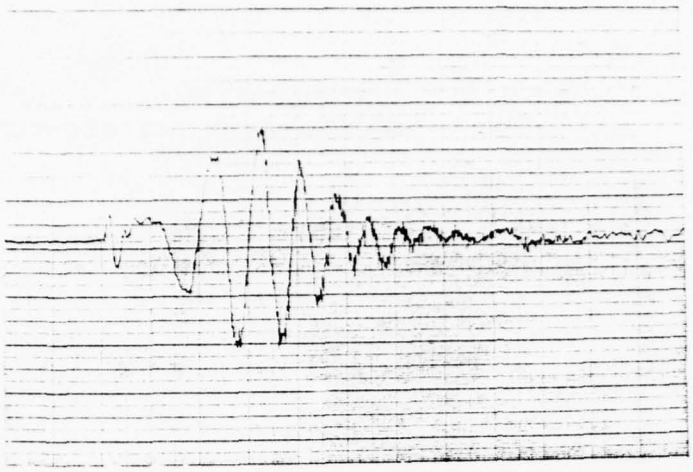

a) z = 27 cm

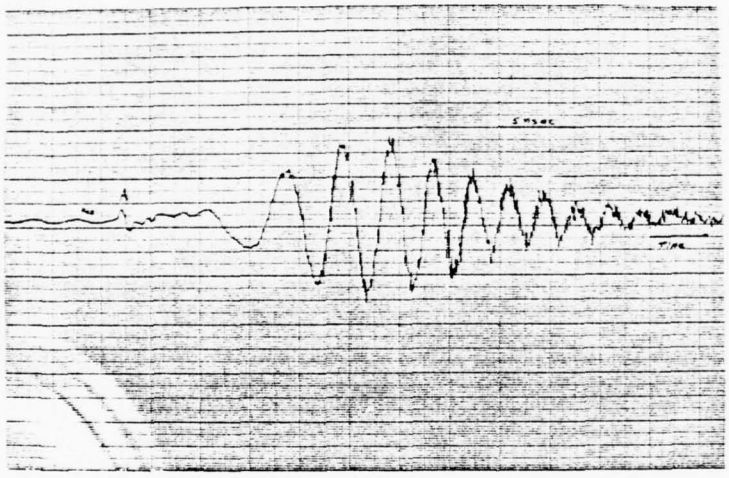

b) z = 56 cm

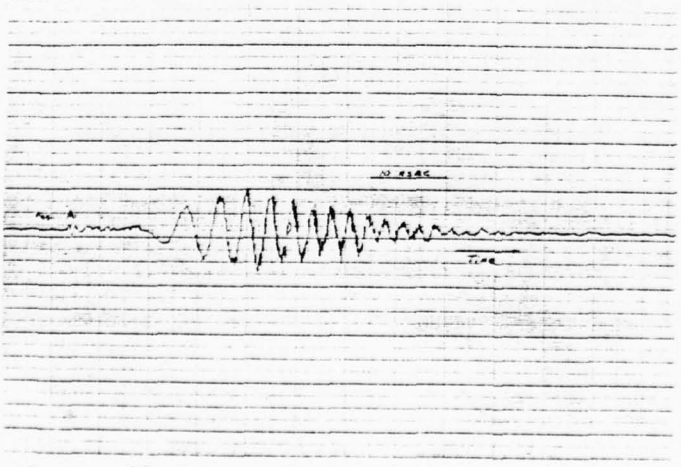

c) z = 90 cm

Fig. 4.4 Linear Oscillograms for different Receiver positions (positive pulse) f_p = 1.4 GHz

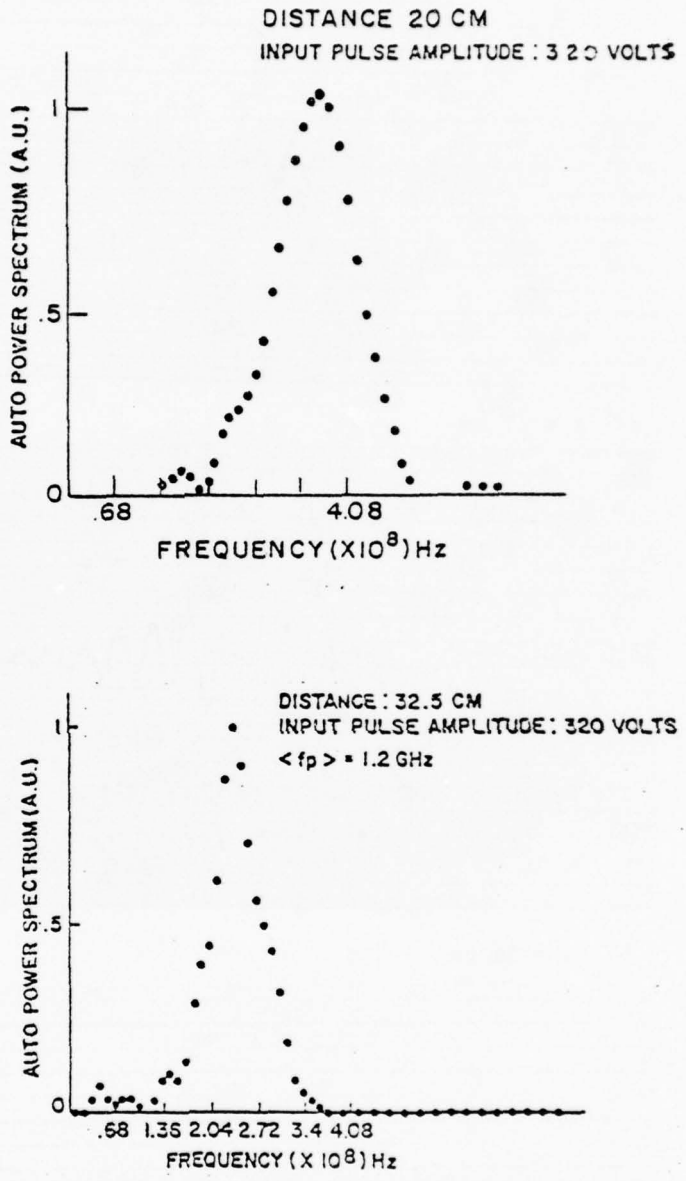

Fig. 4.5 Fourier transform of wavepacket for different positions

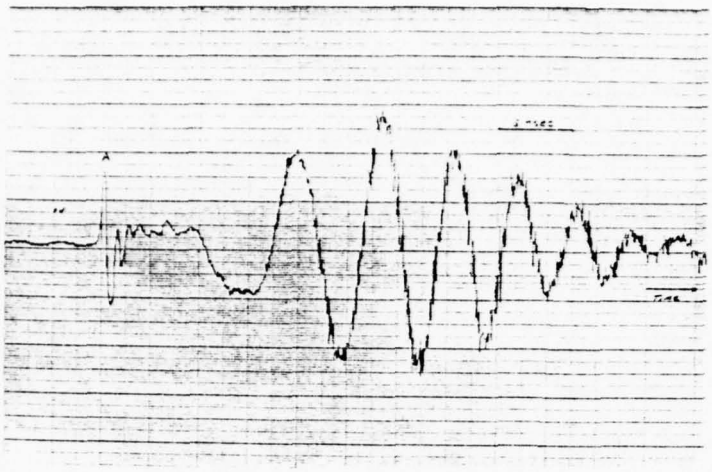

a) f_p = .76 GHz

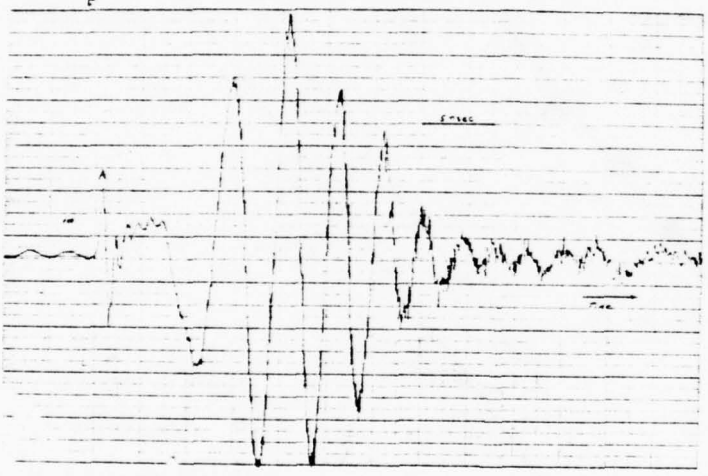

b) f_p = . 9 GHz

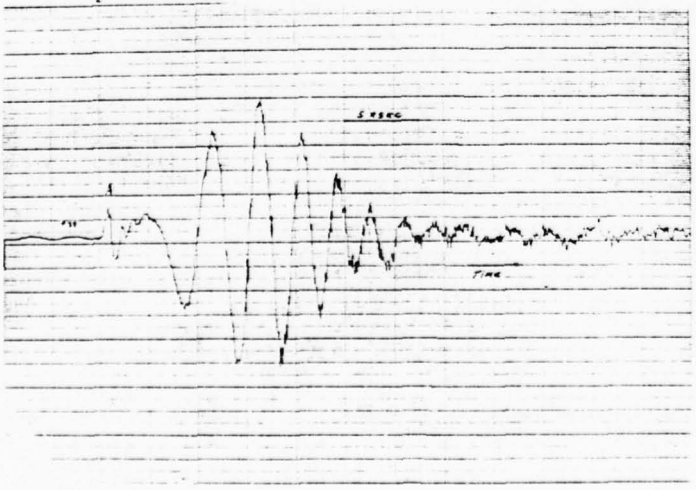

c) f_p = 1.4 GHz

Fig. 4.6 Linear Oscillograms for different plasma frequencies z = 27 cm.

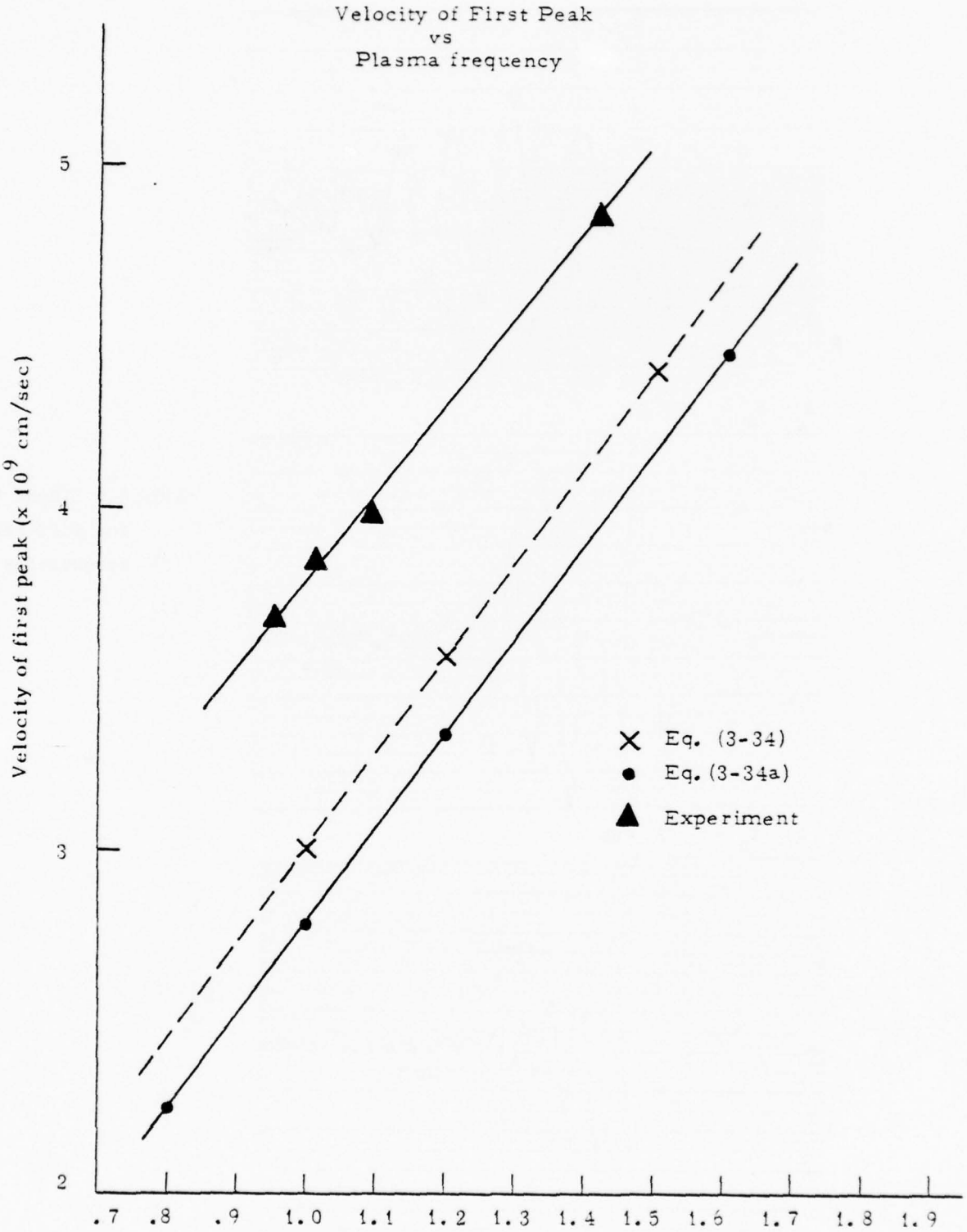
Velocity of First Peak
vs
Plasma frequency
Velocity of first peak (x 10^9 cm/sec)
5
4
3
2
.7
.8
.9
1.0
1.1
1.2
1.3
1.4
1.5
1.6
1.7
1.8
1.9
Eq. (3-34)
Eq. (3-34a)
Experiment

Figure 4.7

For receiver positions far away from the launcher, i.e., at large values of z, the far field solution, equation (3-54) is applicable. This implies that the observed oscillograms should behave as Airy functions of argument $\omega_p (t - z/v_o) / (3\alpha' z/b)^{1/3}$. Using the asymptotic approximation for the Airy function, the solution (3-54) takes the form:

$$E_z \sim \frac{1}{\sqrt{\pi}} \frac{1}{(3\alpha' z' t')^{1/4}} \sin\left[2/3\ t'^{3/2} + \pi/4\right] t > z/v_o$$

where $t' = \omega_p (t - z/v_o)/(3\alpha' z')^{1/3}$ $z' = z/b$

the zeros of the above equation occur at:

$$t' = (n - 1/4)^{2/3} \frac{3}{4} \pi^{2/3} (3\alpha' z')^{1/3} \qquad (4-1)$$

These values can be directly compared to the properly normalized zeros of the observed oscillograms. In Table (4-1), we tabulate the zeros obtained from equation (4-1) and from two different oscillograms. These are also plotted in Figure (4-8). If instead of using the average plasma frequency as measured using the Cavity method, a plasma frequency is chosen as to fit the nth experimental crossing to the nth theoretical crossing; we observe that all other (n-1) crossings fall to within 6% of the theoretically predicted values. Larger deviations are obtained for the n = 0 and n = 1 crossings where the asymptotic expansion does not provide an accurate representation. The value of ω_p obtained in this fashion is 20% off from the value measured by the Cavity method. The discrepancy lies in the fact that, the Cavity method measures the average plasma frequency of a non uniform plasma column, whereas the ω_p obtained by matching the nth zero is obtained from a theory that assumes an uniform column. The plasma frequency thus derived corresponds to a value near the edge of the non uniform column. Thus, we have developed a method for measuring the plasma frequency, near the edge of the column, from the zero crossings of the observed time oscillograms. It has a higher resolution than the Cavity method as seen from Figs.

Table 4.1

Parameters:

Receiver distance (z) = 54.375 cm
Column Radius (b) = .66 cm
Normalized distance (z′) = 82.386
a' = 1.48887
v_o (experimental) = 3.895×10^9 cm/sec.
f_p (from cavity) = .9 GHz

Zero crossing (n)	t′	Experimental t′ (ω_p measured using cavity)	Experimental t′ (ω_p chosen so as to fit nth zero crossing)	
			(a)	(b)
0	9.14898	12.16	9.623	9.8
1	19.02	28.16	22.28	22.7
2	33.43	43.34	34.33	34.99
3	45.19	57.11	*45.19	46.0
4	55.56	69.33	54.85	55.9
5	65.020	80.	63.30	64.528
6	74.01	90.65	71.71	73.10
7	82.3131	102.07	80.75	*82.3131
8	90.2908	111.23	88.	89.7
9	97.899	121.1	95.82	97.68
10	105.1395	130.293	103.08	105.06
11	112.28	139.4490	110.32	112.45
	119.158	148.55	117.52	119.79
	125.821	156.187	123.56	125.9

*nth zero matched

f_p corresponding to column { (a) = .712 GHz; (b) = .725 GHz

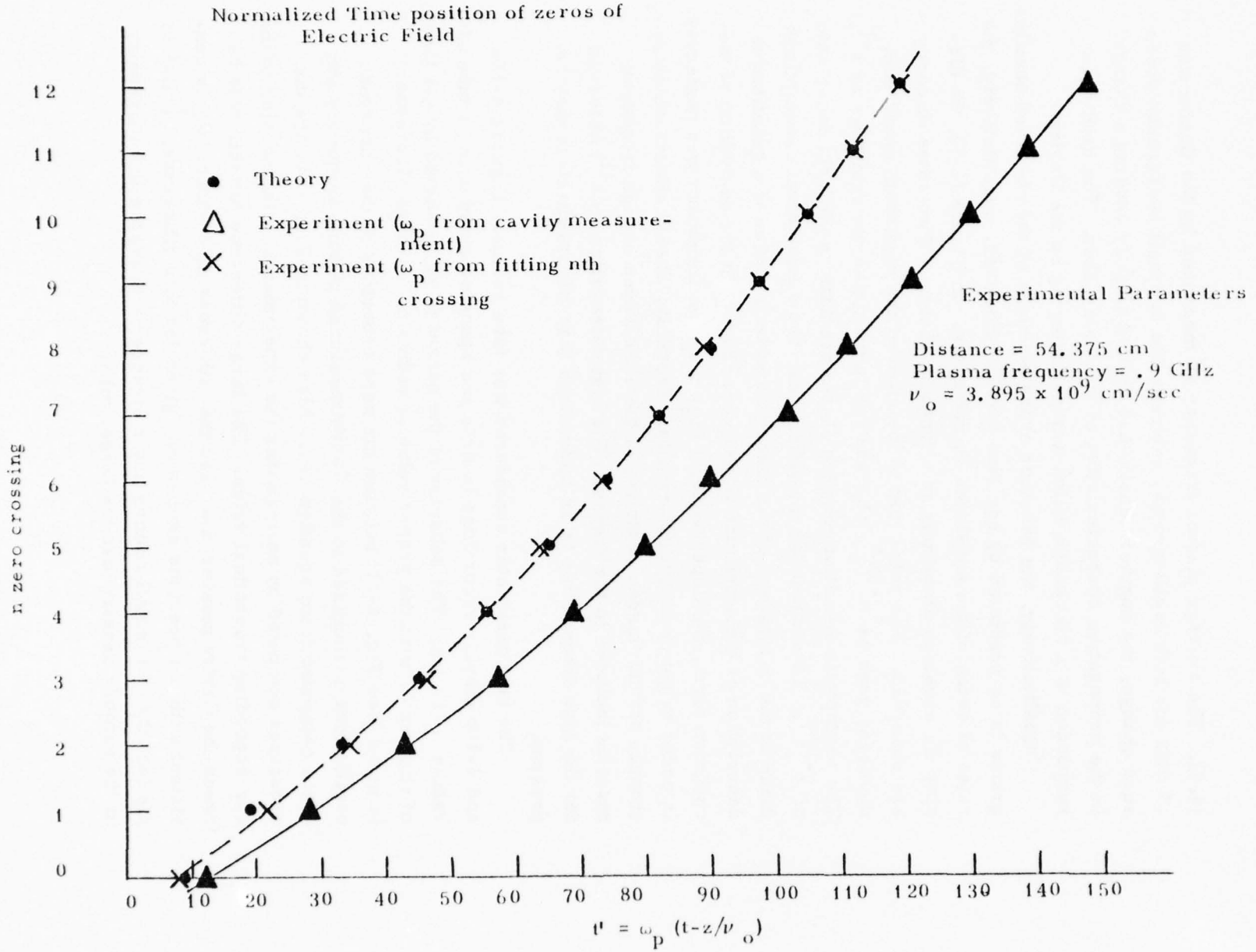
Normalized Time position of zeros of Electric Field
Theory
Experiment (ω_p from cavity measurement)
Experiment (ω_p from fitting nth crossing
Experimental Parameters
Distance = 54.375 cm
Plasma frequency = .9 GHz
ν_o = 3.895 x 10^9 cm/sec
n zero crossing
0
1
2
3
4
5
6
7
8
9
10
11
12
0
10
20
30
40
50
60
70
80
90
100
110
120
130
140
150
$t' = \omega_p (t-z/\nu_o)$

Figure 4.8

(4.8). The average plasma frequency as measured by the Cavity was .9 GHz for both oscillograms, whereas due to small background pressure change, the number density had drifted slightly causing a change in the propagation characteristics of the wavepacket. The drift corresponded to a 5% change which was not detected by the Cavity.

Qualitatively, the behavior of the envelope of the observed oscillograms is as predicted by equation (3-54). However, quantitatively, the rates of decay of the envelopes do not agree. In Figure (4-9), we display the envelope amplitude as a function of time. Two rates of decay are observed. For rates just to the right of the maximum amplitude, the decay goes as $t^{-3/4}$, whereas for large times the rate goes as t^{-1}. The asymptotic result of equation (3-54) predicts an uniform decay rate of $t^{-1/4}$. To account for the difference, two fundamental assumptions made in the derivation of the theory must be modified if a quantitative description of the amplitude is desired. First, in the desivation of the collision term, the dependence of $(\psi_\alpha, \nu\, \psi_\alpha)$ on frequency was neglected in order to get at analytical results. Secondly, sheath effects which introduce strong landau dampling of the slow waves at high frequency must be included in the theory. The high attenuation ($\sim t^{-1}$) observed for the high frequencies is an indications that this mechanism may be present.

The last parameter considered was tube radius. Figures 4-10a and 4-10b display recordings in time and space obtained using a tube of radius .325 cm. The behavior of the packet is as predicted by the theory of chapter III with the proper value of radius b. A large discrepancy is noted (see Fig. 4-11) between the zero crossings of the observed oscillations normalized to the Cavity measured plasma frequency and those computed from equation 4-1. Also shown in Fig. 4-11 are the crossings computed by normalizing the experimental nth crossing to the corresponding theoretical value. The large difference for this tube between the Cavity measured ω_p and the nth crossing computed ω_p is consistent with the previous explanation given for this difference. It lies in the fact that the small column has a stronger transverse inhomogeneity in the number density than the larger tube.

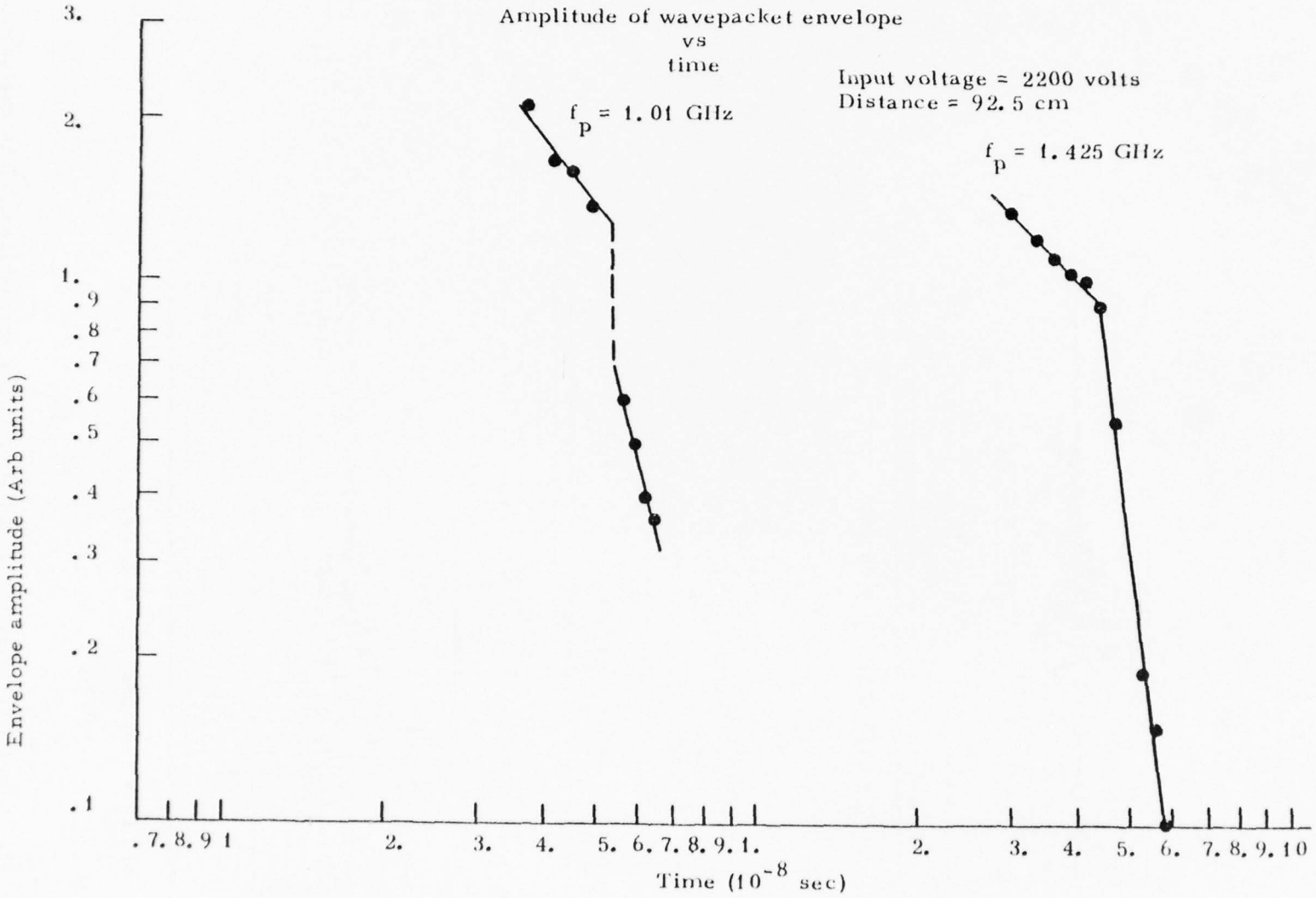
Amplitude of wavepacket envelope
vs
time
Input voltage = 2200 volts
Distance = 92.5 cm
f_p = 1.01 GHz
f_p = 1.425 GHz
Envelope amplitude (Arb units)
3.
2.
1.
.9
.8
.7
.6
.5
.4
.3
.2
.1
.7 .8 .9 1
2.
3.
4.
5.
6.
7.
8.
9.
1.
2.
3.
4.
5.
6.
7.
8.
9.
10
Time (10^{-8} sec)

Figure 4.9

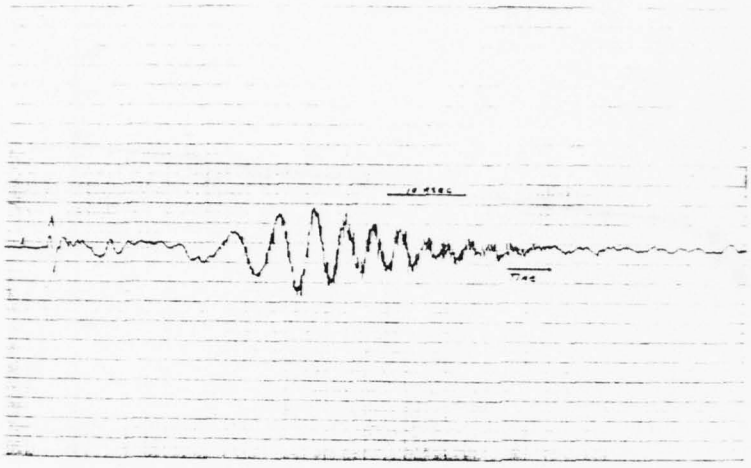

a) f_p = .79 GHz z = 56 cm

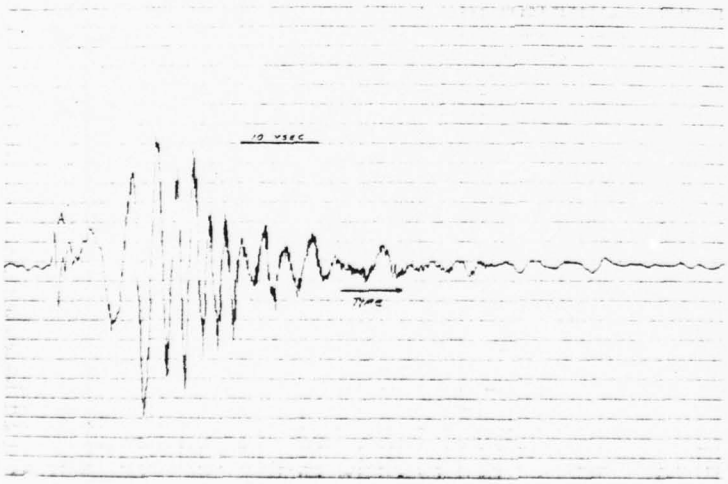

b) f_p = .79 GHz z = 27 cm.

Fig. 4.10 Oscillograms for different plasma frequencies. Tube radius = .3 cm.

Figure 4.11 Zero Crossing for Small Tube

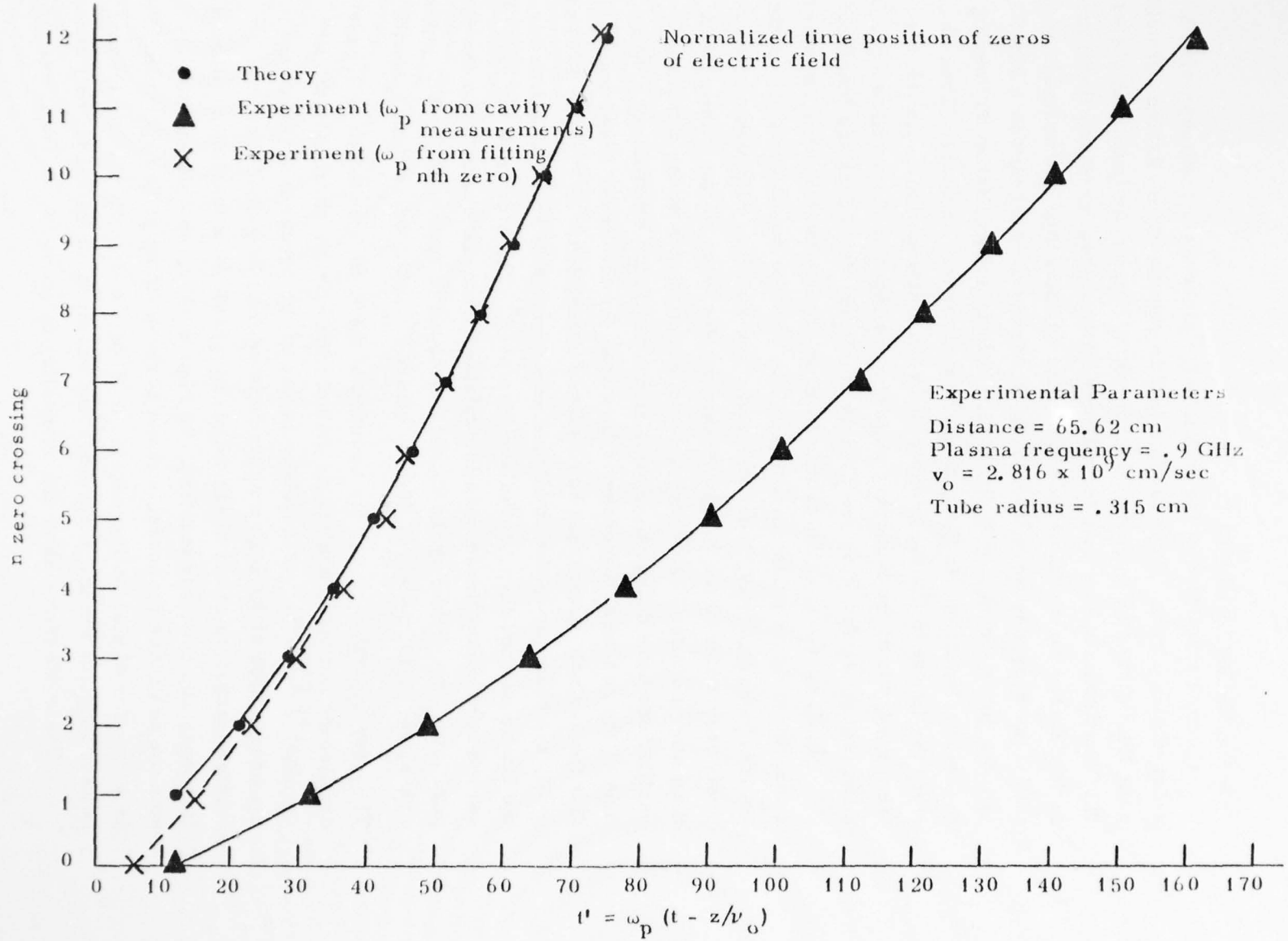

4.1.2 Nonlinear Regimes

As the amplitude of the initial pulse increases, nonlinear effects start to play a role. Experiments in this regime were carried out using peak field strengths greater than 600 volts/cm, at the launching plates. It is important to note that for all experiments (both zero and finite magnetic fields), the signals observed in the oscilloscope are normalized so that if the response were linear, the observed oscillogram as a function of input pulse strength will coincide. This is accomplished by keeping the total attenuation, in the path the signal travel, constant. Thus to go from the linear to the nonlinear regime, the attenuation is transferred from the input of the launching plates to the input of the oscilloscope. In this fashion, effects that are clearly amplitude dependent are identified.

In Figure 4-12, the profile in time of the wavepacket is shown as a function of input pulse amplitude. The positive pulse was used as the source. Qualitatively, these diagrams are similar, although quantitatively they differ in the law governing the decrease of the amplitude in time and in space. Moreover, the characteristics of the first two oscillations have changed. Note that the maximum normalized amplitude of the nonlinear response is less than for the linear case, implying that the surface wavepacket has reached saturation. In Figures 4-13 and 4-14, the behavior of the amplitude as a function of space and time for the linear and nonlinear cases are displayed. The slower decay rate observed for the non linear case is explained from the dynamics of the propagation as described by the model developed in section 3.3. For positive pulse, $E_z(0,t) \sim - \mid E_p(0,t) \mid$, where E_p is the pulse field strength. Thus for any value of σ, the solution of the K de V equation is always oscillatory and the character of the solution is very similar to the linear result.[42] A physical understanding of the processes taking part in the propagation of the high amplitude pulse may be gained from the fourier transform of the observed oscillograms as a function of plasma frequency and receiver location. In Figure 4-15, we display side by side the nonlinear response, and the corresponding power spectrum as a function of plasma frequency. In Figure 4-16, the plasma frequency is kept constant and the recordings are shown for 3 different positions.

These diagrams show the channeling of energy from the lower fre-

RESPONSE AS A FUNCTION OF INPUT PULSE STRENGTH

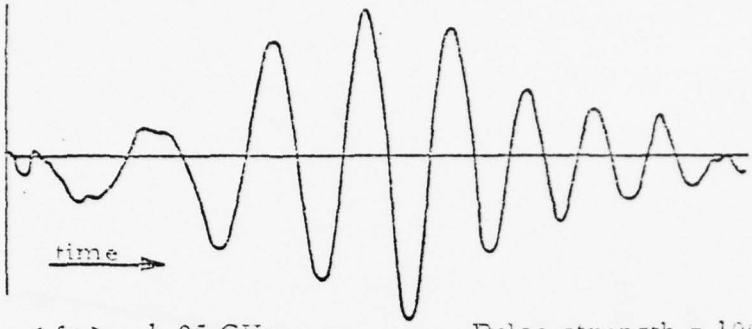

< fp > = 1.05 GHz Pulse strength = 100 v/cm

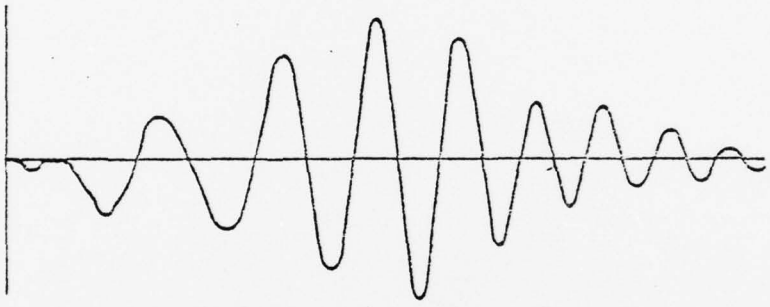

< fp > = 1.05 GHz Pulse strength = 600 v/cm

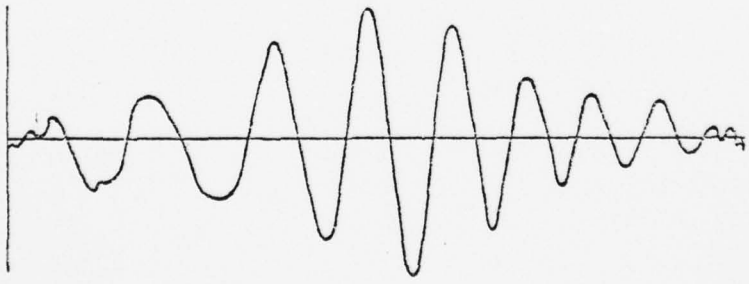

< fp > = 1.05 GHz Pulse strength = 1100 v/cm

Figure 4.12

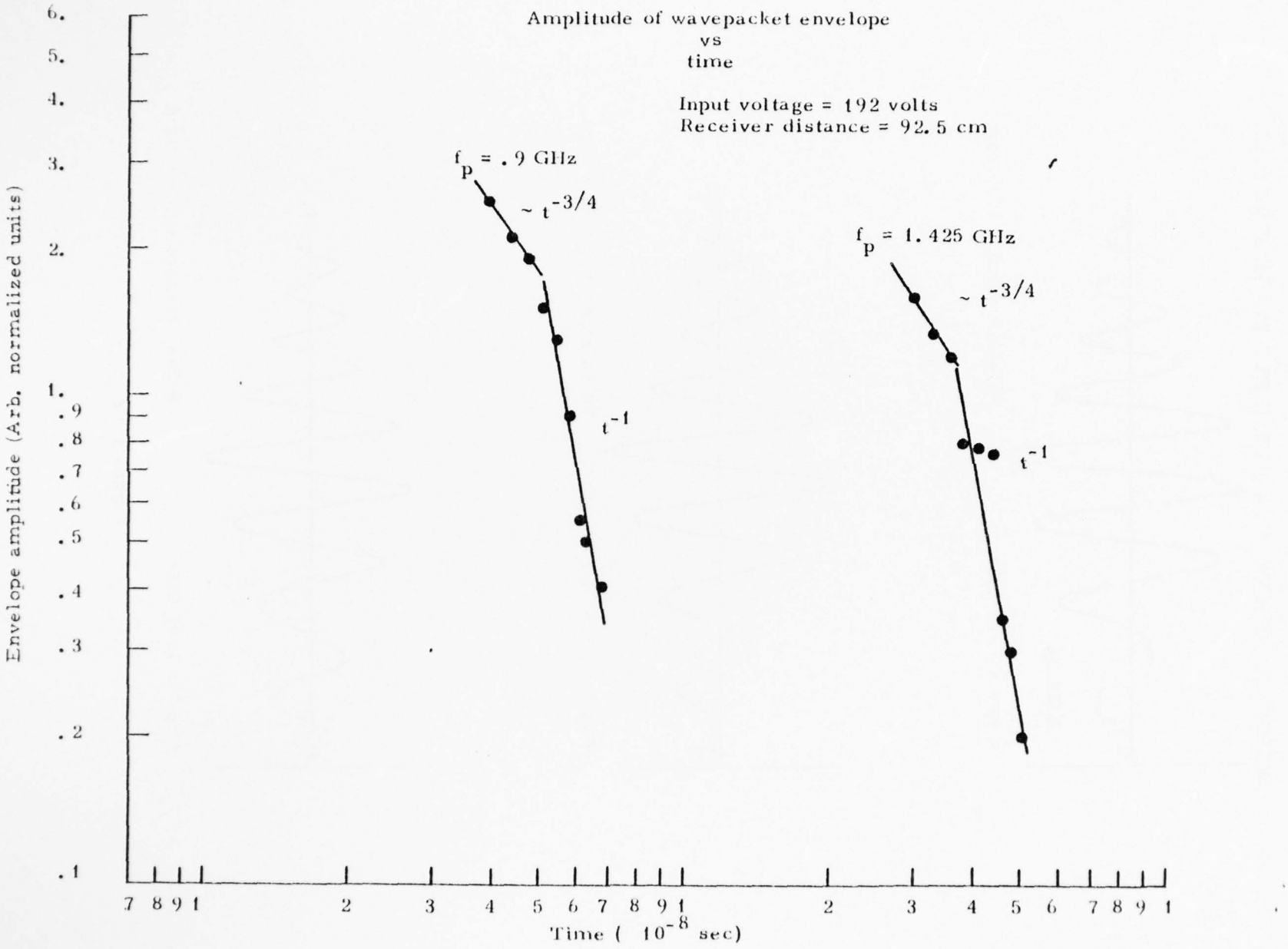
Amplitude of wavepacket envelope
vs
time
Input voltage = 192 volts
Receiver distance = 92.5 cm
f_p = .9 GHz
~ $t^{-3/4}$
t^{-1}
f_p = 1.425 GHz
~ $t^{-3/4}$
t^{-1}
Envelope amplitude (Arb. normalized units)
6.
5.
4.
3.
2.
1.
.9
.8
.7
.6
.5
.4
.3
.2
.1
7 8 9 1 2 3 4 5 6 7 8 9 1 2 3 4 5 6 7 8 9 1
Time (10^{-8} sec)

Fig. 4.13

Figure 4.14
Amplitude of wavepacket
vs
distance

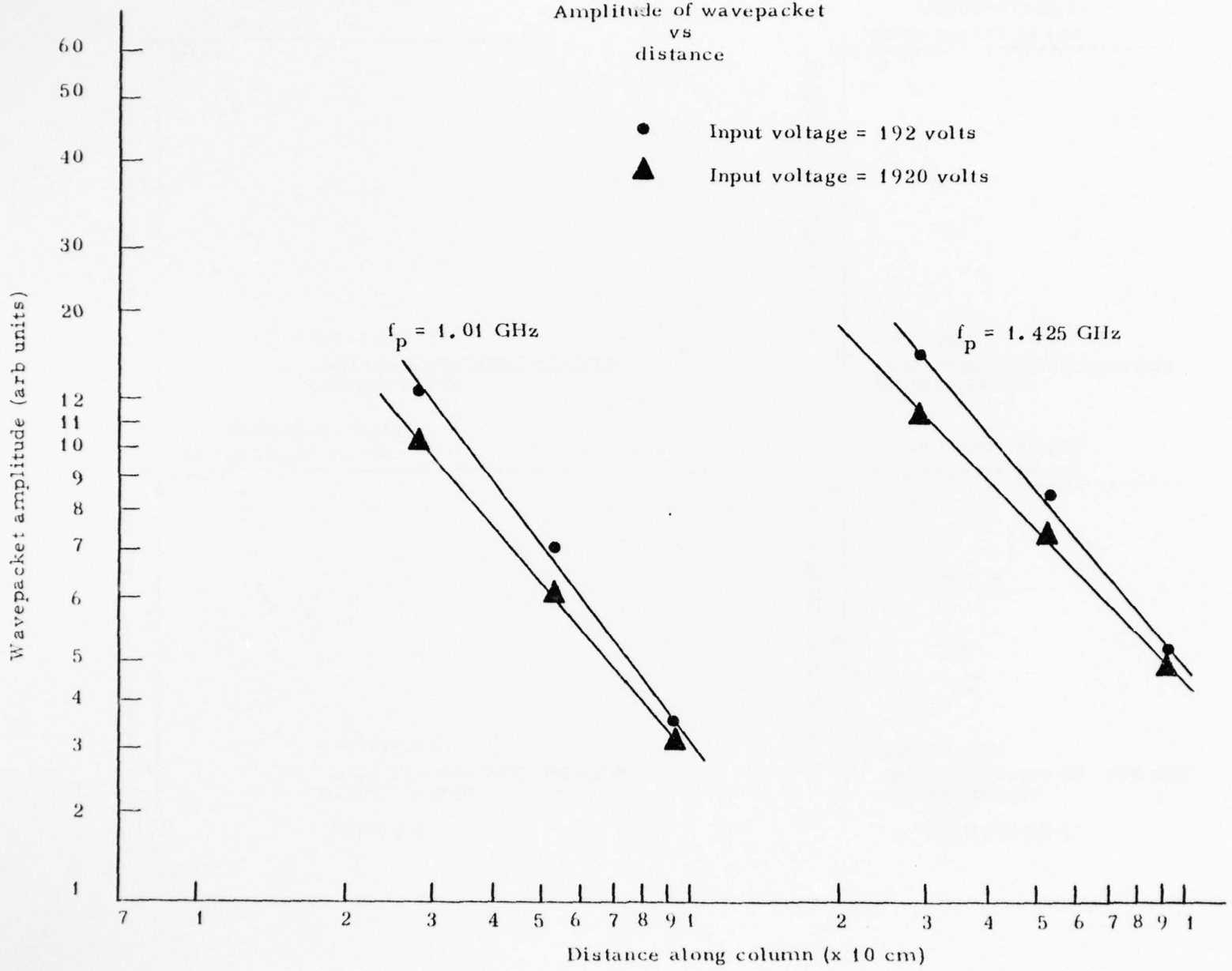

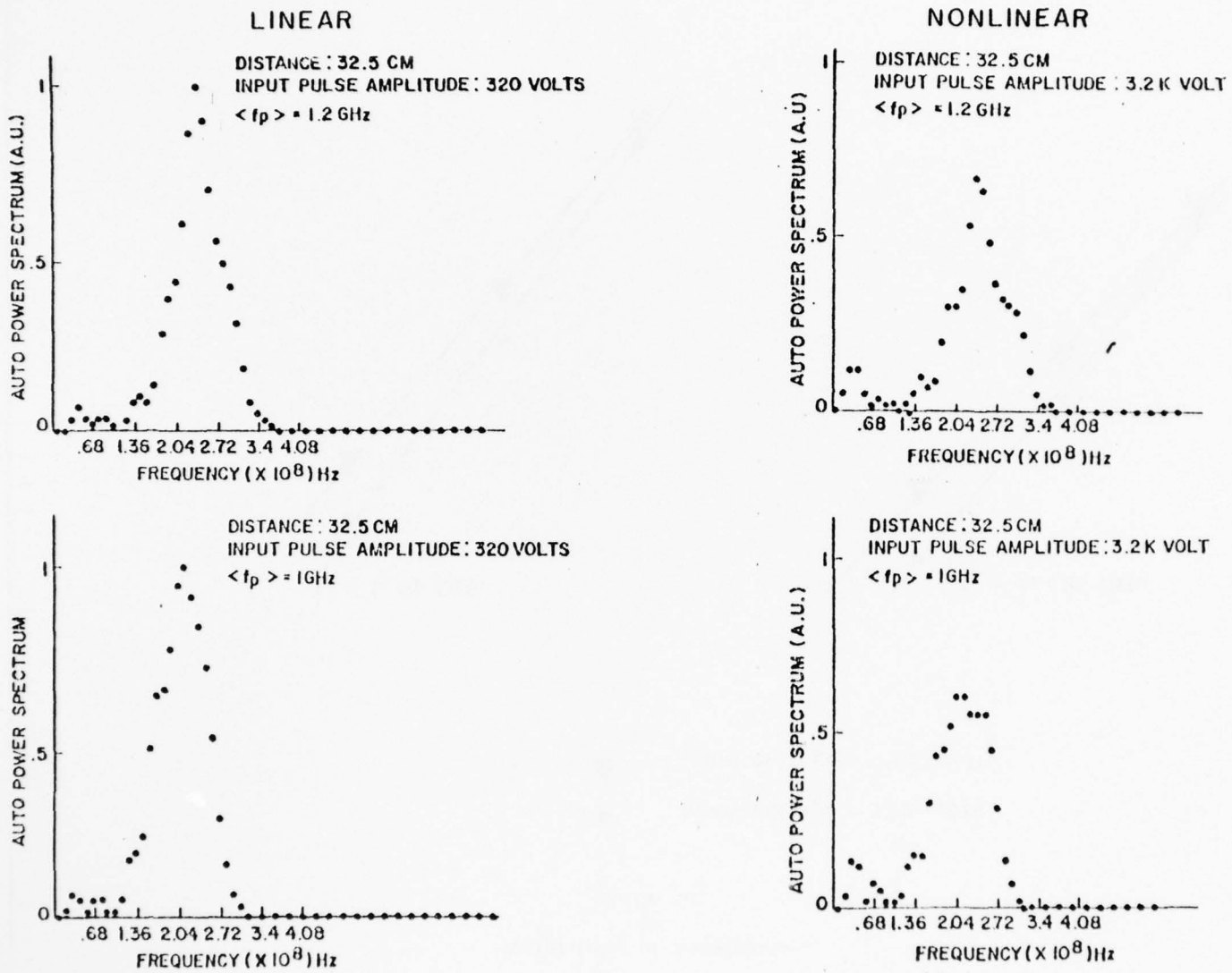

Fig. 4.15 Linear and Nonlinear Spectrum for different plasma frequencies.

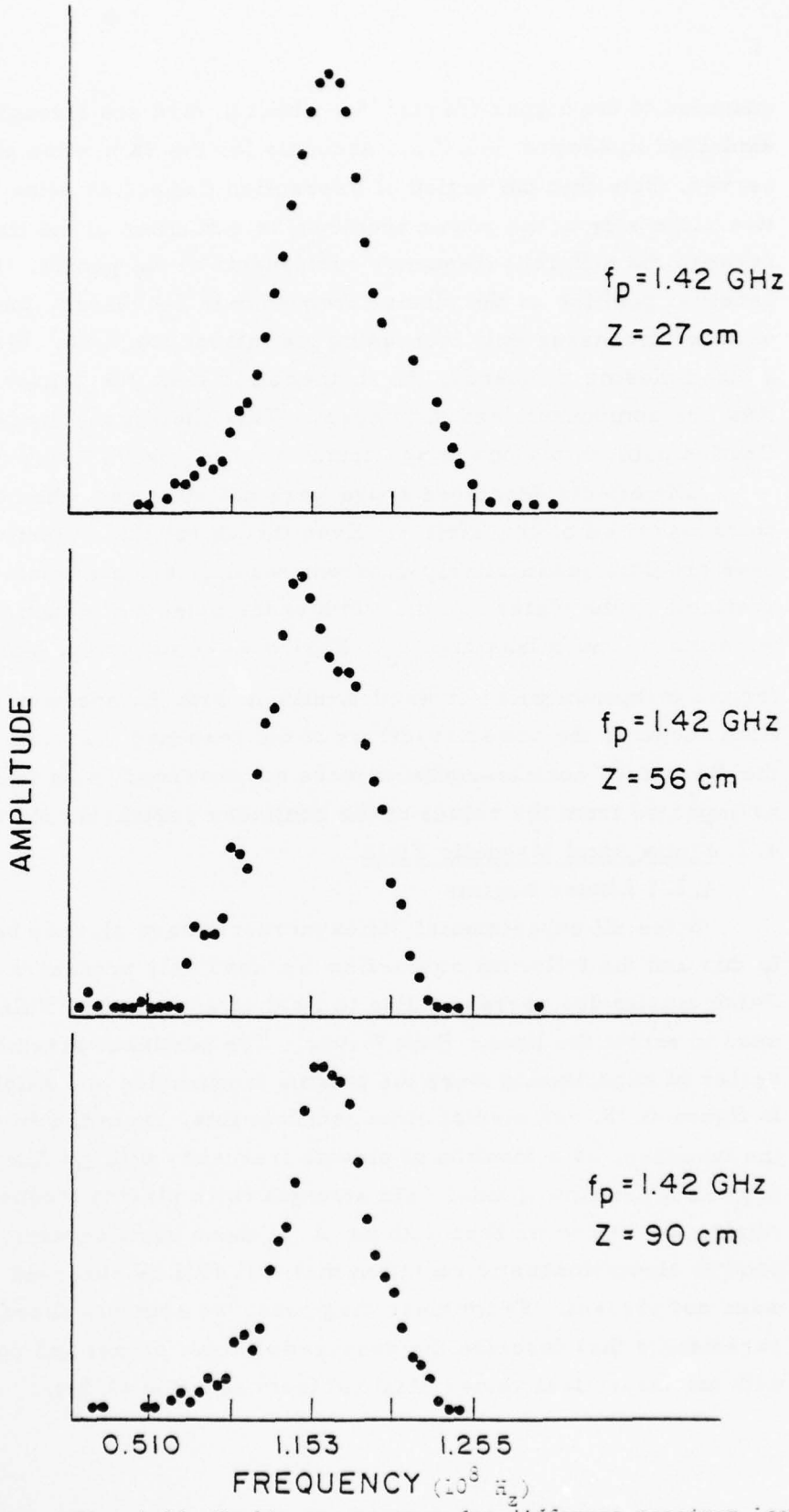

Fig. 4.16 Nonlinear spectrum for different receiver locations.

quencies to the higher frequencies which in turn are strongly attenuated as explained in section 3-3. This accounts for the saturation phenomena observed. Note that the region of interaction (inflection point retion in negative slope side of the power spectrun) is a function of the time of interaction between the different frequency components of the packet. For a fixed receiver position as the plasma frequency is decreased, the packet velocity decreases thus increasing the interaction time. Similarly, for a fixed plasma frequency, the further away from the launcher the more time the components had to interact. This phenomena causes the inflection point in the power spectrum to move toward lower frequencies.

The effects described above were not observed when the negative pulse was used as the exciter. Even though for this polarity Equation 3-48 predicts quantitatively different results, the maximum amplitude available at the plates and the width of the pulse were such that σ is always much, much less than σ_c. Figure 4-17 shows the plasma response for the maximum pulse strength available with the negative generator. Also shown is the power spectrum of the response. As can be seen from the diagrams, nonlinear effects were not observed using this excitation as expected from the values of the nonlinear parameter for this pulse.

4.2 Finite Axial Magnetic Field

4.2.1 Linear Regime

Since all experimental "idiosyncrasis" have already been discussed. In this and the following subsection we need only present the results. Pulse amplitudes corresponding to field strengths of 61 Volts/cm were used to excite the linear Bulk Waves. The pertinent parameters for this series of experiments were the plasma frequencies and axial field strength. In figure 4.18, we display time oscillograms, recorded 48 cm away from the launcher, as a function of plasma frequency with $\underset{\sim}{B}o$ fixed and in Fig. 4.19 as a function of axial field strength (with plasma frequency fixed). Again, the region marked with an A in these oscillograms, correspond to electromagnetic radiation that will still be observed if the plasma were not present. From these diagrams, we compute characteristic parameters that describe the propagating wave packet and compare them with the theoretical values obtained from equation (3.54).

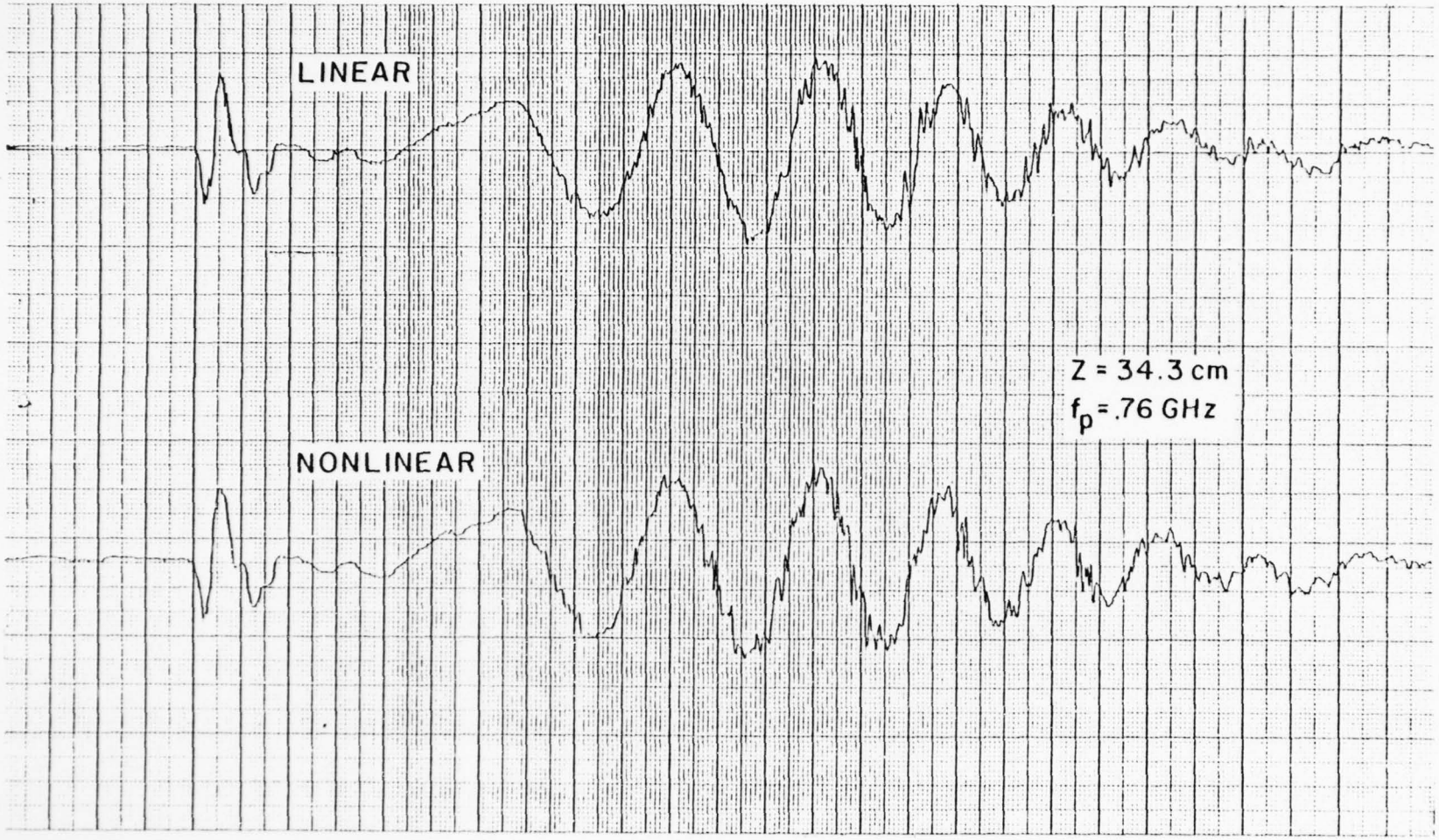

Fig. 4 - 17 Response to high negative pulse.

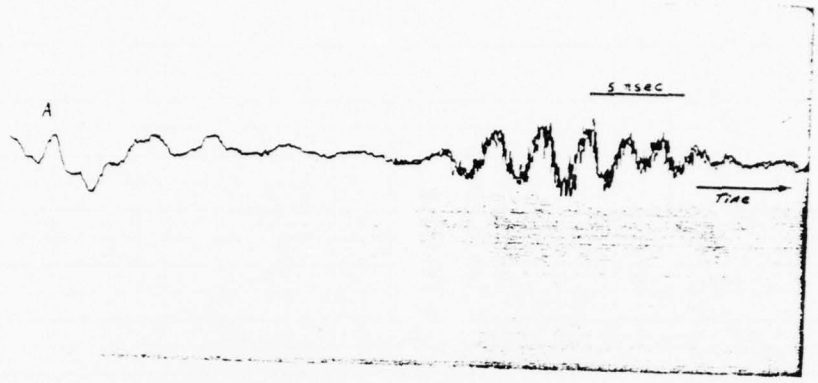

a) f_p = 1.4 GHz

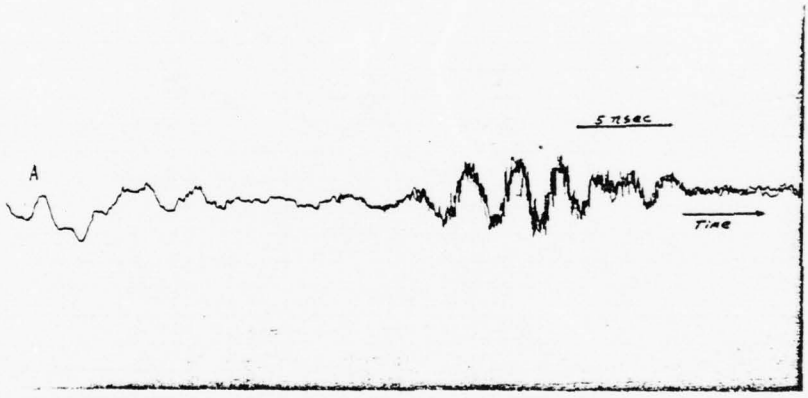

b) f_p = 1.6 GHz

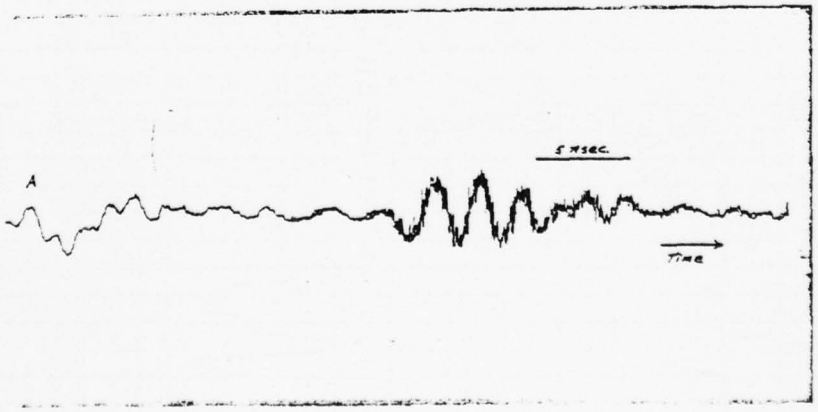

c) f_p = 1.7 GHz

Fig. 4.18 Linear Oscillograms for different plasma frequencies
Cyclotron frequency = .6 GHz

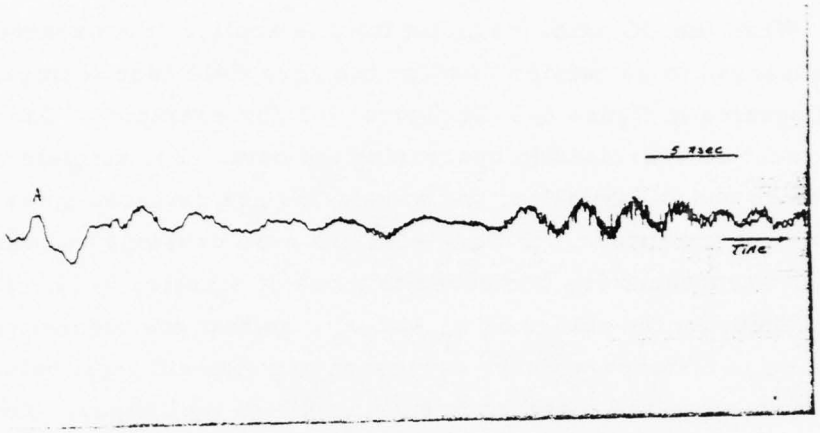

a) f_c = . 6

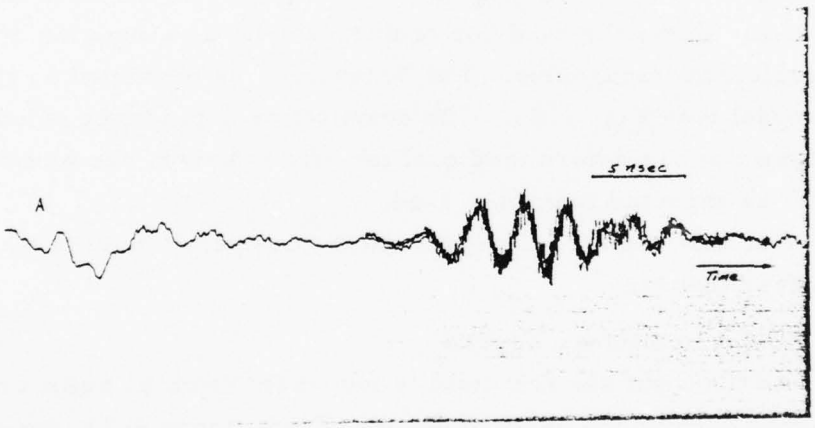

b) f_c = .84 GHz

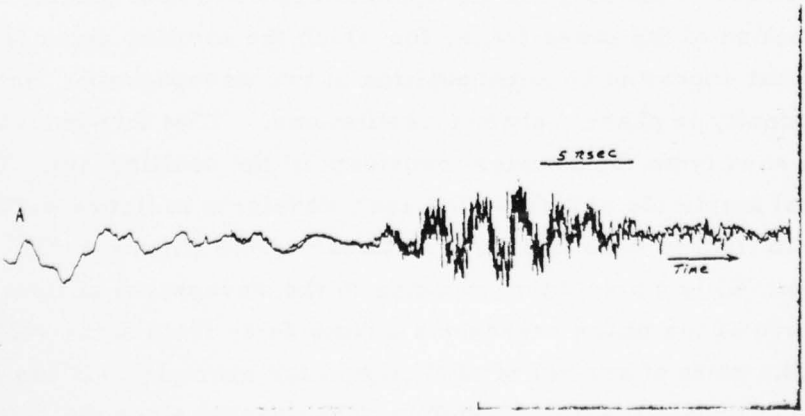

c) f_c = 1 GHz

Fig. 4.19 Linear Oscillograms for different Cyclotron frequencies.

When the DC axial magnetic field is applied, the wavepackets are observed to be noisier than for the zero field case (compare the oscillograms in figure 4-18 to figure 4-2 for example). Therefore care must be exercised in processing the data. To calculate zero crossings and to digitalize, the waveforms are retraced so as to smooth out the jitters. In fig. 4-20, the zero crossings of the experimental wavepacket are compared to those of equation 3-54. For this case, choosing the values of ω_p and ω_c so that one theoretical zero-crossing is matched with the corresponding experimental value, all other crossings are matched to within 10% of each other. The chosen value of up is within 20% of that measured by the cavity and ω_c is within 8% of that measured using a Gauss meter. Another characteristic of the wavepacket is the velocity of the first peak. Fig. 4-21 shows the behavior of this velocity as a function of plasma and cyclotron frequencies. The behavior is as predicted by the theoretical model (see Fig. 3.3). The quantitative dependance of amplitude vs. time was not determined qualitatively however, the waveforms behave as expected from eq. 3-54.

For this regime, the experiments compared quite favorably to the linear theory.

4.2.2 Nonlinear Regime

As the input electric field is increased from 61 volts/cm, gross nonlinear phenomena begin to occur. From figure 4-22, one observes that signals arrive sooner than the linear waves and considerable modification of the original wavepacket begins to take place. Close examination of the lower trace, for which the exciting pulse is largest, show what appear to be superposition of two wavepackets. Note the discontinuity in phase between oscillations. That this indeed is so can be seen from the Fourier transform of the oscillogram. The spectral amplitude and phase for each waveform in figure 4-22 is shown in figures 4-23 to 4-26. At linear levels (figure 4-23), only one peak (C) is shown corresponding to the wavepacket of figure 4-22a. The slope of the phase represents a time delay from some reference point (the point of arrival of EM signal for example). It can be used to calculate the group velocity of the packet since the distance the signal has travelled is also known.

Figure 4.20

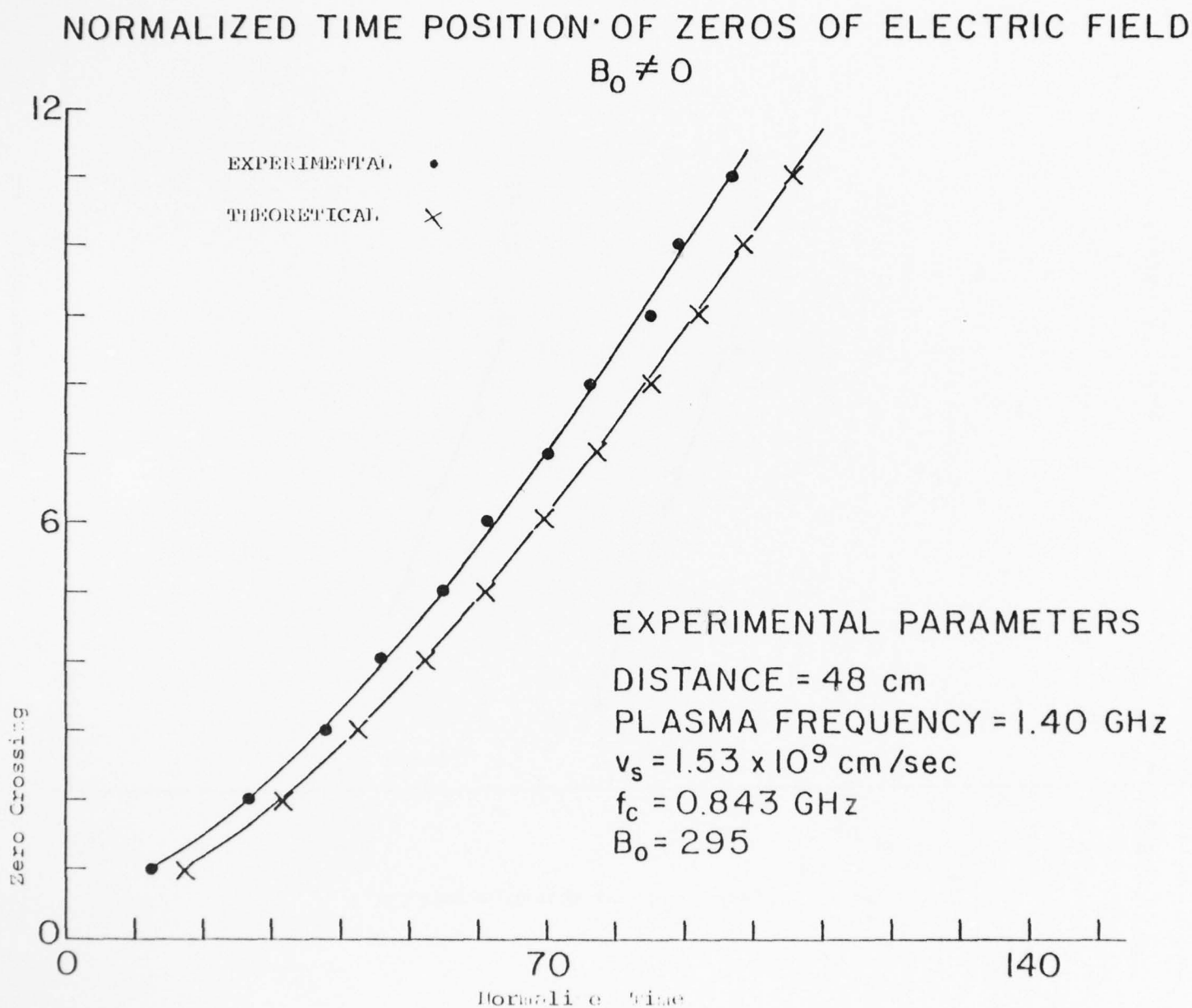
NORMALIZED TIME POSITION OF ZEROS OF ELECTRIC FIELD
$B_0 \neq 0$
EXPERIMENTAL
THEORETICAL
12
6
0
Zero Crossing
0
70
140
Normalized Time
EXPERIMENTAL PARAMETERS
DISTANCE = 48 cm
PLASMA FREQUENCY = 1.40 GHz
$v_s = 1.53 \times 10^9$ cm/sec
$f_c = 0.843$ GHz
$B_0 = 295$

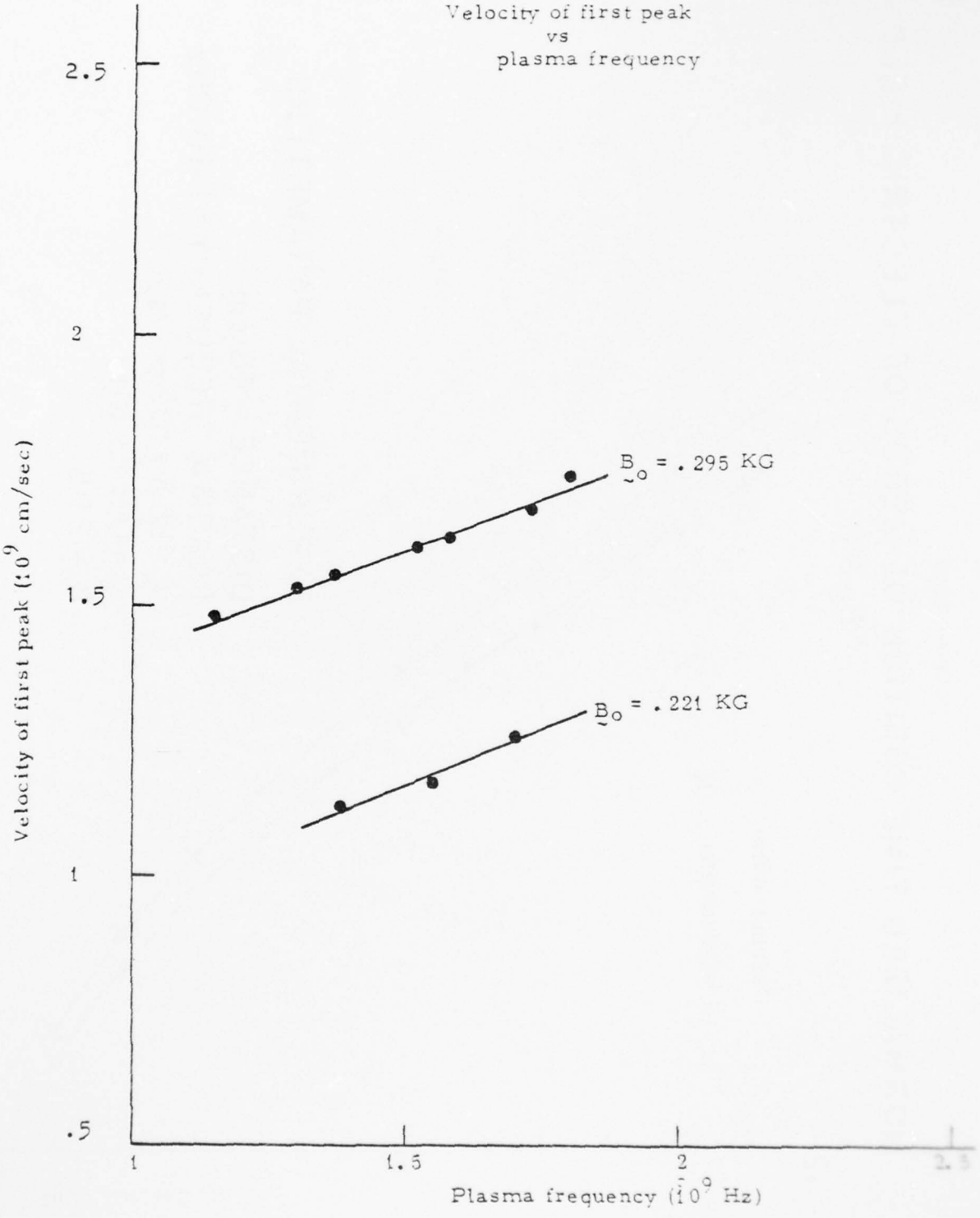
Velocity of first peak
vs
plasma frequency
2.5
2
1.5
1
.5
Velocity of first peak ($\times 10^9$ cm/sec)
B_o = .295 KG
B_o = .221 KG
1
1.5
2
Plasma frequency ($\times 10^9$ Hz)

Figure 4.21

AD-A071 017 POLYTECHNIC INST OF NEW YORK FARMINGDALE DEPT OF ELE--ETC F/G 20/9
STUDIES ON THE INTERACTIONS BETWEEN ELECTROMAGNETIC FIELDS AND --ETC(U)
APR 79 B R CHEO, E E KUNHARDT, S P KUO AFOSR-74-2668

UNCLASSIFIED POLY-EE-79-053 AFOSR-TR-79-0752 NL

2 OF 4

AD A071017

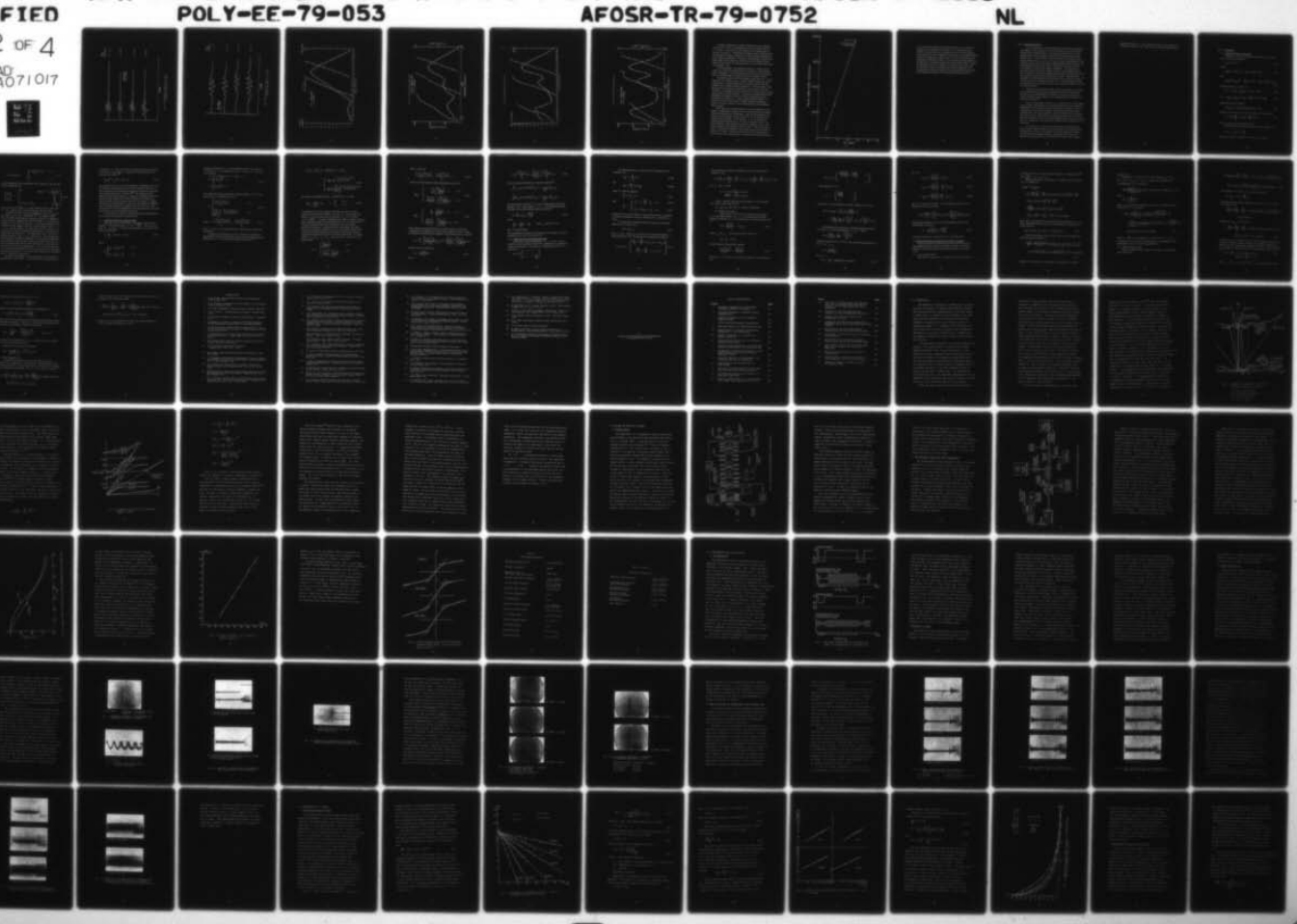

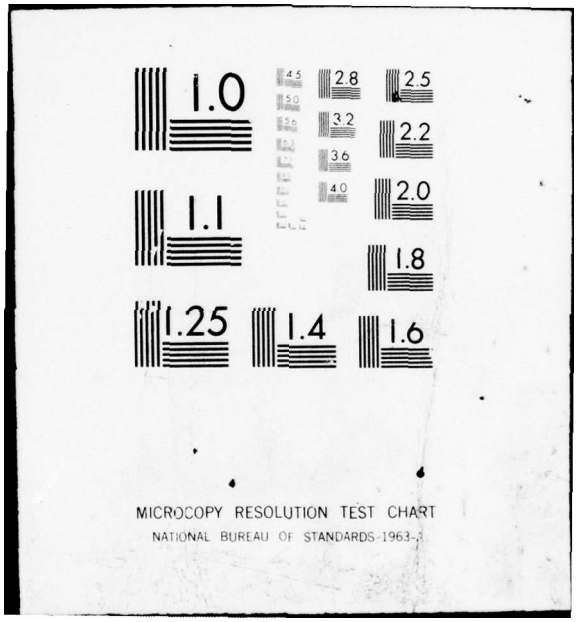
1.0
1.1
1.25
1.4
1.6
1.8
2.0
2.2
2.5
2.8
3.2
3.6
4.0
4.5
5.0
5.6
MICROCOPY RESOLUTION TEST CHART
NATIONAL BUREAU OF STANDARDS-1963-A

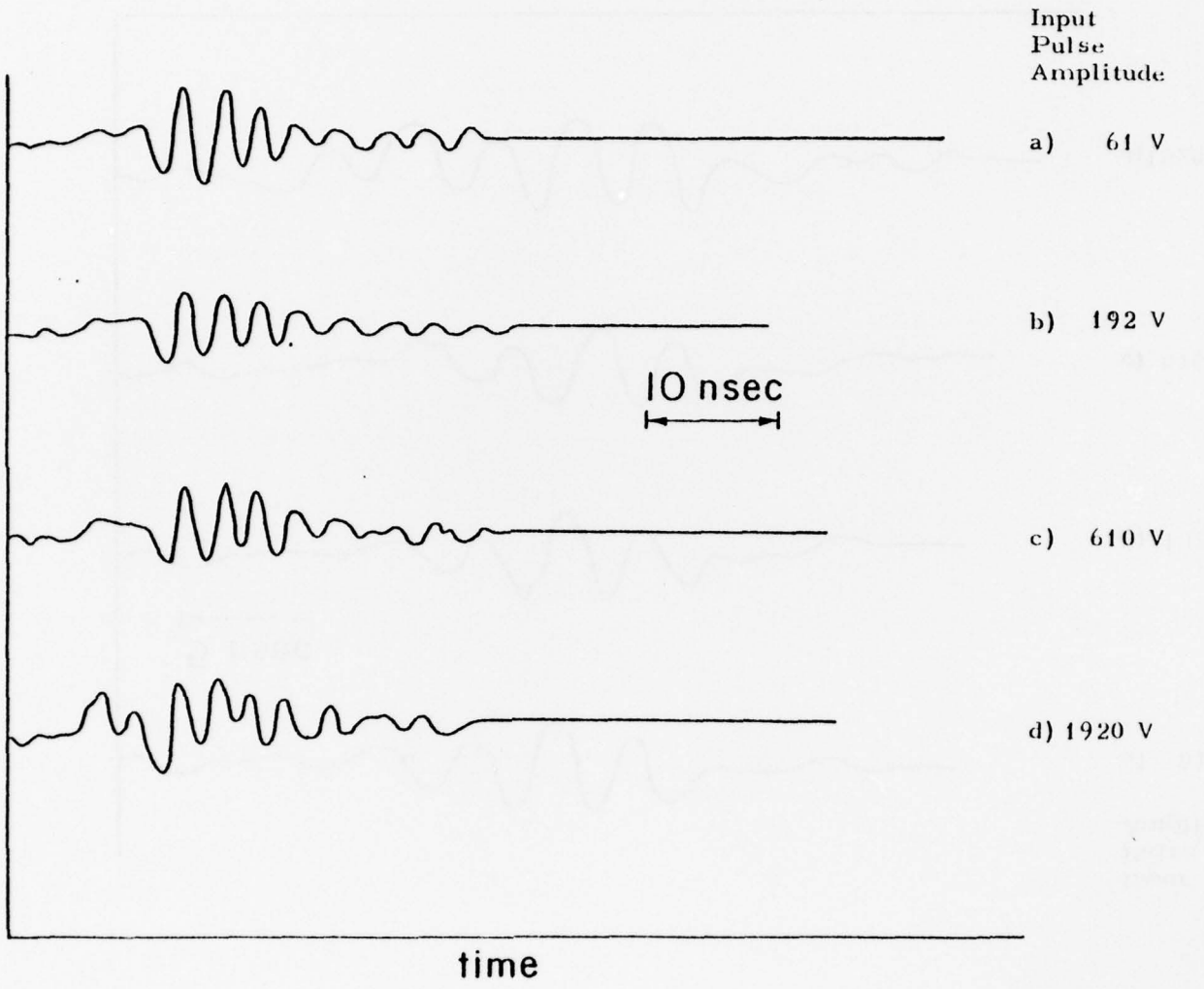

Fig. 4.22 Oscillogram taken at z = 56 cm
Cyclotron frequency = .6 GHz

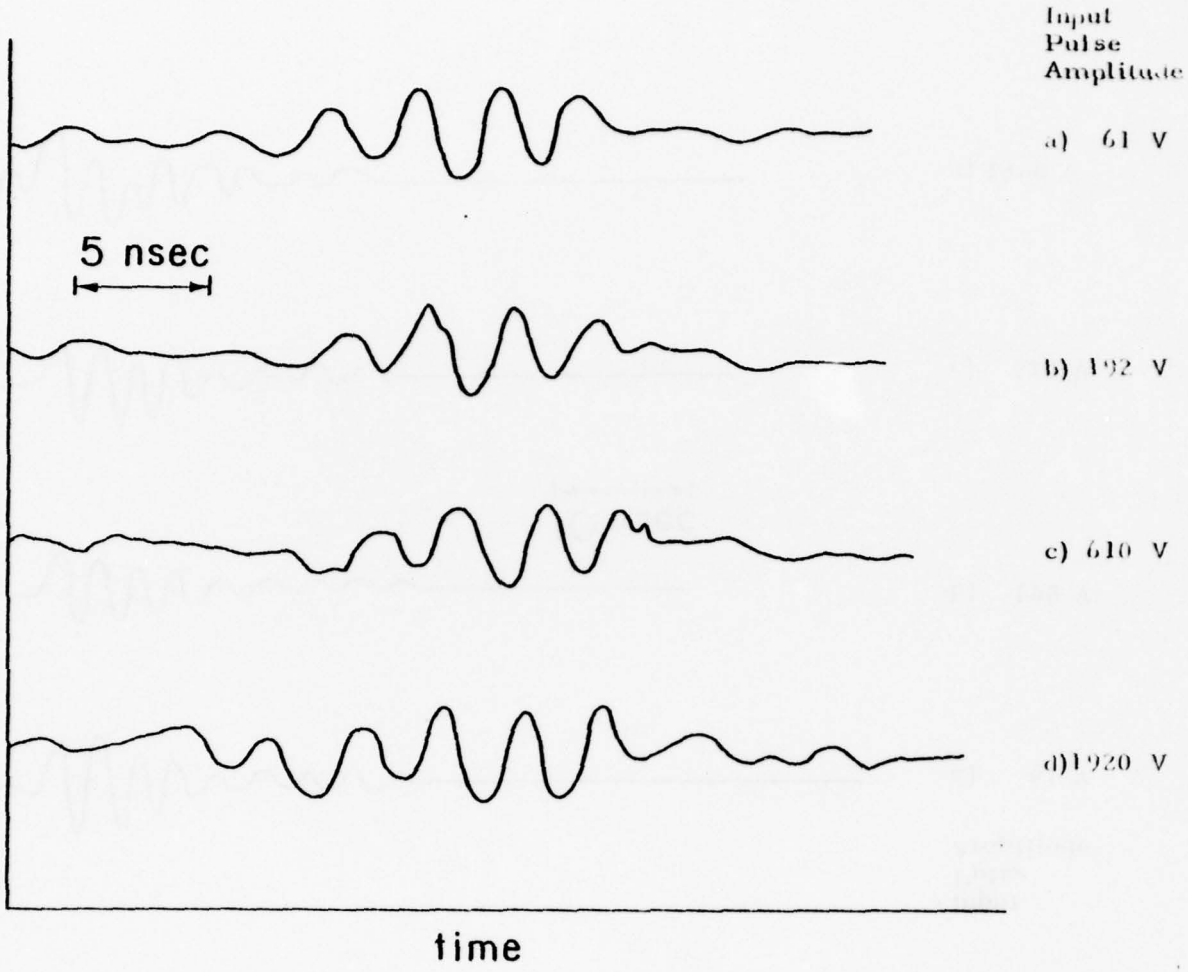

Fig. 4.22a Oscillogram taken at z = 34 cm
Cyclotron frequency = .6 GHz

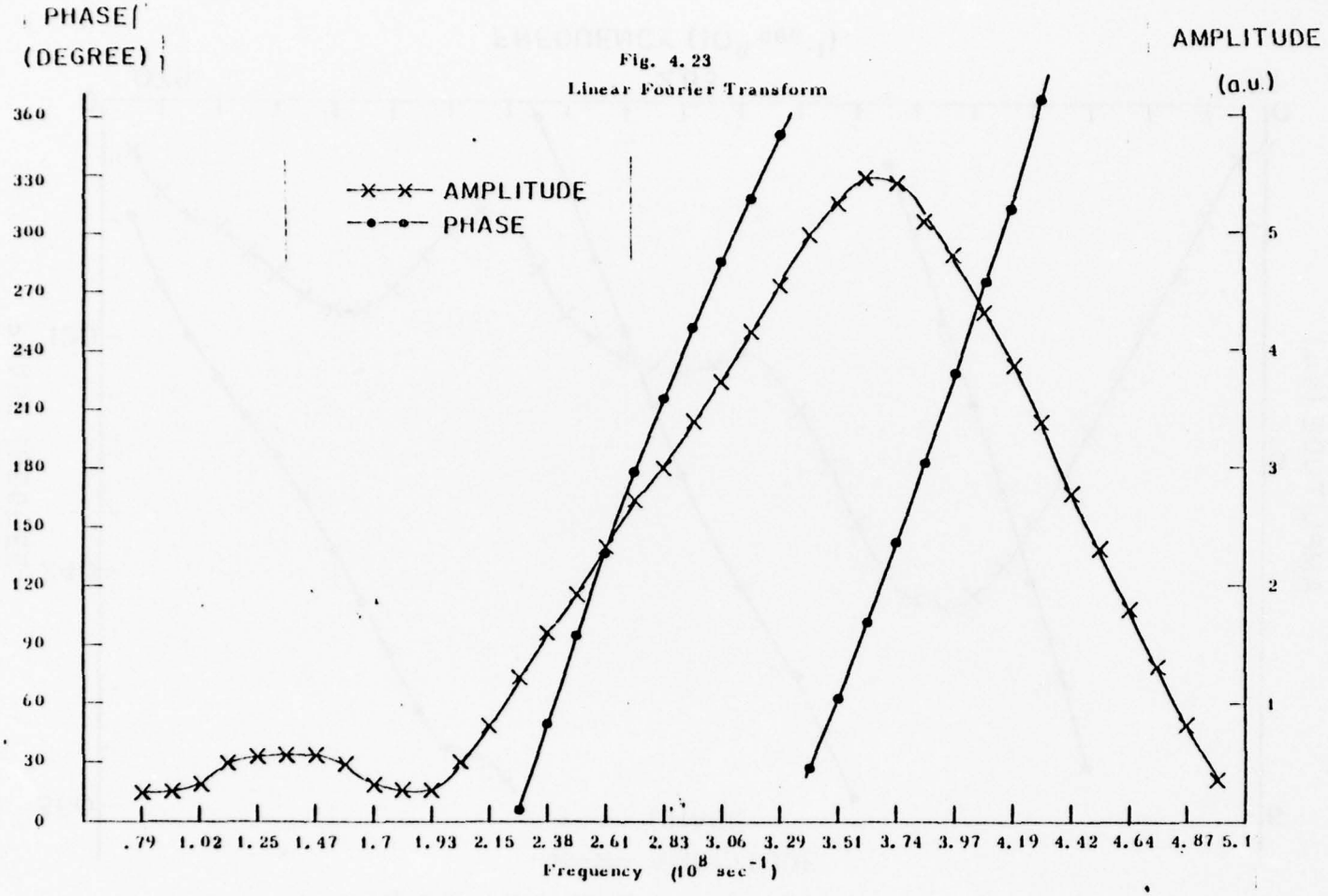

Fig. 4.23
Linear Fourier Transform

Fig. 4. 24 Fourier Transform of Figure 4. 22b

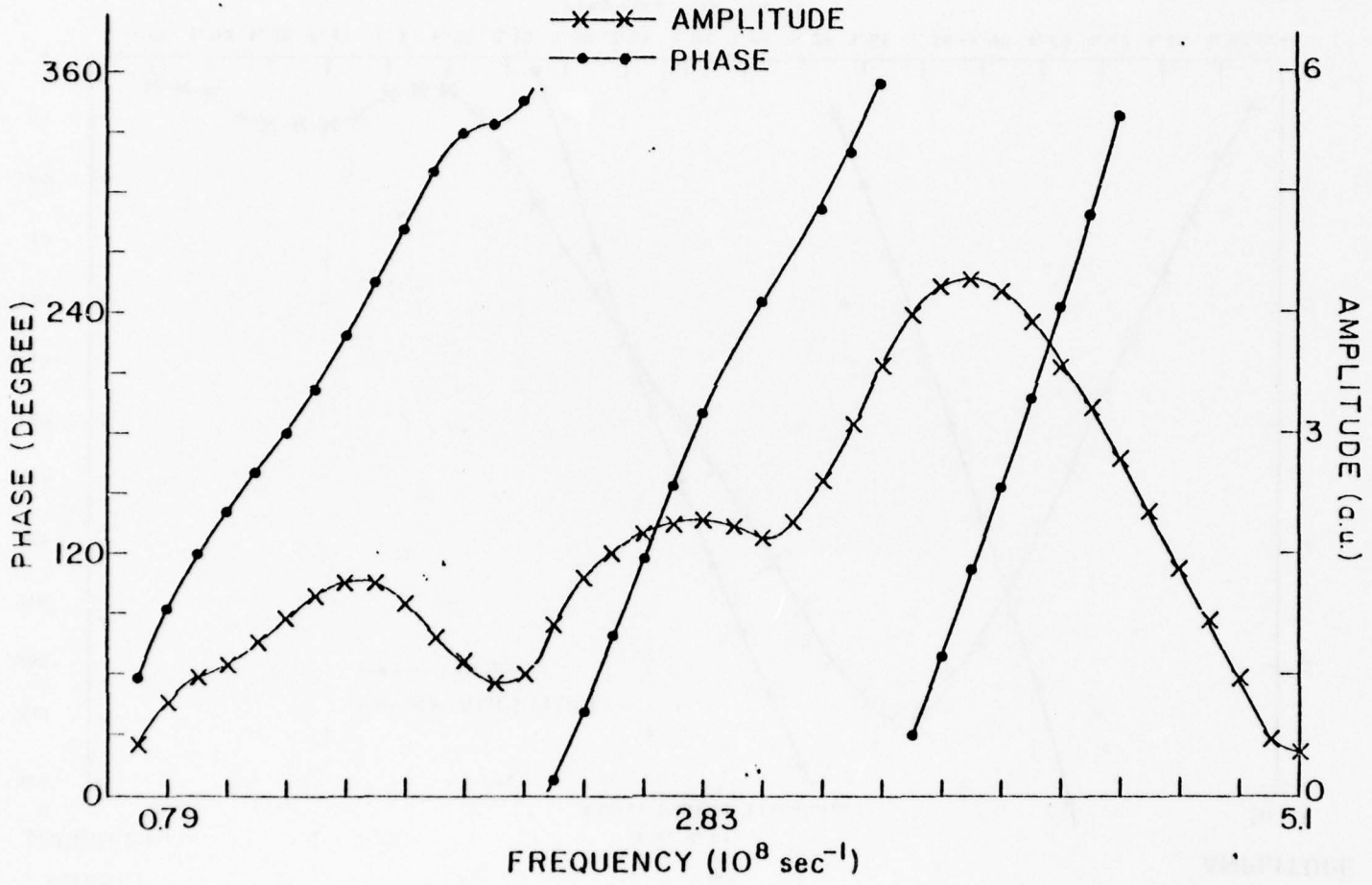

Fig. 4. 25 Fourier Transform of Fig. 4. 22c

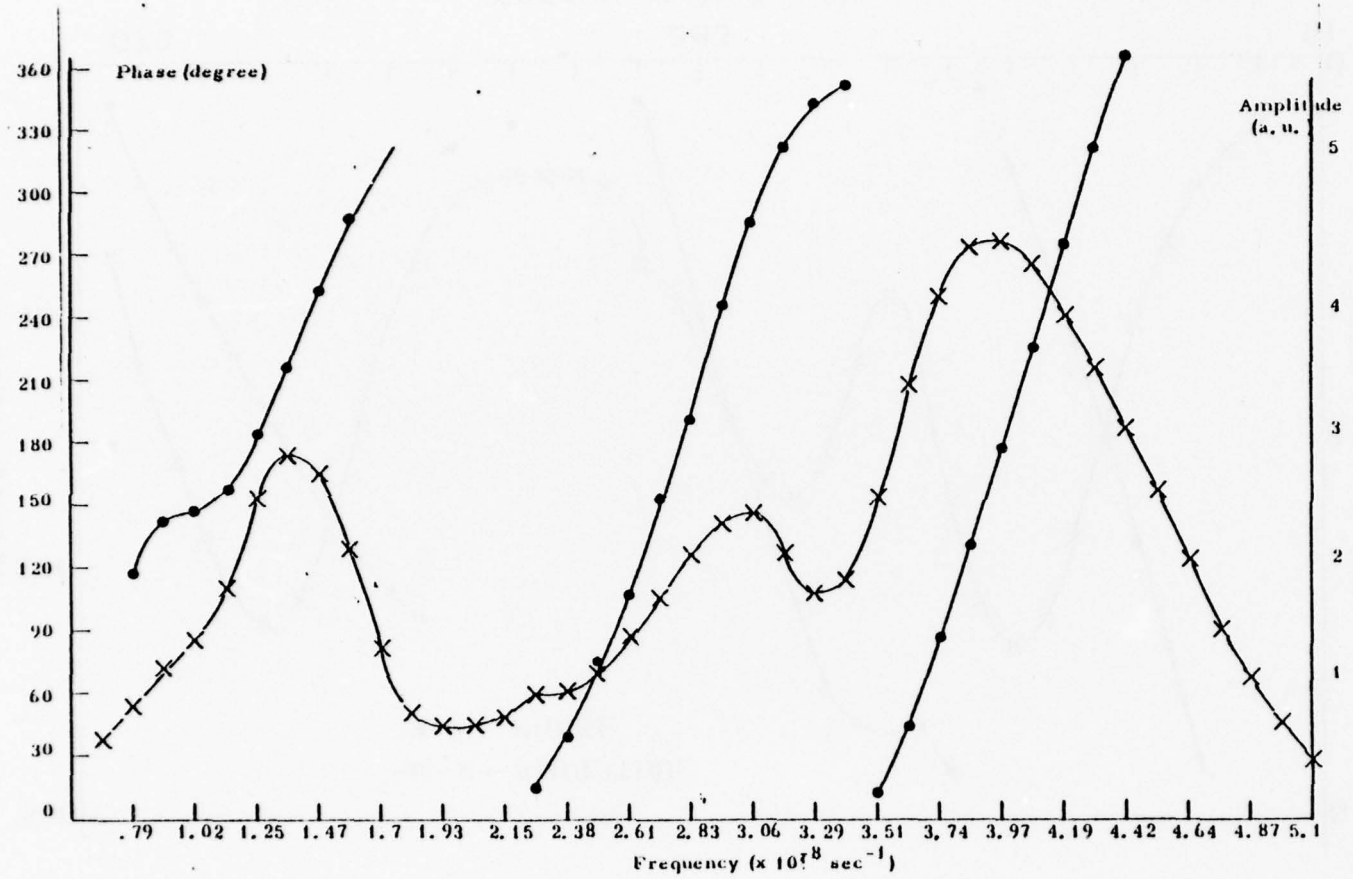

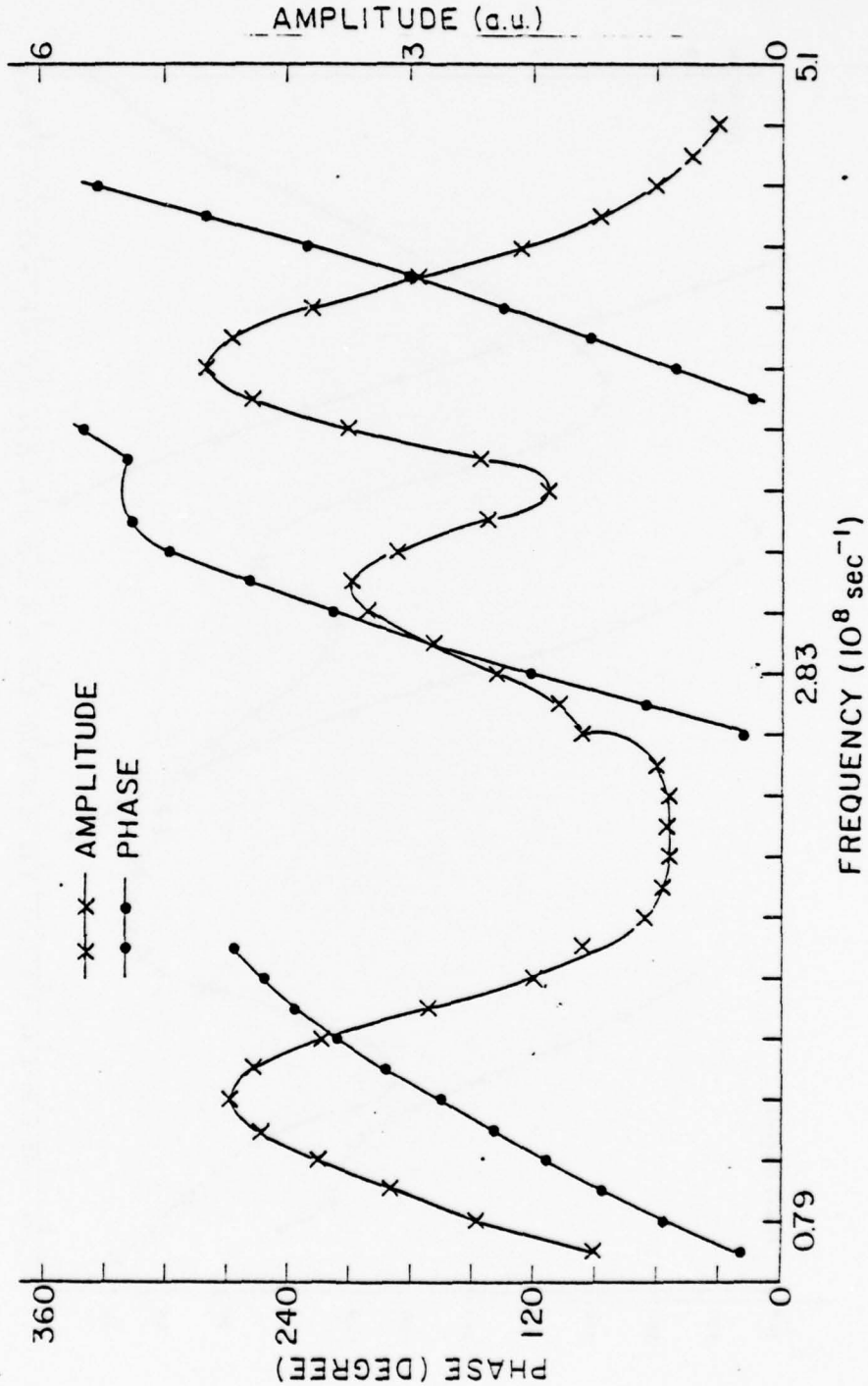

Fig. 4.26 Fourier Transform of Figure 4.22 d

At higher amplitude two distinct phenomena occurred (figures 4-24 to 4-26). First is the appearance of a low frequency peak at f = .14 GHz (A), and second is the splitting of the original peak (C) into two ((B) and (C)). Recalling the technique used in obtaining these oscillograms (loop gain constant) it is evident that these changes are due to nonlinear phenomena. Moreover, the possibility of these peak being higher order modes was ruled out by the fact that the group delay for these modes is much greater than for the lowest order mode (see equation 3-37).

From this figure , the amplitude of peak A is observed to increase very rapidly as the input level is increased. The frequency shift is negligible. No further analysis has been made of this packet but it is suspected that it belongs to the class of solitary waves.

The main concern is with the splitting of the packet (C). As the input level is increased, there is a shift to higher frequencies of the original peak. A gradual appearance of another peak B at the low frequency side indicates another wavepacket. From the slopes of the phase at these two peaks the difference in group velocity has been calculated. The higher frequency packet (C) was found to have a longer delay and hence a lower velocity. According to the modulation theory, the difference between the time of arrival is proportional to the amplitude (see section 3.3). This is clearly shown in figure 4-27; moreover the observation that the higher frequency wavepacket travels at a lower velocity is also in agreement with the modulation theory results.

Since there is no absolute measure of the field strengths in the plasma, a quantitative comparison of this velocity difference between theory and experiment is not possible. But from the measured time difference and the group velocity of the wave, we can calculate the required field amplitude. From equation 3-63 , to achieve the largest observed separation of 3.4 ns over a distance of 56 cm, the wave amplitude of the wavepacket required is about 50 v/cm. This field represents a total energy of about 1.3×10^{-9} joules in the wavepacket. The energy contained in the exciting electric field impulse is about 3×10^{-5} joules. Since most of the energy of the impulse goes into the dummy load and radiated to outside the parallel plate structure,

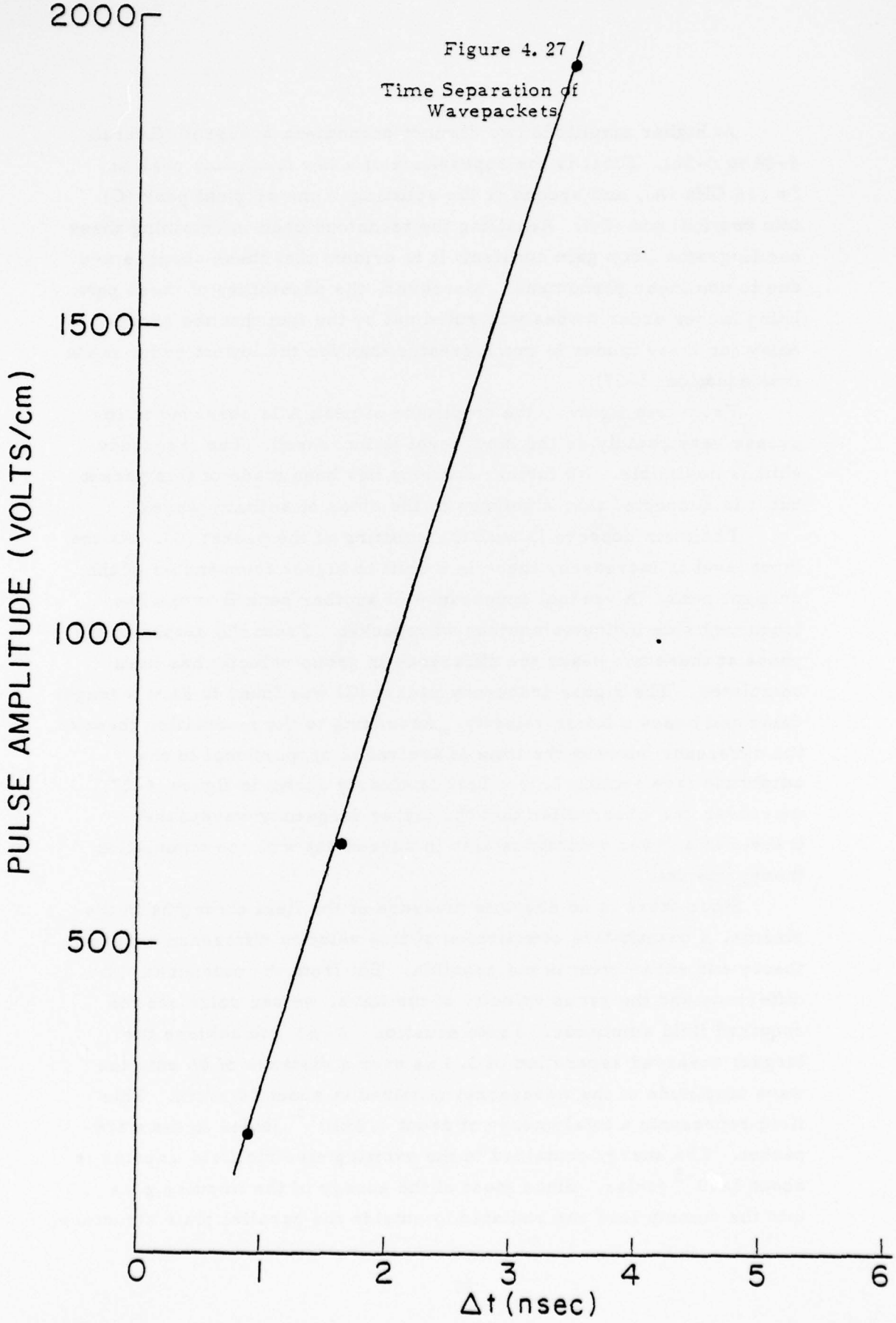

Figure 4. 27

Time Separation of Wavepackets

it is of interest to estimate the coupling efficiency, i.e. how much energy can be coupled into the plasma. As a rough upper bound estimate, assume that when the impulse field arrives at the plasma tube, the 2kV/cm field is applied to all electrons in the region between the plates during the pulse duration ($\Delta t \approx 0.4$ ns), and each electron would gain a momentum of $eE\Delta t$. The total kinnetic energy gained by all electrons in the region in this way is of the order of 9×10^{-7} joules. Comparing the orders of magnitude of the three energy levels, the 50 v/cm field required to produce the measured separation of the wavepackets is certainly reasonable for the experimental setup used. The modulational splitting of the wavepacket has been observed.

III-5. Concluding Remarks

In the foregoing, we have described an experimental and theoretical investigation of the propagation of finite amplitude slow waves excited by high amplitude baseband pulses. The subject of symmetric slow mode propagation has been incorporated into the framework of nonlinear dispersive waves. Theoretically, it has been shown that for typical experimental conditions (i.e., $\omega_c = 0$, $\omega_c < \omega_p$, $\omega_c >> \omega_p$), the propagation of the symmetric slow mode is described by the Kortewig de Vries equation, with the magnitude and sign of the various coefficients of the KdeV equation being different in the various regimes considered. This implies that given equal initial conditions, different effects in the propagation mode will be observed. The close interplay between theory and experiment leads to a good understanding of the experimental results. Although linear experiments on the propagation of this mode have previously been done,[31] far better resolution has been obtained here. To our knowledge, neither the experimental nor theoretical results of the nonlinear problem have been previously reported.

There are two areas which need further investigation. The results of that investigation will further substantiate the theory developed here and will aid in the experimental verification of the general theoretical results obtained for non-stationary waves propagating in accordance with the K de V equation.[42]

First, as mentioned in Section 4.3.3, the nature of the initial peak in the frequency spectrum has not been determined and second, nonlinear experiments where the polarity of the exciting pulse is negative must still be performed. We will not consider the first area further and instead comment only on the second problem. The first implication of reversing the polarity is that, theoretically, the phenomena observed for the weak field case should now occur for the zero magnetic field case and vice versa. This is a consequence of the sign of the nonlinear term in equations (3-47) and (3-48).

In conclusion, it must be noted that in order to experimentally obtain a wider range of parameters, the experiment as described should be modified in two ways: the duration of the pulse should be increased, and the cathode arrangement changed. Increasing the pulse duration enhances the nonlinear effects (see equations(3-57) and (3-58)), whereas

changing the cathode, to a flat cathode for instance, will eliminate the rotational instability of the column, observed at high magnetic fields.

III-6. Appendices

6.1 Formal derivation of operators

Equation (3-10) may be written approximately up to second order in the field variables as:

$$\underset{\sim}{u} = \underset{\sim}{u}^{(1)} + \underset{\sim}{u}^{(2)} \tag{6-1}$$

where,

$$m d_t \underset{\sim}{u}^{(1)} + m\nu_c \underset{\sim}{u}^{(2)} = - en_o \underset{\sim}{E} - e\mu_o \underset{\sim}{u}^{(1)} \times \underset{\sim}{H}_o \tag{6-2}$$

and

$$m d_t \underset{\sim}{u}^{(2)} + m\nu_c \underset{\sim}{u}^{(2)} = - \frac{m}{n_o} \nabla . \underset{\sim}{u}^{(1)} \underset{\sim}{u}^{(1)} - e\tilde{n} \underset{\sim}{E} - e\mu_o \underset{\sim}{u}^{(2)} \times \underset{\sim}{H}_o \tag{6-3}$$

Formally solving (6-2) and (6-3),

$$\underset{\sim}{u}^{(1)} = - (m d_t \underset{\approx}{1} - e\mu_o \underset{\sim}{H}_o \times \underset{\approx}{1} + m\nu_c \underset{\approx}{1})^{-1} en_o \underset{\sim}{E} \tag{6-4}$$

$$u^{(2)} = - (m d_t \underset{\approx}{1} - e\mu_o \underset{\sim}{H}_o \times \underset{\approx}{1} + m\nu_c \underset{\approx}{1})^{-1} \left[\frac{m}{n_o} \nabla . \underset{\sim}{u}^{(1)} \underset{\sim}{u}^{(1)} + e\tilde{n} \underset{\sim}{E} \right] \tag{6-5}$$

Defining the inverse operator:

$$\Pi (d_t, \underset{\sim}{H}_o, \nu_c) = (m d_t \underset{\approx}{1} - e\mu_o \underset{\sim}{H}_o \times \underset{\approx}{1} + m\nu_c \underset{\approx}{1})^{-1} en_o \tag{6-6}$$

the total current from (6-1)≅ (6-4)-(6-6) and (3-13) is given by:

$$\underset{\sim}{u} = - \Pi \{ \underset{\sim}{E} + \frac{m}{n_o^2 e} \nabla . \underset{\approx}{\pi} \underset{\sim}{E} \underset{\approx}{\pi} \underset{\sim}{E} - \frac{\epsilon_o}{en_o} \underset{\sim}{E} \nabla . \underset{\sim}{E} \} \tag{6-7}$$

which is used to arrive at equations (3-15).

Defining the time Fourier transform of a field variable as:

$$f(\underset{\sim}{r}, t) = \int_{-\infty}^{\infty} f(\underset{\sim}{r}, \omega) e^{-i\omega t} \frac{d\omega}{2\pi}$$

Applying the above to equations (6-6) and (6-7), we obtain:

$$\underset{\approx}{\Pi}(\omega, \underset{\sim}{H}_o, \nu_c) \rightarrow \begin{pmatrix} \Pi_1 & -\Pi_2 & 0 \\ \Pi_2 & \Pi_1 & 0 \\ 0 & 0 & \dfrac{n_o e}{im^*\omega} \end{pmatrix} \qquad \Pi_1 = \dfrac{n_o e}{im^*\omega\left[1 - \dfrac{(e\mu_o H_o/m^*)^2}{\omega^2}\right]}$$

$$\Pi_2 = \dfrac{n_o e(e\mu_o H_o/m^*)}{m^*\omega^2\left[1 - \dfrac{(e\mu_o H_o/m^*)^2}{\omega^2}\right]} \qquad (6\text{-}8)$$

$$\underset{\sim}{u}(\underset{\sim}{\Omega}, \omega) = -\underset{\approx}{\Pi}(\omega_1 \underset{\sim}{H}_o, \nu_c)\left\{\underset{\sim}{E}(\underset{\sim}{\Omega}, \omega) + \frac{m}{n_o^2 e}\int \nabla.\underset{\approx}{\Pi}(\omega_1, \underset{\sim}{H}_o, \nu_c)\underset{\sim}{E}\omega_1 \underset{\approx}{\Pi}(\omega_2, \underset{\sim}{H}_o, \nu_c)\underset{\sim}{E}\omega_2 d\lambda\right.$$

$$\left. - \frac{\epsilon_o}{en_o}\int \underset{\sim}{E}\omega_1 \nabla.\underset{\sim}{E}\omega_2 d\lambda\right\} \qquad (6\text{-}9)$$

where $m^* = m(1 + i\nu_c/\omega)$

and for any two vectors $\underset{\sim}{F}(\underset{\sim}{\Omega}, t)$ and $\underset{\sim}{G}(\underset{\sim}{\Omega}, t)$,

$$\int \underset{\sim}{F}\omega_1 \underset{\sim}{G}\omega_2 d\lambda = \int \underset{\sim}{F}(\underset{\sim}{r}, \omega_1)\, \underset{\sim}{G}(\underset{\sim}{r}, \omega_2)\delta(\omega - \omega_1 - \omega_2)d\omega_1 d\omega_2$$

Using (6-8) and (6-9), the transform of L in equation (3-16) is given by

$$L(-i\omega, \nabla_t \rightarrow i \qquad \begin{pmatrix} i\omega\epsilon_o\left[\underset{\approx}{1} + \dfrac{e}{\epsilon_o\omega}\underset{\approx}{\Pi}(\omega, H_o, \nu_c)\right] & \nabla_t x \underset{\approx}{1} \\ -\nabla_t x \underset{\approx}{1} & i\omega\mu_o \underset{\approx}{1} \end{pmatrix}$$

6.2 Evaluation of the eigenvectors

The eigenvalue equation (3-19) may be expressed solely in terms of the transverse components of ψ_α as:[40]

$$\omega\left(\underset{\approx}{\epsilon}_t \epsilon_o - \frac{1}{\omega^2\mu_o}\underset{\sim}{z}_o x \nabla_t \nabla_t x \underset{\sim}{z}_o\right) \cdot \underset{\sim}{E}_{\alpha_t} = \kappa_\alpha \underset{\sim}{H}_{\alpha_t} x \underset{\sim}{z}_o$$

$$\omega\left(\mu_o \underset{\approx}{1}_t - \frac{1}{\omega^2\epsilon_o}\underset{\sim}{z}_o x \nabla_t \frac{1}{\epsilon_3}\nabla_t x \underset{\sim}{z}_o\right) \cdot \underset{\sim}{H}_{\alpha_t} = \kappa_\alpha \underset{\sim}{z}_o x \underset{\sim}{E}_{\alpha_t} \qquad (6\text{-}10)$$

where

$$\underline{\underline{\epsilon}} = \underline{\underline{\epsilon}}_t + \underline{z}_o \underline{z}_o \epsilon_3 = \begin{cases} \underline{\underline{1}} + \frac{e}{\epsilon_o \omega} \underline{\underline{\Pi}}(\omega, H_o, \nu_c) & \rho < b \\ \\ \underline{\underline{1}} & \rho > b \end{cases} \tag{6-11}$$

and the longitudinal field components may be obtained from the transverse components via:

$$\begin{pmatrix} E_{\alpha_z} \\ H_{\alpha_z} \end{pmatrix} = \begin{pmatrix} 0 & (i\omega\epsilon_3\epsilon_o)^{-1} \nabla_t \times \underline{z}_o \\ -(i\omega\mu_o)^{-1} \nabla_t \times \underline{z}_o & 0 \end{pmatrix} \begin{pmatrix} \underline{E}_{\alpha_t} \\ \underline{H}_{\alpha_t} \end{pmatrix} \tag{6-12}$$

Note that since the operator L_o takes different forms in the range $0 < \rho < \infty$, likewise $\underline{\psi}_\alpha$'s will have different representations.

In general, the total field corresponding to $\underline{E}_{\alpha_t}$ and $\underline{H}_{\alpha_t}$ will have both E_{α_z} and H_{α_z} components.[40] This implies that no TE or TM mode representation is possible; therefore a complete set of modes must be composed of TE and TM modes. In the following analysis, we will restrict to the cases: a) zero static magnetic field, b) infinitely large magnetic field and c) weak magnetic fields, i. e. $\omega_{te} < \omega_{pe}$, and the column is surrounded by a perfect condition. The first two cases result in substantial simplification in the form of the eigenvectors and eigenvalues. For these cases, Eqs. (2-3) can be satisfied with either E_{α_z} or H_{α_z} equal to zero. This implies that two independent solutions are possible. Since neither the nonlinearity nor the boundary couple the two solutions and since initially only E modes are generated by the electric current source, only these will be considered in the field representation. For the low magnetic field case, we make the assumption that the waves are slow and, therefore, are primarily TM type, i. e., the actual field eigenvectors are approximated by quasistatic eigenvectors.

An implicit assumption, when representing the total fields as a superposition of modal fields, is that the modal set (or eigenvectors)

is complete, i.e., they form a basis in terms of which any arbitrary vector may be represented. A statement of completeness may be expressed as follows:[40]

$$\sum_{\alpha} \psi_{\alpha_t^*}^{(\Omega')} \; \psi_{\alpha_t}^{(\Omega)} = \underset{\approx}{1} \, \delta(\underset{\sim}{\Omega} - \underset{\sim}{\Omega}') \tag{6-13}$$

The sumation in (6-13) is to be interpreted as an integral for the case of continuous spectrum and as a sum for the discrete spectrum. A direct procedure for determining the spectrum utilizes the characteristic Green's function for E modes.[40] The properties of the Green's function in the complex κ_α plane are investigated; and from pole and branch singularities, which contribute to the integral of Green's function along a suitable contour in the complex κ_α plane, the eigenvectors are obtained. In this case, the question of completeness is assured although normalization as in (3-19a) is not. This procedure will be used subsequently for the determination of the mode vectors of the zero axial magnetic field case.

For the other two cases, we proceed directly to obtain that part of the spectrum associated with guided waves.

6.2.1 Eigenvectors for zero magnetic field

When $\underset{\sim}{H}_o$ is zero, then tensor $\underset{\approx}{\epsilon}$ degenerates into a scalar quantity. In the plasma region, $\underset{\approx}{\epsilon} \rightarrow \underset{\approx}{1}\left(1 - \frac{\omega_p^2}{\omega^2}\right)$. Since for an E mode $\nabla_t \cdot \underset{\sim}{z}_o \times \underset{\sim}{E}_{\alpha_t} = 0$, we have (from equation (6-10) for the scalar Green's function:[40]

$$\nabla_t \cdot \frac{\epsilon}{\kappa_\perp^2} \cdot \nabla_t g + \epsilon g = -\delta(\rho - \rho') \tag{6-14}$$

where

$$\kappa_{\perp_i}^2 = \begin{cases} \kappa_{\perp_1}^2 = \omega^2 \mu_o \epsilon_o \epsilon - \kappa_\alpha^2 & \rho < b \\ \kappa_{\perp_2}^2 = \omega^2 \mu_o \epsilon_o - \kappa_\alpha^2 & \rho < b \end{cases}$$

Boundary conditions for g may be obtained from (6-14), since it is valid for all ρ. By integrating across $\rho = b$ and $\rho = \rho'$, we have the conditions:

$$\begin{aligned} &1)\ g \text{ is continuous at } \rho = b \text{ and } \rho = \rho' \\ &2)\ \frac{\epsilon}{\kappa_{\perp i}^2} \nabla_t g \Big/_{\rho'_-}^{\rho'_+} = -1 \\ &3)\ \frac{\epsilon}{\kappa_{\perp i}^2} \nabla_t g \Big/_{b_-}^{b^+} = 0 \end{aligned} \tag{6-15}$$

for a symmetric source of electric current located at $\rho = b^+$, the solution to (6-14) satisfying (6-15) is:

$$g = \begin{cases} \dfrac{-J_o(\kappa_{\perp 1} b)\, J_o(\kappa_{\perp 1} \rho)}{\Delta} & \rho < b \\ \dfrac{-J_o^2(\kappa_{\perp 1} b)}{H_o^2(\kappa_{\perp 2} b)} \dfrac{H_o(\kappa_{\perp 2} b)\, H_o(\kappa_{\perp 2} \rho)}{\Delta} & \rho > b \end{cases} \tag{6-16}$$

$$\text{where } \Delta = \frac{\epsilon\, J_1(\kappa_{\perp 1} b) H_o(\kappa_{\perp 2} b)}{\kappa_{\perp 1}} - \frac{J_o(\kappa_{\perp 1} b) H_1(\kappa_{\perp 2} b)}{\kappa_{\perp 2}} \tag{6-17}$$

and J_1, J_o, H_o, H_1 are Bessel functions of the first and second kind, respectively.

The spectral representation in (6-13) may now be obtained by integrating the scalar Greens function along a contour that encloses all singularities of g. The desired relationship is given by[40]:

$$\sum_{\alpha} \phi_{\alpha}(\kappa_{\perp i}\rho)\,\phi_{\alpha}^{*}(\kappa_{\perp i}\rho) = \frac{1}{2\pi i}\oint_{c} g(\rho,\rho';\kappa_{\alpha})\,d\kappa_{\alpha}$$

$$= \begin{cases} -\dfrac{1}{2\pi i}\oint_{c} \dfrac{J_o(\kappa_{\perp 1}b)\,J_o(\kappa_{\perp 1}\rho)\,d\kappa_{\alpha}}{\Delta} \\ -\dfrac{1}{2\pi i}\oint_{c} \dfrac{J_o^2(\kappa_{\perp 1}b)}{H_o^2(\kappa_{\perp 2}b)}\,\dfrac{H_o(\kappa_{\perp 2}b)\,H_o(\kappa_{\perp 2}\rho)\,d\kappa_{\alpha}}{\Delta} \end{cases} \qquad (6\text{-}18)$$

the transverse component of $\underset{\sim}{E}_{\alpha}$ is obtained from ϕ_{α} using,

$$\underset{\sim}{E}_{\alpha_t} = -\frac{\kappa_{\alpha}}{\kappa_{\perp i}^2 \omega\epsilon_o}\nabla_t g \qquad i = \begin{cases} 1 & \rho < b \\ 2 & \rho > b \end{cases} \qquad (6\text{-}19)$$

The integrand in (6-18) is analytic everywhere except for a finite number of poles and branch points. For real κ_{α}, only a single pole exists at $\Delta = 0$; the branch point corresponds to $\kappa_{\perp 2} = 0$ for which $\kappa_{\alpha} = \pm\,\omega\sqrt{\mu_o\epsilon_o}$. The pole contribution gives rise to a guided surface mode, while the branch cut contribution gives rise to a radiation field.[46] For the excitation problem both contributions must be included, specially at the source. In the far field we only consider the guided wave, but as observed in Chapter III; we do not know the absolute field strength of the guided mode since we neglect to include the amount of energy extracted from the source by the other mode types. For guided modes, $\kappa_{\perp 1} = i|\kappa_{\perp 1}|$, $\kappa_{\perp 2} = i|\kappa_{\perp 2}|$ and from (6-18), we have for the guided modes:

$$\phi_{\alpha} = \begin{cases} \dfrac{I_o(\kappa_{\perp 1}\rho)}{\sqrt{\partial_{\kappa_{\alpha}}\Delta}} & \rho < b \\ \dfrac{I_o(\kappa_{\perp 1}b)}{K_o(\kappa_{\perp 2}b)}\,\dfrac{K_o(\kappa_{\perp 2}\rho)}{\sqrt{\partial_{\kappa_{\alpha}}\Delta}} & \rho > b \end{cases}$$

with κ_a given by:

$$\frac{\epsilon\, I_1(\kappa_{\perp 1} b)\, K_o(\kappa_{\perp 2} b)}{\kappa_{\perp 1}} + \frac{I_o(\kappa_{\perp 1} b)\, K(\kappa_{\perp 2} b)}{\kappa_{\perp 2}} = 0 \tag{6-20}$$

From (6-19) the transverse field components are given by:

$$\underset{\sim}{E}_{a_t} = \begin{cases} \dfrac{\kappa_a\ I_o'(\kappa_{\perp 1}\rho)}{\omega\epsilon_o \kappa_{\perp 1}\sqrt{\partial_{\kappa_a}\Delta}}\ \underset{\sim}{\rho} & \rho < b \\ -\dfrac{I_o(\kappa_{\perp 1} b)}{K_o(\kappa_{\perp 2} b)}\ \dfrac{\kappa_a\ K_o'(\kappa_{\perp 2}\rho)}{\kappa_{\perp 2}\omega\epsilon_o\sqrt{\partial_{\kappa_a}\Delta}}\ \underset{\sim}{\rho} & \rho > b \end{cases} \tag{6-21}$$

$$\underset{\sim}{H}_{a_t} = \begin{cases} \dfrac{\epsilon}{\kappa_{\perp 1}}\ \dfrac{I_1(\kappa_{\perp 1}\rho)}{\sqrt{\partial_{\kappa_a}\Delta}}\ \underset{\sim}{\theta} & \rho < b \\ -\dfrac{I_o(\kappa_{\perp 1} b)}{K_o(\kappa_{\perp 2} b)}\ \dfrac{K_1(\kappa_{\perp 2}\rho)}{\kappa_{\perp 2}\sqrt{\partial_{\kappa_a}\Delta}}\ \underset{\sim}{\theta} & \rho > b \end{cases} \tag{6-22}$$

Even though the potential functions are orthonormal; the transverse components of the eigenvector do not satisfy condition (3-19a). Proper normalization is introduced by defining a normalization factor as follows:

$$N_a = 2\int_o^b \frac{I_1^2(\kappa_{\perp 1}\rho)\,\epsilon\,\kappa_a}{\kappa_{\perp 1}^2\sqrt{\partial_{\kappa_a}\Delta}\ \omega\epsilon_o}\,\rho\,d\rho + 2\,\frac{I_o^2(\kappa_{\perp 1} b)}{K_o^2(\kappa_{\perp 2} b)}\int_b^\infty \frac{K_1^2(\kappa_{\perp 2}\rho)}{\kappa_{\perp 2}^2\omega t_o\sqrt{\partial_{\kappa_a}\Delta}}\,\rho\,d\rho$$

the above can be rewritten as:

$$N_a = \frac{2\beta\,\kappa_a}{\omega\epsilon_o\,\partial_{\kappa_2}\Delta} \tag{6-23}$$

where

$$\beta = \int_0^b \frac{I_1^2(\kappa_{\perp 1}\rho)\,\epsilon}{\kappa_{\perp 1}^2}\rho\,d\rho + \frac{I_0^2(\kappa_{\perp 1}b)}{K_0^2(\kappa_{\perp 2}b)}\int_b^\infty \frac{K_1^2(\kappa_{\perp 2}\rho)}{\kappa_{\perp 2}^2}\rho\,d\rho \qquad (6\text{-}24)$$

(6-24) is evaluated explicitly by using the formulae[47]:

$$\int_0^b I_1(\kappa_{\perp 1}\rho)\rho\,d\rho = -\tfrac{1}{2}b^2\{I_1'^2(\kappa_{\perp 1}b) - (1 + \frac{1}{\kappa_{\perp 1}^2 b^2})I_1^2(\kappa_{\perp 1}b)\}$$

$$\int_0^\infty K_1^2(\kappa_{\perp 2}\rho)\rho\,d\rho = \tfrac{1}{2}b^2\{K_1'^2(\kappa_{\perp 2}b) - (1 + \frac{1}{\kappa_{\perp 2}^2 b^2})K_1^2(\kappa_{\perp 2}b)\}\ ,$$

the characteristic equation (6-20), and the approximate dispersion equation (3-15). In the region $\kappa_{\perp 1} b < 1$, we can expand the Bessel functions in the small argument regime and obtain:

$$\beta = \frac{b^2}{2} I_0(\kappa_{\perp 1}b)\,\frac{\omega_p^2 v_d^2}{\omega^4} \qquad (6\text{-}25)$$

where

$$\frac{1}{v_d^2} = \frac{1}{\omega_p^2 v_o^2} - \frac{1}{C^2} \qquad \text{with } v_o \text{ given by (3-34)}$$

and $C \equiv$ speed of light.

The longitudinal component of the eigenvector as defined in (3-22) is obtained from (6-23), (6-21) and (6-12).

6.2.2 Eigenvectors for large Magnetic fields

In the limit of large magnetization, i.e., $\omega_c/\omega >> 1$ $\omega_c >> \omega_p$; transverse electron motion is effectively inhibited and the plasma becomes non-gyrotropic. The tensor $\underline{\underline{\epsilon}}$ in equation (6-10) for $\rho < b$ reduced to:

$$\underline{\underline{\epsilon}} \longrightarrow \begin{pmatrix} 1 & 0 & 0 \\ 0 & 1 & 0 \\ 0 & 0 & 1 - \frac{\omega_p^2}{\omega^2} \end{pmatrix}$$

The guided eigenvector components may be obtained from a potential ϕ as:

$$\underset{\sim}{E}_{\alpha_t} = - \frac{\kappa_\alpha}{\kappa_{\perp 2}^2} \nabla_t \phi \tag{6-26a}$$

and

$$\underset{\sim}{H}_{\alpha_t} = \frac{\omega \epsilon_o}{\kappa_\alpha} \underset{\sim}{z}_o \times \underset{\sim}{E}_{\alpha_t} \tag{6-26b}$$

where ϕ obeys the equation:

$$\nabla_t^2 \phi + \kappa_{\perp i}^2 \phi = 0 \tag{6-27}$$

with

$$\kappa_{\perp i}^2 = \begin{cases} \kappa_{\perp 1}^2 = (1 - \frac{\omega_p^2}{\omega^2}) \kappa_{\perp 2}^2 & \rho < b \quad (6\text{-}28) \\ \kappa_{\perp 2}^2 = (\omega^2 \mu_o \epsilon_o - \kappa_\alpha^2) & \rho > b \quad (6\text{-}29) \end{cases}$$

equation (6-27) is solved subject to two different boundary conditions: 1) column surrounded by a perfect conductor and 2) column in free space.

1) for a perfect conducting boundary the solution with proper behavior at $\rho = 0$ and $\rho = b$ is:

$$\phi = A J_o(\kappa_{\perp 1} \rho) \tag{6-30}$$

with $\kappa_{\perp 1} b = p_n$, where p_n is the n^{th} zero of the Bessel function J_o. Using (6-26) and (6-12), the eigenvector components are given by:

$$\psi_\alpha \longrightarrow A' \begin{pmatrix} \frac{\kappa_\alpha}{\kappa_{\perp 1}} (1 - \frac{\omega_p^2}{\omega^2}) J_1(\kappa_{\perp 1} \rho) \underset{\sim}{\rho} + i J_o(\kappa_{\perp 1} \rho) \underset{\sim}{z} \\ \\ \frac{\omega \epsilon_o}{\kappa_{\perp 1}} (1 - \frac{\omega_p^2}{\omega^2}) J_1(\kappa_{\perp 1} \rho) \underset{\sim}{\theta} \end{pmatrix} \tag{6-31}$$

the normalization constant is determined from the orthonormality condition (3-19a):

$$1 = A' \int_0^b \{(i\kappa_\alpha)^* \frac{i\omega\epsilon_o}{\kappa_{\perp 1}^2}\left(1-\frac{\omega_p^2}{\omega^2}\right) J_1^2(\kappa_{\perp 1}\rho) + i\kappa_\alpha \left(\frac{i\omega\epsilon_o}{\kappa_{\perp 1}^2}\left[1-\frac{\omega_p^2}{\omega^2}\right] J_1^2(\kappa_{\perp 1}\rho)\right)^* \} \rho\, d\rho$$

for κ_α real, we have

$$A' = \frac{\kappa_{\perp 1}}{\sqrt{\omega\kappa_\alpha\epsilon_o}\left(1-\frac{\omega_p^2}{\omega^2}\right) b\, J_1(\kappa_{\perp 1} b)}$$

If the α index is separated into two indecis: m ≡ mode type, n ≡ mode in mode type; we have:

$\psi_\alpha \rightarrow \psi_{mn} \rightarrow \psi_n$ since only E modes are considered.

2) Column in free space

The solution (6-30) of (6-28) is still valid in the region $\rho < b$, the plasma region. For $\rho > b$, the solution that satisfies boundary conditions at $\rho = b$ and appropriate to the discrete spectrum is:

$$\phi = A' \frac{J_o(\kappa_{\perp 1} b)}{K_o(\kappa_{\perp 2} b)} K_o(\kappa_{\perp 2}\rho) \qquad (6\text{-}31)$$

where $\kappa_{\perp 2}$ and $\kappa_{\perp 1}$ are real and given by (see 6-29):

$$\kappa_{\perp 2}^2 = \kappa_\alpha^2 - \omega^2\mu_o\epsilon_o$$

and the boundary characteristic equation

$$\frac{\kappa_{\perp 1} J_1(\kappa_{\perp 1} b)}{J_o(\kappa_{\perp 1} b)} = \frac{\kappa_{\perp 2} K_1(\kappa_{\perp 2} b)}{K_o(\kappa_{\perp 1} b)} \qquad (6\text{-}32)$$

from (6-30), (6-31) and (6-26); the field components of the eigenvector are:

$$\underline{\underline{\nu}} = L - L_o = i \begin{pmatrix} \dfrac{-i\omega\epsilon_o\omega_p^2\nu_c^2}{(\omega^2+\nu_c^2)\omega^2} + \dfrac{\epsilon_o\nu_c\omega_p^2}{(\omega^2+\nu_c^2)} & & 0 \\ & \ddots & \\ 0 & & 0 \end{pmatrix}$$

in the regime $\nu_c/\omega \ll 1$,

$$\underline{\underline{\nu}} = i \begin{pmatrix} \dfrac{\omega_p^2\nu_c\epsilon_o}{\omega^2+\nu_c^2} & & 0 \\ & & \\ 0 & & 0 \end{pmatrix}$$

using above, we can expand the collision coefficient as in (3-21)

$$\gamma(\omega) = (\psi_\alpha, \underline{\underline{\nu}}\,\psi_\alpha) = i \int_o^b \underset{\sim}{E}_\alpha \cdot \underset{\sim}{E}_\alpha^* \frac{\omega_p^2\nu_c\epsilon_o}{\omega^2+\nu_c^2}\, \rho d\rho$$

$$= \frac{i\,\omega_p^2\nu_c}{\omega^2+\nu_c^2} \frac{\kappa_\alpha}{\omega 2\beta} \left\{ \int_o^b \frac{I_1(\kappa_{\perp 1}\rho)}{\kappa_{\perp 1}^2}\, \rho d\rho + \int_o^b \frac{I_o^2(\kappa_{\perp 1}\rho)}{\kappa_\alpha^2}\, \rho d\rho \right\}$$

The integrals in the bracket are evaluated using the formulae in section 6.2. After approximating in $\kappa_{\perp 1}\, b < 1$ region:

$$\gamma(\omega) = \frac{i\omega_p^2\nu_c}{(\omega^2+\nu_c^2)} \frac{\kappa_\alpha}{2\omega\beta} \frac{b^2 I_o^2(\kappa_{\perp 1}\, b)}{\kappa_\alpha^2}$$

using the expression for β from 6.2 and the linear approximation for κ_α i.e. $\kappa_\alpha \sim \omega/v_o$

$$\gamma(\omega) = \frac{i\ \omega^2}{(\omega^2+\nu_c^2)v_o}$$

for $\nu_c/\omega < 1$,

$$\gamma(\omega) \sim \frac{i\,\nu_c}{v_o} \quad \text{independent of frequency.} \qquad (6\text{-}35)$$

for $\rho < b$,

$$E_{a_z} = iA' \frac{J_o(\kappa_{\perp 1} b)}{K_o(\kappa_{\perp 2} b)} K_o(\kappa_{\perp 2}\rho) \tag{6-33a}$$

$$E_{a_\rho} = -A' \frac{J_o(\kappa_{\perp 1} b)}{K_o(\kappa_{\perp 2} b)} \frac{\kappa_a}{\kappa_{\perp 2}} K_1(\kappa_{\perp 2}\rho) \tag{6-33b}$$

$$H_{a_\theta} = -A' \frac{J_o(\kappa_{\perp 1} b)}{K_o(\kappa_{\perp 2} b)} \frac{\omega\epsilon_o}{\kappa_{\perp 2}} K_1(\kappa_{\perp 2}\rho) \tag{6-33c}$$

for $\rho > b$, solution (6-31) holds. The normalization constant A' is obtained via (3-19a) as follows:

$$1 = 2A'^2 \frac{\kappa_a \omega\epsilon_o}{\kappa_{\perp 2}} \left\{ \int_o^b \frac{\kappa_{\perp 1}^2}{\kappa_{\perp 2}} J_1^2(\kappa_{\perp 1}\rho)\rho\, d\rho + \frac{J_o^2(\kappa_{\perp 1} b)}{K_o^2(\kappa_{\perp 2} b)} \int_b^\infty K_1^2(\kappa_{\perp 2}\rho)\rho\, d\rho \right\}$$

evaluating the integral as in (6-24); the approximate value for the normalization constant is:

$$A' = \frac{\kappa_{\perp 2}}{\omega_p b J_o(\kappa_{\perp 1} b)} \sqrt{\frac{\omega}{\kappa_a \epsilon_o}} \tag{6-34}$$

the desired eigenvector is given by (6-31), (6-33) and (6-34).

6.3 Explicit evaluation of nonlinear and collision operators

Using the eigenvectors derived in the previous section and the approximate dispersion relations presented in section 3.2, we can explicitly evaluate the collision and nonlinear operators in equation (3-28).

6.3.1 Zero Magnetic field

When $\underset{\sim}{H}_o = 0$, the operator $\underline{\underline{\nu}}$ in equation (3-21) takes the form:

the above equation is the same equation obtained by Trivelpiece et al[8] since $\frac{\partial \kappa_\alpha}{\partial \omega} \sim v_o$ for $\omega << \omega_p$.

Neglecting the effects of collisions, the nonlinear term in equation (2-21) is expanded as:

$$i\left[\underset{\sim}{E}_\alpha(\omega), N'(\mathcal{A}_\alpha \underset{\sim}{E}_\alpha(\omega))\right]$$

$$= \frac{1}{\omega}\int\{\left(\frac{e\epsilon_o}{m}\frac{\omega_p^2}{\omega_1\omega_2} + \frac{e\epsilon_o}{m}\right)\left[\mathcal{A}_\alpha(z,\omega_1)\mathcal{A}_\alpha(z,\omega_2)\nabla_T\cdot \underset{\sim}{E}_\alpha^{\omega_2}(\underset{\sim}{E}_\alpha^{\omega_1}, \underset{\sim}{E}_\beta^{*\omega}) \right.$$

$$\left. + \mathcal{A}_\alpha(z,\omega_1)\partial_z \mathcal{A}_\alpha(z,\omega_2)\underset{\sim}{E}_\alpha^{\omega_2}(\underset{\sim}{E}_\alpha^{\omega_1}, \underset{\sim}{E}_\beta^{*\omega})\right]$$

$$+ \frac{e\omega_p^2\epsilon_o}{\omega_1\omega_2 m}\mathcal{A}_\alpha(z,\omega_2)\left[\underset{\sim}{E}_\alpha^{\omega_2}\cdot(\underset{\sim}{z}_o\partial_z \mathcal{A}_\alpha(z,\omega_1)\underset{\sim}{E}_\alpha^{\omega_1}) \right.$$

$$\left. + \mathcal{A}_\alpha(z,\omega_1)\underset{\sim}{E}_\alpha^{\omega_2}\cdot\nabla_T\underset{\sim}{E}_\alpha^{\omega_1}\right], \underset{\sim}{E}_\alpha^{*\omega}\}\delta(\omega-\omega_1-\omega_2)d\omega_1 d\omega_2$$

where $\underset{\sim}{E}_\alpha^{\omega_i}$ is the eigenvector associated with the amplitude $\mathcal{A}_\alpha(z,\omega_i)$. In order to simplify the above equation, we expand $\mathcal{A}_\alpha(z,\omega_1)\partial_z \mathcal{A}_\alpha(z,\omega_2)$ up to second order as:

$$\mathcal{A}_\alpha(z,\omega_1)\partial_z \mathcal{A}_\alpha(z,\omega_2) = \mathcal{A}_\alpha(z,\omega_1)\, i\kappa_\alpha(\omega_2)\mathcal{A}_\alpha(z,\omega_2) \qquad (6-36)$$

Using this expansion, the first square bracket term becomes zero while the second is expanded to:

$$= \frac{e\epsilon_o\omega_p^2}{m\omega}\int\frac{\mathcal{A}_\alpha(z,\omega_1)\mathcal{A}_\alpha(z,\omega_2)}{\omega_1\ \omega_2}\cdot\{\int_o^b[E_{\alpha\rho}^{\omega_2}\partial_\rho E_{\alpha\rho}^{\omega_1}E_{\alpha\rho}^{\omega^*} + E_{\alpha\rho}^{\omega_2}\partial_\rho E_{\alpha\rho}^{\omega_1}E_{\alpha z}^{\omega^*}$$

$$+ i\,\kappa_\alpha(\omega_1)E_{\alpha z}^{\omega_2}E_{\alpha\rho}^{\omega_1}E_{\alpha\rho}^{\omega^*} + i\,\kappa_\alpha(\omega_1)E_{\alpha z}^{\omega_2}E_{\alpha z}^{\omega_1}E_{\alpha z}^{\omega^*}]\,\rho\,d\rho\}\delta(\omega-\omega_1-\omega_2)d\omega_1 d\omega_2$$

(6-37)

putting in for the eigenvector components from section 6-2 we obtain

equation (3-29).

Putting in for β from section 6.2 and letting $I_1(\kappa_{\perp 1}\rho) \sim \frac{1}{2}\kappa_{\perp 1}\rho$, $I_1^{(2)'} \sim \kappa_{\perp 1}^{(2)}/2\, I_o(\kappa_{\perp 1}\rho)$ i.e. $\kappa_{\perp 1} b < 1$ regime, the nonlinear term corresponding to P is evaluated as:

$$= \frac{e}{m}\int \frac{\omega_1\omega_2\omega\, b^4}{2^6(\omega_p^2 v_d v_o^3 b^6 \epsilon_o)^{\frac{1}{2}}}\, \mathcal{A}_\alpha(z,\omega_1)\, \mathcal{A}_\alpha(z,\omega_2)\,\delta(\omega-\omega_1-\omega_2)\,d\omega_1 d\omega_2 \qquad (6-38)$$

where

$$v_d^2 = \frac{v_o^2}{(1-v_o^2/c^2)}$$

and for $\kappa_\alpha(\omega)$ the linear contribution has been used. Similarly the contribution due to ω is evaluated

$$= -\frac{e}{m}\int \Bigg\{ \frac{\omega_1^2\,\omega}{(\epsilon_o b^6 \omega_p^6 v_o v_d^6)^{\frac{1}{2}}}\; \frac{1}{I_o^{(1)} I_o^{(2)} I_o^{(o)}} \int_o^b \frac{I_o^{(2)} I_1^{(o)} I_1^{(1)}}{\kappa_{\perp 1}^{(1)}\,\kappa_{\perp 1}^{(o)}}\,\rho\, d\rho$$

$$- \frac{v_o\omega_2}{(v_o b^6 v_d^6 \epsilon_o)^{\frac{1}{2}}}\; \frac{1}{I_o^{(1)} I_o^{(2)} I_o^{(o)}} \int_o^b \Big[I_o^{(1)} I_o^{(2)} I_o^{(o)} - \kappa_{\perp 1}^{(1)}\, \frac{I_1^{(1)} I_1^{(2)} I_o^{(o)}}{\kappa_{\perp 1}^{(2)}} \Big]\rho\, d\rho \Bigg\}$$

$$\mathcal{A}_\alpha(z,\omega_1)\mathcal{A}_\alpha(z,\omega_2)\,\delta(\omega-\omega_1-\omega_2)\, d\omega_1 d\omega_2 \qquad (6-39)$$

letting $I_1 \sim \frac{\kappa_{\perp 1}}{2} I_o$ and expanding I_o to first order (for $\kappa_{\perp 1} b < 1$), the integrals in (6-39) can be readily evaluated. Combining the result with equation (6-38), we arrive at equation (3-39).

6.3.2 Infinite Magnetic field.

When the magnetic field is large, the nonlinear term in equation (3-21) reduces to:

$$i[N(\mathcal{A}_\alpha \underset{\sim}{E}_\alpha, \underset{\sim}{E}_\alpha)] = \frac{\epsilon_o e}{m\omega} \int \{ (\frac{2\omega_p}{\omega_1\omega_2} + 1) \mathcal{A}_\alpha(z,\omega_2) \partial_z \mathcal{A}_\alpha(z,\omega_1) \int_o^b E_{\alpha_z}^{\omega_2} E_{\alpha_z}^{\omega_1} E_{\alpha_z}^{\omega} \rho \, d\rho$$

$$+ \mathcal{A}_\alpha(z,\omega_1) \mathcal{A}_\alpha(z,\omega_2) \int_o^b E_{\alpha_z}^{\omega_2} \nabla_T \cdot \underset{\sim}{E}_{\alpha_T}^{\omega_1} E_{\alpha_z}^{\omega^*} \rho \, d\rho \} \delta(\omega - \omega_1\omega_2) d\omega_1 d\omega_2 \quad (6-40)$$

from equation (3-13) and (3-10), we have to first order:

$$\nabla_T \cdot \underset{\sim}{E}_{\alpha_T} = -i\kappa_\alpha (1 - \frac{\omega_p^2}{\omega^2}) E_{\alpha_z}$$

Using above equation and the expansion of (6-36) in (6-39), we obtain for nonlinear term:

$$= \frac{\epsilon_o e}{m\omega} \int \{ (\frac{2\omega_p}{\omega_1\omega_2} + \frac{\omega_p^2}{\omega_1^2}) \, i \, \kappa_\alpha(\omega_1) \mathcal{A}_\alpha(z,\omega_1) \mathcal{A}_\alpha(z,\omega_2) \int_o^b E_{\alpha_z}^{\omega_1} E_{\alpha_z}^{\omega_2} E_{\alpha_z}^{\omega^*} \rho \, d\rho \}$$

$$\delta(\omega - \omega_1 - \omega_2) d\omega_1 d\omega_2 \quad .$$

Putting in for E_{α_z} from section 6.2,

$$= -\frac{\epsilon_o e}{m\omega} \int \{ (\frac{2\omega_p}{\omega_1\omega_2} + \frac{\omega_p^2}{\omega_1^2}) \, \kappa_\alpha(\omega_1) \mathcal{A}_\alpha(z,\omega_1) \mathcal{A}_\alpha(z,\omega_2) A'(\omega) A'(\omega_2) A'(\omega_3)$$

$$\int_o^b J_o^3 (\kappa_{\perp 1} \rho) \rho \, d\rho \} \, \delta(\omega - \omega_1 - \omega_2) d\omega_1 d\omega_2 \quad (6-41)$$

the form of (6-41) is the same for both cases: column in free space and column surrounded by perfect conductor. The difference lies in the explicit form the normalization coefficient $A'(\omega)$ takes. When the column is surrounded by a perfect conductor the normalization is (from section 6.2):

$$A'(\omega) = \frac{\kappa_{\perp 1}}{b} \frac{1}{(\omega\kappa_\alpha\epsilon_o)^{\frac{1}{2}} (1 - \frac{\omega_p^2}{\omega^2}) \, b \, J_1(\kappa_{\perp 1} b)} \quad (6-42)$$

where $\kappa_{\perp 1} b = p_n$. p_n is the n^{th} zero of J_o. Assuming that only the

lowest order mode is present (higher order modes are slower and consequently attenuated at a faster rate)[34],

$$\kappa_{\perp 1} b = 2.405$$

and equation (6-41) becomes:

$$= + \frac{e}{m} \int \{ \frac{(2\omega_1 + \omega_2)}{\omega_p^4} \left(\frac{v_\infty}{\epsilon_o} \right)^{\frac{1}{2}} \frac{(2.405)^3}{b^6} \frac{\int_o^b J_o^3(\kappa_{\perp 1} \rho) \rho \, d\rho}{J_1^3(\kappa_{\perp 1} b)} \} \mathcal{A}_\alpha(z, \omega_1)$$

$$\mathcal{A}_\alpha(z, \omega_2) \, \delta(\omega - \omega_1 - \omega_2) d\omega_1 d\omega_2 \qquad (6\text{-}43)$$

In the above derivation, it is assumed that $\omega < \omega_p$, so that the linear portion of the dispersion equation gives the maximum contribution to the nonlinear term. For the column in free space,

$$A'(\omega) = \frac{\kappa_{\perp 2}}{\omega_p b J_o(\kappa_{\perp 1} b)} \sqrt{\frac{\omega}{\kappa_\alpha \epsilon_o}} \qquad (6\text{-}44)$$

and (6-41) becomes

$$= \frac{e}{m} \int \{ \frac{(2\omega_1 + \omega_2)}{\omega_p v_\infty^3 b^3} \sqrt{\frac{v_\infty}{\epsilon_o}} \frac{\int_o^b J_o^3(\kappa_{\perp 1} \rho) \rho \, d\rho}{J_o^3(\kappa_{\perp 1} b)} \} \mathcal{A}_\alpha(z, \omega_1) \mathcal{A}_\alpha(z, \omega_2) \delta(\omega - \omega_1 - \omega_2) d\omega_1 d\omega_2 \qquad (6\text{-}45)$$

where the same assumptions leading to (6-43) have been used. (6-43) and (6-45) lead to (3-42).

The collision operator for large magnetic fields is given by:

$$\underline{\underline{\nu}} = L - L_o = i \begin{pmatrix} -i\omega\epsilon_o \underline{\underline{\epsilon}}' & 0 \\ 0 & 0 \end{pmatrix}$$

where

$$\epsilon' = \begin{pmatrix} 0 & 0 & 0 \\ 0 & 0 & 0 \\ 0 & 0 & \frac{\nu_c^2 \omega_p^2}{\omega^3(\omega^2 + \nu_c^2)} + i \frac{\nu_c \omega_p^2}{\omega^2(\omega^2 + \nu_c^2)} \end{pmatrix}$$

The collision term takes the form (for $\nu/\omega < 1$),

$$(\psi_\alpha, \overset{\nu}{=} \psi_\alpha) = i \int_o^b E_{\alpha_z} E^*_{\alpha_z} \left(\frac{\omega_p^2 \nu_c \epsilon_o}{\omega^2+\nu_c^2}\right) \rho \, d\rho$$

putting in for the longitudinal component of the eigenvector,

$$= i \left[\int_o^b A'^2(\omega) \, J_o^2(\kappa_{\perp_1} \rho) \rho \, d\rho \right] \frac{\omega_p^2 \nu_c \epsilon_o}{\omega^2 + \nu_c^2} \qquad (6\text{-}46)$$

Again, the above form applies for both column in free space and column surrounded by conductor. Using (6-42), the collision coefficient when the column is surrounded by a perfect conductor is,

$$\gamma(\omega) = \frac{\kappa_{\perp_1}^2 \infty}{\omega_p^2 b^2} \qquad \frac{\int_o^b J_o^2(\kappa_{\perp_1} \rho) \rho \, d\rho}{J_1^2(\kappa_{\perp_1} b)} \qquad \text{for } \nu_c/\omega < 1$$

and again we have assumed that $\omega < \omega_p$, so that the major contribution to κ_α arises from the linear term.

Similarly, for the column in free space:

$$\gamma(\omega) = \frac{\nu_c}{\nu_\infty b^2 J_o^2(\kappa_{\perp_1} b)} \int_o^b J_o^2(\kappa_{\perp_1} \rho) \rho \, d\rho$$

6.3.3 Weak Magnetic field.

To obtain the Kernel given in (3-30); the nonlinear term in equation (2-21) is expanded in component form, and consistent with the slow mode assumption, we only retain the term arising from the coupling of the longitudinal electric field. For $\omega < \omega_c < \omega_p$, this term is given by:

$$= i \int \left[\frac{n_o e^3}{m^2} \left(2 - \frac{\omega_p^2}{\omega_p^2 + \omega_c^2}\right) \frac{1}{\omega_1 \omega_2 \omega} + \frac{\epsilon_o e}{m} \frac{1}{\omega} \frac{\omega_p^2 \omega_c^2}{\omega_1^2 (\omega_p^2 + \omega_c^2)} \right] \kappa_\alpha(\omega_1) Q_\alpha(z, \omega_1) Q_\alpha(z, \omega_2)$$

$$(E_z^{(1)} E_z^{(2)}, E_z^*) \, \delta(\omega - \omega_1 - \omega_2) \, d\omega_1 d\omega_2$$

Using the expression for the z component of the eigenvector (from 6. 2. 3) to explicitly write the inner product:

$$= \frac{-e\epsilon_o}{m} \int [(2 - \frac{\omega_p^2}{\omega_p^2+\omega_c^2}) \frac{\omega_p^2}{\omega_1\omega_2\omega} + \frac{\omega_p^2\omega_c^2}{\omega\omega_1^2(\omega_p^2+\omega_c^2)}] \kappa_\alpha(\omega_1) \mathcal{J}_\alpha(z,\omega_1) \mathcal{J}_\alpha(z,\omega_2)$$

$$A(\omega_1) A(\omega_2) A(\omega) \int_o^b J_o^3 (\kappa_{\perp 1} \rho) \rho d\rho \quad \delta(\omega-\omega_1-\omega_2) d\omega_1 d\omega_2$$

Putting in for the normalization coefficient $A(\omega)$ and proceeding as in 6. 3. 2 , we arrive at the final form (3-44).

REFERENCES

1. W. B. Kunkel, "Plasma Physics in Theory and Applications," McGraw Hill (1966).

2. V. L. Ginzburg, "Propagation of Electromagnetic Waves in Plasma" Gordon and Breach (1960).

3. T. H. Stix, "The Theory of Plasma Waves," McGraw - Hill (1962).

4. V. N. Tsytovich, "Nonlinear Effects in Plasma," Plenum Press (1970).

5. R. C. Davidson "Methods in Nonlinear Plasma Theory," Academic (1972).

6. F. Einaudi, R. N. Sudan, "A Review of the Nonlinear Theory of Plasma Oscillations," Plasma Phys. 11, pp. 359- 389 (1969).

7. Y. Akao and Y. Ida, "Electron Density Measurements of a Plasma Column by Surface Wave Resonances" J. Applied Physics, Vol. 35 pp. 2565-2570, (1964).

8. A. Trivelpiece and R. W. Gould, "Space Charge Waves in Cylindrical Plasma Columns," J. Applied Phys, Vol 30 pp. 1784-1793, (1959).

9. M. A. Heald and C. B. Wharton, "Plasma Diagnostics with Micro-Waves," John Wiley & Sons (1965).

10. V. M. Ristic, S. A. Self and F. W. Crawford
J. Applied Phys. 40 pp. 52-44, (1969).

11. R. J. Briggs, "Electron-Stream Interaction with Plasmas," MIT Press (1964).

12. A. V. Longinov, "Excitation of Electromagnetic Waves in a Plasma by Longitudinal Electric Fields" Soviet Physics - Technical Physics Vol. 17, pp. 1273-1282, (1973).

13. P. J. Barrett, H. G. Jones and R. N. Franklin, "Dispersion of Electron Plasma Waves" Plasma Physics Vol. 10, pp. 911-918, (1968).

14. B. B. O'Brien Jr., "Slow Wave: Transmission Modes of an Isotropic Inhomogeneous Cylindrical Hot Plasma." Plasma Physics Vol. 9, pp. 369-400, (1967).

15. C. N. Lashmore - Davies, "Theory of High Frequency Electrostatic Waves in a Non-Uniform Plasma in the presence of Magnetic Field," Plasma Physics, Vol. 11 pp. 271-284, (1969).

16. W. P. Allis, S. J. Buchsbaum and A. Berss "Waves in Anisotropic Plasma" MIT Press., (1963).

17. P. A. Sturrock, "Nonlinear Effects in Electron Plasma." Proc. Roy. Soc., A242:277 (1957).

18. L. A. Turlock, C. R. James, "Nonlinear Interation of Electromagnetic Waves in Bounded Plasma," IEEE Trans. AP-16:737 (1968).

19. A. N. Kondratenko, V. I. Liolunovich and P. N. Rybin, "Nonlinear Theory of Electromagnetic Waves in a Bounded Plasma," Izvestiya Vuz. Radiofizika p. 176 April (1966).

20. R. F. Whitmer, E. B. Barrett, "Nonlinear Interaction of an Electromagnetic Wave with a Plasma Layer in the Presence of a Static Magnetic Field, I. Theory of Harmonic Generation," Phys. Rev. 121: 661 (1961).

R. F. Whitmer, E. B. Barrett, "II. Higher Harmonics and a Nonlinear Propagation Theory," Phys. Rev. 125, 1478 (1962).

E. B. Barrett, R. F. Whitmer and S. J. Tetenbaum, "III. Theory of Mixing," Phys. Rev. 135A:369 (1964).

S. J. Tetenbaum, R. F. Whitmer and E. B. Barrett, "IV Experimental Results," Phys. Rev. 135A:374 (1964).

21. C. N. Lashmore - Davis "The Coupled Mode Approach to Nonlinear Wave Interactions and Parametric Instabilities," Plasma Phys. Vol. 17, pp. 281-303, (1975).

22. G. Laval, R. Pellat and M. Perulli, Plasma Phys. 11, 579 (1969).

23. J. Larsen "Nonlinear Wave Interaction in a Plasma Column" Stanford University. Institute for Plasma Research SU-IPR-R-493, Oct. 1972.

24. L. Kunh "An Experimental and Theoretical Study of Wave Mixing in a Bounded Magnetoplasmas" Columbia University Sci., Report #6 August, 1968.

25. P. Heymann and K. Saver "Surface Wave Echo on a Plasma Column" Physics Letters. Volume 35A., p. 51, (1971).

26. Ajmera, R. and K. Lonngren, "Nonlinear Excitation of Propagating Surface Waves on a Plasma Column," Journal of Applied Physics Vol. 19 #5, pp. 2265-2268, April 1968.

27. H. J. Schmith, "Plasma Diagnostics with short Electromagnetic Pulses." IEEE Transactions on Nuclear Science. pp. 125-136, (1964).

28. J. R. Proni Jr., W. O. Doggett and W. H. Bennett "Signal Propagation Studies in a Low Density Plasma." Plasma Physics Vol. 13, pp. 191-198, (1971).

29. J. P. Treguier and D. Henry - "Propagation D'une Impulsion Hyperfrequence Sur le Mode Electrostatigue Longitudinal Dans un Plasma de Laboratorie. Plasma Physics, Vol. 14, pp. 667-675, (1972).

30. B. Anicin, and V. Babovic, "Excitation of Nanosecond Waves on Positive Columns," Journal Plasma Physics, Vol. 7, pp. 403-416, (1972).

31. O. Demokan, H. C. Hsuan, K. Lonngren and B. Anicin, "A Time of Flight Study of Waves Guided By a Plasma Column," Plasma Phys., Vol. 13, pp. 29-52, (1971).

32. D. L. Landt, H. C. S. Hsuan and K. E. Lonngren "Properties of Waves Guided by a Plasma Column as determined by Time-Of-Flight Measurements" Plasma Physics Vol. 16., pp. 407-412, (1974).

33. A. Sindoris, "Linear & Nonlinear Impulse Stimulated Emission from a Plasma Column," Ph. D. Thesis, NYN School of Eng. & Sci., October 1971.

34. H. Ikezi, P. J. Barrett, R. B. White and A. Y. Wong, "Electron Plasma Waves and Free Streeming Electron Bursts" Phys. Fluids Vol. 14, pp. 1997-2005 (1971).

35. Huddlestone and Leonard "Plasma Diagnostic Technique."

36. S. Sen, and S. Mukhopadhyays, "Microwave Measurement of Electron Collision Frequency in Mercury Vapor D. C. Glow Discharge Plasma Column," Institute of Radio Physics & Electronics, Calcutta University.

37. N. Marcuvitz, Lecture Notes on Plasma Dynamics, NYU School of Eng. & Sci.

38. P. C. Clemmow, J. P. Dougherty, "Electrodynamics of Plasmas," Addison-Wesley (1969).

39. G. Georges, Nonlinearities in Plasmas & Theoretical Investigation of Harmonic Generation in Stratified Geometry, Ph. D. Thesis, NYU, May 1971.

40. L. B. Felsen, and N. Marcuvitz, "Radiation and Scattering of Waves," Prentic Hall, (1973).

41. H. Washimi and T. Tanuiti, "Propagation of Ion-Acoustic Solitary Waves of Small Amplitude" Phys. Rev. Lett. 17, pp. 996-998, (1966).

42. Y. A. Berezin and V. I. Karpman, "Theory of Nonstationary Finite-Amplitude Waves in a Low-Density Plasma," JETP 19, pp. 1265-1271 (1964). "Nonlinear Evolution of Disturbances in Plasmas and Other Dispersive Media," JETP 24, pp. 1049-1056 (1967).

43. B. Kadomtsev and V. Karpman, "Nonlinear Waves," Soviet Physics Uspekhi, Vol. 14, #1, p. 40, (1971).

44. A. Scott, F. Chu and D. McLaughlin, "The Solition: A New Concept in Science," Proc. IEEE, Vol. 61 #10, p. 1443, (1973).

45. G. B. Whitham "Linear and Nonlinear Waves" John Wiley & Sons, (1974).

46. R. E. Collin "Field Theory of Guided Waves" McGraw-Hill, NY, (1960).

47. G. N. Watson "Theory of Bessel Functions."

48. K. Saeki and H. Ikezi "Electron Plasma Wave Shocks in a Bounded Plasma" Physical Review Letters 29, pp. 253-255, (1972).

49. W. M. Manheimer "Nonlinear Development of an Electron Plasma Wave in a Cylindrical Waveguide" The Physics of Fluids 12, pp. 2426-2428, (1969).

IV
Evolution of Parametrically Excited Instabilities in a Magneto Plasma Column

LIST OF ILLUSTRATIONS

Figure		Page
1	Dispersion Diagram for an Unbounded, Isotropic Electron-ion Plasma	130
2	Scattering Diagram of Parametric Decay Instabilities	131
3	Dispersion Diagram for an Unbounded, Magneto Plasma	133
4	Hollow Cathode Discharge Plasma Device	138
5	Microwave System and Experimental Set-up	141
6a	Radial Profile of Density and Electron Temperature in the Plasma Beam	145
6b	Density Variations as a Function of Baffle Current I_B	147
6c	Typical Double Probe Curve for Different Microwave Pump Levels	149
7	Microwave Power Modulation and Growth and Decay of Electrostatic Ion Cyclotron Wave	153
8	Comparison of Frequency Spectrum at 0 Watt and 150 Watt Levels, with or without High-pass Filter	158
9	Frequency Spectrum of Electrostatic Ion Cyclotron Wave and its Harmonics	160
10	Electrostatic Ion Cyclotron Wave in Time Domain	160
11	Evolution of Electrostatic Ion Cyclotron Wave with Microwave Power Modulation	161
12	Low Frequency Spectrum as a Function of Microwave Pump Power	164
13	Decay of Electrostatic Ion Cyclotron Wave from Steady State Amplitude into Noise	168

Figure		Page
14	Evolution of Electrostatic Ion Cyclotron Wave from One Steady State Amplitude to Another, as both Pump Levels Are Above Threshold	172
15	Amplitude of the Decaying Wave as a Function of Time for Various Power Levels	178
16	Steady State Amplitude Versus Power Difference ($P - P_{TH}$)	181
17	Comparison of Decay Process Predicted by Phenomenological Model and Exponential Decay Process	183
18	Data Fitting for Wave Decay Against Theoretically Calculated Curve from Model	186
19	Decay Rate of Wave into Noise as a Function of Pump Power	187
20	Data Fitting for Wave Growth Against Theoretically Calculated Curve from Model	188
21	Growth Rate of Wave from One Steady State Amplitude to Another as a Function of Pump Power	190
22	Decay and Growth Rate y as a Function of Pump Power	191
23	Configuration of Vectors with Respect to Static Magnetic Field B Oriented Along z	207
24	Dispersion Diagram for Magneto-Plasma from Kinetic Model	217

IV-1. INTRODUCTION

The parametric excitation of instabilities in plasma has been the subject of intensive and extensive studies, both theoretically and experimentally in the past decade. A recent surge in interest has been prompted by the fact that anomolous absorption of microwave power through parametric interaction can be an effective method of heating the plasma.[1-5] A complete survey and review on this subject can be found in a recent work of Porkolab.[6] Essentially we can group the results into unmagnetized and magnetized cases, and a brief summary on its development is given.

In a parametric interaction, a pump wave supplies the energy to the coupled modes to overcome their natural damping mechanisms. These decay instabilities in turn may act as a pump to generate other oscillations. The process can be viewed as the background plasma being modified by the external microwave pump of sufficient power; the threshold level is arrived when the imaginary part of the complex frequency of the wave (assuming a time variation of $\exp(-i\omega t)$) becomes zero. The existence of this threshold level is an important characteristic of the parametric decay phenomenon; any further increase in power above this level drives the excited waves unstable.

There has been numerous work done on this subject.

Nishikawa,[7] using a general coupled mode formulation, obtained the expressions for the growth rate, frequency, and threshold for the onset of the instabilities, when two natural modes of the system are coupled and driven unstable by a third oscillation. Then these results are applied to a fluid model electron-ion plasma, in which a microwave pump drives an electron plasma wave and ion acoustic wave unstable.[8] Dubois and Goldman derived the non-linear susceptabilities using quantum, statistical-mechanics approach,[9] and in a later paper,[10] using the collisionless Boltzmann-Vlasov equation by perturbative method. Instead of the quantum-statistical method used in [9], Lee and Su[11] obtained the same results using the fluid model of an electron-ion plasma. In anisotropic medium, the derivations are much more involved since the model used is the kinetic description. Aliev, et al[12] used the Vlasov equation to obtain the background and perturbed distribution, solving by transfomation into an oscillating frame. The electrostatic approximation is used to obtain the dispersion relation, which is valid for longitudinal modes only. Porkolab[13] analyzed this dispersion relation for different sets of coupled modes. A new theoretical development using the Hamiltonian approach for the parametric mode coupling is performed as a concurrent effort to this project.[14]

The first attempt to parametrically excite the decay

instabilities was performed in 1966;[15] many other experiments have followed ever since. A typical representative sample to illustrate certain key points is given. In a Double Plasma machine without static magnetic field,[16] a RF signal acting as the pump is launched in a parallel grid structure. Both the parametrically excited high and low frequency signals are picked up by probes when the pump field strength exceeded the threshold level. The frequency matching condition of $\omega_o = \omega_1 + \omega_s$ is observed, where ω_o, ω_1 and ω_s are the frequencies of the pump, electron plasma, and ion acoustic waves, respectively. By using two probe correlation measurements, the wave number matching, $\underline{k}_o = \underline{k}_1 + \underline{k}_s$, is also observed. It is therefore apparent that, for the case of isotropic plasma ($B_o = 0$), the modes involved in the interaction, as observed in the parametric experiments,[15-19] are limited to the natural modes of the two component plasma, the two aforementioned waves plus the optic mode. The dispersion relation of these modes, which are found in any plasma text, are represented by each branch of the diagram in fig.1. Two parametric decay interactions are represented in the diagram, depending on the value of $\underline{k}_o$, being zero or finite. With $\underline{k}_o = 0$, the backscattering process is illustrated by the parallelogram, which shows the electromagnetic pump with frequency ω_o', decaying into electron plasma and ion acoustic waves. Not only is the frequency

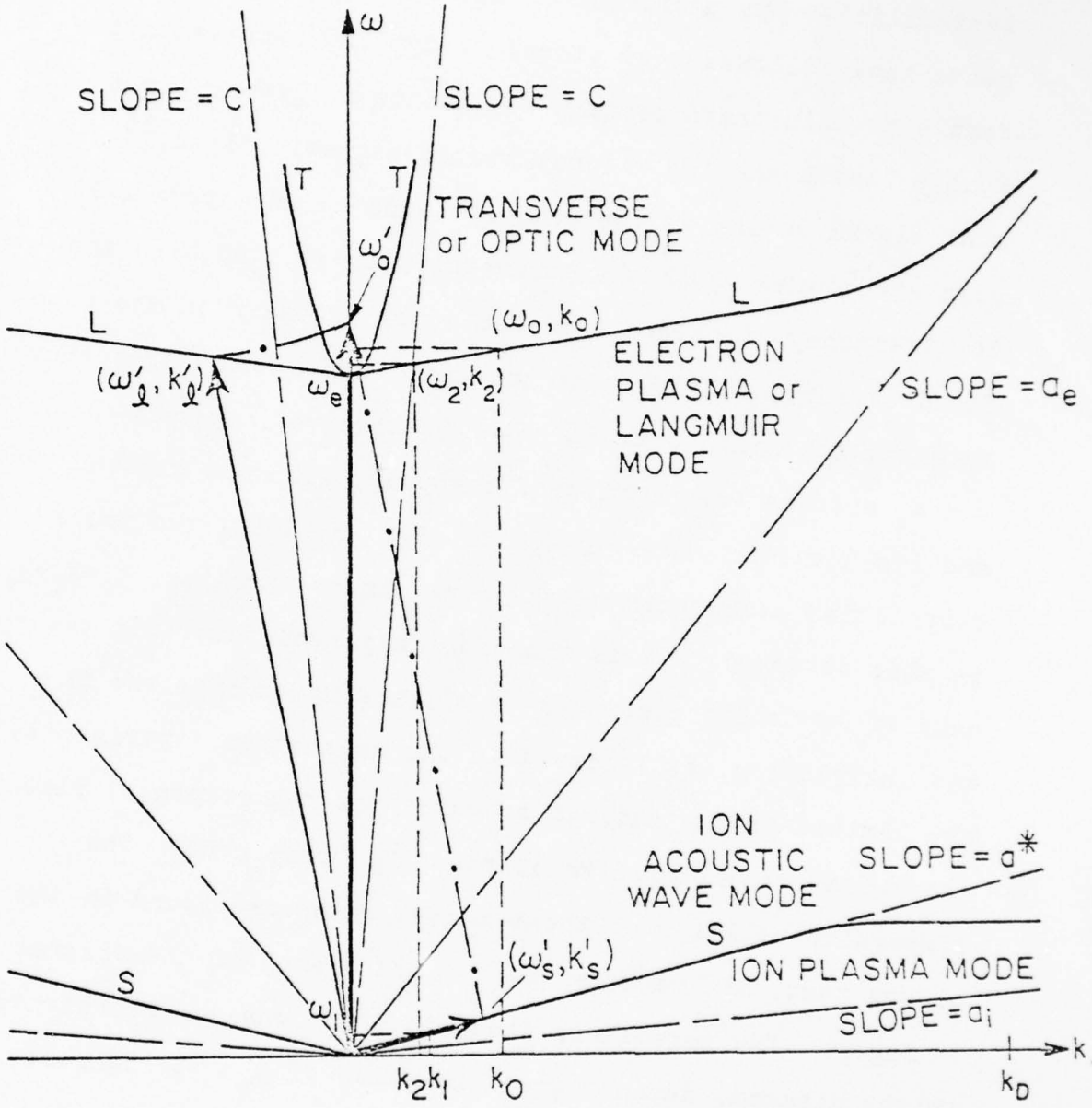

FIG. 1: DISPERSION DIAGRAM FOR AN UNBOUNDED, ISOTROPIC ELECTRON-ION PLASMA

a^* = ion acoustic speed

a_e = electron thermal speed

a_i = ion thermal speed

c = speed of light

(energy) conserved, i.e.

$$\omega_o' \longrightarrow \omega_1' + \omega_s' \tag{1.1}$$

but also is the wave number (momenta):

$$\underline{k}_o' \longrightarrow \underline{k}_1' + \underline{k}_s' \tag{1.2}$$

For $\underline{k}_o = 0$, we have $\underline{k}_1' = -\underline{k}_s'$

For $\underline{k}_o \neq 0$, the conservation equations given above obviously hold, as shown by the dashed lines in the diagram, with the unprimed quantities. The general process of the decay process can also be represented in a scattering diagram, as in fig. 2.

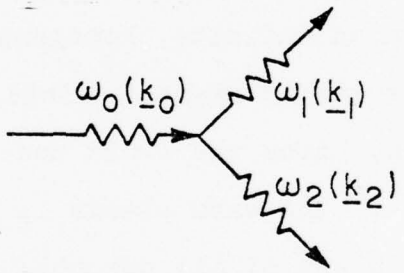

FIG. 2: SCATTERING DIAGRAM OF PARAMETRIC DECAY INSTABILITY

In a four mode interaction, we can describe the phenomenon as a combination of two three-mode processes in a similar fashion. Then the pump at ω_o couples energy into oscillations at ω_s, and $\omega_o \pm \omega_s$, with $\omega_o - \omega_s$ being the Stokes, and $\omega_o + \omega_s$ the anti-Stokes frequencies. From the dispersion diagram, we can see that

the electromagnetic wave can decay into a combination of, either electromagnetic and ion-acoustic waves, or electromagnetic and electron plasma waves. The first process is called Brillouin Scattering, and the latter, Raman Scattering. Also, in an overdense plasma, i.e., pump frequency ω_o is less than the plasma frequency ω_p, a non-oscillatory instability, the Oscillating Two-Stream Instability may be excited.[7, 8, 20]

Turning attention to a magneto-plasma, the number of natural modes which can exist, is much greater; therefore, we expect the possible combinations of modes to be involved in a parametric decay interaction is no longer as limited as before. In an infinite, homogeneous and two-component plasma, with a static magnetic field, B_o oriented along z direction, using the fluid model, the dispersion relation[21-23] of the warm plasma is plotted in fig. 3. A more complete set of all possible modes is obtainable with the kinetic description.[22, 24] Some of these, especially the modes involved in our experiment, are derived and plotted in section 4.4. The values of the ω labeled in the diagram are defined as follows, often simplified with proper approximations:

$$\omega_2 = \frac{\Omega_e}{2} + \left(\frac{\Omega_e^2}{4} + \omega_{pe}^2 \right)^{\frac{1}{2}}$$

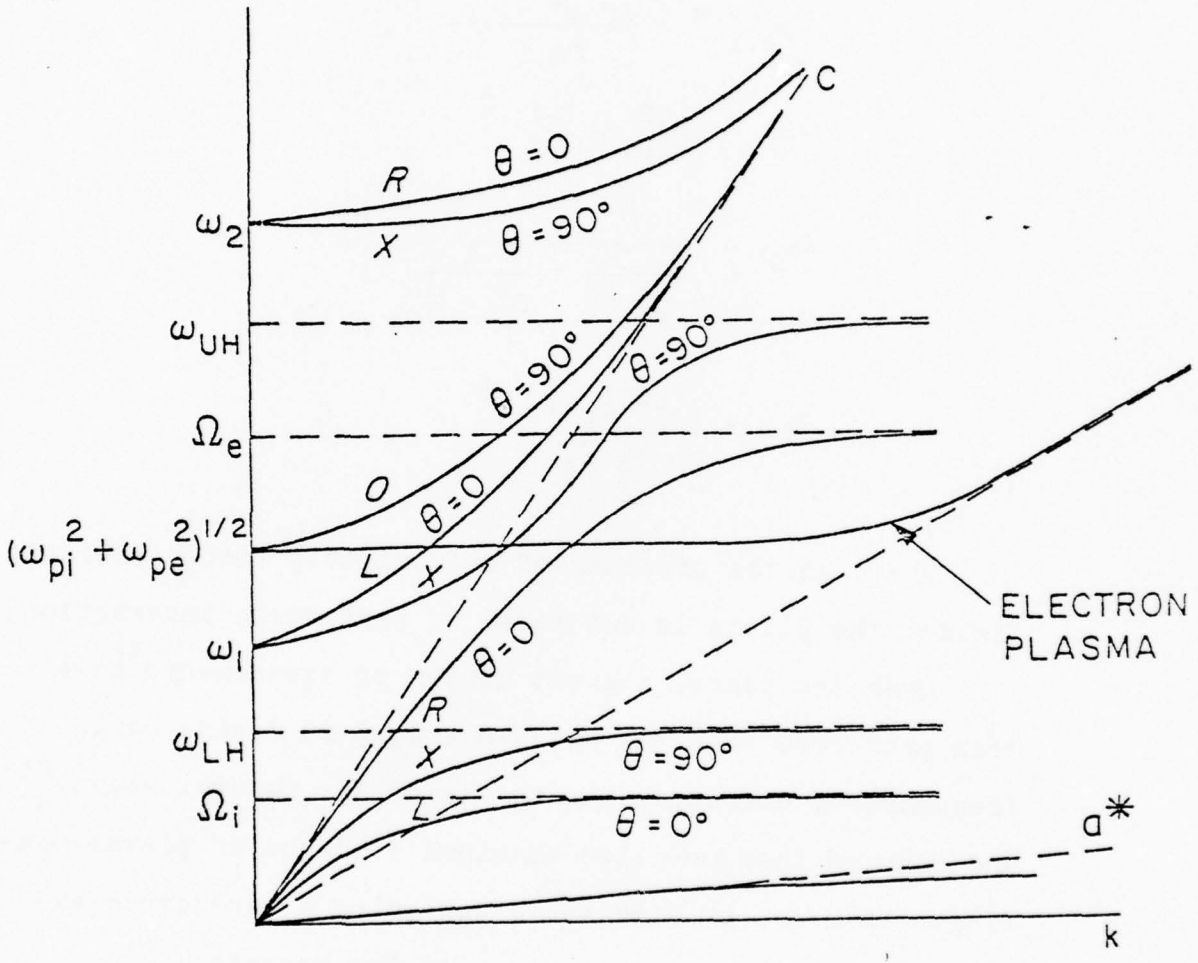

FIG. 3: DISPERSION DIAGRAM FOR AN UNBOUNDED, MAGNETO PLASMA

$$\omega_1 = -\frac{\Omega_e}{2} + \left(\frac{\Omega_e^2}{4} + \omega_{pe}^2 \right)^{\frac{1}{2}}$$

$$\Omega_{e,i} = \frac{q_{e,i} B_o}{c\, m_{e,i}}$$

$$\omega_{p_{e,i}} = \left(\frac{4\pi e^2 n_{e,i}}{m_{e,i}} \right)^{\frac{1}{2}}$$

$$\omega_{UH} = \left(\omega_{pe}^2 + \Omega_e^2 \right)^{\frac{1}{2}}$$

$$\omega_{LH} = \left(\frac{1}{\frac{1}{\Omega_e^2 \Omega_i^2} + \frac{1}{\Omega_i^2 + \omega_{pi}^2}} \right)^{\frac{1}{2}}$$

$$k_{De} = \left(\frac{4\pi n_e e^2}{k_B T_e} \right)^{\frac{1}{2}}$$

Thus, in the presence of sufficiently strong electric fields, the plasma is subjected to parametric interactions.

Over the years, a great number of experiments have been performed with the microwave pump at a wide range of frequencies, corresponding to one of the natural modes,[25-32] and many of them have also obtained evidence of plasma heating. However, to succeed in achieving a parametric excitation experiment, not only must the momenta $\underline{k}$ be matched, often a well defined wave number $\underline{k}$ is in order. Then this would yield decay instabilities with fixed frequencies of highly spiked spectra, rather than a broad range of frequencies being excited.

Hiroe and Ikegami[25] performed their experiment in a mercury plasma discharge tube inserted in a waveguide. The fixed microwave pump frequency is close to the upper hybrid mode, and when the pump power exceeded the threshold power level, sharply spiked spectral components appear, with frequencies corresponding to upper hybrid and lower hybrid modes; these are traveling waves. In experiments performed by Porkolab, et al,[26] and Franklin, et al,[33] the microwave launcher used, like in Stenzel and Wong's,[16] is composed of a parallel grid. A Lisitano coil is also often used to launch a spiraling slow wave as done in [34]. In a well confined magneto plasma of sharp boundaries such as the Polytechnic Hollow Cathode Discharge device, it is possible to excite parametric instabilities with a high power microwave signal. It is with this interest in mind that the present research was started.

The plasma device, which utilizes a small hollow tube as a cathode, produces an argon arc discharge between the negatively biased cathode and the grounded baffle anode. This anode is hollow at the center, thus allowing part of the plasma, which has escaped the magnetic mirror at the source region , to flow into an experimental drift region. By controlling the voltage applied to the cathode, and/or the magnetic field strength, and/or neutral gas flow, we can gradually change the characteristics of the background

plasma such as density from 10^{13} to 10^{11}/c.c. A horn antenna is mounted on the anode end plate such that the cross section of the plasma beam is being shined by the microwave field. The electric field is polarized in a direction perpendicular to the beam and the static magnetic field. With all the background parameters adjusted to ideal conditions for the excitation of the decay instabilities, the microwave pump power with frequency at 9.23 GHz, is increased gradually. When the power exceeded a definite value, excited signals are observed simultaneously at two frequencies, one close to the pump frequency, and the other, at about 260 KHz; the threshold power level is experimentally estimated first, and later confirmed by calculation, to be about 65 watts, which corresponds to an electric field strength of 16 V/cm. The microwave signal is square wave modulated in such a way that for about 90% of the period, the power is fixed at a level above the threshold, and the remaining 10%, the power level is varied gradually over a range of values. As the power is switched to a level below threshold, the amplitude of the electrostatic ion cyclotron wave decays from a saturated level into noise. Decay rates thus obtained enable us to confirm their linear dependence as a function of power; the threshold power and the natural damping rates are also calculated. The growth rate for each power level is also obtained as the power exceeded the thres-

hold; from the saturated amplitude and the phenomenological model, it is found that there are two competing saturation mechanisms, namely the anomolous diffusion or the harmonic generation. The dispersion relation of the modes involved in our parametric interaction are also derived, and it is found in the range of our parameters, these modes are the third harmonic of electron cyclotron and the electrostatic ion cyclotron waves.

In IV-2 , a detailed description of the plasma device and the microwave system is given. The experiment of parametric excitation and typical observations are in IV-3 . IV-4 contains the analysis of the data, the presentation of the phenomenological model which not only describes the growth and decay, but also the saturation of the waves, and the derivation of the dispersion relation for the modes involved. A brief conclusion and possible future research are given in IV-5.

IV-2. PLASMA AND MICROWAVE SYSTEMS

A- Plasma Device

The experiments of the parametric decay instabilities are performed in the Hollow Cathode Discharge (HCD) device built a few years back. It has been used to study the charged particle loss processes,[35, 36] and low frequency instabilities.[37] This linear device, as shown in fig. 4, consists of two regions, a turbulent source region, and a relatively quiescent experimental region immersed in an uniform magnetic field. The plasma is an argon arc discharge between a hollow tantalum cathode and a baffle anode. The neutral gas is fed into the hollow cathode where, through the application of a RF breakdown oscillator and a high negative bias, it breaks down initially. After the plasma is started and becomes self-sustaining by thermionic action at the cathode, the electrons are accelerated towards the baffle anode. Part of the electrons which are not collected, flow through a hole in the baffle anode and enters the experimental drift region. Ions then follow into the region, and the quasi-neutrality condition is achieved. While many features of this HCD are similar to others, it is distinguished from the rest due to its length (a 2 m long vacuum chamber) and due to the capability of maintaining a pressure ratio (10:1) between the 2 regions through the

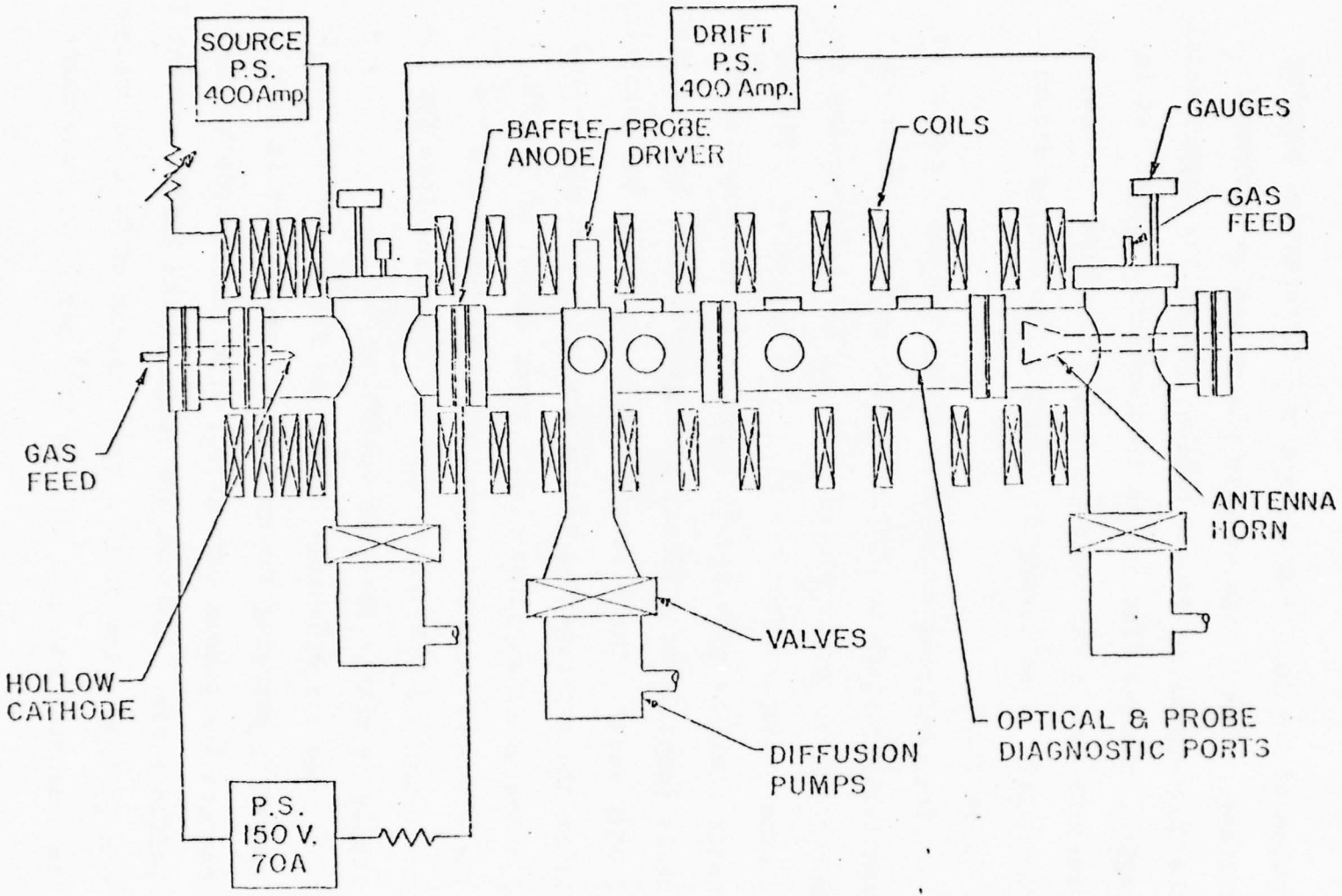

FIG. 4: HOLLOW CATHODE DISCHARGE PLASMA DEVICE

action of the baffle anode and the differential pumping systems. Thus a high density plasma can be generated in the high-pressure source region, yet in the experimental region, the gas flow can be independently controlled in order to obtain various degrees of ionization. It has the capability of achieving an almost fully ionized plasma (90% or more).

The confining magnetic field in the drift region is spatially uniform to within 1% over an axial length of 1 meter. Mirror coils placed over the baffle determine the plasma transport from one region to the other. The magnetic field is provided by a set of 15 water cooled PEM coils (capable of 3 KGauss strength) of very low resistance (.03 Ω each). The 4 source region coils and the remaining 11 in the experimental region are independently powered by 2 HuMac power supplies with a power output of 320 KW. The 4 source coils are connected in series with a low resistance of 0.25 Ω so that the operating load for the supply is within the safe operating region.

Once the discharge is on, the plasma density can be varied by changing the cathode voltage, which in turn changes the plasma current I_B, from the cathode to the baffle anode. Although the range of the baffle current I_B can go from a low of 14 A to a maximum of 40 A (corresponding to a density range of 10^{11} to 10^{13} per c.c.), the magnetic

field in the drift region may have to be readjusted to correspond to the optimum conditions for a stable plasma. The experimental drift region is normally terminated by a movable water cooled anode, which can be grounded or floated; however, in our experiment it is replaced by an insulating plate onto which a microwave antenna horn is mounted. Thus this experimental set-up resembles that of a Q-machine, except the source is of arc origin.

B- The Microwave System and Power Measurement.

The electromagnetic pump required to excite the plasma instabilities is provided by a microwave system as illustrated in fig. 5. The source is an x-band signal generated by an ultra-stable microwave oscillator (LFE, model 814- S), with a power output of 80 mW. This oscillator is a highly stable, wide band source (8.5- 10 GHz), with a klystron oscillator and a stabilizing feedback loop, which consists of a tunable reference cavity and a low noise d-c amplifier. Through the action of the cavity and a differential amplifier, any klystron frequency change is converted into a voltage change, which is in turn applied to the repeller electrode of the klystron. Thus any fluctuation in frequency will be offset by a change in the repeller voltage, and the output can be held very close to the originally set frequency.

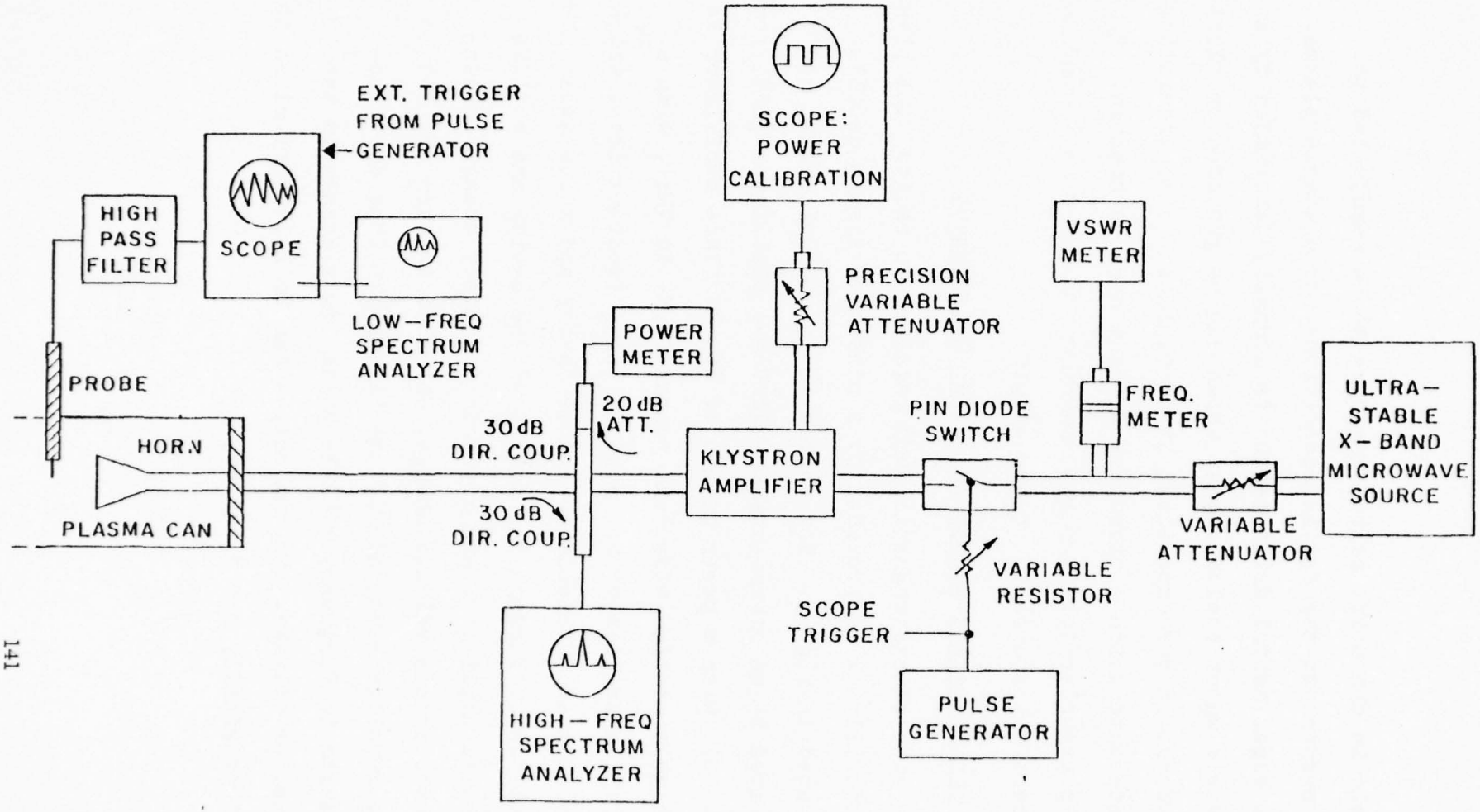

FIG. 5: MICROWAVE SYSTEM AND EXPERIMENTAL SET-UP

Through a series of variable attenuators, this microwave signal is fed into a highly sophisticated, self-contained microwave generator built by G.E. . This unit, which can be operated either as a source generator or a 50 dB amplifier with a maximum power output of 1 KW CW , consists mainly of a Varian klystron tube, VA- 922 series. Each tube is factory tuned to a specified center frequency, and has a 15 MHz bandwidth. It incorporates a series of protective circuitry that automatically shuts off the system if any failures unexpectedly occur. At the input arm, a pin diode switch (HP 8735A series) is employed for the necessary signal modulation. Thus, through the action of this fast microwave switch (rise time of 30 nanoseconds) and the series of microwave attenuators, the power level of the pump signal can be changed accurately from one level to another by simply varying the bias to the pin diode switch. The amplified microwave signal is then fed into a horn antenna (US Army Signal Corps AT- 158/U, 3" W, 2¼" H, and 4 " L), mounted to the anode end of the plasma device. Since the plasma beam ends exactly at the throat of the horn, it must be electrically insulated in order to avoid drawing current, thus changing the characteristics of the plasma system. This is accomplished by connecting a thin teflon sheet between sections of waveguide. A microwave pressure window is also connected for a hermitical seal of the plasma system.

Power level of the pump at CW mode of operation is measured from the output arm of the microwave generator/ amplifier by picking up a fraction of the signal, i.e., through a directional coupler of 30 dB rating and a 20 dB attenuator (exact value only 49.6 db at 9.234 GHz), to a thermoelectric power meter (Microwave Associates, model 454A). However, in our experiment, the power level is first set to a level above the threshold for the onset of the parametric decay instabilities. A power reading is made after optimum operational conditions, which give the sharpest peak in the frequency spectra, are achieved. Then the pump signal is square wave modulated, with 90% of the period at this level, and the remaining 10% at a variable power level. Therefore, the direct power measurement method can no longer be done. This is done, as outlined in fig. 5, by displaying via a diode detector the modulated output, after passing through a fixed 30 dB attenuator, and a precision variable attenuator (HPX- 382A), in a dual trace oscilloscope. With the variable attenuator set at zero, the 2nd trace of the scope used for reference, is made to align with the top level of the square wave, which corresponds to the power level read from the power meter at CW . Then, the variable attenuator is increased until the lower level of the square wave aligns with the reference trace. The value on the variable attenuator

therefore simply corresponds to the number of dB the power level is away from original CW power reading.

Since the variable power level is controlled by the pin diode modulator, which in turn is controlled by the negative bias supplied by a pulse generator (GR model 1340), one can minutely and accurately change this level. A final note on this must be added. Since the original power reading is obtained by assuming a 50 dB attenuation before the power meter to simplify readings (instead of using the actual 49.6 dB at this frequency), and the horn is about 11 ft away from the location where power is read, a correction factor of 1 db (attenuation due to waveguide is 0.06 db/ft[38]) must be subtracted from the meter reading to arrive at the actual power.

C- Basic Plasma Parameters

The HCD device is operated with no major modifications compared to the system previously used, with the exception of the horn antenna replacing the movable anode, and of the low percentage of ionization encountered in our experiment. Therefore, many of the previously obtained plasma parameters or system characteristics are expected to be unchanged, for example, the radial profile of the density and temperature (fig. 6a). It should be noted that, since the microwave pump frequency is factory set (no attempt is made to change

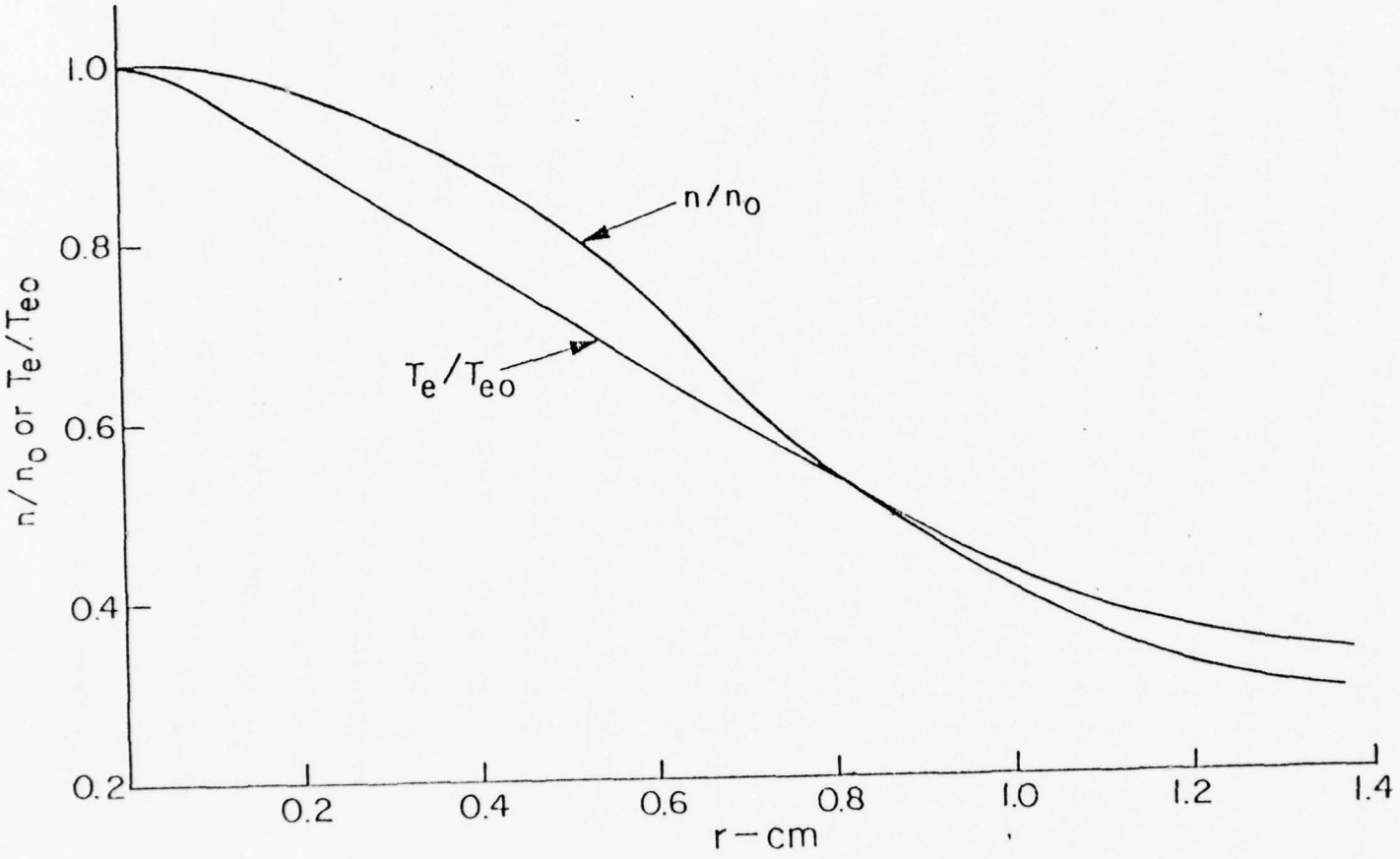

FIG. 6a: RADIAL PROFILE OF DENSITY AND ELECTRON TEMPERATURE IN THE PLASMA BEAM

it even though the klystron tube is tunable $\pm$ 360 MHz around its center frequency), the plasma parameters must be meticulously adjusted until all the conditions are proper for the parametric excitation to take place. It is due to this that the gas flow, magnetic field and baffle current must be properly set to specific values. Therefore, with this in mind, we obtain the variation of density as a function of baffle current I_B.

The electron temperature and density are measured by the single or double probe technique.[39-41] This Langmuir probe method is simple to use. Essentially, a bias voltage is applied between one probe and another reference point, which can be another nearly identical probe (for double probe measurement), or a point in contact with the plasma. As the voltage is changed, the current flowing through the probe also varies, thus giving us a V-I characteristic curve from which the density and temperature is obtained. In a magnetized plasma, however, the electron collection area of the cylindrical probe must be modified to only the rectangular cross section of the probe, and the double probe must be oriented perpendicular to the magnetic field $B_o\underline{z}$, otherwise, a electron retardation can occur if the 2 probes are along z. A typical plot of the density versus baffle current I_B is in fig. 6b. Since the density of approximately 10^{12} particles/cc yield a plasma fre-

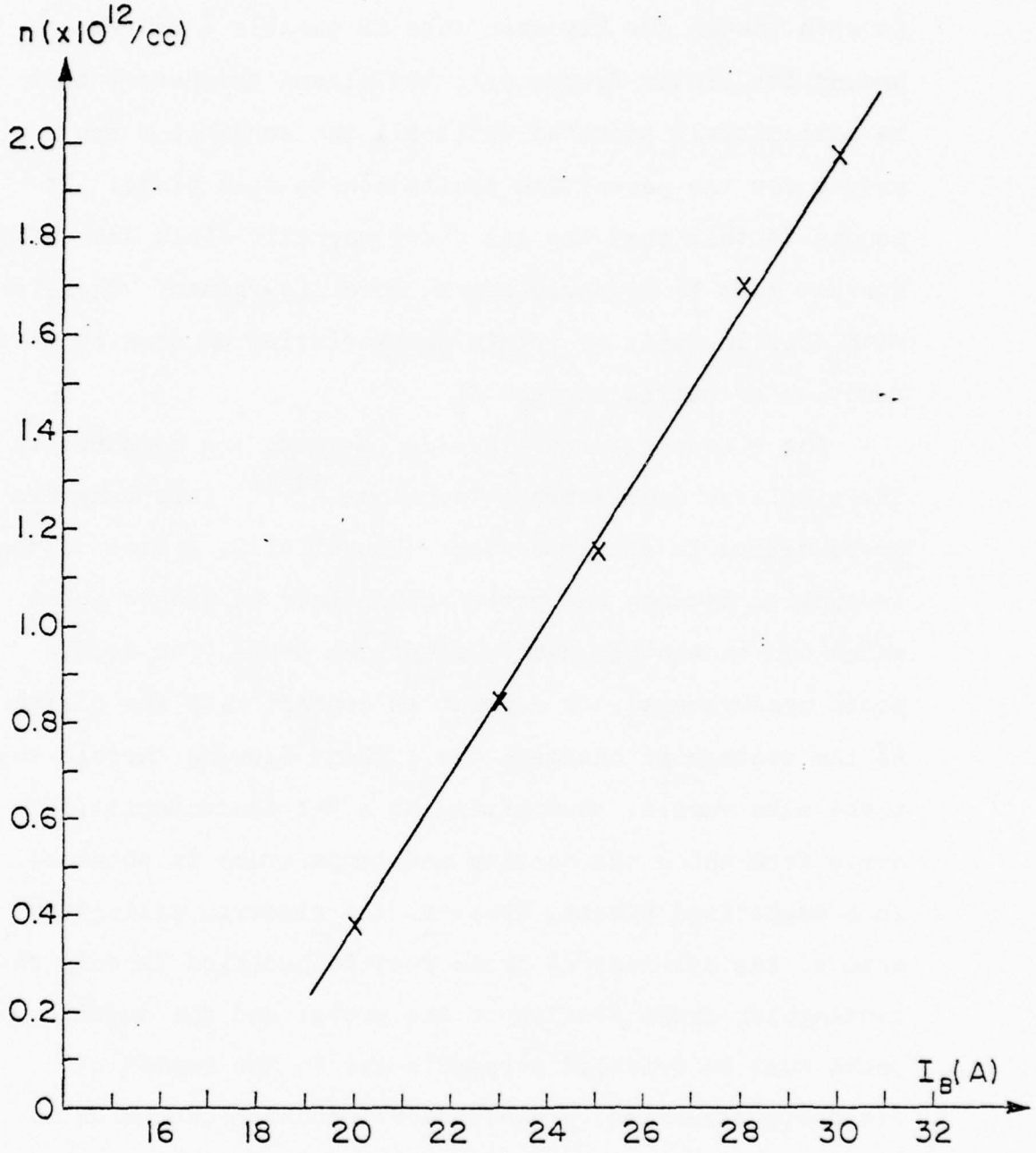

FIG. 6b: DENSITY VARIATION AS A FUNCTION OF BAFFLE CURRENT I_B

quency f_{pe} of 9 GHz, the baffle current I_B below 25A is chosen to be the operating range for the experiment (the microwave pump frequency is fixed at 9.234 GHz).

At the operating condition of I_B = 15A, a static magnetic field of approximately 1 KGauss, and a neutral pressure of 2 micron of Hg, the parametric instabilities are excited when pump power exceeds the threshold level. The electron temperature and density are found to have increased little with the microwave pump on, approximately 20% and 50% respectively. At zero power, electron temperature (density) is only 1.86 ev (5×10^{12}/cc), and at 100 watt, 2.2 ev (8×10^{12}/cc). Further increase in power (up to 350 watt) yields no appreciable change on both parameters as shown in fig. 6c; other basic plasma parameters pertinent to the operating region given above are summarized in Table 1.

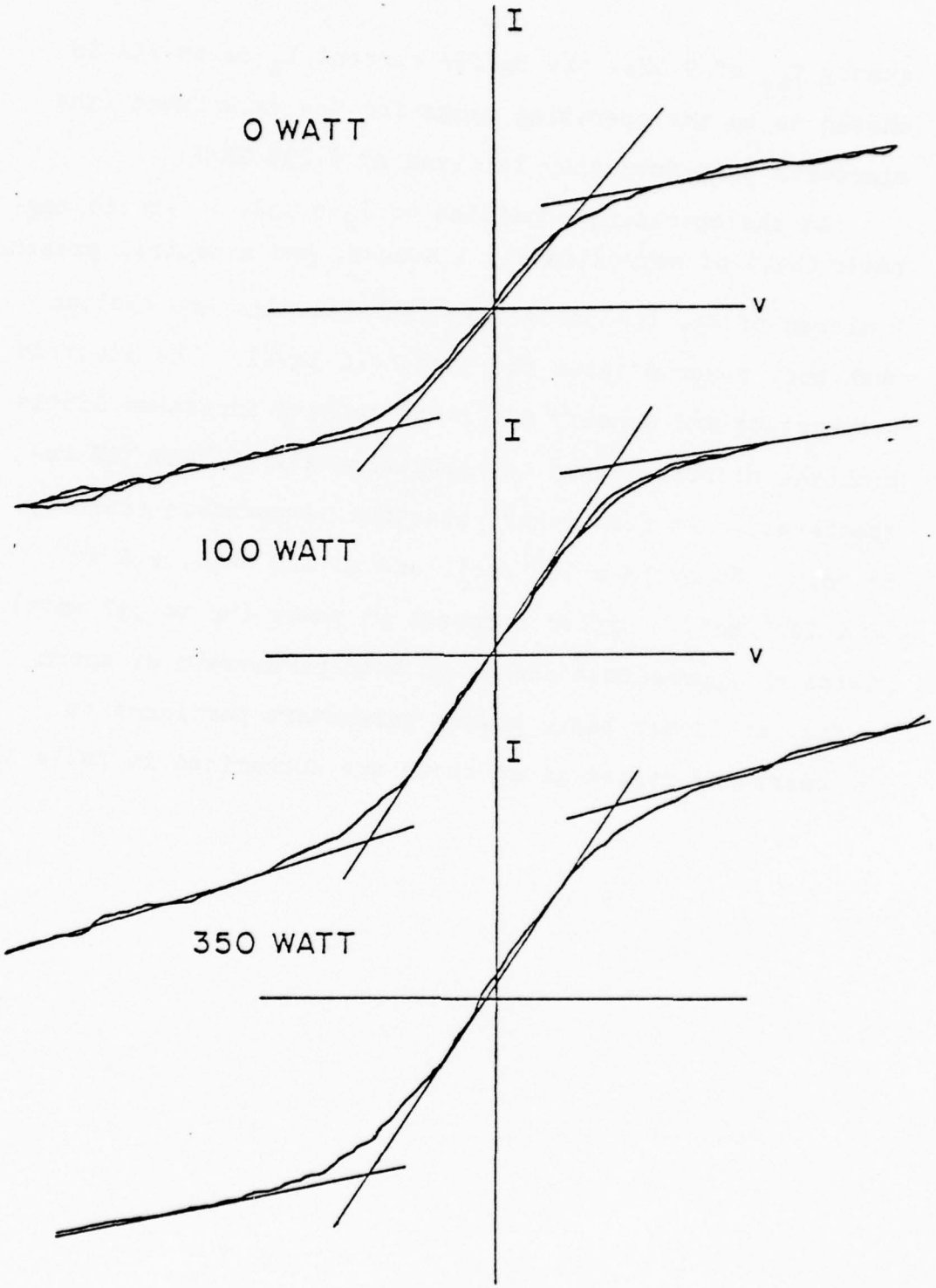

FIG. 6c: TYPICAL DOUBLE PROBE CURVE FOR DIFFERENT MICROWAVE PUMP LEVELS. Top vertical scale half of others.

Table 1

HCD Plasma Parameters

Neutral Density (at 2u)	$6.5 \times 10^{13}/cm^3$
Percent Ionization	12.5%
Magnetic Field B_o (at 160A; 100A = 680 Gauss)	1088 Gauss
Electron Cyclotron Frequency	1.92×10^{10}/sec 3.05×10^{9} Hz
Ion Cyclotron Frequency	2.61×10^{5}/sec 4.15×10^{4} Hz
Electron (Ion) Density	$8 \times 10^{12}/cm^3$
Electron Temperature	2 eV
Ion Temperature	.6 eV
Electron Plasma Frequency	1.6×10^{11}/sec 2.5×10^{10} Hz
Electron Thermal Speed	9.5×10^{7} cm/sec
Ion Thermal Speed	1.9×10^{5} cm/sec
Electron Larmor Radius	5.1×10^{-3} cm
Ion Larmor Radius	.76 cm
Debye Wavelength	3.7×10^{-3} cm
Debye Wavenumber	$1.69 \times 10^{3}/cm$

Table 1 (cont'd)

HCD Plasma Parameters

Microwave Pump Frequency	5.80×10^{10}/sec 9.23×10^{9} Hz
Third Harmonic Electron Cyclotron Frequency	5.76×10^{10}/sec 9.17×10^{9} Hz
Electrostatic Ion Cyclotron Frequency	1.63×10^{6}/sec 2.60×10^{5} Hz
Electron Neutral Collision Frequency	2.59×10^{6}/sec
Ion Neutral Collision Frequency	1.64×10^{5}/sec
Wave Number k_i	7.5/cm

IV-3 EXPERIMENTAL SET-UP AND RESULTS

A- The Experiment

The experimental study of the time-evolution of the parametric instabilities is conducted in the HCD device described in the earlier chapter. Fig. 5 shows the microwave system and the whole experimental set-up. The background conditions are initially adjusted so that the microwave pump can parametrically excite the electrostatic ion cyclotron wave. These parameters are readjusted until the oscillogram of the waves being the most coherent, or equivalently the peak in the frequency spectrum being the sharpest. After these adjustments, the pump signal is modulated as shown in fig. 7, and the instability grows or decays depending on the power level. A typical frequency of the square wave is 1 KHz, with its total period T of 1 msec. divided into an on-off ratio of 9 to 1, i.e., during 90% of the time, the microwave power is at a level above threshold power, P_{TH}, while the remaining 10% of the time, the power level is varied over a range of power levels. This type of modulation is often called unsymmetrical square wave modulation, and the chosen duty cycle assures us of a fairly constant background, and the time period of T_2 long enough for the instability to reach steady state.

Two sets of distinct experiments are performed although both are often conducted together. The first set, to mea-

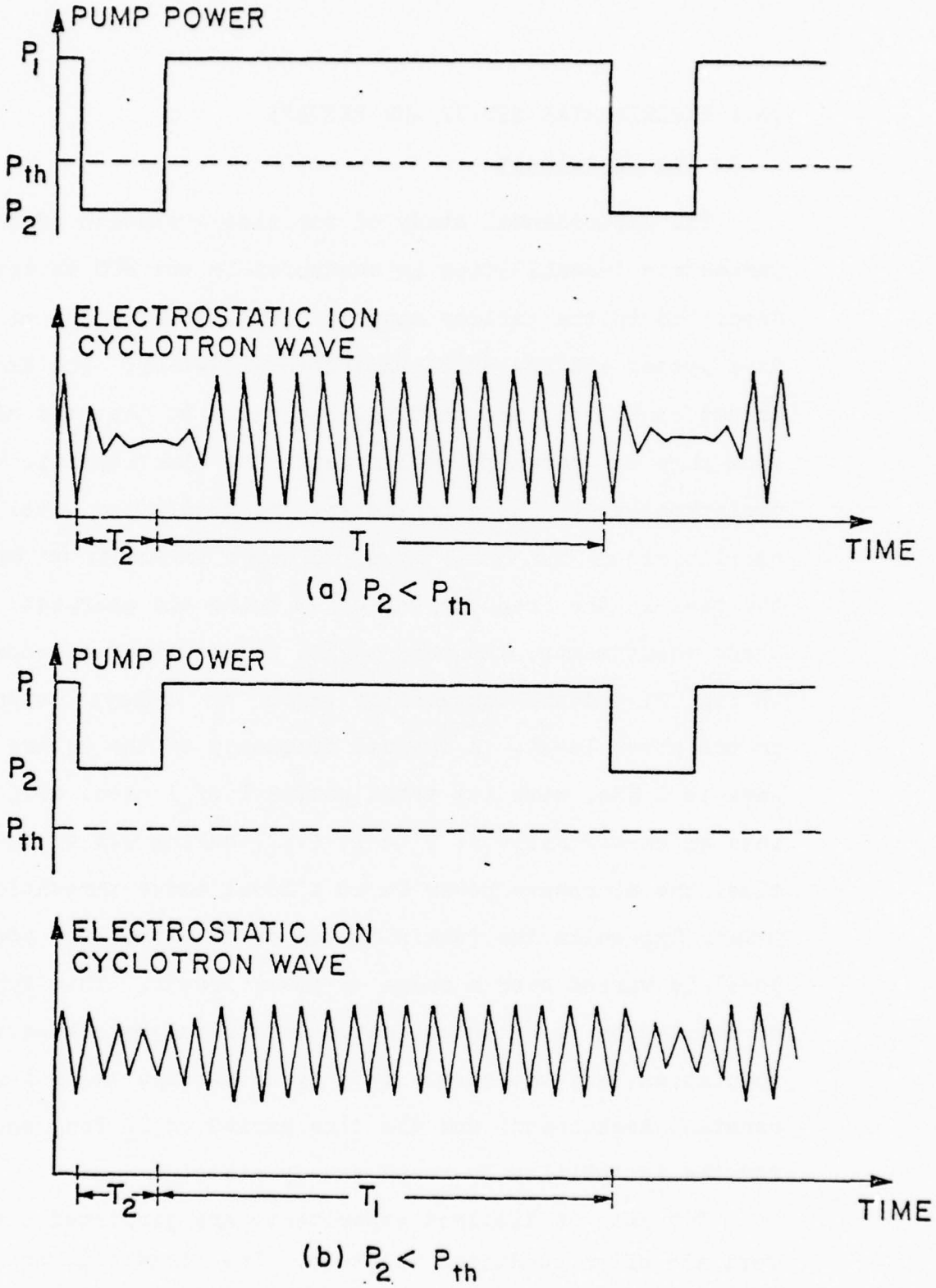

FIG. 7: MICROWAVE POWER MODULATION AND GROWTH AND DECAY OF ELECTROSTATIC ION CYCLOTRON WAVE

sure the decay time of the parametric instability, is done with the power level P_2 varied gradually from 0 watts to about 65 watts, the threshold power level; and to measure the growth time, the power level P_2 increased from P_{TH} to P_1 level. Thus, during the period T_1, the electrostatic ion cyclotron waves reaches a finite steady state. At the end of time T_1, the microwave power is switched to a new level P_2. If P_2 is below P_{TH}, then the amplitude of the wave decays into noise. If P_2 is above P_{TH}, the wave amplitude decays from one steady state level to another non-zero level. An important fact must be considered in order to conduct these experiments for measuring the decay and growth time. As the pump is switched, the rise and fall times of the microwave signal must be smaller than those of the waves. This is assured since the pin diode switch and the square wave generator which drives the modulator have rise and fall times in the nanosecond region (30 ns. and 5 ns., respectively); therefore, the modulated microwave signal has a much smaller value compared to those of the instabilities which are in the microsecond range.

B- Detection of Waves

The detection of the instabilities are done by observations in the time domain through oscilloscope, or in the frequency domain through spectrum analyzers. The parame-

trically excited high frequency signal, the 3rd harmonic of the electron cyclotron wave, is observed through the reflected signal from the waveguide, with its frequency spectrum displayed in a high frequency spectrum analyzer. The high frequency spectrum typically shows a center peak at the pump frequency of 9.234 GHz. When the pump power exceeds the threshold, two sidebands, approximately 250 KHz from the peak, simultaneously appear. These correspond to the Stokes and anti-Stokes frequencies.

The electrostatic ion cyclotron wave is observed through electrostatic or Langmuir probes. These probes are connected to a Tektronix 551 scope, which is equipped with a isolation transformer. Therefore, the probes are floating, and no appreciable current is drawn through them to locally disturb the plasma. One probe is connected to a homemade 50 Ω coaxial tube capable of rotation and movement along the plasma beam. Essentially the probe is made of a fine tungsten wire (10 mil thick) which is electrically insulated with ceramic tubing (Al_2O_3) except at the exposed tip of approximately 60 mil, oriented along the static magnetic field direction z. A second probe is also used; it is inserted through one of the several ports located on top of the device. With its dimension nearly identical to the first one, this is a transverse probe since its orientation is perpendicular to the z-direction. Using these two nearly-

identical probes, it is found that the transverse probe picks up a much larger signal strength of the instability, even though by comparison, the longitudinal probe is more sensitive. Therefore, we conclude that the observed instability is transversely polarized. In a similar experiment but different mode of operation in this device, the same result and conclusion have been obtained.[14]

The low frequency signal can also be observed optically as done by Klein.[19, 42] Using a lens focused to the center of the plasma beam, light intensity change is detected and transmitted by optical fiber bundles to a photomultiplier tube. Thus modulation in light intensity is due to the local variation in density caused by the electrostatic ion cyclotron wave. In instances when the electron density increases, the number of electron-neutral collisions increases, causing the bound electrons of the neutrals to be excited into a higher energy level. When these electrons relax back to the ground state, light is emitted. Therefore, the fluctuation in light intensity observed is equivalent to the oscillation of the wave in question. This method is not used extensively because the signal strength is too weak since the location of the optical fibers are away from the plasma beam, and because of other signals being also picked up. These low frequency instabilities, which often mar the intended observations,

are thought to be inherent of the arc plasma.[43] This method of detection provides an alternative to compliment the observations through electrical probes.

C- Typical Observations

Since there are inherent instabilities, which are originated from the source region and are all under 100 KHz, we must try to filter them out in order to study the electrostatic ion cyclotron wave at about 250 KHz. This is accomplished by using a variable electronic filter set to high pass filter for frequencies greater than 200 KHz. The output is then fed into a high gain differential amplifier (Tektronix plug-in unit 1A7), and into the spectrum analyzer, as sketched in fig. 5. A typical observation of the low frequency spectra is shown in fig. 8, with or without the incorporation of the filter. In picture a, with no microwave pump nor filter, the only coherent signal existing in the plasma is a low frequency oscillation of below 50 KHz. With pump power increased to 150 watts, well above threshold, the parametric interaction takes place as shown by the frequency component of the electrostatic ion cyclotron wave at 260 KHz; the 50 KHz signal has been suppressed but still visible slightly, as in picture b. In the last picture, the activation of the high-pass filter allows us to increase the sensitivity greatly. Note that

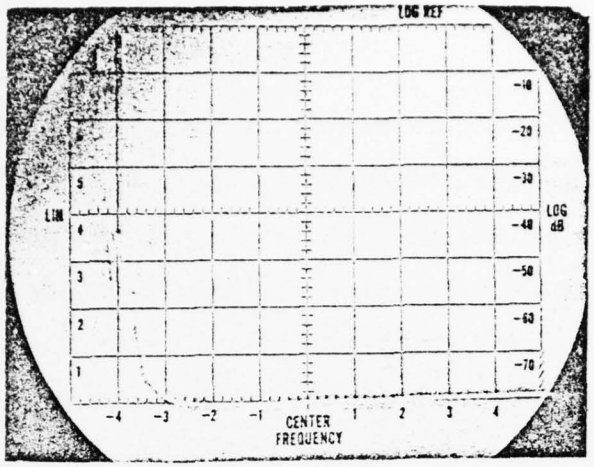

a) Without filter
Signal
Frequency 50 KHz
Power = 0 Watt

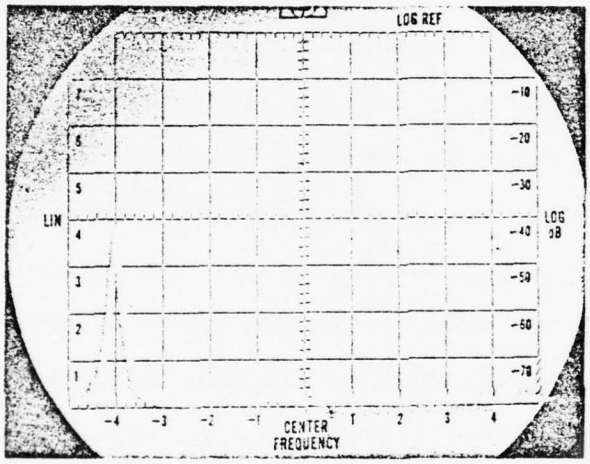

b) Without filter
Signal
Frequency 260 KHz
Power = 150 Watt
1st Peak at
-4 Scale = 0 Hz

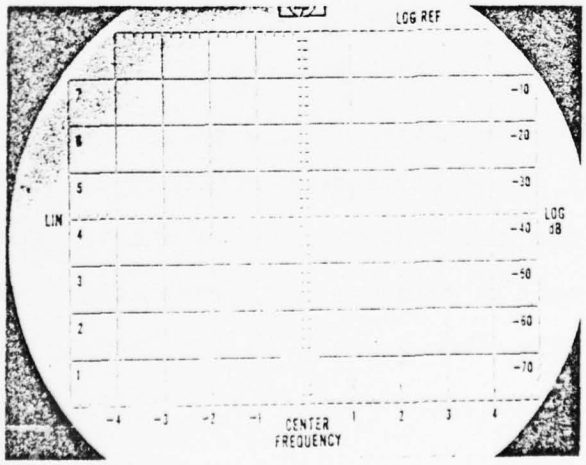

c) With filter
Signal
Frequency 260 KHz
Power = 150 Watt

FIG. 8: COMPARISON OF FREQUENCY SPECTRUM AT 0 WATT AND 150 WATT LEVELS, WITH OR WITHOUT HIGH-PASS FILTER

the 2nd harmonic of the signal is barely visible at approximately 520 KHz. It is beyond doubt that there is indeed a oscillation at 260 KHz, which is excited only when the microwave pump is sufficiently high; the filter merely helps to eliminate other unwanted signals. When the power level is further increased to 200 watts, the higher harmonics begin to appear (fig. 9). In the time domain, the signal is seen as a coherent oscillation with a period of approximately 4 usec. as shown in fig. 10.

The electrostatic ion cyclotron wave is more evident when the pump power is switched from one level above threshold to one below in the fashion described earlier. As predicted by the parametric theory, the parametric decay instabilities can only be excited when the power level is above the threshold; this is illustrated in a series of snapshots of the oscilloscope in fig. 11. As opposed to fig. 10, these are double and single trace photographs. Only a portion of the total period is shown. In a, the lower trace of the square wave corresponds to a power level of 0 watts, and the upper line, a power level of 200 watts; as shown, only noise of random frequency exists during time T_1, and the amplitude of the coherent signal begins to grow and reach a steady state level after power is switched on. The same process is depicted in b, except for a change to greater sensitivity. While two traces

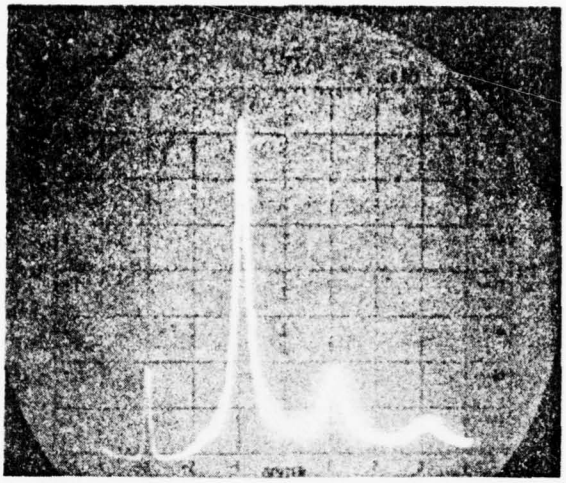

P = 200 Watt Scanwidth = 100 KHz/cm (uncal.)
Bandwidth = 10 KHz/cm

FIG. 9: FREQUENCY SPECTRUM OF ELECTROSTATIC ION CYCLOTRON WAVE AND ITS HARMONICS

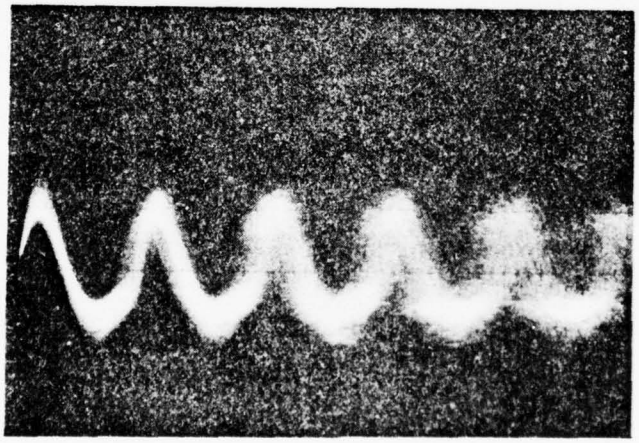

H = 2 usec/cm V = 0.1 V/cm

FIG. 10: ELECTROSTATIC ION CYCLOTRON WAVE IN TIME DOMAIN

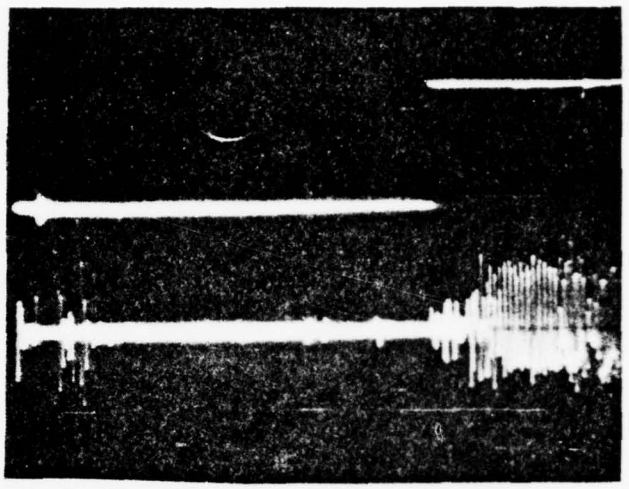

a) Square wave and instability, double trace
H = 20 usec/cm

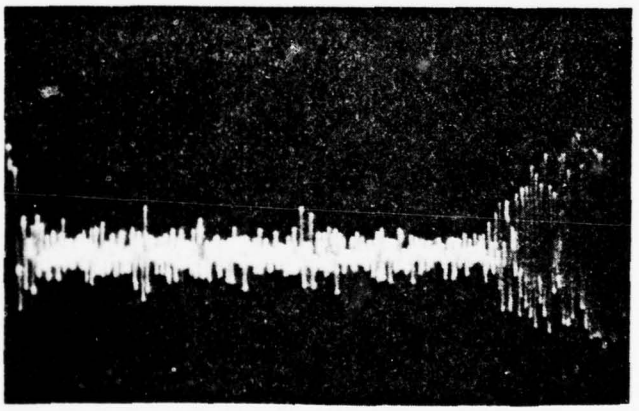

b) Instability growing from noise level to steady state amplitude, double trace
H = 50 usec/cm(uncal.)

FIG. 11: EVOLUTION OF ELECTROSTATIC ION CYCLOTRON WAVE WITH MICROWAVE POWER MODULATION

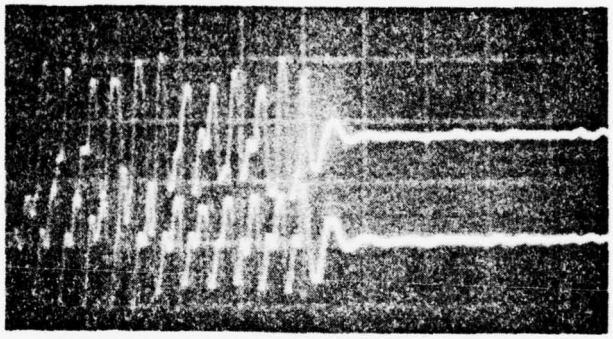

c) Instability decaying into noise level, single trace

FIG. 11: EVOLUTION OF ELECTROSTATIC ION CYCLOTRON WAVE WITH MICROWAVE POWER MODULATION (Cont'd)

are superimposed on the previous two photographs, in c, we have two single trace pictures, with the scope reset to show the on-cycle first. In this last picture, we see the amplitude of signal oscillates 1½ more cycles before decaying to noise level even after the pump has been shut off (set to be exactly at the middle of the screen).

The frequency dependence of the electrostatic ion cyclotron wave on power and on temperature is depicted in the next series of photographs on fig. 12. Although the sequence shows only a variation in power, it has been shown in section 2.3 that we found a temperature rise of 25% as power is increased from 0 to 100 W; therefore, a power variation corresponds also to a temperature change (recall that we found only a initial increase only, no further temperature change as power increased above 100 W). In the first 3 pictures, we must discount the first peak since it is due mainly to the response of the electronic high pass filter set at 200 KHz. As power is increased, the general noise level rises, but the filter cuts off frequencies below the preset frequency, therefore giving a false peak. At power level of 79 W, the 2nd peak corresponding to the excited instability begins to rise out of the noise. This peak becomes clearer in picture c, with power level set at 87 W; also the 2nd harmonic is beginning to show. And in the final two pictures, at power levels of 117 and

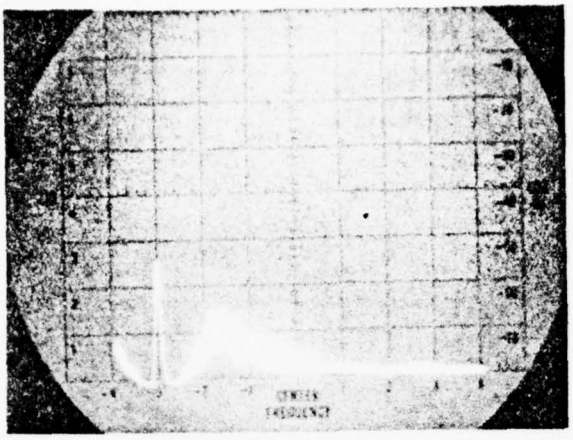

a) Power = 59 Watt

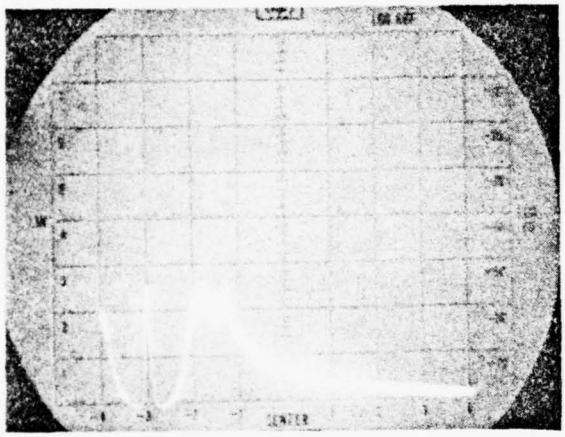

b) Power = 79 Watt

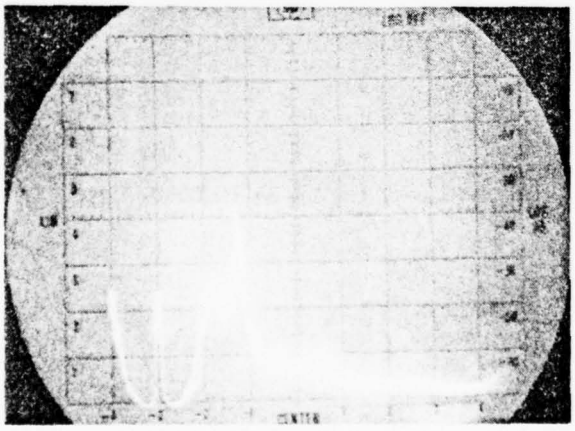

c) Power = 87 Watt

FIG. 12: LOW FREQUENCY SPECTRUM AS A FUNCTION OF MICROWAVE PUMP POWER

Zero Reference Peak set at -3
Signal Frequency = 260 KHz

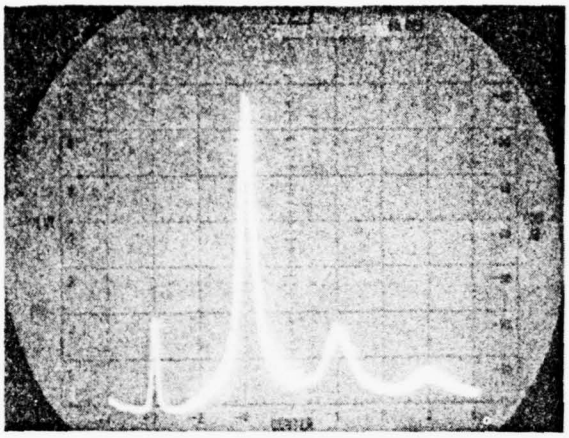

d) Power = 117 Watt

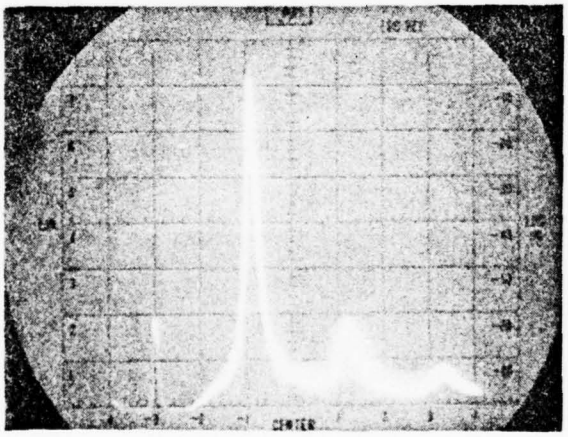

e) Power = 222 Watt

FIG. 12: LOW FREQUENCY SPECTRUM AS A FUNCTION OF MICROWAVE PUMP POWER (Cont'd)

Horizontal Scale = 100 KHz/div. (Uncal.)
Signal Frequency = 260 KHz
2nd Harmonic = 520 KHz
3rd Harmonic = 780 KHz

220 W, the peaks of the fundamental and higher harmonics become clearly defined. It is of interest to point out the slight shift in frequency of the instability. In the first 3 snapshots, we see the peak at 1.8 divisions while it is at 2.0 divisions in the last two; this corresponds to a change from 235 KHz to 260 KHz.

D- Decay and Growth of Electrostatic Ion Cyclotron Wave

A convincing evidence of the parametric excitation is, besides the existence of a definite threshold power level, to be able to show the growth and decay rates of the decay instability are linearly related to the pump power. This is the main subject of this section.

The decay of the electrostatic ion cyclotron wave is studied by switching the microwave pump power from a fixed level above threshold, to various levels below. Although single trace snapshots as in fig. 11 can be used to calculate the decay rate, it is found that the results are too inconsistent due to the instantaneous fluctuations of the background. Multitrace photographs are used to average out this randomness. Thus, with the repetition rate of the square wave at 1000 cycles per second, a camera exposure time of 1/50 sec. gives us 20 traces; and at 2000 cycles per second, it gives us 40 traces. Thus, the data are obtained by using this photograph averaging technique,

which is equivalent to averaging out the results obtained from many single trace pictures.

A typical set of photographs showing the decay of the wave as a function of the pump power is shown in fig. 13. The square wave frequency is set at 500 Hz. At camera exposure of 1/10 sec., we have about 50 traces in each of those photographs. The square wave has an on-off ratio of 9:1. On the photographs, only the time period T_2 is fully shown, i.e., the time during which the power is below threshold. At the end of T_2, which corresponds to 200 usec., power level is switched back to the level above threshold for the next 1.8 msec. (only a portion of which is shown), and the cycle starts.

Although the initial level of power P_1 can also be varied and its effects on the rates studied, it is found that results are dependent only on the difference of 2 power levels; therefore changing P_1 and readjusting P_2 yield the same results. Although decay rate γ is only expressed as a function of power level P_2, dependence on P_1 is implicitly included. One must not increase the level of P_1 to a very high level since this can detune the plasma background, and we are no longer in the optimum operational range. P_1 is normally kept to approximately twice the estimated threshold level of 65 W.

In our set of decay experiments, the decay time of the electrostatic ion cyclotron wave can not be measured

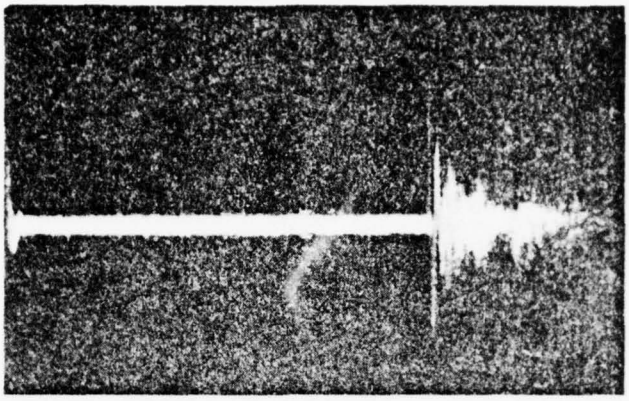

a) Power = 0 Watt

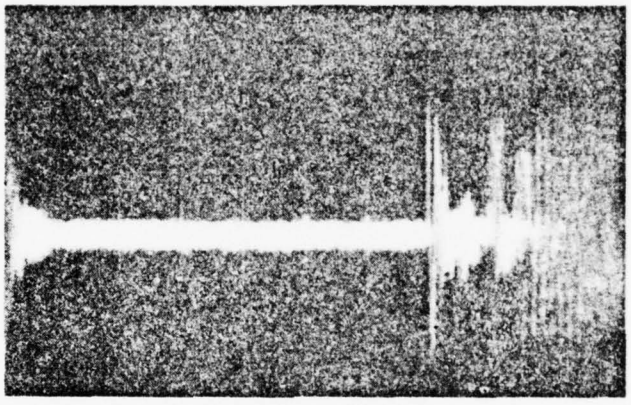

b) Power = 21 Watt

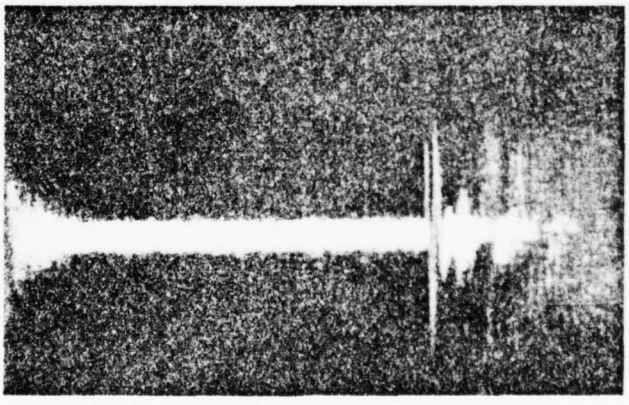

c) Power = 32 Watt

FIG. 13: DECAY OF ELECTROSTATIC ION CYCLOTRON WAVE FROM STEADY STATE AMPLITUDE INTO NOISE

V = Arbitrary H = 32.5 usec/cm
f_2 = 260 KHz Square Wave Frequency = 500 Hz
p^2 = 2u I_B = 15A B_o = 1088 Gauss

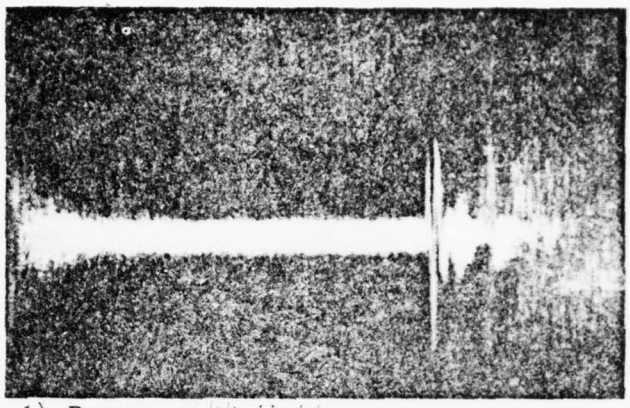

d) Power = 44 Watt

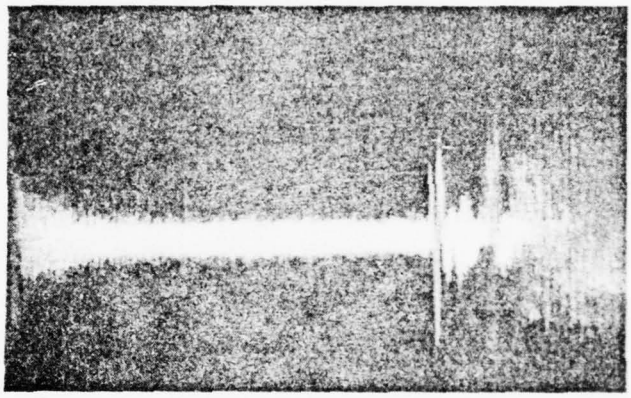

e) Power = 50 Watt

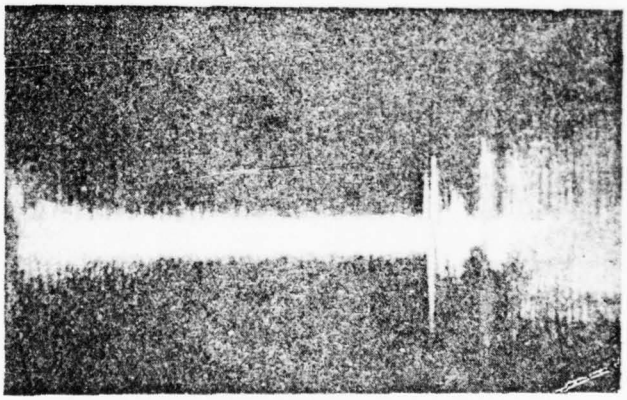

f) Power = 54 Watt

FIG. 13: DECAY OF ELECTROSTATIC ION CYCLOTRON WAVE FROM STEADY STATE AMPLITUDE INTO NOISE (Cont'd)

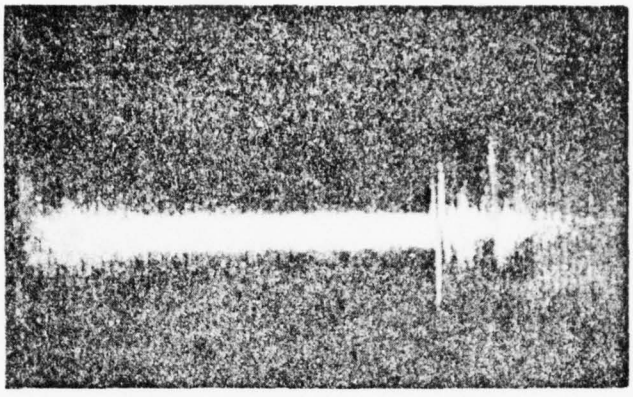

g) Power = 59 Watt

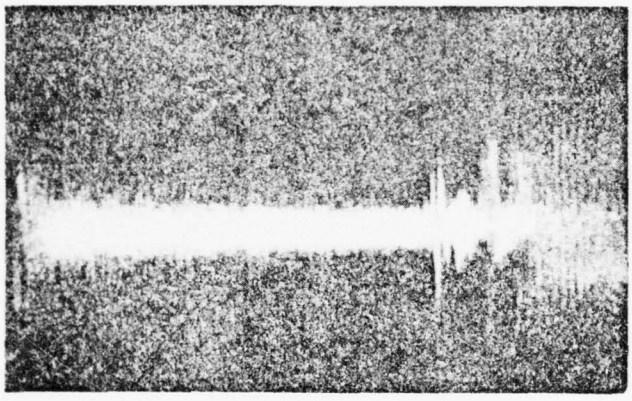

h) Power = 60 Watt

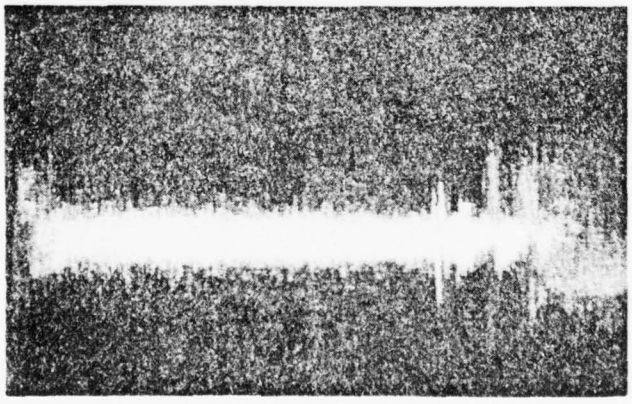

i) Power = 63 Watt

FIG. 13: DECAY OF ELECTROSTATIC ION CYCLOTRON WAVE FROM STEADY STATE AMPLITUDE INTO NOISE (Cont'd)

directly since it is very difficult to discern the exact time it takes to reach the noise level. Fortunately, it is possible to distinguish the general shape of the amplitude decaying, and from this envelope, it is possible to estimate the decay rate, which is done in the next chapter.

The linear growth rate γ of the instability is done in a similar fashion. A set of photographs depicting the wave amplitude evolving from one steady state level to another is shown in fig. 14; it is simply the continuation of the set given earlier except now the power level P_2 is higher than the threshold. At the end of the time period T_2 of 200 usec., the microwave power is switched back to P_1 of 135 W. As the power level P_2 is gradually changed, the wave amplitude no longer decays into noise since it is above threshold, but to a new steady amplitude. This new amplitude level and the time it takes to reach steady state are dependent on the level of power P_2, as clearly shown in fig. 14. Because of the transient signals introduced by the jump in power, the growth rate is measured from the time it takes to decay to a new saturation amplitude. The effects of this transient lessen as the power P_2 approaches the level of P_1. In the last few photographs of the set, we can clearly see not only the decay, but also the growth of the wave amplitude.

Besides this detailed study of the electrostatic ion cyclotron wave as a function of the pump power, the change

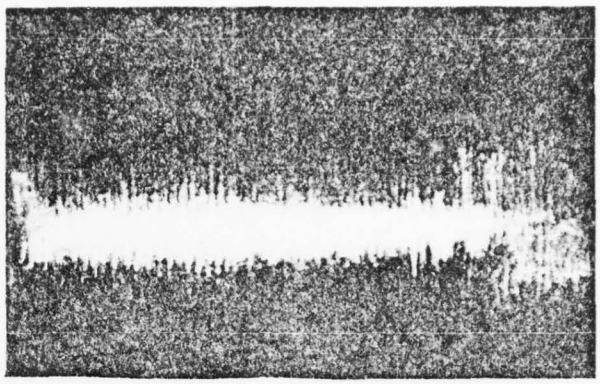

a) Power = 69 Watt

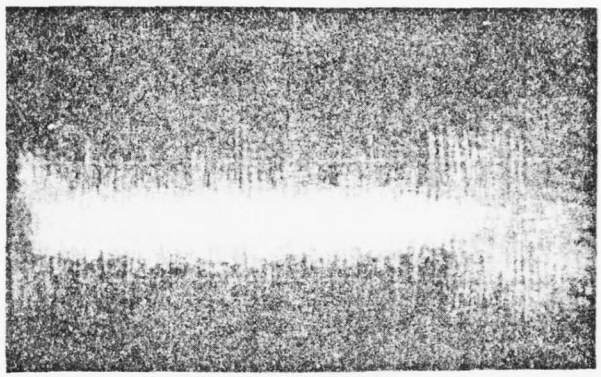

b) Power = 73 Watt

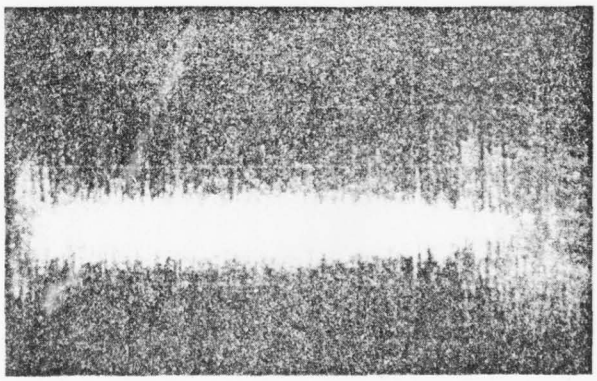

c) Power = 81 Watt

FIG. 14: EVOLUTION OF ELECTROSTATIC ION CYCLOTRON WAVE FROM ONE STEADY STATE AMPLITUDE TO ANOTHER, AS BOTH PUMP LEVELS ARE ABOVE THRESHOLD

(Settings same as in Fig. 13)

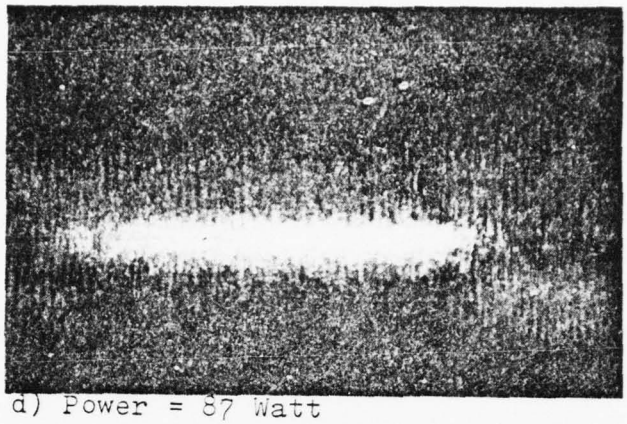

d) Power = 87 Watt

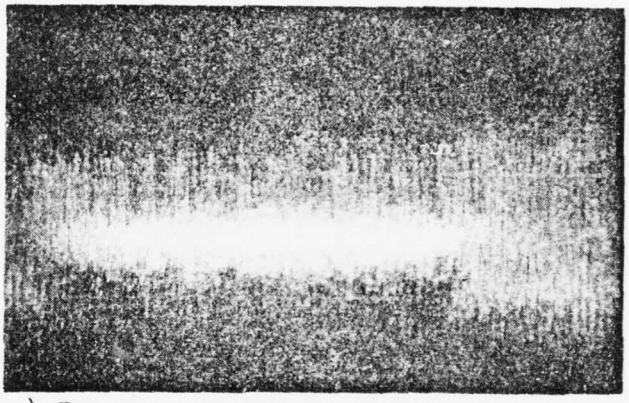

e) Power = 92 Watt

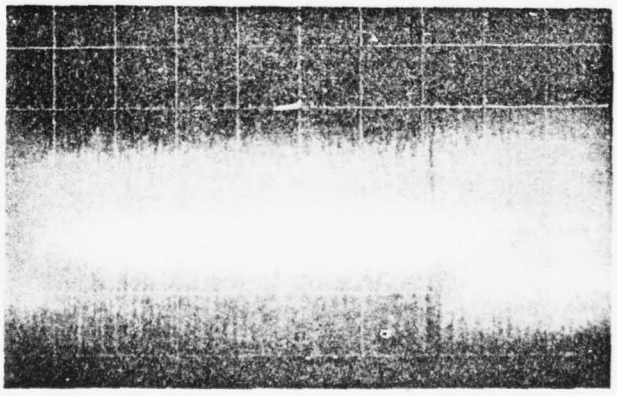

f) Power = 99 Watt

FIG. 14: EVOLUTION OF ELECTROSTATIC ION CYCLOTRON WAVE FROM ONE STEADY STATE AMPLITUDE TO ANOTHER, AS BOTH PUMP LEVELS ARE ABOVE THRESHOLD (Cont'd)

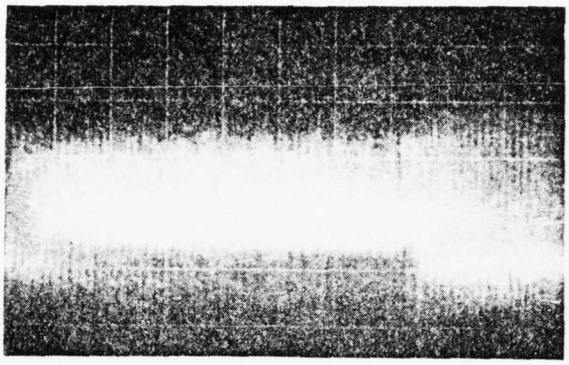

g) Power = 101 Watt

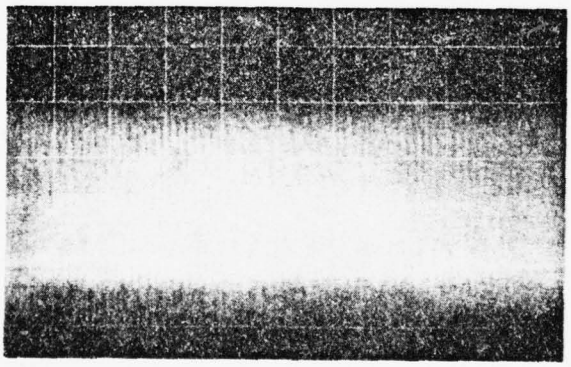

h) Power = 121 Watt

FIG. 14: EVOLUTION OF ELECTROSTATIC ION CYCLOTRON WAVE FROM ONE STEADY STATE AMPLITUDE TO ANOTHER, AS BOTH PUMP LEVELS ARE ABOVE THRESHOLD (Cont'd)

in frequency due to temperature increase has been mentioned earlier. Effects of other parameters, such as neutral pressure, baffle current, or static magnetic field, are not obtained because of the limited range these variables can be varied. Any change beyond this detunes the plasma background, making it no longer conducive for parametric decay instabilities.

IV-4 INTERPRETATION OF RESULTS

A- The Phenomenological Model

It has been shown in numerous papers that a high frequency electromagnetic wave with power exceeding the threshold level can parametrically couple and drive various natural modes of the plasma unstable. These waves grow exponentially in time from the noise level. This has been shown in our sets of experimental data in the previous chapter. Most of these theories, however, show the exponential growth of the instability out of the noise level, and not from another steady state level already in existence; often the saturation phenomena is not incorporated into their theories even though the experimental results invariably show that instabilities saturate. The theory we plan to use here has been developed previously by Klein and Cheo;[19, 42] it would be modified and expanded to fit our results. A phenomenological model is used to accurately describe the experimental observations, not only the growth or decay depending on the power level of the pump, but also taking the saturation into account. Aside from the similarity in the quasi-exponential behavior and saturation of the amplitude, our model shows a drastic difference in form which agrees well with our experiment; this is due to the difference in the saturation mechanism.

Before we embark into the development of the phenome-

nological model, the quasi-exponential form becomes more evident if one plots the amplitude of the electrostatic ion cyclotron wave from a set of decay photographs, versus time on semi-log scale, as shown in fig. 15. The plots show a straight line behavior; therefore, the evolution of the amplitude can be approximated as an exponential to obtain rough estimates of the initial decay rate.

The amplitude of the wave decays or grows depending on the value of the microwave power. Therefore the phenomena can be described by a differential equation of the form similar to Nishikawa's, except for the saturation term:

$$\frac{dA}{dt} = (C_1 P - C_2)\, A - C_3 A^{n+1} \qquad (4.1)$$

The term C_1 is the coefficient which couples the microwave pump and the excited waves through non-linear interactions.[44] C_2 represents the linear damping of the wave, accounting for the natural phenomena which cause the wave to damp unless a threshold level of the pump power is exceeded. $C_3 A^n$ is the non-linear damping term which causes the amplitude to saturate instead of growing indefinitely.[45-47] n is an integer whose value can be obtained through experimental data. C_1, C_2, and C_3 are assumed to be independent of time and power. The solution of equation (4.1), for n positive, is

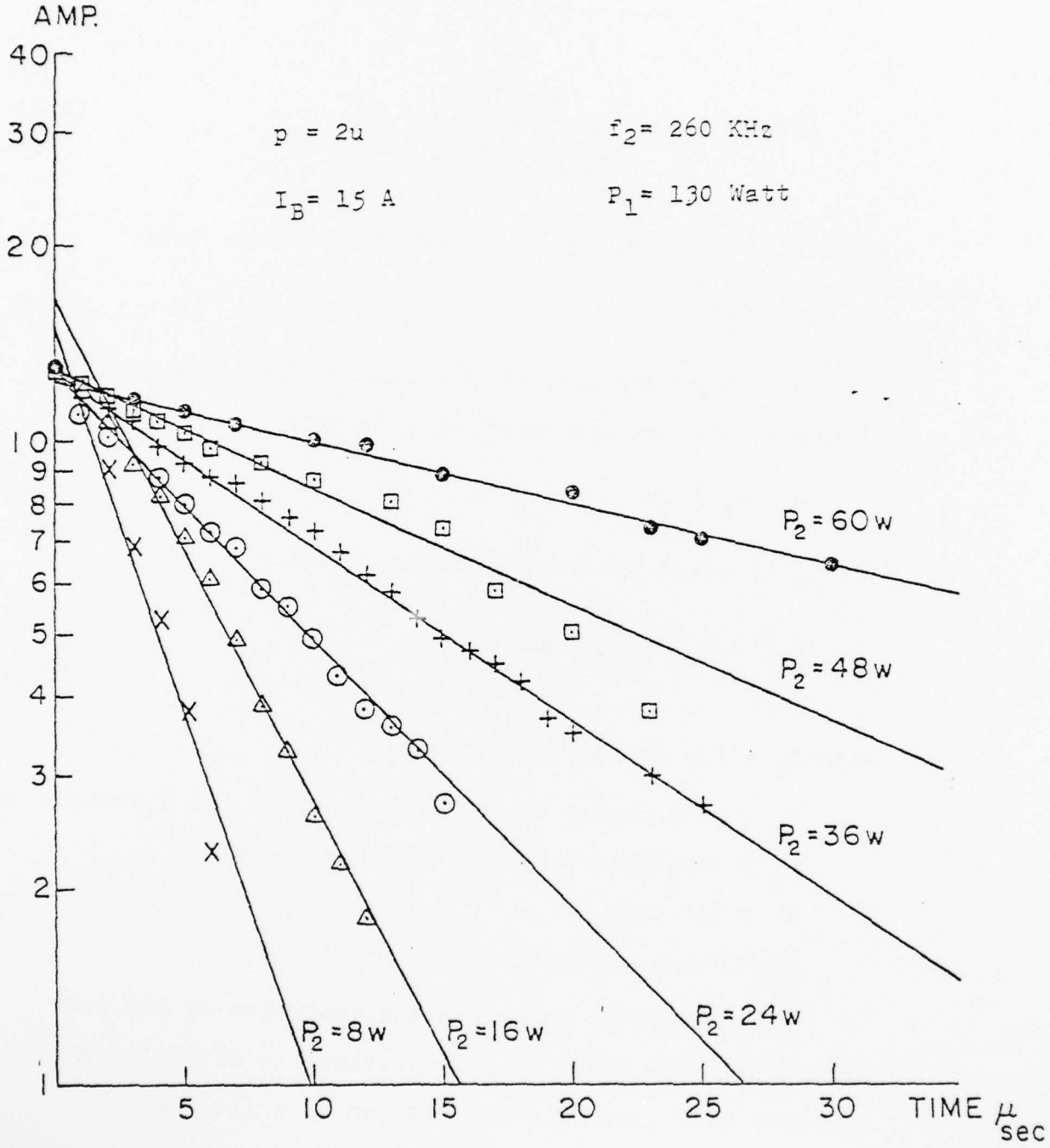

FIG. 15: AMPLITUDE OF THE DECAYING WAVE AS A FUNCTION OF TIME FOR VARIOUS POWER LEVELS

$$A(t) = \frac{A_o e^{yt}}{1 + \frac{A_o^n C_3}{y} (e^{nyt} - 1)^{1/n}} \tag{4.2}$$

where $A_o = A(0)$, the initial amplitude of the wave.

$$y = C_1 P - C_2 \tag{4.3}$$

y is the imaginary part of the complex frequency ω of the electrostatic ion cyclotron wave, namely

$$\omega = \Omega_k + iy \tag{4.4}$$

and Ω_k is given by the dispersion relation

$$\Omega_k^2 = \Omega_i^2 + \frac{k_i^2 \, T_e/M}{1 + k_i^2/k_{De}^2} \tag{4.5}$$

with Ω_i = ion cyclotron frequency

k_i = wave number of the electrostatic ion cyclotron wave

T_e = temperature of the electron, in eV

M = ion mass

k_{De} = Debye wavenumber

Equation (4.2) describes the evolution of the wave amplitude. The value of y is critical to determine whether the wave will grow or decay; it can be written as

$$y = C_1(P - P_{TH}) \tag{4.6}$$

Thus, for P less than P_{TH}, y is negative and

$$A(\infty) = 0 \tag{4.7}$$

and, for P larger than P_{TH}, y is positive and

$$A(\infty) = A_\infty \tag{4.8}$$

The steady state amplitude A_∞ for y positive can be evaluated simply from (4.1), by setting $\frac{dA}{dt} = 0$ and obtaining

$$\frac{C_1 P - C_2}{C_3} = A_\infty^n \tag{4.9}$$

Therefore, a plot of the nth power of the steady state amplitude from experimental observations, versus power gives us the correct value of n for our model, i.e. the value of n which is a straight line if we set n = 1, 2, 3, etc. Another alternative to evaluate the value of n is to plot the results, after some mathematical manipulation, in a log-log scale, i.e., from equation (4.9), we have

$$A_\infty^n = \frac{C_1}{C_3} (P - P_{TH}) \tag{4.10}$$

Fig. 16 shows several plots of the saturated amplitude A_∞ versus power $(P - P_{TH})$ in logarithmic scale, where P_{TH} is set to be 65 W. The lines in fig. 16 give us the correct n if the inverse of their slope is taken to the

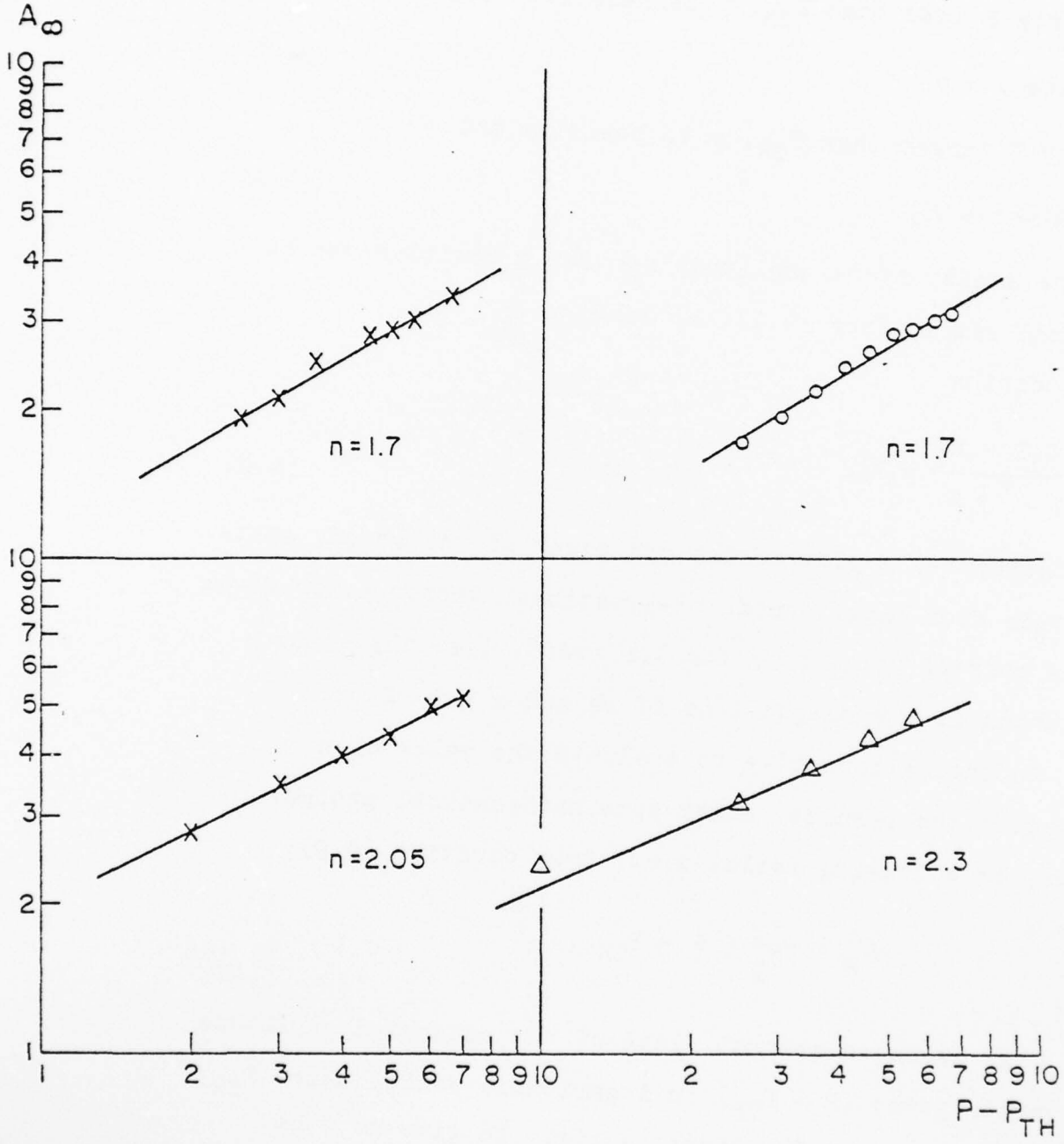

FIG. 16: STEADY STATE AMPLITUDE VERSUS POWER DIFFERENCE ($P - P_{TH}$)
n = 1/slope

nearest integer, which is found to be 2.

Therefore, our experimental observations are best described by the following equations

$$\frac{dA}{dt} = yA - C_3A^3 \tag{4.11}$$

$$A(t) = \frac{A_o\, e^{yt}}{\left[1 + A_o^2\, \frac{C_3}{y}(e^{2yt} - 1)\right]^{\frac{1}{2}}} \tag{4.12}$$

and

$$A(\infty) = \left(\frac{y}{C_3}\right)^2 = \frac{C_1^2}{C_3^2}\,(P - P_{TH})^2 \tag{4.13}$$

From the expression for A(t) and from fig. 15, it is apparent that the amplitude indeed follows the exponential form only for small values of t. For y negative, the amplitude decays quasi-exponentially; the deviation from the regular exponential curve depends on the ratio $A_o^2C_3/|y|$, or, in terms of power levels, $P_{TH}/|P - P_{TH}|$. This last result is obtained by using a typical value of $P = 2P_{TH}$ for y positive case. A plot of $A(t)/A_o$ versus yt, for P_{TH} = 65 watt, and for various values of $A_o^2C_3/|y|$, is shown in fig. 17. An exponential decay curve is also shown for comparison; it is obvious that the curves can not be approximated by an exponential, especially for those power levels close to the threshold. Therefore the results obtained by using the expo-

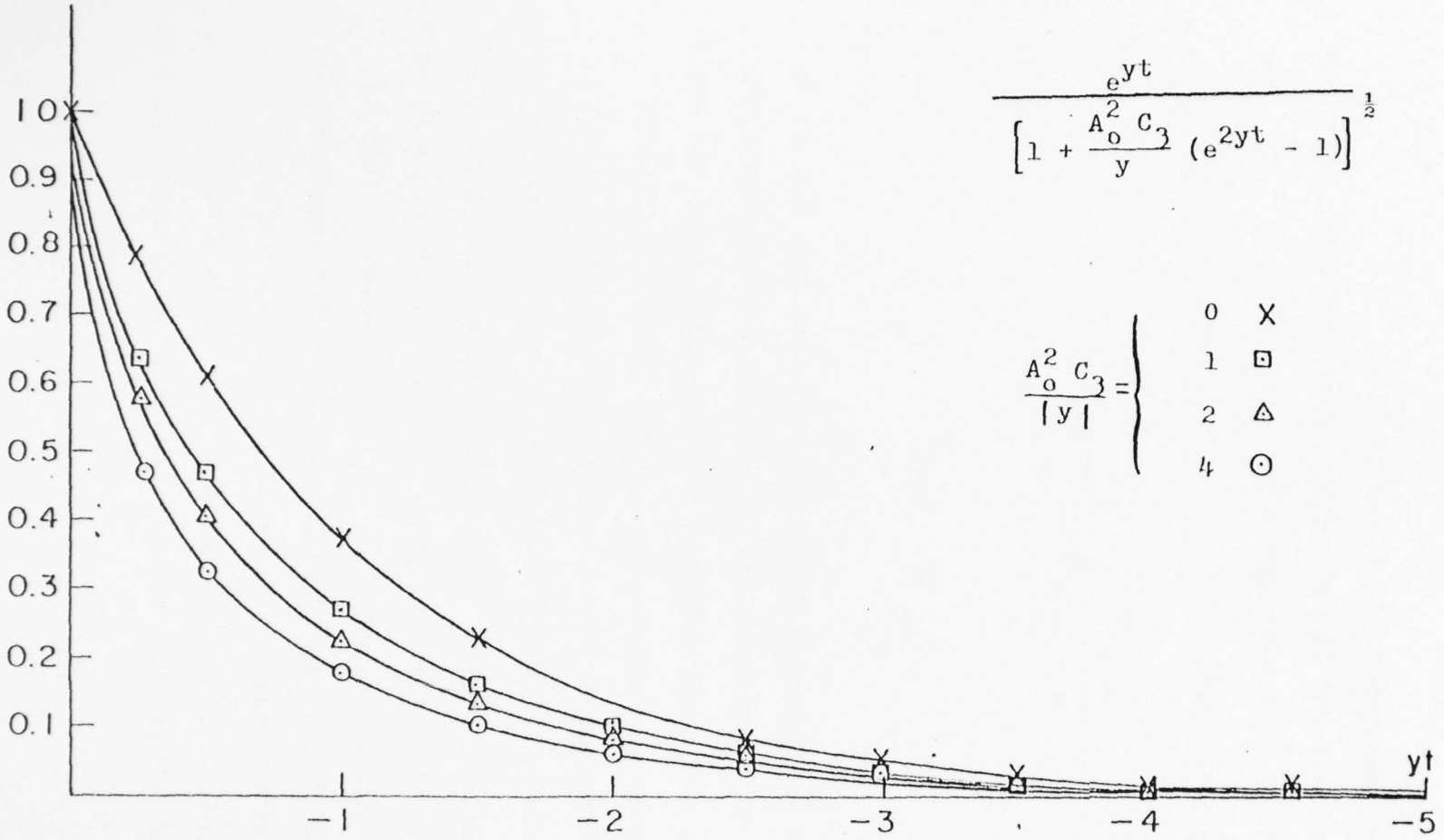

FIG. 17: COMPARISON OF DECAY PROCESS PREDICTED BY PHENOMENOLOGICAL MODEL AND EXPONENTIAL DECAY PROCESS

nential curve give us incorrect values; for example, the value thus obtained for y-intercept, i.e. values from fig. 15, is found to be about twice the natural damping term from the expression (4.12). As for y positive, the amplitude of the wave definitely grows and saturates according to (4.12). The steady state amplitude is given by (4.13), independent of the initial amplitude A_o. Now we have developed the proper model to describe an observations, we then proceeded to analyze the data for the decay and growth process.

B- Calculation of Decay and Growth Rate

The set of decay photographs in fig. 13 is used to evaluate the decay rate y. Since we have already discussed in the previous section, we can not use the method of e-folding time, i.e., the time for the wave amplitude to decay to 0.37 of the initial amplitude A_o, nor the method of obtaining the exact decay time for the wave amplitude to reach the noise level. However, the envelope of the decaying amplitude can be followed quite clearly through the photographic averaging technique. Using the experimental values of P_{TH} and P, the normalized amplitude $A(yt)/A_o$ obtained from (12) is plotted first. Then the experimental data from fig. 13 are fitted, by trial and error, into these calculated curves by choosing the proper values of y.

The procedure is illustrated in fig. 18, where a series of experimental data is being fitted on the curve calculated for each pump power level. The decay rate y is then obtained by simply dividing the graphical scale yt by the corresponding experimentally measured value of t.

A set of values for y is plotted against the pump power; a linear dependence of y on power agrees well with the proposed theory and model, as seen in fig. 19. Other information may also be inferred from this plot, such as the values of C_1 and C_2, the slope and intercept of the straight line respectively. The threshold power can also be obtained, which is simply the point corresponding to $y = 0$.

The same procedures are used to calculate the linear growth rate. As mentioned earlier, the linear growth rate is calculated from the data of the wave amplitude decaying from one higher level to another, rather than growing to a higher amplitude level. Fig. 20 shows the curve fitting procedure for each value of power. The smooth lines correspond to the curve calculated from equation (4.12), rewritten into the following form:

$$\frac{A(t)}{A_o} = \frac{e^{yt}}{\left[1 + \frac{A_o^2}{A_\infty^2}\left(e^{2yt} - 1\right)\right]^{1/2}} \qquad (4.14)$$

AD-A071 017 POLYTECHNIC INST OF NEW YORK FARMINGDALE DEPT OF ELE--ETC F/G 20/9
STUDIES ON THE INTERACTIONS BETWEEN ELECTROMAGNETIC FIELDS AND --ETC(U)
APR 79 B R CHEO, E E KUNHARDT, S P KUO AFOSR-74-2668

UNCLASSIFIED POLY-EE-79-053 AFOSR-TR-79-0752 NL

3 OF 4
AD A071017

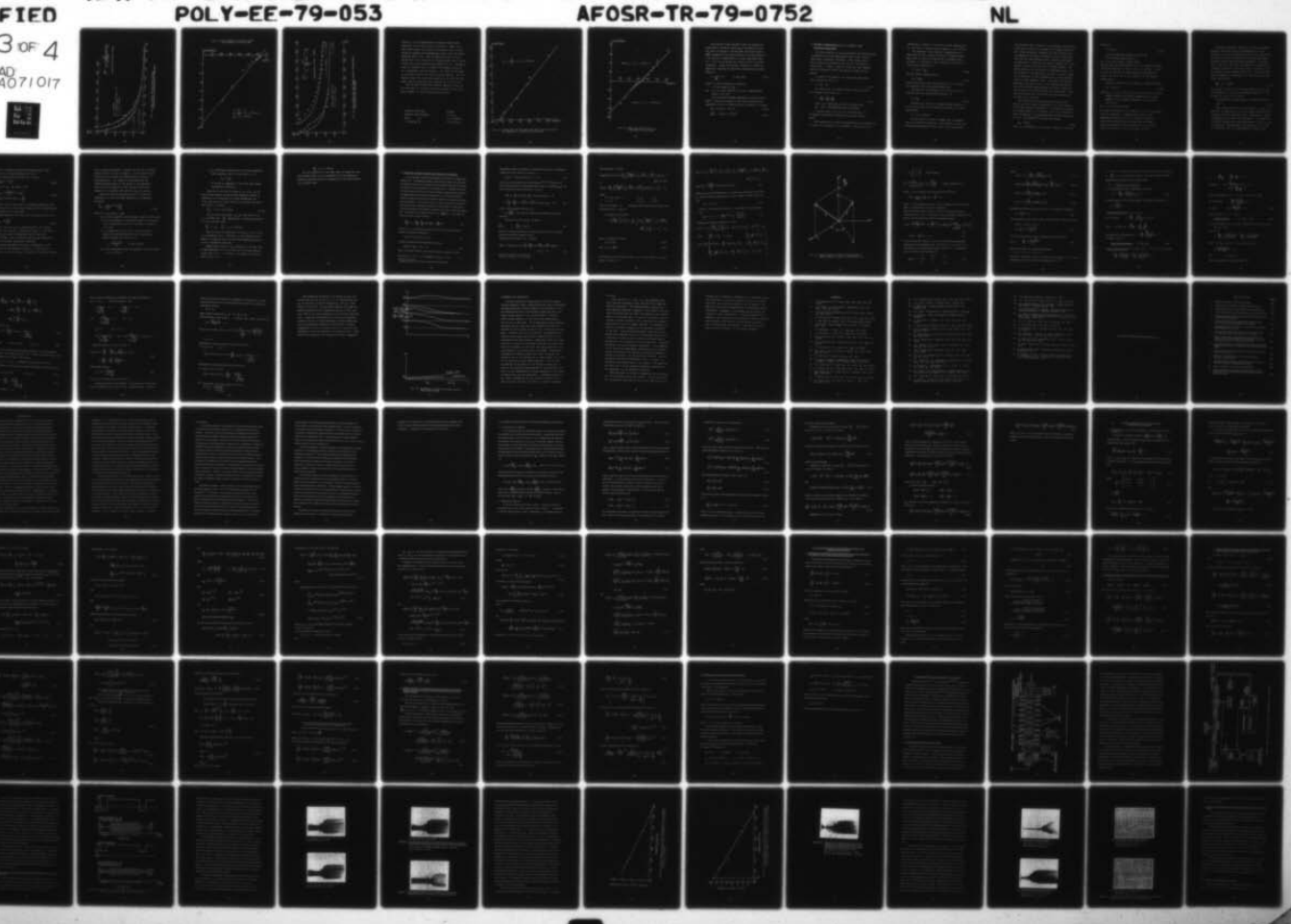

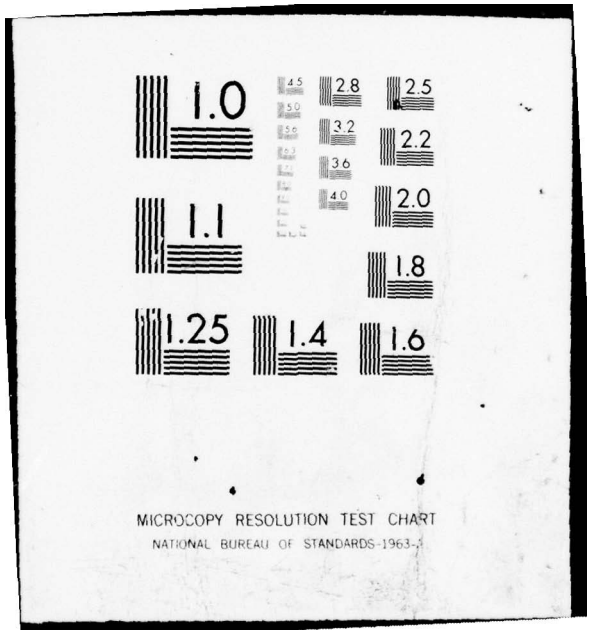
1.0
1.1
1.25
1.4
1.6
1.8
2.0
2.2
2.5
2.8
3.2
3.6
4.0
4.5
5.0
5.6
6.3
MICROCOPY RESOLUTION TEST CHART
NATIONAL BUREAU OF STANDARDS-1963-A

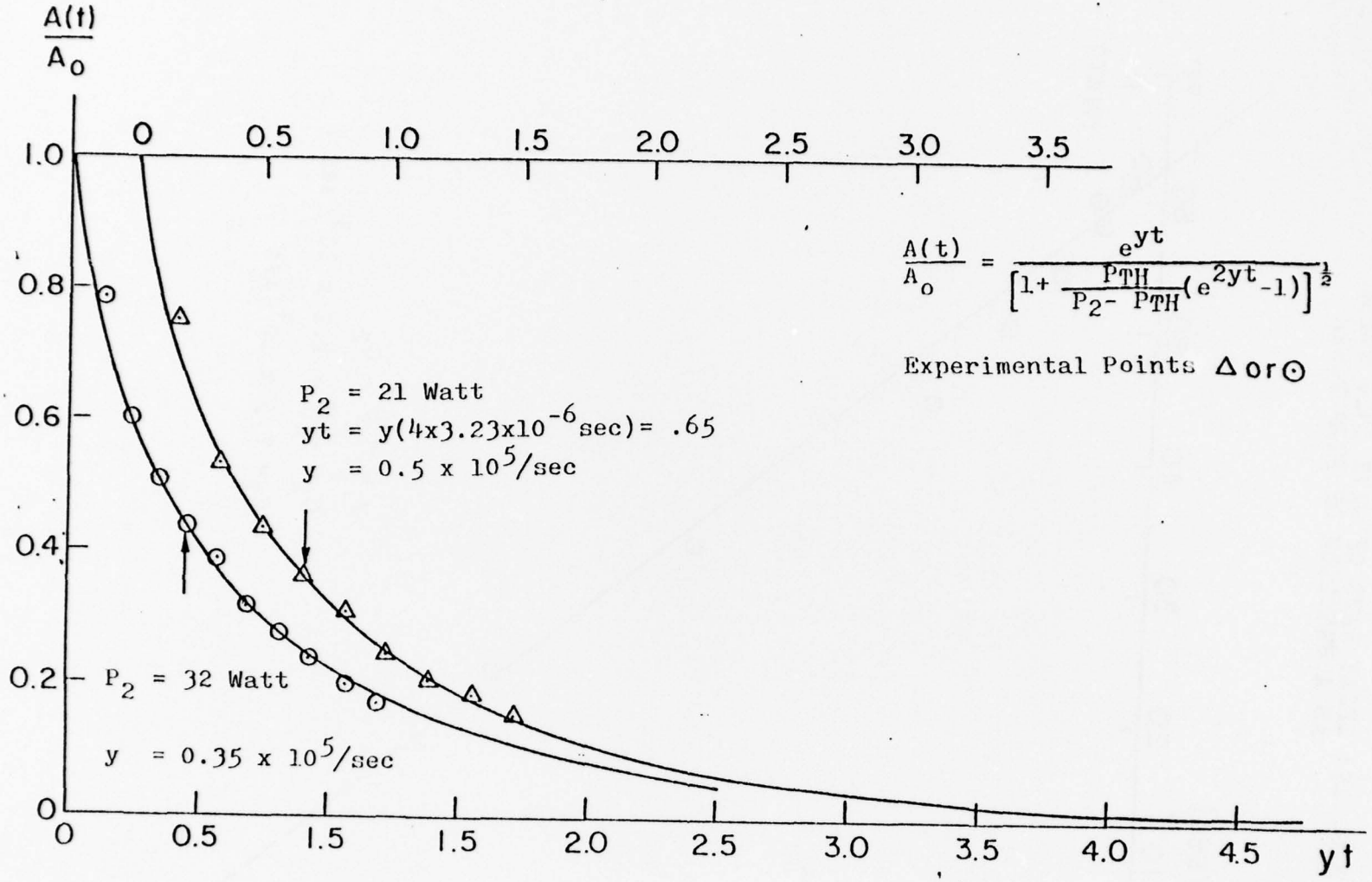

FIG. 18: DATA FITTING FOR WAVE DECAY AGAINST THEORETICALLY CALCULATED CURVE FROM MODEL

FIG. 19: DECAY RATE OF WAVE INTO NOISE
AS A FUNCTION OF PUMP POWER

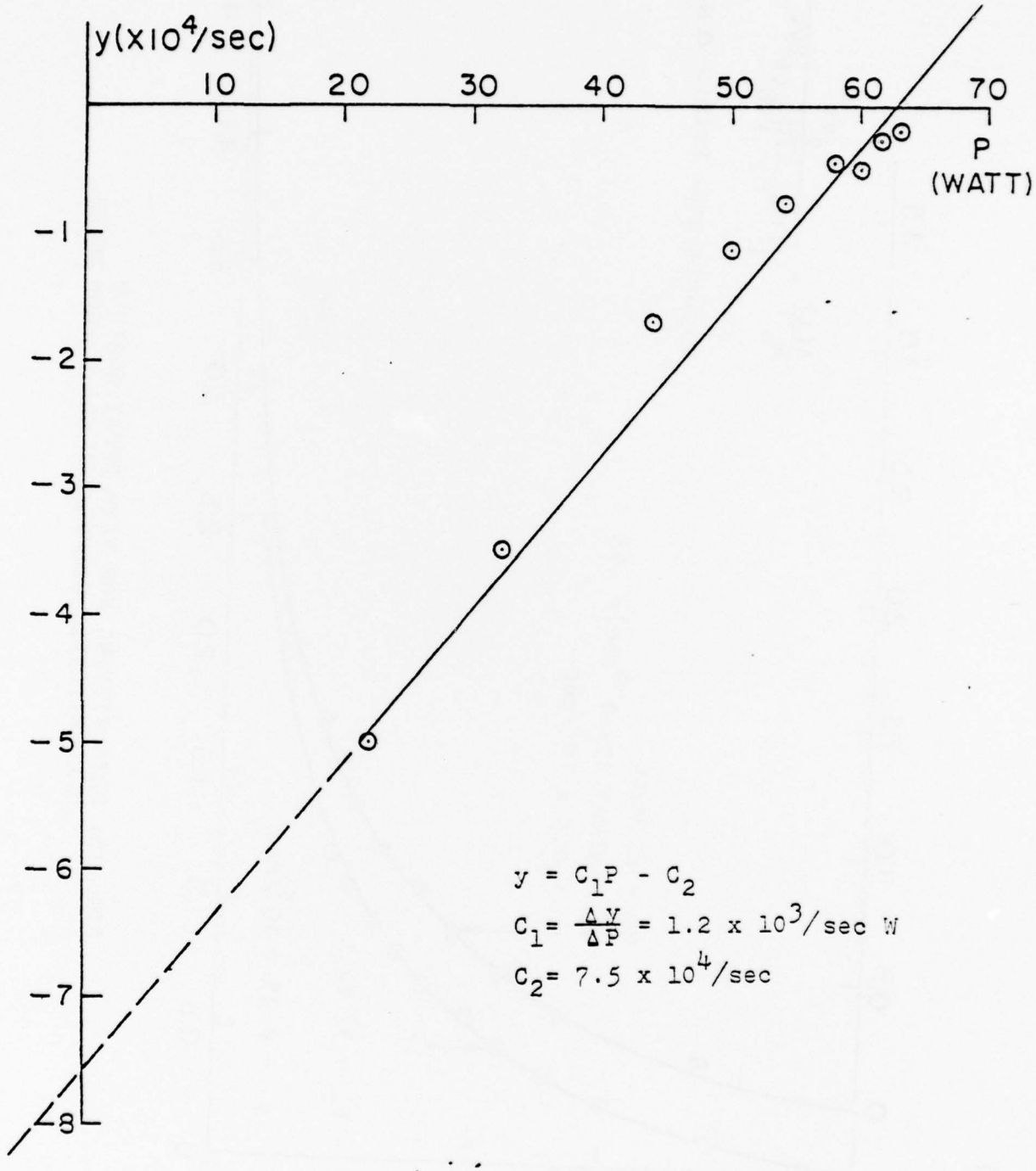

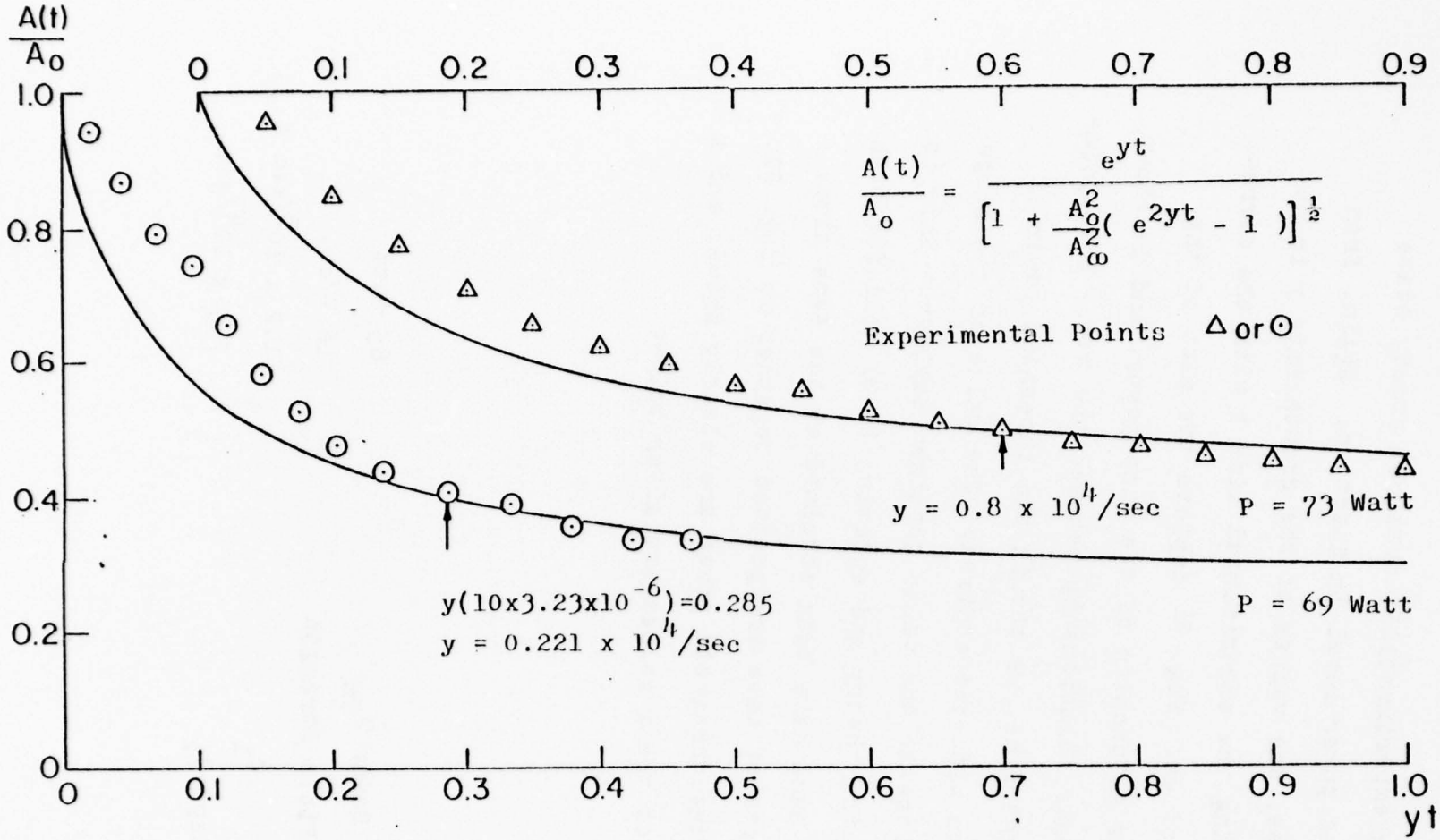

FIG. 20: DATA FITTING FOR WAVE GROWTH AGAINST THEORETICALLY CALCULATED CURVE FROM MODEL

where A_∞ is the experimentally obtained steady state amplitude for the power level in question. Again, from the fitted curves, the values of the growth rate y is obtained by matching the experimental time t with the corresponding value of yt. Fig. 21 depicts the plot of the growth rate y as a function of the pump power, and it shows clearly the linear relationship between the two. Extrapolating the straight line, we obtain the threshold power at the interception with the abcissa. The value of the slope C_1 is fairly close to the value obtained earlier. This is expected since the theory and equation (4.3) hold for both cases, and the data have been obtained at the same time.

The two sets of data are plotted together in fig. 22. The slope and the threshold power are clearly shown, and a brief summary of their values are given below:

Threshold Power P_{TH}	65 watt
Electric Field Strength	16 V/cm.
slope C_1	1.2×10^3/sec W
y- intercept C_2	7.5×10^4/sec.

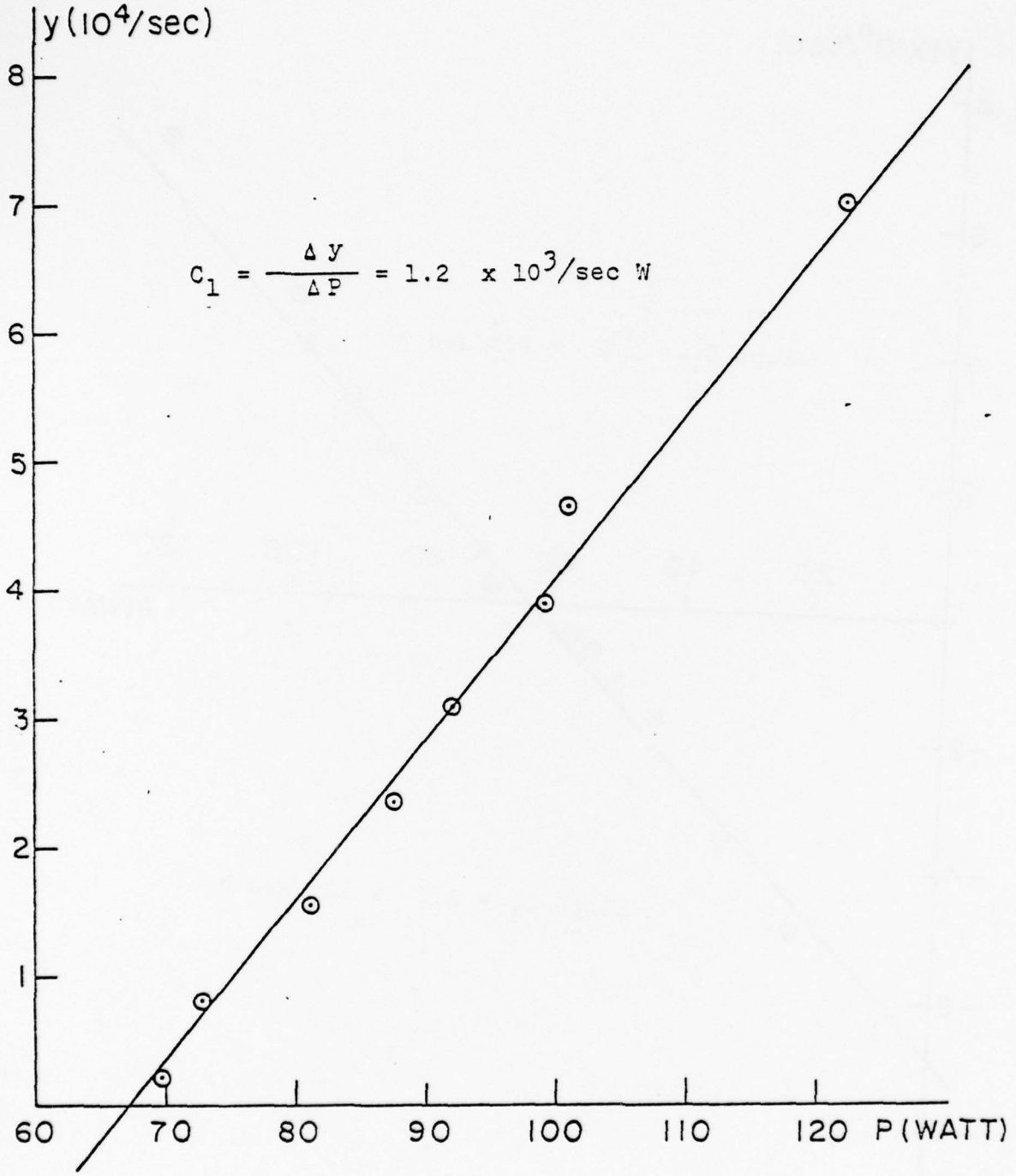

FIG. 21: GROWTH RATE OF WAVE FROM ONE STEADY STATE AMPLITUDE TO ANOTHER AS A FUNCTION OF PUMP POWER

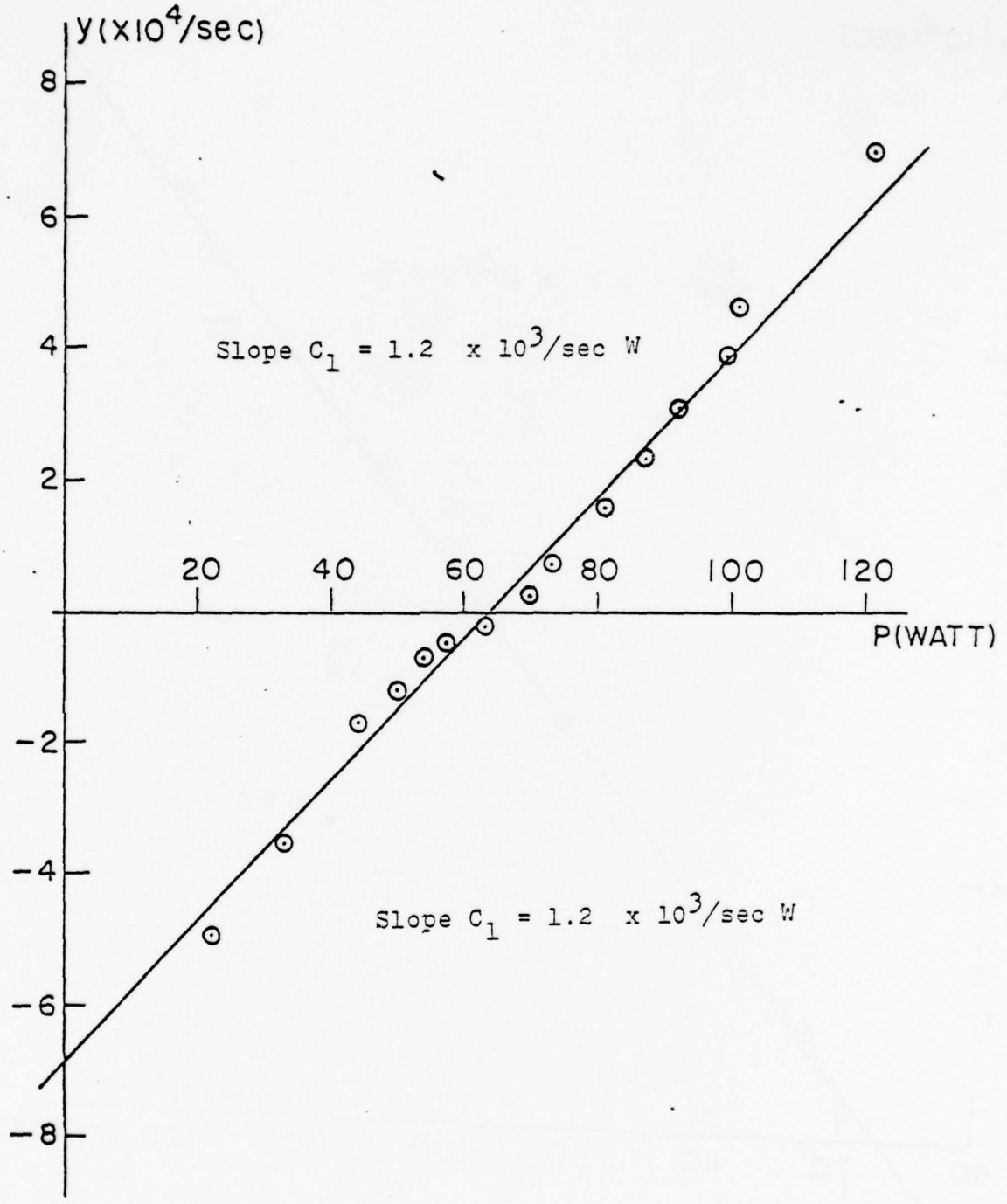

FIG. 22: DECAY AND GROWTH RATE y AS A FUNCTION OF PUMP POWER

The electric field strength inside the plasma corresponding to threshold power P_{TH} is obtained by using TE_{10} mode of analysis. Knowing that the plasma beam is small compared to the cross section of the can (radius of 1 cm. and 8 cm. respectively, or cross sectional ratio of 1 : 64), we can assume the electric field is uniform throughout. Using the Poynting theorem, we obtain an expression relating the power and corresponding electric field as:

$$P = \frac{E_p^2}{8\pi} c \times A \qquad \text{in cgs units} \tag{4.15}$$

where P is power expressed in ergs/sec.

c is the speed of light

and A is the cross section of the can, approximately equal to 64π cm^2

E is the field strength expressed in stat-volts/cm. Since 1 stat-volt is equal to 300 volts, rewriting the expression, with P in watts and E_p in volts/cm., we obtain

$$E_p^2 = 3.75 \times P \quad v^2/cm.^2 \tag{4.16}$$

$$E_{rms}^2 = 1.88 \times P \quad v^2/cm.^2 \tag{4.17}$$

C- Physical Interpretation of C_1, C_2 and C_3, and Saturation Mechanisms

The time behavior of the electrostatic ion cyclotron wave is governed by the phenemenological model which included some terms of physical importance. These terms, which can be easily calculated from the plot of the decay or growth rate y versus power as in fig. 22, are compared with the theories so that some physical insight can be gained.

In terms of the power P, the decay rate near threshold is given by (4.3), as

$$y = C_1 P - C_2 \tag{4.18}$$

The value of C_1 is obtained simply from the slope of the straight line in fig. 22,

$$C_1 = \frac{\Delta y}{\Delta P} = \frac{y_1 - y_2}{P_1 - P_2} \tag{4.19}$$

where Δy = difference between two decay rates

and ΔP = corresponding power difference

A typical value of C_1 is 1.15×10^3/watt-sec.; it is simply a coefficient coupling the pump and excited waves.

The constant C_2 is found by extrapolating the straight line to obtain the intercept of the ordinate. This point, which

corresponds to power P = 0 W is the natural damping rate C_2. The value obtained from the graph is 7.5×10^4/sec.

The intercept of the abcissa, corresponding to a decay rate of zero, yields the value of threshold power P_{TH}, which is found to be around 65 W (average value). In terms of threshold power, equation (4.18) can be conveniently expressed as

$$y = C_1(P - P_{TH}) \tag{4.20}$$

and the natural damping rate as

$$C_2 = C_1 P_{TH} \tag{4.21}$$

These results have been used earlier in (4.6) to obtain the expression for the saturated amplitude.

The physical interpretation of the term C_2 can be obtained from the coupled mode theories,[7] as

$$C_2 = \frac{\nu_i}{2} \tag{4.22}$$

Therefore the natural or linear damping frequency ν_i is twice the value of the intercept at power P = 0, more specifically,

$$\nu_i = 1.5 \times 10^5/\text{sec}.$$

Now this value is used to compare with the damping due to all possible mechanisms. Even though the ions are rotating around magnetic field lines, the electrostatic

ion cyclotron wave, consists of ion bunching, and the electrons play no role but to conserve the charge neutrality and field shielding. Therefore the main contribution to the damping of the wave in question is due to ions only, while for the high frequency mode, electron involvement is predominant. There are two kinds of damping to be considered, either the collisional or Landau damping. The Landau damping for both species is negligibly small, not only because of the large ratio of k_D/k, but also because of the direction of wave propagation of $\underline{k}$ being perpendicular to static magnetic field. Therefore, the dominant phenomena, with values close to our experimental results, can be collisional damping among the species, namely the collision due to electron-neutral and ion-neutral; others, such as electron-ion, ion-ion and electron-electron are too small to be involved.

The value of the electron-neutral collision frequency ν_{en}, which plays an important role in the damping of the high frequency instability, is obtained by assuming the thermal speed of the electron to be 1.03×10^8 cm/sec, which corresponds to our experimental electron temperature of 2 eV. From [Brown],[48] we have the relation

$$\nu_{en} = p_o P_c v_e \qquad (4.23)$$

where P_c = probability of collision, related to the cross

section by

$$\sigma = p_o P/n_o \qquad (4.24)$$

p_o is the neutral pressure in mm of Hg,

n_o is neutral density per c.c.

and v_e is the electron thermal speed.

Substituting the experimental values, the electron-neutral collision frequency is found to be 2.6×10^6/sec. Since we have not studied the high frequency instability in detail, the value can not be compared with the experimental result.

Using the formula given in [Rose and Clark],[49] namely

$$\nu_{in} = \sigma_{in} v_i n_o \qquad (4.25)$$

where $\sigma_{in} = 1.2 \times 10^{-14}$ cm.^{2}, total cross section including charge transfer from [37] by assuming the ion temperature of the present experiment to be close to their value.

and v_i = ion thermal speed

We obtain the values of 1.6×10^5/sec for the ion-neutral collision frequency. Comparing this value to the experimental result ($C_2 = 1.5 \times 10^5$/sec.), there is less than a 10% difference; we conclude the linear damping mechanisim of the electrostatic ion cyclotron wave is due mainly to the ion-neutral collision.

The last coefficient, namely C_3, can also be experimentally calculated using our phenomenological model. However, it is not of interest to solve for C_3 exclusively; we choose to obtain the term C_3A^2 for being more experimentally feasible and physically meaningful. The first point lies in the fact that, although one can measure the voltage oscillation on the scope easily, in reality A is the electric field strength of the wave. The second point becomes apparent by examining (4.1), rewritten here with slight modification

$$\frac{dA}{dt} = yA - (C_3A^2)A \tag{4.26}$$

Thus, C_3A^2 is simply the non-linear damping term causing the saturation of the wave as explained earlier; now, we proceed to solve for this value.

At saturation or steady state, we obtain from above

$$C_3A^2 = y \tag{4.27}$$

For a fixed power level P_2 which gives $y = C_1P_2 - C_2$ positive, the amplitude of the wave begins to grow with no influence from the saturation term. Therefore, to obtain a reading of y, one must use only small t. A snapshot of the growth experiment is shown previously in fig. 11b, for this purpose. The amplitude is growing from 0 W to 180 W. The growth rate y is experimentally obtained from

fig. 11b; and we have obtained a value for the non-linear damping $C_3 A^2 = 1.4 \times 10^5/\text{sec}$.

Now, we proceed to find a saturation mechanism which agrees with our experimental findings. Recalling in fig. 16, the plot of saturation amplitude versus power, we have found that the proper value of n is 2. Among the experimental results, we have observed the harmonic generation process take place (see fig. 12). Thus, we should examine whether this is indeed the phenomenon which can contribute to the wave saturation. The harmonic generation process can be described mathematically, in a simplified form, as

$$\frac{dA_2}{dt} + \gamma_1 A_2 = C_A A_1^2 \qquad (4.28)$$

where A_2, A_1 are the amplitudes of the 2nd harmonic and fundamental signal,

γ_1 is the linear damping term of the 2nd harmonic and C_A is a constant coefficent; $C_A A_1^2$ is just the energy acting as a pump to the harmonic generation process. So, at steady state, we have:

$$\gamma_1 A_2 = C_A A_1^2 \qquad (4.29)$$

Now, at equilibrium, the energy being lost by the fundamental $\gamma_{NL} A_1^2$, must be equal to the energy gained by the

harmonic to overcome the natural damping $\gamma_1 A_2^2$, where γ_{NL} is the non-linear damping term of A_1.
Writing this equilibrium condition, we have

$$\gamma_{NL} A_1^2 = \gamma_1 A_2^2 \tag{4.30}$$

Solving for γ_{NL}, and using (4.29)

$$\gamma_{NL} = \gamma_1 \left(\frac{C_A A_1}{\gamma_1}\right)^2 = C_4 A_1^2 \tag{4.31}$$

where we have set $C_4 = \frac{C_A^2}{\gamma_1}$

Therefore, we have shown that the harmonic generation process does give us a non-linear damping which is proportional to the square of the amplitude.

Experimentally, this value can be obtained from (4.30)

$$\gamma_{NL} = \gamma_1 \left(\frac{A_2}{A_1}\right)^2 \tag{4.32}$$

Since the value of A_2/A_1 is approximately 0.53, taking bandwidth into account, consequently $\gamma_{NL} \simeq 2.1 \times 10^4$/sec is more than one order of magnitude smaller than $C_3 A^2$ (1.4×10^5/sec), and we conclude that harmonic generation is not the dominant saturation mechanism.

A second phenomenon which also corresponds to the n = 2 case is the anomalous diffusion. This diffusion process is not due to binary collisions of different species

as in classical diffusion. Briefly, we can use the quasi-particle point of view to explain. As the excited instabilities can be treated as corresponding to bunches of quasi-particles, the number of quasi-particles are related proportionally to the square of the amplitude. These extra quasi-particles thus can give additional pressure to the plasma, and cause the ions to diffuse.

Using the results developed by Kuo,[14] we have an expression for the non-linear damping due to anomalous diffusion,

$$\gamma^{D}_{NL} = \frac{c^2}{4B_o^2} k_i^2 r_a^2 \frac{A^2}{2C_2} \qquad (4.33)$$

where c is the speed of light

B_o is static magnetic field strength, equal to 1088 Gauss

k_i is the wavenumber of the electrostatic ion cyclotron wave, calculated from (4.5), its value is found to be 7.5/cm

A is the amplitude of the wave, in stat volts/cm, calculated experimentally from the oscilloscope signal strength of 0.12 volt, i.e.

$$A = \frac{k_i \times 0.12}{300} \quad \text{in stat volt/cm}$$

C_2 is the experimental natural damping rate, which equals 0.75×10^5/sec

r_a is coefficient relating the two field components, and is greater than 0 or less than 1; i.e.

$$A_y = r_a A_x$$

It is the y- component of the field that causes the anomalous diffusion.

Since we do not have the value of r_a or A_y, we can still check whether the non-linear damping is caused by diffusion if we substitute all known parameters into (4.33) and find out later whether r_a is indeed less than 1. From (4.33), we obtain

$$\gamma^D_{NL} = 6.42 \times 10^5 \, r_a^2/\text{sec} \qquad (4.34)$$

Now, the total non-linear γ_{NL} has been found to be 1.4×10^5/sec and, γ^H_{NL}, damping due to harmonic generation is 0.21×10^5/sec then,

$$\gamma^D_{NL} = \gamma_{NL} - \gamma^H_{NL} = 1.2 \times 10^5/\text{sec}$$

From the last two equations, we have $r_a = 0.43$, which is a reasonable value. Therefore, we can conclude with a degree of certainty that the non-linear damping mechanism is due to anomalous diffusion.

Applying this value of r_a to another set of data, with voltage amplitude of 0.14 volt and the non-linear damping $C_3 A_1^2$ term to be 1.1×10^5/sec, the anomalous diffusion term is found to be

$$\gamma^{D}_{NL} = 1.7 \times 10^{5}/\text{sec}$$

The two values are of the same order of magnitude, and this further bears out our hypothesis that the anomalous diffusion process causes the saturation of the electrostatic ion cyclotron wave.

D- Derivation of Modes Involved in the Parametric Experiment

In this section, we derive the dispersion relation for a magnetized, infinite, and homogeneous plasma via the kinetic model, and show that the modes involved in our experiment are indeed the harmonic of electron cyclotron and the electrostatic ion cyclotron waves. Although the formal derivation starts with the set of Vlasov-Maxwell equations which provides a complete kinetic description of the plasma, we use the perturbative method to obtain the macroscopic plasma response to a given electromagnetic disturbance. The dielectric tensor, which contains all the information about the electromagnetic properties of the plasma, is determined from the calculation of the plasma response to an electric field disturbance $\delta \underset{\sim}{E}$, which gives us an induced current $\delta \underset{\sim}{J} = \frac{i\omega}{4\pi}\left[\epsilon\,(\underset{\sim}{k}, \omega) - \underset{\approx}{I}\right] \cdot \delta \underset{\sim}{E}(\underset{\sim}{k}, \omega)$

We start with the Vlasov equation

$$\frac{\partial f_{\sigma o}}{\partial t} + \underset{\sim}{v} \cdot \frac{\partial f_{\sigma o}}{\partial \underset{\sim}{r}} + \frac{q_\sigma}{m_\sigma} \left(\underset{\sim}{E} + \frac{\underset{\sim}{v}}{c} \times \underset{\sim}{B}\right) \cdot \frac{\partial f_{\sigma o}}{\partial \underset{\sim}{v}} = 0 \qquad (1)^*$$

where $\sigma = e, i$, designating the species involved, and the distribution function is already normalized as

$$n_\sigma (\underset{\sim}{r}, t) = n_\sigma \int f_{\sigma o} (\underset{\sim}{r}, \underset{\sim}{v}, t)\, d\underset{\sim}{v} \,. \qquad (2)$$

Assume an electric field disturbance of the form

$$\delta \underset{\sim}{E} \exp\left[i\,(\underset{\sim}{k} \cdot \underset{\sim}{r} - \omega\, t)\right] + cc \qquad (3)$$

Then, associated with this, and through Maxwell's equation, we have

$$\delta \underset{\sim}{B} \exp\left[i(\underset{\sim}{k} \cdot \underset{\sim}{r} - \omega t)\right] + cc = \left(\frac{c}{\omega}\right)(\underset{\sim}{k} \times \delta \underset{\sim}{E}) \exp\left[i(\underset{\sim}{k} \cdot \underset{\sim}{r} - \omega t)\right] + cc \qquad (4)$$

* Equations in this section are renumbered sequentially

Responding to these disturbances, the distribution functions are departed slightly from their stationary values, as

$$f_{\sigma o}(\underset{\sim}{v}) + \quad \delta f_{\sigma}\ (\underset{\sim}{v}) \exp\left[i(\underset{\sim}{k} \cdot \underset{\sim}{r} - \omega t) + cc \right] \tag{5}$$

and $\delta f_{\sigma}\ (\underset{\sim}{v})$ can be obtained by substituting eqs. (3), (4), (5) with eq. (1).* After some calculation, collecting the terms linear in $\delta \underset{\sim}{E}$ and $\delta f_{\alpha o}\ (\underset{\sim}{v})$, we have the linearized Vlasov equation in $\delta f_{\sigma}\ (\underset{\sim}{v})$ as

$$\left[\frac{\partial}{\partial t} + \underset{\sim}{v} \cdot \frac{\partial}{\partial \underset{\sim}{r}} + \Omega_{\sigma}\ (\underset{\sim}{v} \times \hat{z}) \cdot \frac{\partial}{\partial \underset{\sim}{v}} \right] \cdot \delta f_{\sigma}\ (\underset{\sim}{v}) \exp\left[i(\underset{\sim}{k} \cdot \underset{\sim}{r} - \omega t) \right]$$

$$= - \frac{q_{\sigma}}{m_{\sigma}} \left(\frac{\partial f_{\sigma o}}{\partial \underset{\sim}{v}} \right) \cdot \left[\left(1 - \frac{\underset{\sim}{k} \cdot \underset{\sim}{v}}{\omega}\right) \underset{\approx}{1} + \frac{\underset{\sim}{k} \cdot \underset{\sim}{v}}{\omega} \right] \cdot \delta \underset{\sim}{E} \exp\left[i(\underset{\sim}{k} \cdot \underset{\sim}{r} - \omega t) \right] \tag{6}$$

where, static magnetic field $\underset{\sim}{B} = B_o \hat{z}$

$\Omega_{\sigma} = \dfrac{q_{\sigma} B_o}{m_{\sigma} c}$, the cyclotron frequency, including the sign of the charge q_{σ}.

In order to solve for $\delta f_{\sigma}\ (\underset{\sim}{v})$, we define

$$\frac{d\underset{\sim}{r}}{dt} = \underset{\sim}{v} \qquad , \qquad \frac{d\underset{\sim}{v}}{dt} = \Omega_{\sigma}(\underset{\sim}{v} \times \hat{z}) \tag{7}$$

This set of equation determines an unperturbed free orbit of a charged particle in a uniform magnetic field B_o.

Then, along this trajectory, eq. 6 becomes

$$\frac{d}{dt} \delta_{\sigma}\ (v) \exp\left[i(\underset{\sim}{k} \cdot \underset{\sim}{r} - \omega t) \right] = - \frac{q_{\sigma}}{m_{\sigma}} \left(\frac{\partial f_{\sigma o}}{\partial \underset{\sim}{v}} \right) \cdot \left[\left(1 - \frac{\underset{\sim}{k} \cdot \underset{\sim}{v}}{\omega}\right) \underset{\approx}{1} + \frac{\underset{\sim}{k}\ \underset{\sim}{v}}{\omega} \right] \cdot \delta \underset{\sim}{E} \exp$$

$$\left[i(\underset{\sim}{k} \cdot \underset{\sim}{v} - \omega t) \right] \tag{8}$$

---

* Refers to equation 1 of this section.

and integrating, we obtain

$$\delta f_\sigma(\underset{\sim}{v})\exp[\,i(\underset{\sim}{k}.\underset{\sim}{r}-\omega t)] = -\frac{q_\sigma}{m_\sigma}\int_{-\infty}^{t}\left[\frac{\partial f_{\sigma o}(\underset{\sim}{v}')}{\partial \underset{\sim}{v}'}\right].\left[(1-\frac{\underset{\sim}{k}.\underset{\sim}{v}'}{\omega})\underset{\approx}{1}+\frac{\underset{\sim}{k}\,\underset{\sim}{v}'}{\omega}\right].\delta\underset{\sim}{E}\exp[\,i(\underset{\sim}{k}.\underset{\sim}{r}'-\omega t')]\,dt'$$

or

$$\delta f_\sigma(\underset{\sim}{v}) = -\frac{q_\sigma}{m_\sigma}\int_{0}^{\infty}\left[\frac{\partial f_{\sigma o}(\underset{\sim}{v}')}{\partial \underset{\sim}{v}'}\right].\left[(1-\frac{\underset{\sim}{k}.\underset{\sim}{v}'}{\omega})\underset{\approx}{1}+\frac{\underset{\sim}{k}\,\underset{\sim}{v}'}{\omega}\right].\delta\underset{\sim}{E}\exp\left[-i\phi(\tau)\right]d\tau \qquad (9)$$

where

$$\phi(\tau) = \underset{\sim}{k}.(\underset{\sim}{r}-\underset{\sim}{r}') - \omega\tau \qquad r = r(t) \qquad v = v(t)$$

$$\tau = t - t' \qquad r' = r(t') \qquad v' = v(t')$$

Now, we can obtain an expression for the induced current $\delta\underset{\sim}{J}$ from the expression for $\delta f_\sigma(\underset{\sim}{v})$, as

$$\delta\underset{\sim}{J} = \sum_\sigma q_\sigma n_\sigma \int \underset{\sim}{v}\,\delta f_\sigma(\underset{\sim}{v})d\underset{\sim}{v}$$

$$= -\sum_\sigma \frac{q_\sigma^2 n_\sigma}{m_\sigma}\int_0^{2\pi}d\theta\int_0^{\infty}v_\perp\,dv_\perp\int_{-\infty}^{\infty}dv_\parallel\int_0^{\infty}d\tau\,\underset{\sim}{v}\left[\frac{\partial f_{\sigma o}(v')}{\partial \underset{\sim}{v}'}\right].\left[(1-\frac{\underset{\sim}{k}.\underset{\sim}{v}'}{\omega})\underset{\approx}{1}+\frac{\underset{\sim}{k}\,\underset{\sim}{v}'}{\omega}\right]\exp\left[-i\,\phi(\tau)\right] \qquad (10)$$

Since, by definition, we know

$$\delta\underset{\sim}{J} = \underset{\approx}{\sigma}\,\delta\underset{\sim}{E} \qquad (11.a)$$

and $$\underset{\approx}{\varepsilon} = \underset{\approx}{1} - \frac{4\pi}{i\omega}\,\underset{\approx}{\sigma} \qquad (11.b)$$

The expression for the dielectric tensor $\underset{\approx}{\varepsilon}$ is simply obtained by comparing eqs. 10 and 11, or

$$\underset{\approx}{\varepsilon}(\underset{\sim}{k},\omega) = \underset{\approx}{1} + \sum_{\sigma} \frac{\omega_{p\sigma}^2}{i\omega} \int_0^{2\pi} d\theta \int_0^{\infty} v_{\perp}\, dv_{\perp} \int_{-\infty}^{\infty} dv_{\parallel} \int_0^{\infty} d\tau \left[\frac{\partial f_{\sigma o}(\underset{\sim}{v}')}{\partial \underset{\sim}{v}'} \right] \cdot \left[(1 - \frac{\underset{\sim}{k}\cdot\underset{\sim}{v}'}{\omega}) \underset{\approx}{1} + \frac{\underset{\sim}{k}\underset{\sim}{v}'}{\omega} \right]$$

$$\exp\left[-i\phi(\tau) \right]$$

with $\omega_{p\sigma}^2 = \dfrac{4\pi q_\sigma^2 n_\sigma}{m_\alpha}$, the plasma frequency (12)

Before carrying out the integrations, we choose the orientation of the vector $\underset{\sim}{k}$, without losing any generalities, on the x-z plane as shown in fig. 23, then

$$\underset{\sim}{k} = k_\perp \hat{x} + k_\parallel \hat{z} \tag{13}$$

Assume the distribution function f_o is Maxwellian for each species σ as,

$$f_o(\underset{\sim}{v}) = f_o(v_\perp, v_\parallel) = \left(\frac{m}{2\pi T}\right)^{3/2} \exp\left[-\frac{v_\perp^2 + v_\parallel^2}{2(T/m)} \right] \tag{14}$$

Omitting the algebraic calculation, we find

$$\underset{\approx}{\varepsilon}(\underset{\sim}{k},\omega) = \underset{\approx}{1} - \sum_{\sigma} \frac{\omega_{p\sigma}^2}{\omega^2} \left\{ \sum_{n=-\infty}^{\infty} \frac{z_o^\sigma}{z_n^\sigma} \underset{\approx}{\pi}(\beta_\sigma, z_n^\sigma; n) \left[1 - W(z_n^\sigma) \right] - z_o^{\sigma 2} \hat{z}\hat{z} \right\} \tag{15}$$

where

$$\underset{\approx}{\pi}(\beta_\sigma, z_n^\sigma; n) = \begin{bmatrix} \dfrac{n^2}{\beta_\sigma} \Lambda_n(\beta_\sigma) & in\,\Lambda_n'(\beta_\sigma) & \dfrac{k_\parallel}{|k_\parallel|} \dfrac{n}{\sqrt{\beta}} z_n^\sigma \Lambda_n(\beta_\sigma) \\ -in\,\Lambda_n'(\beta_\sigma) & \dfrac{n^2}{\beta_\sigma} \Lambda_n(\beta_\sigma) - 2\beta_\sigma \Lambda_n'(\beta_\sigma) & -i \dfrac{k_\parallel}{|k_\parallel|} \sqrt{\beta_\sigma} z_n^\sigma \Lambda_n'(\beta_\sigma) \\ \dfrac{k_\parallel}{|k_\parallel|} \dfrac{n}{\sqrt{\beta_\sigma}} z_n^\sigma \Lambda_n(\beta_\sigma) & i \dfrac{k_\parallel}{|k_\parallel|} \sqrt{\beta_\sigma} z_n^\sigma \Lambda_n'(\beta_\sigma) & z_n^{\sigma 2} \Lambda_n(\beta_\sigma) \end{bmatrix}$$

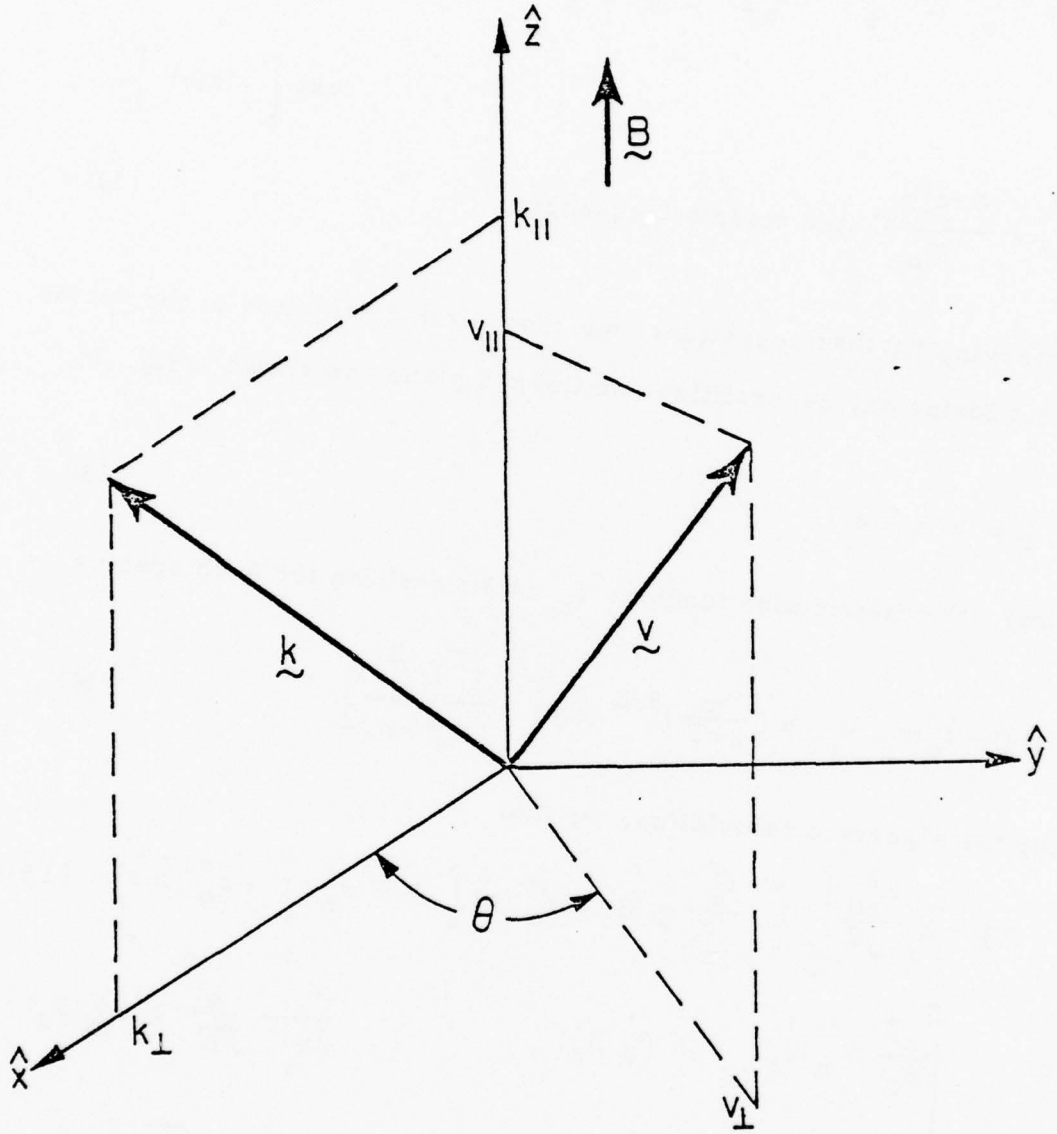

FIG. 23: CONFIGURATION OF VECTORS WITH RESPECT TO STATIC MAGNETIC FIELD B ORIENTED ALONG $\hat{z}$

$$\underset{\approx}{1} = \begin{pmatrix} 1 & 0 & 0 \\ 0 & 1 & 0 \\ 0 & 0 & 1 \end{pmatrix} \quad , \quad \text{the unit tensor} \ .$$

$$z_n^\sigma = \frac{\omega - n\Omega_\sigma}{|k_{||}|(T_\sigma/m_\sigma)^{1/2}} \ , \ \beta_\sigma = \frac{k_\perp^2 T_\sigma}{m_\sigma \Omega_\sigma^2} \quad , \quad \Lambda_n(\beta_\sigma) = I_n(\beta_\sigma) \exp(-\beta_\sigma)$$

where I_n is the modified Bessel function of the n^{th} order

$$W(z) = \frac{1}{\sqrt{2\pi}} \int_{\bar{c}} \frac{x}{x-z} \exp\left(-\frac{x^2}{2}\right) dx \ .$$

where $\bar{c}$ is the integration contour, which is deformed in such a way that point z is always above the path of integration.

From the dielectric tensor $\underset{\approx}{\epsilon}(\underset{\sim}{k}, \omega)$, we can now obtain the dielectric response function, $\epsilon_L(k, \omega)$ which gives us the longitudinal properties of the plasma, and the dispersion relation of longitudinal modes

$$\epsilon_L(\underset{\sim}{k},\omega) = \frac{\underset{\sim}{k} \cdot \underset{\approx}{\epsilon}(\underset{\sim}{k},\omega) \cdot \underset{\sim}{k}}{k^2} = 1 + \sum_\sigma \frac{k_{D\sigma}^2}{k^2} \left\{ 1 + \sum_n \frac{\omega}{\omega - n\Omega_\sigma} \left[W\left(\frac{\omega - n\Omega_\sigma}{|k_{||}| \left(\frac{T_\sigma}{m_\sigma}\right)^{\frac{1}{2}}} \right) - 1 \right] \Lambda_n(\beta_\sigma) \right\} \tag{16}$$

$$\det \left| \underset{\approx}{\epsilon} - \left(\frac{kc}{\omega}\right)^2 \underset{\approx}{1}_T \right| = 0 \ . \tag{17}$$

From the dispersion relation, we can now consider waves propagating perpendicular to the magnetic field. For this case, $k_{||} = 0$ and $k_\perp \neq 0$, and using the same configuration as given in Fig. 23 , the dielectric tensor is written in the following form:

$$\underset{\approx}{\epsilon}_1(\underset{\sim}{k},\omega) = \begin{pmatrix} \epsilon_1 & -i\epsilon_x & 0 \\ i\epsilon_x & \epsilon_2 & 0 \\ 0 & 0 & \epsilon_3 \end{pmatrix} \tag{18}$$

where

$$\epsilon_1(k,\omega) = 1 - \sum_\sigma \frac{k_{D\sigma}^2}{k^2} \sum_n \frac{(n\Omega_\sigma)^2}{\omega(\omega - n\Omega_\sigma)} \Lambda_n(\beta_\sigma) \tag{19.a}$$

$$\epsilon_2(k,\omega) = 1 - \sum_\sigma \frac{k_{D\sigma}^2}{k^2} \sum_n \frac{(n\Omega_\sigma)^2}{\omega(\omega - n\Omega_\sigma)} \left[\Lambda_n(\beta_\sigma) - \frac{2\beta_\sigma^2}{n^2} \Lambda_n'(\beta_\sigma) \right] \tag{19.b}$$

$$\epsilon_3(k,\omega) = 1 - \sum_\sigma \frac{\omega_{p\sigma}^2}{\omega^2} \sum_n \frac{\omega}{\omega - n\Omega_\sigma} \Lambda_n(\beta_\sigma) \tag{19.c}$$

$$\epsilon_x(k,\omega) = \sum_\sigma \frac{\omega_{p\sigma}^2}{\omega^2} \sum_n \frac{\omega}{\omega - n\Omega} n\Lambda_n'(\beta_\sigma) \tag{19.d}$$

Substituting the result for $\underset{\sim}{\epsilon}(\underset{\sim}{k}, \omega)$ into eq. 17, we obtain two equations:

$$\text{A)} \quad \left(\frac{kc}{\omega}\right)^2 = \epsilon_3 \tag{20}$$

This coresponds to the ordinary mode, with polarization (transverse mode)

$$E_z \neq 0 \quad \text{and} \quad E_x = E_y = 0$$

$$\text{B)} \quad \left(\frac{kc}{\omega}\right)^2 = \frac{\epsilon_1\epsilon_2 - \epsilon_x^2}{\epsilon_1} \tag{21}$$

This is the extraordinary mode, with polarization (hybrid mode).

$$E_z = 0 \qquad \frac{E_x}{E_y} = i\,\frac{\epsilon_2 - \left(\frac{kc}{\omega}\right)^2}{\epsilon_x} \tag{22}$$

From eq. 21 and eq. 22, we note the following:

1) as $k \to \infty$, $\epsilon_1 \to 0$ or $E_y \to 0$

Therefore, in the limit of large k, we have the E_x component only, or purely longitudinal mode as the direction of propagation $\underset{\sim}{k} = k\hat{x}$.

2) as $k \to 0$, we have, from eq. 19 $\epsilon_1 = \epsilon_2$, and from eq. 21, $\epsilon_1 = \pm \epsilon_x$ or $\frac{E_x}{E_y} = \pm i$, the wave becomes right or left hand circularly polarized.

Examining the individual cases in greater detail:

B1 - * For $k \to \infty$, or $\epsilon_1 = 0$ *

a) for high frequency case, neglecting the ion terms,

$$\epsilon_1 = 1 - \frac{k_{De}^2}{k^2} \sum_n \frac{(n\Omega_e)^2}{\omega(\omega - n\Omega_e)} \Lambda_n(\beta_e) = 0 \qquad (23)$$

Assuming also that we have strong magnetic field and cold plasma, i.e.,

$$\beta_e = \frac{k_\perp^2 T_e}{m\Omega_e^2} << 1 ,$$

* In the frequency range of $\Omega_e < \omega < 2\Omega_e$

eq. 23 becomes $$1 - \frac{k_{De}^2}{k^2} \frac{\omega\Omega_e^2}{\omega(\omega - \Omega_e^2)} 2\Lambda_1(\beta_e) = 0$$

since $$2\Lambda_1(\beta_e) \sim \beta_e = \frac{k^2 T_e}{m\Omega_e} = \frac{k^2}{k_{De}^2} \frac{\omega_{pe}^2}{\Omega_e^2}$$

we obtain further approximation of $1 - \frac{k_{De}^2}{k^2} \frac{\frac{k^2}{k_{De}^2}\omega_{pe}^2}{\omega^2 - \Omega_e^2} = 0$.

Or finally, we have

Upper Hybrid Resonance: $$\omega^2 = \Omega_e^2 + \omega_{pe}^2 \qquad (24)$$

* In the frequency range of $\omega = n|\Omega_e|(1+\Delta n)$, $n \geq 2$. eq. 23 becomes

$$1 - \frac{k_{De}^2}{k^2} \frac{\omega\Omega_e^2 2\Lambda_1(\beta_e)}{\omega(\omega^2 - \Omega_e^2)} - \frac{k_{De}^2}{k^2} \cdot \frac{(n\Omega_e)^2 \Lambda_n(\beta_e)}{(n\Omega_e)^2 \Delta n} = 0$$

or $$1 - \frac{\omega_{pe}^2}{\omega^2 - \Omega_e^2} - \frac{k_{De}^2}{k^2}\frac{\Lambda_n}{\Delta n} = 0$$

solving for $$\Delta n = \frac{k_{De}^2 \Lambda_n}{k^2\left[1 - \frac{\omega_{pe}^2}{(n^2-1)\Omega_e^2}\right]} << 1 \quad .$$

And for warm plasma, as $k \to \infty$, $\beta_e >> 1$ are $k^2 >> k_{De}^2$

eq. 23 becomes: $$1 - \frac{k_{De}^2}{k^2}\frac{(n\Omega_e)^2\Lambda_n}{(n\Omega_e)^2\Delta n} \simeq 0$$

or, again, $$\Delta n = \frac{k_{De}^2 \Lambda_n(\beta_e)}{k^2} << 1 \qquad (25.a)$$

Thus, knowing $\Delta n << 1$, we have

Bernstein modes: $$\omega = n|\Omega_e|(1 + \Delta n) . \qquad (25.b)$$

b) for low frequency case, no longer rejecting the ion terms, we have,

for $\Omega_i < \omega < \Omega_e$,

from eq. 23

$$1 - \frac{k_{De}^2}{k^2}\sum_n \frac{(n\Omega_e)^2 \Lambda_n(\beta_e)}{\omega(\omega - n\Omega_e)} - \frac{k_{Di}^2}{k^2}\sum_n \frac{(n\Omega_i)^2\Lambda_n(\beta_i)}{\omega(\omega - n\Omega_i)} = 0$$

Since $\omega << \Omega_e$, and $\beta_i << 1$ for cold ions, we have

$$\sum_n \frac{(n\Omega_e)^2 \Lambda_n(\beta_e)}{\omega(\omega - n\Omega_e)} \sim -\beta_e \ .$$

and $$2\Lambda_1(\beta_i) \sim \beta_i$$

Then, the equation can be further reduced to

$$1 + \frac{\omega_{pe}^2}{\Omega_e^2} - \frac{k_{Di}^2}{k^2} \quad \frac{\omega(\Omega_i)^2 \beta_i}{\omega(\omega^2 - \Omega_i^2)} = 0$$

or

$$1 + \frac{\omega_{pe}^2}{\Omega_e^2} - \frac{\omega_{pi}^2}{\omega^2 - \Omega_i^2} = 0$$

Solving for ω :

$$\omega^2 = \Omega_i^2 + \frac{\omega_{pi}^2}{1 + \frac{\omega_{pe}^2}{\Omega_e^2}} = \Omega_e \Omega_i \frac{\omega_{pe}^2 + \Omega_e \Omega_i}{\Omega_e^2 + \omega_{pe}^2} \qquad (26)$$

which corresponds to Lower Hybrid Resonance

B2-* for $k \to 0$, or $\epsilon_1 = \pm \epsilon_x$

Considering only high frequency modes, thus rejecting ion terms,

case a) for $\epsilon_1 = - \epsilon_x$, right handed circularly polarized waves, using eq. 19, we obtain

$$1 - \frac{k_{De}^2}{k^2} \sum_n \frac{(n\Omega_e)^2}{\omega(\omega - n\Omega_e)} \Lambda_n(\beta_e) = - \frac{\omega_{pe}^2}{\omega^2} \sum_n \frac{\omega}{\omega - n\Omega_e} n\Lambda'_n(\beta_e) \qquad (27)$$

As $k \to 0$, $\beta_e << 1$, setting $\omega = n|\Omega_e|(1+\Delta n)$, where $\Delta n << 1$ (28)

For $n = 1$, values substituted into eq. 27 would give $\Delta \cong \frac{\omega_{pe}^2}{\Omega_e^2}$, then conditions set on eq. 28 would not hold, therefore n cannot be 1 .

For $n \geq 2$, $\omega = n|\Omega_e|(1 + \Delta n)$, and $\Delta n << 1$ eq. 24 yields

$$1 - \frac{\omega_{pe}^2}{\omega^2 - \Omega_e^2} - \frac{k_{De}^2}{k^2} \frac{|n\Omega_e|^2 \Lambda_n}{|n\Omega_e|^2 \Delta n} = - \frac{\omega_{pe}^2}{\omega^2} \frac{\omega\Omega_e}{\omega^2 - \Omega_e^2} + \frac{\omega_{pe}^2}{\omega^2} \frac{n\omega\Lambda'_n}{|n\Omega_e| \Delta n} \qquad (29)$$

After some simplification, we obtain

$$1 - \frac{\omega_{pe}^2}{n(n-1)\Omega_e^2} = \frac{1}{\Delta n}\left[\frac{k_{pe}^2}{k^2}\Lambda_n + \frac{\omega_{pe}^2}{n\Omega_2^2}\Lambda'_n\right]$$

$$= \frac{1}{\Delta n}\left[\frac{k_{pe}^2}{k^2}\left(\frac{\beta_e}{n}\Lambda_{n-1} - \frac{\beta_e\Lambda_n}{n}\right)\right]$$

$$\approx \frac{1}{\Delta n}\left[\frac{\omega_{pe}^2}{n\Lambda_e^2}\Lambda_{n-1}\right]$$

Solving for Δn

$$\Delta n = \frac{\omega_{pe}^2}{n\Omega_e^2}\Lambda_{n-1}(\beta_e)\ \frac{1}{1 - \frac{\omega_{pe}^2}{n(n-1)\Omega_e^2}} << 1 \qquad (30.a)$$

and

we have $\omega = n|\Omega_e|\,(1+\Delta n)$ for $n \geq 2$ (30.b)

It is of interest to point out that equation 30.a, for given plasma frequency, Δ_n changes sign from - to +, which is important when we plot the dispersion curve later in this section.

case b) for $\epsilon_1 = \epsilon_x$, left handed circularly polarized waves.

Similar to previous case, the same development is followed, and we obtain

$$\omega = n|\Omega_e|(1+\Delta n) \qquad \text{for } n \geq 2 \qquad (31.a)$$

and

$$\Delta n = \frac{\omega_{pe}^2}{n\Omega_e^2}\ \frac{\Lambda_n(\beta_e)}{1 - \frac{\omega_{pe}^2}{n(n+1)\Omega_e^2}} \qquad (31.b)$$

with Δn always > 0.

Now, we turn to equation 16, and consider the range of frequency as

$\Omega_i < \omega << \Omega_e$, and these range of values

$$\frac{\omega}{|k_{\parallel}|\sqrt{\frac{T_e}{m_e}}} << 1 , \qquad \frac{\omega}{|k_{\parallel}|\sqrt{\frac{T_i}{m_i}}} >> 1 .$$

and $$\frac{\omega - n\Omega_\sigma}{|k_{\parallel}|\sqrt{\frac{T_\sigma}{m_\sigma}}} >> 1 \qquad \text{for} \quad \neq 0$$

$\beta_e << 1$ and $\beta_i << 1$

$$W\left(\frac{\omega}{|k_{\parallel}|\sqrt{\frac{T_e}{m_e}}}\right) \sim 1 \quad \text{and} \quad W\left(\frac{\omega - n\Omega_\sigma}{k_{\parallel}|\sqrt{\frac{T_\sigma}{n_\sigma}}}\right) \approx 0 \text{ for } n \neq 0 .$$

Using these values in eq. 16, we obtain:

$$\epsilon_L(k,\omega) = 1 + \frac{k_{De}^2}{k^2} - \frac{k_{Di}^2}{k^2}\left[\sum_n \frac{n\Omega_i}{\omega - n\Omega_i}\Lambda_n(\quad_i)\right] = 0 \tag{32}$$

$$1 + \frac{k_{De}^2}{k^2} - \frac{k_{Di}^2}{k^2}\,\frac{k^2 T_{i/mi}}{\omega^2 - \Omega_i^2} = 0$$

which finally leads to

$$\omega^2 = \Omega_i^2 + \frac{k^2 T_{e/Mi}}{1 + k^2/k_{De}^2} \tag{33}$$

This is the electrostatic ion cyclotron mode.

Summarizing these results obtained in this section, we have derived from the dielectric tensor $\underset{\sim}{\epsilon}(\underset{\sim}{k}, \omega)$, the dispersion relation. From the

range of frequency and direction of propagation of interest to us , we obtained the expression for the modes which are involved in our parametric experiment, namely,

As $k \rightarrow \infty$

Upper hybrid modes, from eq. 24: $\omega^2 = \Omega_e^2 + \omega p_e^2$,

Bernstein Modes, from eq. 25. b: $\omega = n|\Omega_e|(1 + \Delta n)$ where, from eq. 25. a:

$$\Delta n \cong \frac{k_{De}^2 \Lambda_n(\beta_e)}{k^2} << 1$$

Lower hybrid modes, from eq. 26: $\omega^2 = \Omega_i^2 + \dfrac{\omega_{pi}^2}{1+\dfrac{\omega_{pe}^2}{\Omega_e^2}} = \Omega_e \Omega_i \dfrac{\omega_{pe}^2 + \Omega_e \Omega_i}{\Omega_e^2 + \omega_{pe}^2}$

As $k \rightarrow 0$

Right handed circularly polarized waves, from eq. 30. b

$\omega = n|\Omega_e|(1+\Delta n)$, $n \geq 2$

where, from eq. 30. a: $\Delta n = \dfrac{\omega_{pe}^2}{n\Omega_e^2} \Lambda_{n-1}(\beta_e) \dfrac{1}{1 - \dfrac{\omega_{pe}^2}{n(n-1)\Omega_e^2}} << 1$

Left handed circularly polarized waves, from eq. 31,

$\omega = n|\Omega_e|(1 + \Delta n)$ for $n \geq 2$

where, from 31. b: $\Delta n = \dfrac{\omega_{pe}^2}{n\Omega_e^2} \dfrac{\Lambda_n(\beta_e)}{1 - \dfrac{\omega_{pe}^2}{n(n+1)\Omega_e^2}}$

and Electrostatic ion cyclotron mode, from eq. 33,

$$\omega^2 = \Omega_i^2 + \frac{k^2 Te/Mi}{1 + k^2/k_{De}^2}$$

The dispersion relations of the modes we have just derived are plotted in fig. 24. In our experimental set-up, the electron cyclotron frequency Ω_e, for B_o = 1088 Gauss, is 3.05 GHz; the microwave pump and the high frequency instability with frequencies around 9.2 GHz, are very close to the third harmonic of the electron cyclotron wave. Using the electrostatic ion cyclotron dispersion relation (33) and the experimentally observed parameters, such as instability frequency of 260 KHz and electron temperature of 2 eV, we obtain a value of 7.5/cm for the wavenumber of the electrostatic ion cyclotron wave. These values and others have been tabulated in Table 1(page150).

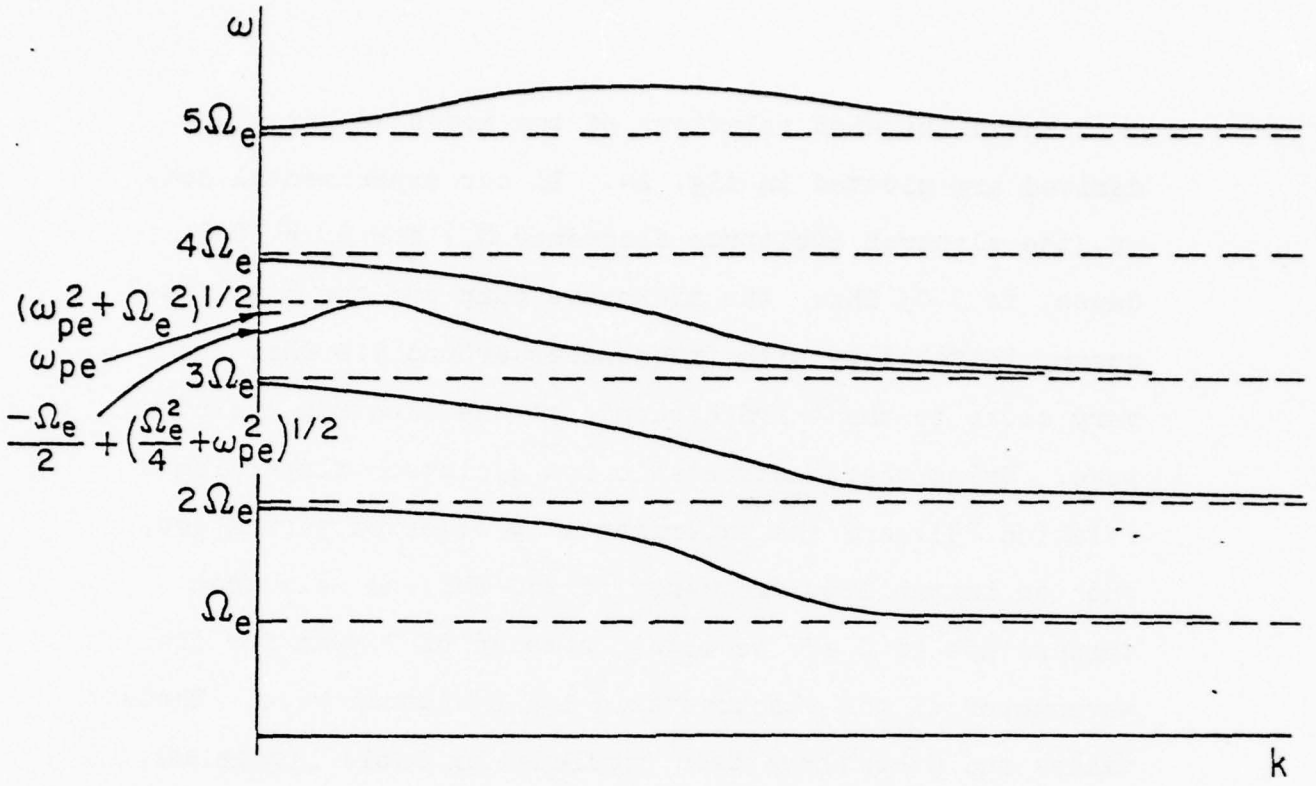

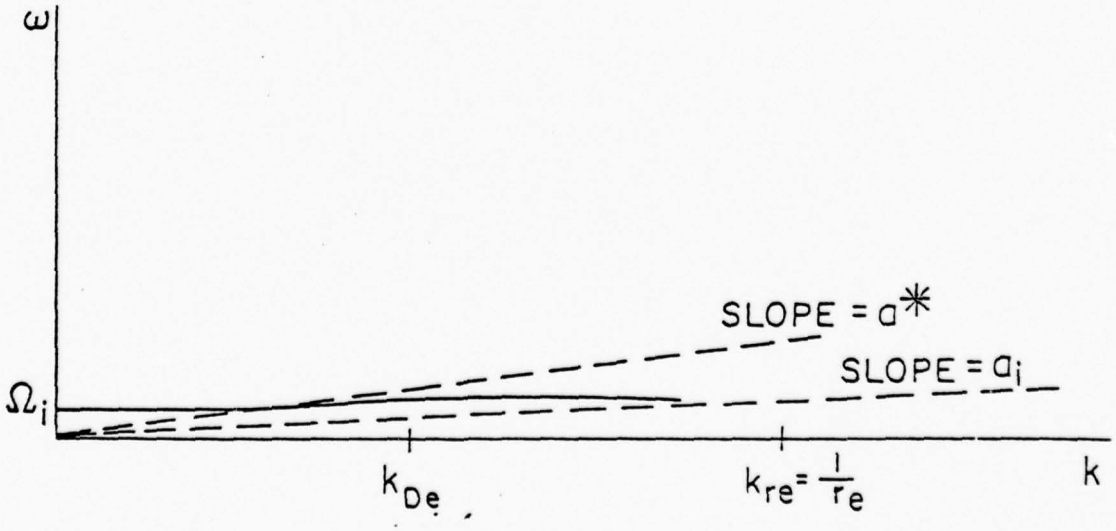

FIG. 24: DISPERSION DIAGRAM FOR MAGNETO-PLASMA FROM KINETIC MODEL

IV-5. SUMMARY AND CONCLUSIONS

We have described an experiement in which microwave induced parametric decay instabilities have been investigated. Although parametric theories predict the excitation of decay instabilities with a sufficiently large pump which can supply enough energy to the coupled waves to overcome their natural damping, it has been found experimentally this is not an easy task. In the Polytechnic Hollow Cathode Discharge device, there are many variables that must be adjusted to their proper values for the interaction to take place. However, once this is achieved; the parametric excitation takes place, and various characteristics of the interaction have been observed. Employing a fast pin diode modulator to switch the microwave pump from one fixed level above the threshold to one below, the decay process of the electrostatic ion cyclotron wave is studied. Continually increasing the variable pump level until it exceeds the threshold value, the instability no longer decays into noise but to a definite steady state amplitude. This not only illustrated the existence of the threshold power level, which is an important characteristic of the parametric process, it also demonstrated a linear dependence of the decay or growth rate with the pump power. A phenomenological model, which incorporates all the observed features of the wave evolution including saturation, is used to interpret

the data.

From the plot of $y = C_1P - C_2$, the threshold power level has been accurately found, and also the linear damping term evaluated. This experimentally obtained natural damping frequency, compared to the values of the possible collisions that can cause the damping of the electrostatic ion cyclotron wave, is found to be close to the ion-neutral collision frequency, thus indicating the dominant decay process is due to charge transfer. An important finding of the present research is the saturation mechanism of the wave. Using the phenomenlogical model and the experimentally obtained values of the saturated amplitude as a function of power, we have found the nonlinear term is proportional to the square of the wave amplitude. Plausible mechanisms include the harmonic generation. But comparison of the value from experimental observations to the theoretically calculated value excludes the harmonic generation process as the cause for the saturation process. Another mechanism which also corresponds to the $n = 2$ case, i.e., saturation term proportional to the square of the amplitude, and turns out to be the dominant saturation phenomenon in our experiment, is the anomalous diffusion.

Areas possible for future investigations as a continuation of the present effort are several. First ion and electron temperature measurements must be done carefully as ion

heating due to parametric interaction is a desirable result. The measurement of the wave number k is still to be done. With this, the k-matching condition can be checked. The HCD device has built-in capabilities of mixing and feeding other gases. Changing to a different gas to recheck our findings is also a possibility. From the present mode of operation, the plasma has been switched to become a microwave induced system, this has also showed promise because a less noisier plasma is attained. Some work has already been done as an extension to the present research.

REFERENCES

1. H.W. Hendel and J.T. Flick, Phys. Rev. Lett. 31, 199 (1973).

2. R.B. White, C.S. Liu and M.N. Rosenbluth, Phys. Rev. Lett. 31, 520 (1973).

3. C.S. Liu, M.N. Rosenbluth and R.B. White, Phys. Fluids 17, 1211 (1974).

4. B. Grek and M. Porkolab, Phys. Rev. Lett. 30, 836 (1973).

5. P. Kaw and J.M. Dawson, Phys. Fluids 12, 2586 (1969).

6. M. Porkolab, Physica 82C, 86-110 (1976), N. Holland Pub. Co.

7. K. Nishikawa, J. Phys. Soc. Japan 24, 916 (1968).

8. K. Nishikawa, J. Phys. Soc. Japan 24, 1152 (1968).

9. D.F. Dubois and M.V. Goldman, Phys. Rev. Lett. 14, 544 (1965).

10. D.F. Dubois and M.V. Goldman, Phys. Rev. Lett. 164, 207 (1967).

11. Y.C. Lee and C.H. Su, Phys. Rev. 152, 129 (1966).

12. Y.M. Aliev, V.P. Silin and C. Watson, Sov. Phys. JETP 28, 626 (1966).

13. M. Porkolab, Nuclear Fusion 12, 329 (1972).

14. S.P. Kuo, "Studies of Parametric Decay Instabilities in Magneto Plasmas," PH.D. Thesis, PINY, June 1977.

15. R.A. Stern and N. Tzoar, Phys. Rev. Lett. 17, 903 (1966).

16. R. Stenzel and A.Y. Wong, Phys. Rev. Lett. 28, 274 (1972).

17. M.M. Widner, H.C.S. Hsuan and K.E. Lonngren, Phys. Lett. 26A, 553 (1968).

18. S. Ikezawa and T. Okuda, App. Phys. Lett. 21, 205 (1972).

19. L.A. Klein, B.R. Cheo and R.A. Stern, J. App. Phys. 45, 5218 (1974).

20. E.S. Cassedy and P. Mulser, Phys. Rev. 10, 2349 (1974).

21. T.H. Stix, "Theory of Plasma Waves," McGraw Hill.

22. N. Marcuvitz, "Plasma Dynamics Class Notes," NYU, Unpublished.

23. F.F. Chen, "Introduction to Plasma Physics," Nostrand.

24. S. Ichimaru, "Basic Principles of Plasma Physics," Benjamin.

25. S. Hiroe and H. Ikegami, Phys. Rev. Lett. 19, 1414 (1967).

26. B. Grek and M. Porkolab, Phys. Rev. Lett. 30, 836 (1973).

27. R.P.H. Chang, M. Porkolab and B. Grek, Phys. Rev. Lett. 28, 206 (1972).

28. M. Okabayashi, K. Chen and M. Porkolab, Phys. Rev. Lett. 31, 1113 (1973).

29. R.P.H. Chang and M. Porkolab, Phys. Rev. Lett. 32, 1227 (1974).

30. V.I. Farenik, V.V. Vlasov and A.M. Rozhkov, Sov. Phys. JETP 18, 240 (1973).

31. R.P.H. Chang and M. Porkolab, Phys. Rev. Lett. 31, 1241 (1973).

32. T.K. Chu, S. Bernabei and R.W. Motley, Phys. Rev. Lett. 31, 211 (1973).

33. R.N. Franklin, S.M. Hamberger, G. Lampis and G.J. Smith, Phys. Rev. Lett. 27, 1119 (1971).

34. M. Porkolab, V. Arunasalam and A.A. Ellis, Jr., Phys. Rev. Lett. 29, 1438 (1972).

35. K.C. Huang, "An Investigation of Charged Particle Loss Process in an Arc Plasma," PH.D. Thesis, PIB (1971).

36. K.C. Huang and K. Chung, Phys. Fluids 16, 1245 (1973).

37. R. Kristal, "Instability and Dynamic Suppression in a Magneto Plasma," PH.D. Thesis, PIB, June 1973.

38. "The Microwave Engineer's Handbook," 1965.

39. E.O. Johnson and L. Malter, Phys. Rev. 80, 58 (1950).

40. R.H. Huddlestone and S.L. Leonard, "Plasma Diagnostic Techniques," Academic Press, 1965.

41. J.D. Swift and M.J.R. Schwar, "Electrical Probes for Plasma Diagnostics," American Elsevier, 1969.

42. L.A. Klein, "Experimental Investigations of the Growth and Decay of Parametrically Excited Ion Acoustic Waves," PH.D. Thesis, NYU, 1973.

43. J.C. Woo and D.J. Rose, Phys. Fluids 10, 893 (1967).

44. G. Van Hoven, Phys. Rev. A3, 153 (1971).

45. B. Bezzerides and J. Weinstock, Phys. Rev. Lett. 28, 481 (1972).

46. A.M. Sleeper, J. Weinstock, and B. Bezzerides, Bull. Am. Phys. Soc., Ser. II, 17, 976 (1972).

47. J. Weinstock and B. Bezzerides, Bull. Am. Phys. Soc., Ser. II, 17, 1016 (1972).

48. S. Brown, "Basic Data of Plasma Physics," Wiley & Sons, 1959.

49. D. Rose and M. Clark, "Plasmas and Controlled Fusion," MIT Press, 1961.

50. D. Baldwin, et. al., "Kinetic Theory of Plasma Waves in a Magnetic Field," in Advances in Plasma Physics, vol. 3, Interscience, 1969.

V
Parametric Excitation of Coupled Plasma Waves

LIST OF FIGURES

		Page
1.	Schematic Diagram of PINY HCD System	265
2.	Simplified Block Diagram of Experimental Apparatus	267
3.	Frequency Spectrum of Electrostatic Ion Cyclotron Wave	268
4.	Time Domain Behavior of Electrostatic Ion Cyclotron Wave	268
5.	Growth and Decay of Electrostatic Ion Cyclotron Waves as a Function of Pump Power	270
6.	Decay and Growth of Electrostatic Ion Cyclotron Wave From One Steady State Amplitude into Another	273
7.	Photograph Shows that There is a Transition Period Before Wave Really Starts to Grow	273
8.	Average Decay Rate of Electrostatic Ion Cyclotron Wave as a Function of Power P_2 with P_1=173 W Fixed	275
9.	Initial Growth Rate of Electrostatic Ion Cyclotron Wave From One Steady State Amplitude to Another as a Function of Power P_2. P_1=173 W, p=1.2μ, f_o=9.23 GHz	276
10.	Decay of Electrostatic Ion Cyclotron Wave from Steady State Amplitude into Noise for Pump Power Just Below Threshold Level.	277
11.	Growth and Decay of Electrostatic Ion Cyclotron Wave for P_1=173 W and P_2=0 W	279
12.	Frequency of Electrostatic Ion Cyclotron Wave as a Function of Pump Power	283
13.	Measured Electrostatic Ion Cyclotron Frequency Shift as a Function of Electron Temperature Change	284
14.	Plasma Density as a Function of Pump Power	284
15.	Square of the Saturated Amplitude of the Electrostatic Ion Cyclotron Wave as a Function of Pump Power for Power Above Threshold	289

LIST OF TABLES

		Page
1.	Experimental and Theoretical Data in Several Pump Power Levels	282
2.	Experimental Parameters	285

V-1. INTRODUCTION

Plasma parametric instabilities occur when the pump amplitude exceeds a threshold which depends on the set of coupled modes and on their damping effects. It has become of special interest following the recognition that such processes play important roles in the absorption of electromagnetic power[1]. Experimental results showed that parametric instabilities may form a channel for efficient transfer of electromagnetic energy into a rather large size hot plasma, and the nonlinear effects of these instabilities may introduce a mechanism which heats plasma more efficiently than classical collisional absorption[2]. Therefore, most of the experimental effort has been expended on observing the plasma heating rates. Besides plasma heating, theoretical and experimental studies of parametric decay instabilities will also yield information about the linear and nonlinear damping rates of the instabilities, and the development of plasma turbulence. In the previous report[3], a detailed experimental study of the dynamics of the process had been given. Klein and Cheo[3,24] introduce a technique for experimentally determining growth and decay characteristics of parametrically excited plasma waves. They found that the dominate linear damping mechanism of the ion acoustic wave in their plasma is due to ionization collisions, not due to ion-neutral collisions which is the usual phenomenon. Theirs is a unmagnetized plasma, while this effort is the continuation of their experimental study into a magnetoplasma. Therefore, different modes are involved. Since there are no available theories for our experiment, a general theory is also developed by using system total Hamiltonian approach to deal with the problem. Comparison with our experiment has also been made.

Indeed, the detailed ways of implementation of the ideas of parametric decay instabilities to plasma heating is still developing. Grek and Porkolab[2],

Porkolab et al.[4], and Okabayashi[5] et al. had performed experiments by shining microwave power onto a plasma column in the extraordinary mode of propagation in the region of the upper hybrid frequency. Wavelength measurements of the decay waves showed decay into upper hybrid waves (and Bernstein waves) and lower hybrid and/or ion acoustic waves. It was shown that significant ion and electron heating occurred only above threshold for parametric instabilities. There were also several experiments[6, 7, 8] performed in the regime of lower hybrid frequency which showed parametric decay into lower hybrid waves and ion acoustic waves, ion cyclotron waves, ion quasi modes, or drift waves may occur. Again, strong plasma heating was observed above threshold for parametric instabilities (both ion and electrons). Experimental technique to observe the plasma heating rates is by using a multigrid energy analyzer to measure the modified electron and ion distribution function. Another technique is also developing by switching the pump power between two levels and using the Fabry-Perot interferometer to measure the ion temperature growth rate.

In the parametric process, the incident pump wave is couples to two or more natural modes of the plasma by satisfying both conservation of frequency and conservation of wave vector relations. The frequency mixing allows energy supplied to the system at one frequency to be converted to another. The physical origin of mode coupling mechanism is fairly easy to understand on a qualitative basis. From linear wave analyses, the dielectric tensor of the plasma is density dependent. Hence it will be modulated by the presence of the vibrational modes of the plasma, resulting in a mixing action such that the input radiation and vibrational modes beat together to produce sum and difference frequencies. These in turn may act as sources for parametric excitations if the frequency and wave vector matching conditions

are satisfied.

By assuming $\exp(-i\omega t)$ time behavior for the mode of interest, decay or growth of the mode will be decided by the dispersion relation of the system. Therefore, most of the theoretical investigations are directed toward finding the modified dispersion relations with the presence of a pump wave in the system. The first work is done by Silin.[9] His theory is largely based on the hydrodynamic equations for a cold plasma. DuBois and Goldman[10] analyze the parametric coupling of Langmuir and ion-acoustic oscillations based on a Green's function perturbative method (harmonic approximation), which is restricted to the case when the radiation-induced energy of the particles is small compared to their thermal energy. They showed that the plasma can be unstable to certain applied frequencies for pump power above a threshold, a characteristic of parametric excitation. Later, Nishikawa,[11] and Lee and Su[12] used hydrodynamic model and obtained same conclusions. However, in order to justify the harmonic approximation for greater intensities, Jackson[13] pointed out that it is important to estimate the range of frequencies which produces instabilities when the intensity is large.

Parametric coupling of electrostatic waves in a magnetized plasma have been treated by Aliev et al.,[14] by Amano and Okamoto,[15] and by Porkolab,[16, 17] and others. These authors used the linearized Vlasov equation with self consistent potential field, which can be solved easily after transformation to the oscillating frame of reference. Alieve et al. found the frequency range of a pump wave in which the plasma is unstable turns out to be much broader than in the case of a unmagnetized plasma. Amano and Okamoto extend the theory to inhomogeneous cases. Porkolab analyzed the resulting dispersion relation of Aliev et al. in the limit of

weak coupling, and obtained threshold powers to excite the upper and lower hybrid (or ion acoustic) modes simultaneously. He also introduced a new type of kinetic-dissipative instability. All of the above investigations are based on electrostatic approximation for the plasma modes and hence valid only for longitudinal waves. In the presence of a static magnetic field, most of the plasma modes become hybrid, and the electrostatic approximation holds only in the limiting case.

In this investigation a general formulation of the parametric coupling equations in a homogeneous magnetized plasma is developed by using Hamiltonian approach.[18] The coupling coefficients of the parametric equations are derived from the collisionless Boltzman-Vlasov equation. With transformation method and trajectory techniques, the induced polarization currents are derived. Applications to various forms of modal coupling are given, and comparison with experimental works is made whenever possible.

A set of experiments in the Poly HCD plasma was performed. A microwave horn is mounted at the end of the plasma beam. In order to obtain a quiescent plasma, a new technique to create an ultrastable microwave sustained plasma is introduced. When the pump signal, at 9.23 GHz, is above the threshold level, the second harmonics of the electron cyclotron wave and the electrostatic ion-cyclotron wave are simultaneously excited. The time evolution process of the electrostatic ion-cyclotron wave is studied by switching the microwave pump power from one level to another. Linear damping rate, initial growth rate, and the threshold power can be obtained.

In addition, the nonlinear saturation mechanisms observed in the experiment are discussed. An analysis by using the guiding center

technique [18] was made and it is established the nonlinear damping is due to the anomalous diffusion produced by the ponderamotive forces of the instabilities. Comparison with experiments is favorable.

V-2. GENERAL FORMULATION FOR THE PARAMETRIC EXCITATION

1. Overall Physical Features

It is well known that the vibrational modes of a medium will modulate the permittivity or polarizability of the medium. Assume that there exist two normal modes or waves, S and L (e.g., a phonon and a plasmon) in the medium with frequencies ω_s and ω_ℓ in the linear regime; then they will modulate the polarizability of the medium resulting from the density perturbation of the medium. The problem can be treated mathematically by expanding the electrostrictive polarizability α_{ij} in a Taylor's series in terms of normal mode vibrational field $\delta\underline{E}_s$ related to S and $\delta\underline{E}_\ell$ related to L

$$\therefore \alpha_{ij} = \alpha_{ij}^{o} + \left(\frac{\partial \alpha_{ij}}{\partial \delta E_{s\sigma}}\right)_o \delta E_{s\sigma} + \left(\frac{\partial \alpha_{ij}}{\partial \delta E_{\ell\sigma}}\right)_o \delta E_{\ell\sigma} \quad \text{where } i, j, \sigma = 1, 2, 3 \text{ or } x, y, z$$

where the Einstein summation convention is understood. Hence the total induced polarization due to the presence of a third wave field $\underline{E}$ is

$$P_i^t = \alpha_{ij} E_j = \left[\alpha_{ij}^{o} + \left(\frac{\partial \alpha_{ij}}{\partial \delta E_{s\sigma}}\right)_o \delta E_{s\sigma} + \left(\frac{\partial \alpha_{ij}}{\partial \delta E_{\ell\sigma}}\right)_o \delta E_{\ell\sigma}\right] E_j = P_i^{o} + \delta P_i + \delta \mathcal{P}_i$$

where $\delta P_i = \left(\frac{\partial \alpha_{ij}}{\partial \delta E_{s\sigma}}\right)_o \delta E_{s\sigma} E_j$ and $\delta \mathcal{P}_i = \left(\frac{\partial \alpha_{ij}}{\partial \delta E_{\ell\sigma}}\right)_o \delta E_{\ell\sigma} E_j$ are the induced polarization associated with the Raman and Brillouin effects. Here we have assumed $|\underline{E}| >> |\delta\underline{E}_s|$ and $|\underline{E}| >> |\delta\underline{E}_\ell|$.

2. Hamiltonian Approach

We first normalize both S and L waves. Assume the particles associated with S and L have reduced masses M and m, momentum K and $\mathcal{K}$, displacements Q and U respectively. The displacement and

momentum variables are the canonical conjugate pairs. Hence the unperturbed Hamiltonian density $H_{os}^{(k)}$ and $H_{o\ell}^{(k)}$ are

$$H_{os}^{(k)} = \frac{1}{2} \sum_{\sigma} \left[\frac{K_{\sigma}^{2}(\underline{k})}{M} + M\omega_{s}'^{2}(\underline{k})\, Q_{\sigma}^{2}(\underline{k}) \right] \tag{2.1}$$

$$H_{o\ell}^{(k)} = \frac{1}{2} \sum_{\sigma} \left[\frac{\mathcal{K}_{\sigma}^{2}(\underline{k})}{m} + m\omega_{\ell}'^{2}(\underline{k})\, U_{\sigma}^{2}(\underline{k}) \right] \tag{2.2}$$

where $\omega_{s}'(\underline{k})$ and $\omega_{\ell}'(\underline{k})$ are the resonant frequencies of the system without the pump field, and the field associated with the corresponding modes are

$$\delta\underline{E}_{s}(\underline{k}) = -\frac{M}{e} \frac{1}{\sqrt{n_o}}\, \omega_{s}^{2}(\underline{k})\, \underline{Q}(\underline{k}) - \frac{\Omega_i}{e\sqrt{n_o}}\, \underline{K}(\underline{k}) \times \hat{z} \tag{2.3}$$

$$\delta\underline{E}_{\ell}(\underline{k}) = \frac{m}{e} \frac{1}{\sqrt{n_o}}\, \omega_{\ell}^{2}(\underline{k})\, \underline{U}(\underline{k}) + \frac{\Omega_e}{e\sqrt{n_o}}\, \underline{\mathcal{K}}(\underline{k}) \times \hat{z} \tag{2.4}$$

where $\omega_{s}(\underline{k})$ and $\omega_{\ell}(\underline{k})$ are the resonant frequencies with the presence of pump field. n_o is the background electron (or ion) density. Ω_e and Ω_i are cyclotron frequencies of the two species including the sign of the charge. Here we also assume that a uniform magnetic field $B_o\hat{z}$ is applied, and the plasma is singly ionized. It is easy to show that the Poisson bracket relations hold:

$$\{ Q_{\sigma}(\underline{k}) \ , \ K_{\beta}(\underline{k}') \} = \delta(\underline{k}, \underline{k}')\, \delta_{\sigma\beta} \tag{2.5}$$

$$\{ U_{\sigma}(\underline{k}) \ , \ \mathcal{K}_{\beta}(\underline{k}') \} = \delta(\underline{k}, \underline{k}')\, \delta_{\sigma\beta} \tag{2.6}$$

The pump field is assumed to be spatially homogeneous (dipole approximation). Hence the induced polarizations corresponding to the frequency

components in question can be expressed as

$$\delta P_{si}^{(k)} = \left(\frac{\partial \alpha_{ij}}{\partial \delta E_{\ell\sigma}^{+}(\underline{k})}\right)_o \delta E_{\ell\sigma}^{+}(\underline{k})\, E_j^{-} + \text{c. c.} \tag{2.7}$$

$$\delta P_{\ell i}^{(k)} = \left(\frac{\partial \alpha_{ij}}{\partial \delta E_{s\sigma}^{-}(\underline{k})}\right)_o \delta E_{s\sigma}^{-}(\underline{k})\, E_j^{+} + \text{c. c.} \tag{2.8}$$

where the superscripts "$+$" denote respectively exp ($\pm i\omega t$). Then the interaction Hamiltonian densities for S and L are

$$H_s'^{(k)} = -\delta P_{si}^{(k)} \delta E_{si}(\underline{k}) = \delta P_{si}^{(k)} \left[\frac{M}{e} \frac{1}{\sqrt{n_o}} \omega_s^2(\underline{k}) Q_i(\underline{k}) + \frac{\Omega_i}{e\sqrt{n_o}} (\underline{K}(\underline{k}) x \hat{z})_i\right] \tag{2.9}$$

$$H_\ell'^{(k)} = -\delta P_{\ell i}^{(k)} \delta E_{\ell i}(\underline{k}) = -\delta P_{\ell i}^{(k)} \left[\frac{m}{e} \frac{1}{\sqrt{n_o}} \omega_\ell^2(\underline{k}) U_i(\underline{k}) + \frac{\Omega_e}{e\sqrt{n_o}} (\underline{\mathcal{K}}(\underline{k}) x \hat{z})_i\right] \tag{2.10}$$

The total Hamiltonian densities of the S and L are

$$H_s^{(k)} = H_{os}^{(k)} + H_s'^{(k)} \tag{2.11}$$

$$H_\ell^{(k)} = H_{o\ell}^{(k)} + H_\ell'^{(k)} \tag{2.12}$$

It is known in general that the equation of motion for any cononical variable A is

$$\left[\frac{d^2}{dt^2} + 2\Gamma \frac{d}{dt} + \Gamma^2\right] A = \{\{A, H\}, H\} \tag{2.13}$$

where $1/\Gamma$ is the phenomenological relaxation time, and H is the total Hamiltonian density. (2.13) together with (2.1) to (2.12) can be used to

derive the coupled mode equations:

Evaluation of the Poisson bracket $\{\{Q_i(\underline{k}),\ H_s^{(k)}\}\ ,\ H_s^{(k)}\}$ with the aid of (2.1), (2.5), (2.9) and (2.11) yields

$$\{\{Q_i(\underline{k}),\ H_s^{(k)}\}\ ,\ H_s^{(k)}\} = -\omega_s'^2(\underline{k})\, Q_i(\underline{k}) - \frac{\omega_s^2(k)}{e\sqrt{n_o}}\,\delta P_{si}^{(k)}$$

Therefore the appropriate equation of motion for $Q_i(\underline{k})$ is given by (2.13),

$$\ddot{Q}_i(\underline{k}) + 2\Gamma_s \dot{Q}_i(\underline{k}) + (\Gamma_s^2 + \omega_s'^2(\underline{k}))\, Q_i(\underline{k}) = -\frac{\omega_s^2(\underline{k})}{e\sqrt{n_o}}\,\delta P_{si}^{(k)} \tag{2.14}$$

with the dot denoting $\frac{d}{dt}$.

Similarly by evaluating $\{\{K_i(\underline{k})\ ,\ H_s^{(k)}\}\ ,\ H_s^{(k)}\}$ with the aid of (2.1), (2.5), (2.9) and (2.11) we have:

$$\{\{K_i(\underline{k})\ ,\ H_s^{(k)}\},\ H_s^{(k)}\} = -\omega_s'^2(\underline{k})K_i(\underline{k}) - M\omega_s'^2(\underline{k})\,\frac{\Omega_i}{e\sqrt{n_o}}\,(\hat{z}\times\delta\underline{P}_s^{(k)})_i$$

and

$$\ddot{K}_i(\underline{k}) + 2\Gamma_s \dot{K}_i(\underline{k}) + (\Gamma_s^2 + \omega_s'^2(\underline{k}))K_i(\underline{k}) = -M\omega_s'^2(\underline{k})\,\frac{\Omega_i}{e\sqrt{n_o}}\,(\hat{z}\times\delta\underline{P}_s^{(k)})_i \tag{2.15}$$

Equation of motion in the variable $\delta\underline{E}_s(\underline{k})$ can be obtained by combining (2.14) and (2.15) with the aid of the relation (2.3). The result is

$$\left[\frac{d^2}{dt^2} + 2\Gamma_s\frac{d}{dt} + (\Gamma_s^2 + \omega_s'^2(\underline{k}))\right]\delta\underline{E}_s(\underline{k}) = \frac{M\omega_s^4(\underline{k})}{n_o e^2}\,\delta\underline{P}_s^{(k)} + \frac{M\omega_s'^2(\underline{k})\Omega_i^2}{n_o e^2}\,(\hat{z}\times\delta\underline{P}_s^{(k)})\times\hat{z} \tag{2.16}$$

Similarly for the L mode we obtain:

$$\left[\frac{d^2}{dt^2}+2\Gamma_{\ell}\frac{d}{dt}+(\Gamma_{\ell}^2+\omega_{\ell}'^2(\underline{k}))\right]\delta\underline{E}_{\ell}(\underline{k})=\frac{m\omega_{\ell}^4(\underline{k})}{n_o e^2}\delta\underline{P}_{\ell}^{(k)}$$

$$+\frac{m\omega_{\ell}'^2(\underline{k})\Omega_e^2}{n_o e^2}(\hat{z}\times\delta\underline{P}_{\ell}^{(k)})\times\hat{z} \qquad (2.17)$$

Thus, we get two coupled wave equations for S and L modes with the presence of the third wave $\underline{E}$. When the pump power is near or above threshold level, collisionless model can be used to calculate the coupling coefficients and replace $\Gamma_s^2+\omega_s'^2(\underline{k})$ and $\Gamma_{\ell}^2+\omega_{\ell}'^2(\underline{k})$ by the shifted resonant frequencies. Then equations (2.16) and (2.17) become

$$\left[\frac{d^2}{dt^2}+2\Gamma_s\frac{d}{dt}+\omega_s^2(\underline{k})\right]\delta\underline{E}_s(\underline{k})=\frac{M\omega_s^4(\underline{k})}{n_o e^2}\delta\underline{P}_s^{(k)}+\frac{M\omega_s'^2(\underline{k})\Omega_i^2}{n_o e^2}(\hat{z}\times\delta\underline{P}_s^{(k)})\times\hat{z} \qquad (2.18)$$

$$\left[\frac{d^2}{dt^2}+2\Gamma_{\ell}\frac{d}{dt}+\omega_{\ell}^2(\underline{k})=\frac{m\omega_{\ell}^4(\underline{k})}{n_o e^2}\delta\underline{P}_{\ell}^{(k)}+\frac{m\omega_{\ell}'^2(\underline{k})\Omega_e^2}{n_o e^2}(\hat{z}\times\delta\underline{P}_{\ell}^{(k)})\times\hat{z}\right. \qquad (2.19)$$

where $\omega_s^2(\underline{k})=\Gamma_s^2+\omega_s'^2(\underline{k})$, $\omega_{\ell}^2(\underline{k})=\Gamma_{\ell}^2+\omega_{\ell}'^2(\underline{k})$

Using the following relations

$$\delta\underline{E}_s(\underline{k})=\delta\underline{E}_s^-(k)+\text{c. c.} \qquad \delta\underline{P}_s^{(k)}=\delta\underline{P}_s^-(\underline{k})+\text{c. c.}$$

$$\delta\underline{E}_{\ell}(\underline{k})=\delta\underline{E}_{\ell}^+(\underline{k})+\text{c. c.} \qquad \delta\underline{P}_{\ell}^{(k)}=\delta\underline{P}_{\ell}^+(\underline{k})+\text{c. c.}$$

and combining the relevant components, equations (2.18) and (2.19) can be rewritten as

$$\left[\frac{d^2}{dt^2}+2\Gamma_s\frac{d}{dt}+\omega_s^2(\underline{k})\right]\delta\underline{E}_s^-(\underline{k})=\frac{M\omega_s^4(\underline{k})}{n_o e^2}\delta\underline{P}_s^-(\underline{k})+\frac{M\omega_s'^2(\underline{k})\Omega_i^2}{n_o e^2}(\hat{z}\times\delta\underline{P}_s^-(\underline{k}))\times\hat{z} \qquad (2.20)$$

$$\left[\frac{d^2}{dt^2}+2\Gamma_\ell\ \frac{d}{dt}+\omega_\ell^2(\underline{k})\right]\delta\underline{E}_\ell^+(\underline{k})=\frac{m\omega_\ell^4(\underline{k})}{n_o e^2}\ \delta\underline{P}_\ell^+(\underline{k})+\frac{m\omega_\ell'^2(\underline{k})\Omega_e^2}{n_o e^2}(\hat{z}\times\delta\underline{P}_\ell^+(\underline{k}))\times\hat{z} \tag{2.21}$$

Here (2.20) and (2.21) fit the standard form of parametric coupled wave equations with δP remaining formal, which is to be derived in the next section.

V-3. KINETIC APPROACH TO CALCULATE THE COUPLING COEFFICIENTS

1. Transformation of the Vlasov Equations to the Oscillating Frame of Reference

To derive the coupling coefficients $(\frac{\partial \alpha_{ij}}{\partial \delta E_{\ell\sigma}})_o$ and $(\frac{\partial \alpha_{ij}}{\partial \delta E_{s\sigma}})_o$ for determing $\delta \underline{P}$, we start from Vlasov equation for a homogeneous background distribution function $f_\alpha^{(o)}$:

$$\frac{\partial f_\alpha^{(o)}}{\partial t} + \frac{e_\alpha}{m_\alpha}\{\underline{E}(t) + \frac{1}{c}\underline{v}_\alpha \times \underline{B}_o\} \cdot \frac{\partial f_\alpha^{(o)}}{\partial \underline{v}_\alpha} = 0 \tag{3.1}$$

where e_α, m_α and $\underline{v}_\alpha$ are respectively the charge, mass, and velocity of a particle of species α. The corresponding solution can be written in the form

$$f_\alpha^{(o)}(\underline{v}_\alpha, t) = f_{\alpha o}(\underline{v}_\alpha - \frac{e_\alpha}{m_\alpha}\int_{-\infty}^{t} dt' \, \underline{\underline{R}}_\alpha(t-t') \cdot \underline{E}(t'), t) = f_{\alpha o}(\underline{v}, t) \tag{3.2}$$

where

$$\underline{\underline{R}}_\alpha(t) = \begin{bmatrix} \cos \Omega_\alpha t & \sin \Omega_\alpha t & 0 \\ \sin \Omega_\alpha t & \cos \Omega_a t & 0 \\ 0 & 0 & 1 \end{bmatrix} \tag{3.3}$$

$$\Omega_\alpha = \frac{e_\alpha B_o}{m_\alpha c}$$

$$\underline{v} = \underline{v}_\alpha - \frac{e_\alpha}{m_\alpha}\int_{-\infty}^{t} dt' \, \underline{\underline{R}}_\alpha(t-t') \cdot \underline{E}(t') \tag{3.4}$$

Hence in the oscillating frame equation (3.1) reduces to

$$\frac{\partial f_{\alpha o}(\underline{v}, t)}{\partial t} + \frac{e_\alpha}{m_\alpha}\frac{1}{c}\underline{v} \times B_i \cdot \frac{\partial f_{\alpha o}(\underline{v}, t)}{\partial \underline{v}} = 0 \tag{3.5}$$

Since any function of $|\underline{v}|$ satisfies (3.5), therefore, let's assume $f_{\alpha o}(\underline{v}, t) = f_{\alpha o}(v_{\parallel}, v_{\perp})$, a Maxwellian distribution.

It can be shown easily that to the first order equation for the perturbative distribution function $\delta f_{\alpha}(\underline{v}_{\alpha}, \underline{r}_{\alpha}, t)$ is

$$\frac{\partial \delta f_{\alpha}(\underline{v}_{\alpha}, \underline{r}_{\alpha}, t)}{\partial t} + \underline{v}_{\alpha} \cdot \frac{\partial \delta f_{\alpha}(\underline{v}_{\alpha}, \underline{r}_{\alpha}, t)}{\partial \underline{r}_{\alpha}} + \frac{e_{\alpha}}{m_{\alpha}} \left[\underline{E}(t) + \frac{1}{c} \underline{v}_{\alpha} \times \underline{B}_{o} \right] \cdot \frac{\partial \delta f_{\alpha}(\underline{v}_{\alpha}, \underline{r}_{\alpha}, t)}{\partial \underline{v}_{\alpha}}$$

$$+ \frac{e_{\alpha}}{m_{\alpha}} \delta \underline{E}(\underline{r}_{\alpha}, t) \cdot \frac{\partial f_{\alpha}^{(o)}(\underline{v}_{\alpha}, t)}{\partial \underline{v}_{\alpha}} = 0 \qquad (3.6)$$

For convenience we transform the original variables $(\underline{v}_{\alpha}, \underline{r}_{\alpha}, t)$ to $(\underline{v}, \underline{r}, t)$ of the oscillating reference frame and introduce the function

$$\psi_{\alpha}(\underline{v}, \underline{r}, t) = \delta f_{\alpha}(\underline{v}_{\alpha}, \underline{r}_{\alpha}, t) = \delta f_{\alpha}\left(\underline{v} + \frac{e_{\alpha}}{m_{\alpha}} \int_{-\infty}^{t} dt' \underline{\underline{R}}_{\alpha}(t-t') \cdot \underline{E}(t'),\ \underline{r} + \underline{\ell}_{\alpha}, t\right) \qquad (3.7)$$

where $\underline{r}_{\alpha} = \underline{r} + \underline{\ell}_{\alpha}$

and $$\underline{\ell}_{\alpha} = \frac{e_{\alpha}}{m_{\alpha}} \int_{-\infty}^{t} dt'' \underline{\underline{R}}_{\alpha}(t'-t'') \cdot \underline{E}(t'') \qquad (3.8)$$

with

$$\frac{\partial}{\partial t} \psi_{\alpha}(\underline{v}, \underline{r}, t) = \frac{\partial \delta f_{\alpha}(\underline{v}_{\alpha}, \underline{r}_{\alpha}, t)}{\partial t} + \frac{e_{\alpha}}{m_{\alpha}} \left\{ \underline{E}(t') + \int_{-\infty}^{t} dt' \underline{\underline{R}}_{\alpha}(t-t') \right\} \cdot \frac{\partial \delta f_{\alpha}(\underline{v}_{\alpha}, \underline{r}_{\alpha}, t)}{\partial \underline{v}_{\alpha}}$$

$$+ \frac{d\underline{\ell}_{\alpha}}{dt} \cdot \frac{\partial \delta f_{\alpha}(\underline{v}_{\alpha}, \underline{r}_{\alpha}, t)}{\partial \underline{r}_{\alpha}}$$

From (3.6), the equation for $\psi_{\alpha}(\underline{v}, \underline{r}, t)$ is then

$$\left[\frac{\partial}{\partial t} + \underline{v}\cdot\frac{\partial}{\partial \underline{r}} + \Omega_\alpha(\underline{v}\times\hat{z})\cdot\frac{\partial}{\partial \underline{v}}\right]\psi_\alpha(\underline{v},\underline{r},t) = -\frac{e_\alpha}{m_\alpha}\,\delta\underline{E}(\underline{r}+\underline{\ell}_\alpha,t)\cdot\frac{\partial f_{\alpha o}(v)}{\partial \underline{v}} \tag{3.9}$$

2. Integration along the unperturbed trajectory in the phase space.

Equation (3.9) can now be solved by the method of characteristics. In this method the perturbative distribution function is calculated in the Lagrangian system of coordinates. Let's define an unperturbed trajectory of the particles as

$$\frac{d\underline{r}}{dt} = \underline{v} \quad , \quad \frac{d\underline{v}}{dt} = \Omega_\alpha(\underline{v}\times\hat{z}) \tag{3.10}$$

The solution of (3.10) is

$$\underline{v}' = \underline{\underline{R}}_\alpha(t'-t)\cdot\underline{v} \tag{3.11}$$

and

$$\underline{r}' = \underline{r} + \frac{1}{\Omega_\alpha}\,\underline{\underline{L}}_\alpha(t'-t)\cdot\underline{v} \tag{3.12}$$

where

$$\underline{\underline{L}}_\alpha(t) = \begin{bmatrix} \sin\Omega_\alpha t & 1-\cos\Omega_\alpha t & 0 \\ -(1-\cos\Omega_\alpha t) & \sin\Omega_\alpha t & 0 \\ 0 & 0 & \Omega_\alpha t \end{bmatrix} = \Omega_\alpha \int_o^t \underline{\underline{R}}_\alpha(\tau)\,d\tau \tag{3.13}$$

and

$$\underline{r} = \underline{r}(t) \quad , \quad \underline{r}' = \underline{r}(t') \quad , \quad \underline{v} = \underline{v}(t) \quad , \quad \underline{v}' = \underline{v}(t')$$

Hence along the unperturbed trajectory (3.10) equation (3.9) may be written

$$\frac{d}{dt}\psi_\alpha(\underline{v},\underline{r},t) = -\frac{e_\alpha}{m_\alpha}\,\delta\underline{E}(\underline{r}+\underline{\ell}_\alpha,t)\cdot\frac{\partial f_{\alpha o}(v)}{\partial \underline{v}} \tag{3.14}$$

Substituting (3.7) in (3.14), we obtain

$$\frac{d}{dt}\,\delta f_\alpha\left(\underline{v}+\frac{e_\alpha}{m_\alpha}\int_{-\infty}^{t} dt'\,\underline{\underline{R}}_\alpha(t-t')\cdot\underline{E}(t')\ ,\ \underline{r}+\underline{\ell}_\alpha,t\right)=$$

$$-\frac{e_\alpha}{m_\alpha}\,\delta\underline{E}(\underline{r}+\underline{\ell}_\alpha,t)\cdot\frac{\partial f_{\alpha o}(v)}{\partial\underline{v}} \qquad (3.15)$$

Because of the spatial homogeneity of the background, we may assume a coordinate dependent of the non-equilibrium increment $\delta f_\alpha \sim e^{i\underline{k}\cdot\underline{r}_\alpha}$ and the perturbed field $\delta\underline{E} \sim e^{i\underline{k}\cdot\underline{r}_\alpha}$. Then (3.15) becomes

$$\frac{d}{dt}\,\delta f_\alpha\left(\underline{v}+\frac{e_\alpha}{m_\alpha}\int_{-\infty}^{t} dt'\,\underline{\underline{R}}_\alpha(t-t')\cdot\underline{E}(t'),\underline{k},t\right)e^{i\underline{k}\cdot(\underline{r}+\underline{\ell}_\alpha)}=-\frac{e_\alpha}{m_\alpha}\,\delta\underline{E}(\underline{k},t)$$

$$\cdot\frac{\partial f_{\alpha o}(v)}{\partial\underline{v}}\,e^{i\underline{k}\cdot(\underline{r}+\underline{\ell}_\alpha)} \qquad (3.16)$$

Let us, however, restrict ourselves to unstable (growing) solutions. We can thus invert this differentiation by integrating (3.16) with respect to time along the unperturbed particle trajectory as

$$\delta f_\alpha\left(\underline{v}+\frac{e_\alpha}{m_\alpha}\int_{-\infty}^{t} dt'\,\underline{\underline{R}}_\alpha(t-t')\cdot\underline{E}(t'),\underline{k},t\right)=-\frac{e_\alpha}{m_\alpha}\int_{-\infty}^{t}\delta\underline{E}(\underline{k},t')$$

$$\cdot\frac{\partial f_{\alpha o}(v')}{\partial\underline{v}'}\,e^{i\underline{k}\cdot(\underline{r}'-\underline{r})}e^{i\underline{k}\cdot\left[\underline{\ell}_\alpha(t')-\underline{\ell}_\alpha(t)\right]}dt' \qquad (3.17)$$

From equation (3.12), let

$$\phi_\alpha(\tau)=\underline{k}\cdot(\underline{r}-\underline{r}')=-\frac{1}{\Omega_\alpha}\,\underline{k}\cdot\underline{\underline{L}}_\alpha(-\tau)\cdot\underline{v}\quad\text{and}\quad\tau=t-t' \qquad (3.18)$$

Then equation (3.17) becomes

$$\delta f_\alpha(\underline{v} + \frac{e_\alpha}{m_\alpha} \int_{-\infty}^{t} dt' \underline{\underline{R}}_\alpha(t-t') \cdot \underline{E}(t'), \underline{k}, t) = - \frac{e_\alpha}{m_\alpha} \int_0^\infty \delta \underline{E}(k, t-\tau)$$

$$\cdot \{ \frac{\partial f_{\alpha o}}{\partial v_\perp} [\cos(\Omega_\alpha \tau + \theta) \hat{x} + \sin(\Omega_\alpha \tau + \theta) \hat{y}]$$

$$+ \frac{\partial f_{\alpha o}}{\partial v_\parallel} \hat{z} \} e^{-i\phi_\alpha(\tau)} e^{i\underline{k} \cdot [\underline{\ell}_\alpha(t-\tau) - \underline{\ell}_\alpha(t)]} d\tau \qquad (3.19)$$

where we have used following relations

$$\underline{v} = v_\perp \cos\theta \hat{x} + v_\perp \sin\theta \hat{y} + v_\parallel \hat{z}$$

and

$$\underline{v}' = v_\perp \cos(\Omega_\alpha \tau + \theta) \hat{x} + v_\perp \sin(\Omega_\alpha \tau + \theta) \hat{y} + v_\parallel \hat{z}$$

then

$$\frac{\partial f_{\alpha o}(v')}{\partial \underline{v}'} = \frac{\partial f_{\alpha o}(v)}{\partial v_\perp} [\cos(\Omega_\alpha \tau + \theta) \hat{x} + \sin(\Omega_\alpha \tau + \theta) \hat{y}] + \frac{\partial f_{\alpha o}}{\partial v_\parallel} \hat{z}$$

Let the time dependence of the pump electric field be

$$\underline{E}(t) = 2\underline{E}_1 \sin\omega_o t + 2\underline{E}_2 \cos\omega_o t \qquad (3.20)$$

then

$$\underline{k} \cdot [\underline{\ell}_\alpha(t-\tau) - \underline{\ell}_\alpha(t)] = - \frac{e_\alpha}{m_\alpha} \int_{t-\tau}^{t} dt' \int_{-\infty}^{t'} dt'' \underline{k} \cdot \underline{\underline{R}}_\alpha(t'-t'') \cdot \underline{E}(t'')$$

$$= (a_{\alpha 1} + b_{\alpha 2}) [\sin\omega_o t - \sin\omega_o(t-\tau)]$$

$$+ (a_{\alpha 2} - b_{\alpha 1}) [\cos\omega_o t - \cos\omega_o(t-\tau)] \qquad (3.21)$$

and

$$\frac{e_\alpha}{m_\alpha}\int_{-\infty}^{t} dt' \underline{\underline{R}}_\alpha(t-t')\cdot\underline{E}(t') = i\frac{e_\alpha}{m_\alpha}\frac{\omega_o}{\omega_o^2-\Omega_\alpha^2}\left[\underline{\underline{A}}_\alpha\cdot(\underline{E}_1^- + \underline{E}_2^-) - \underline{\underline{A}}_\alpha^*\cdot(\underline{E}_1^+ + \underline{E}_2^+)\right] \tag{3.22}$$

where

$$a_{\alpha i} = 2\frac{e_\alpha}{m_\alpha}\frac{\underline{k}\cdot\underline{\underline{A}}'_\alpha\cdot\underline{E}_i}{\omega_o^2-\Omega_\alpha^2}\quad,\qquad b_{\alpha i} = 2\frac{e_\alpha}{m_\alpha}\frac{\Omega_\alpha}{\omega_o(\omega_o^2-\Omega_\alpha^2)}\hat{z}\times\underline{k}\cdot\underline{E}_i\quad,\quad i=1,2$$

and

$$\underline{\underline{A}}'_\alpha = \hat{x}\,\hat{x} + \hat{y}\,\hat{y} + \frac{\omega_o^2-\Omega_\alpha^2}{\omega_o^2}\,\hat{z}\,\hat{z} \tag{3.23}$$

and

$$\underline{E}_1^- = i\,\underline{E}_1\,e^{-i\omega_o t} \qquad \underline{E}_1^+ = -\,i\,\underline{E}_1\,e^{i\omega_o t}$$

$$\underline{E}_2^- = \underline{E}_2\,e^{-i\omega_o t} \qquad \underline{E}_2^+ = \underline{E}_2\,e^{i\omega_o t} \tag{3.24}$$

and

$$\underline{\underline{A}}_\alpha = \hat{x}\,\hat{x} + i\frac{\Omega_\alpha}{\omega_o}(\hat{x}\,\hat{y} - \hat{y}\,\hat{x}) + \frac{\omega_o^2-\Omega_\alpha^2}{\omega_o^2}\,\hat{z}\,\hat{z} \tag{3.25}$$

$\underline{\underline{A}}_\alpha^*$ is the complex conjugate of $\underline{\underline{A}}_\alpha$.

We may then calculate the total induced current from (3.19) as

$$\delta\underline{J}(\underline{k},t) = \sum_\alpha n_\alpha e_\alpha \int d\underline{v}\left[\underline{v} + \frac{e_\alpha}{m_\alpha}\int_{-\infty}^{t} dt' \underline{\underline{R}}_\alpha(t-t')\right.$$

$$\left.\cdot\,\underline{E}(t')\right]\delta f_\alpha\left(\underline{v} + \frac{e_\alpha}{m_\alpha}\int_{-\infty}^{t} dt' \underline{\underline{R}}_\alpha(t-t')\cdot\underline{E}(t'),\underline{k},t\right) \tag{3.26}$$

With the aid of (3.21) and (3.22), (3.26) becomes

$$\delta \underline{J}(k,t) = -\sum_{\alpha} \frac{n_\alpha e_\alpha^2}{m_\alpha} \int d\underline{v} \int_o^\infty d\tau \{\underline{v} + i \frac{e_\alpha}{m_\alpha} \frac{\omega_o}{\omega_o^2 - \Omega_\alpha^2} [\underline{\underline{A}}_\alpha \cdot (\underline{E}_1^- + \underline{E}_2^-) - \underline{\underline{A}}_\alpha^* \cdot (\underline{E}_1^+ + \underline{E}_2^+)]\} \{\frac{\partial f_{\alpha o}}{\partial v_\perp} [\cos(\Omega_\alpha \tau + \theta)\hat{x} + \sin(\Omega_\alpha \tau + \theta)\hat{y}] + \frac{\partial f_{\alpha o}}{\partial v_{||}} \hat{z}\}$$

$$\cdot \delta \underline{E}(\underline{k}, t-\tau) e^{-i\phi_\alpha(\tau)} e^{i\{(a_{\alpha 1} + b_{\alpha 2})[\sin\omega_o t - \sin\omega_o(t-\tau)] + (a_{\alpha 2} - b_{\alpha 1})[\cos\omega_o t - \cos\omega_o(t-\tau)]\}} \tag{3.27}$$

Since

$$e^{i\{(a_{\alpha 1} + b_{\alpha 2})[\sin\omega_o t - \sin\omega_o(t-\tau)] + (a_{\alpha 2} - b_{\alpha 1})[\cos\omega_o t - \cos\omega_o(t-\tau)]\}}$$

$$= \sum_{h,q=-\infty}^{+\infty} (-1)^q J_h(a_{\alpha 1} + b_{\alpha 2}) J_q(a_{\alpha 1} + b_{\alpha 2}) e^{+i(h+q)\omega_o t} e^{-iq\omega_o \tau} \cdot$$

$$\sum_{f,g=-\infty}^{+\infty} (i)^{g-f} J_f(b_{\alpha 1} - a_{\alpha 2}) J_g(b_{\alpha 1} - a_{\alpha 2}) e^{i(f+g)\omega_o t} e^{-ig\omega_o \tau}$$

$$\approx 1 + \frac{1}{2}[(a_{a1} + b_{\alpha 2}) - i(b_{\alpha 1} - a_{\alpha 2})] e^{i\omega_o t}(1 - e^{-i\omega_o \tau})$$

$$- \frac{1}{2}[(a_{\alpha 1} + b_{\alpha 2}) + i(b_{\alpha 1} - a_{\alpha 2})] e^{-i\omega_o t}(1 - e^{i\omega_o \tau}) \tag{3.28}$$

where J_n, J_q, J_f, J_g are Bessel functions and we have assumed $|a_{\alpha i}| << |$, $|b_{\alpha i}| << |$.

For the parametric interaction, we have

$\omega_o = \omega_s + \omega_l$ for the conservation of energy

and

$\underline{k}_s = -\underline{k}_\ell = \underline{k}$ for the conservation of momentum (dipole approximation) where ω_s and ω_ℓ are the characteristic frequencies of two plasma modes in a collisionless plasma with the presence of pump field.

Therefore, the induced current density for the S (or L) mode due to the coupling between L (or S) mode and the pump wave can be obtained with the aid of (3.27) and (3.28) as

$$\delta\underline{J}_s^-(\underline{k},t) = -\sum_\alpha \frac{in_\alpha e^3}{m_\alpha^2}\frac{\omega_o}{\omega_o^2-\Omega_\alpha^2}\Bigg\{\underline{\underline{A}}_\alpha\cdot(\underline{E}_1^-+\underline{E}_2^-)\int d\underline{v}\int_o^\infty d\tau\Big\{\frac{\partial f_{\alpha o}}{\partial v_\perp}\big[\cos(\Omega_\alpha\tau+\theta)\hat{x} + \sin(\Omega_\alpha\tau+\theta)\hat{y}\big] + \frac{\partial f_{\alpha o}}{\partial v_{||}}\hat{z}\Big\}e^{-i\omega_\ell\tau}e^{-i\phi_\alpha(\tau)}$$

$$+\Big[\frac{\underline{k}\cdot\underline{\underline{A}}_\alpha\cdot(\underline{E}_1^-+\underline{E}_2^-)}{\omega_o}\int\underline{v}d\underline{v}\int_o^\infty d\tau\Big\{\frac{\partial f_{\alpha o}}{\partial v_\perp}\big[\cos(\Omega_\alpha\tau+\theta)\hat{x}+\sin(\Omega_\alpha\tau+\theta)\hat{y}\big]+\frac{\partial f_{\alpha o}}{\partial v_{||}}\hat{z}\Big\}$$

$$e^{-i\omega_\ell\tau}e^{i\phi_\alpha(\tau)}(1-e^{i\omega_o\tau})\Bigg\}\cdot\delta\underline{E}_\ell^+(\underline{k},t) \qquad (3.29)$$

and

$$\delta\underline{J}_\ell^+(\underline{k},t) = \sum_\alpha \frac{in_\alpha e^3}{m_\alpha^2}\frac{\omega_o}{\omega_o^2-\Omega_\alpha^2}\Big\{\underline{\underline{A}}_\alpha^*\cdot(\underline{E}_1^++\underline{E}_2^+)\int d\underline{v}\int_o^\infty d\tau\Big\{\frac{\partial f_{\alpha o}}{\partial v_\perp}\big[\cos(\Omega_\alpha\tau+\theta)\hat{x} + \sin(\Omega_\alpha\tau+\theta)\hat{y}\big] + \frac{\partial f_{\alpha o}}{\partial v_{||}}\hat{z}\Big\}e^{i\omega_s\tau}e^{-i\phi_\alpha(\tau)}$$

$$-\Big[\frac{\underline{k}\cdot\underline{\underline{A}}_\alpha^*\cdot(\underline{E}_1^++\underline{E}_2^+)}{\omega_o}\Big]\int\underline{v}d\underline{v}\int_o^\infty d\tau\Big\{\frac{\partial f_{\alpha o}}{\partial v_\perp}\big[\cos(\Omega_\alpha\tau+\theta)\hat{x}+\sin(\Omega_\alpha\tau+\theta)\hat{y}\big]+\frac{\partial f_{\alpha o}}{\partial v_{||}}\hat{z}\Big\}$$

$$e^{i\omega_s\tau}e^{-i\phi_\alpha(\tau)}(1-e^{-i\omega_o\tau})\Big\}\cdot\delta\underline{E}_s^-(\underline{k},t) \qquad (3.30)$$

In carrying out those integrations, we specifically choose the wave vector $\underline{k}$ on the x-z plane and write

$$\underline{k} = k_\perp\hat{x} + k_{||}\hat{z} \qquad (3.31)$$

Equation (3.18) becomes

$$\phi_\alpha(\tau) = \mathcal{J}_\alpha [\sin(\Omega_\alpha \tau + \theta) - \sin\theta] k_{\parallel} v_{\parallel} \tau \tag{3.32}$$

where

$$\mathcal{J}_\alpha = k_\perp v_\perp / \Omega_\alpha \tag{3.33}$$

then we have

$$\exp[-i\phi_\alpha(\tau)] = \sum_{n=-\infty}^{+\infty} \sum_{n'=-\infty}^{+\infty} J_n(\mathcal{J}_\alpha) J_{n'}(\mathcal{J}_\alpha) \exp\{-i[n(\Omega_\alpha \tau + \theta) - n'\theta - k_{\parallel} v_{\parallel} \tau]\} \tag{3.34}$$

Therefore, we obtain following relation

$$\int \underline{v} dv_\perp \int_0^\infty d\tau \left\{ \frac{\partial f_o}{\partial v_\perp} [\cos(\Omega\tau+\theta)\hat{x} + \sin(\Omega\tau+\theta)\hat{y}] + \frac{\partial f_o}{\partial v_{\parallel}} \hat{z} \right\} e^{-i\phi(\tau)} e^{i\omega\tau}$$

$$= \frac{1}{i\omega} \left\{ \sum_{n=-\infty}^{+\infty} \frac{Z_o}{Z_n} \underline{\underline{\Pi}}^*(\beta, Z_n; n) [1 - W(Z_n)] - Z_o^2 \hat{z}\hat{z} \right\} \tag{3.35}$$

for a Maxwellian distribution function f_o .

where

$$Z_n = \frac{\omega - n\Omega}{k_{\parallel}(T/m)^{\frac{1}{2}}} \quad , \quad \beta = k_\perp^2 T/m\Omega^2 \quad \text{and} \quad \Lambda_n(\beta) = I_n(\beta) e^{-\beta} \tag{3.36}$$

and

$$\underline{\underline{\Pi}}(\beta, Z_n; n) = \frac{n^2}{\beta} \Lambda_n(\beta) \hat{x}\hat{x} + \left[\frac{n^2}{\beta} \Lambda_n(\beta) - 2\beta\Lambda_n'(\beta)\right] \hat{y}\hat{y} + Z_n^2 \Lambda_n(\beta) \hat{z}\hat{z} - in\Lambda_n'(\beta)(\hat{x}\hat{y} - \hat{y}\hat{x})$$

$$+ \frac{k_\perp \Omega}{|k_\perp \Omega|} \frac{n}{\sqrt{\beta}} Z_n \Lambda_n(\beta)(\hat{x}\hat{z} + \hat{z}\hat{x}) + \frac{ik_\perp \Omega}{|k_\perp \Omega|} \sqrt{\beta}\, Z_n \Lambda_n'(\beta)(\hat{y}\hat{z} - \hat{z}\hat{y}) \tag{3.37}$$

Substituting (3.35) in (3.29) and (3.30), the results are

$$\delta \underline{J}_s^-(\underline{k},t) = \sum_\alpha \frac{n_\alpha e^3 \omega_o}{m_\alpha T_\alpha (\omega_o^2 - \Omega_\alpha^2)} \delta \underline{E}_\ell^+(\underline{k},t) \cdot \Bigg\{ \Bigg[\sum_n \frac{\Omega_\alpha}{k_\perp (\omega_\ell + n\Omega_\alpha)} [1 - W(Z_{\ell n}^\alpha)] [n\Lambda_n(\beta_\alpha)\hat{x}$$

$$+ i\beta_\alpha \Lambda_n'(\beta_\alpha)\hat{y}] + \frac{W(Z_{\ell n}^\alpha)}{k_\parallel} \Lambda_n(\beta_\alpha)\hat{z} \Bigg] \underline{\underline{A}}_\alpha$$

$$+ \frac{\beta_\alpha \Omega_\alpha^2}{k_\perp \omega_o} \Bigg[\sum_n \frac{1}{k_\perp (\omega_\ell + n\Omega_\alpha)} \underline{\underline{\Pi}}(\beta_\alpha, Z_{\ell n}^\alpha; n) [1 - W(Z_{\ell n}^\alpha)] - \frac{Z_{\ell o}^{\alpha\,2}}{k_\perp \omega_\ell} \hat{z}\hat{z} \Bigg] [\underline{k} \cdot \underline{\underline{A}}_\alpha]$$

$$+ \frac{\beta_\alpha \Omega_\alpha^2}{k_\perp \omega_o} \Bigg[\sum_n \frac{1}{k_\perp (\omega_s - n\Omega_\alpha)} \underline{\underline{\Pi}}(\beta_\alpha, Z_{sn}^\alpha; n) [1 - W(Z_{sn}^\alpha)] - \frac{Z_{so}^{\alpha\,2}}{k_\perp \omega_s} \hat{z}\hat{z} \Bigg] [\underline{k} \cdot \underline{\underline{A}}_\alpha] \Bigg\}$$

$$\cdot (\underline{E}_1^- + \underline{E}_2^-) \qquad (3.38)$$

and

$$\delta \underline{J}_\ell^+(\underline{k},t) = \sum_\alpha \frac{n_\alpha e^3 \omega_o}{m_\alpha T_\alpha (\omega_o^2 - \Omega_\alpha^2)} \delta \underline{E}_s^-(\underline{k},t) \cdot \Bigg\{ \Bigg[\sum_n \frac{\Omega_\alpha}{k_\perp (\omega_s - n\Omega_\alpha)} [1 - W(Z_{sn}^\alpha)] [n\Lambda_n(\beta_\alpha)\hat{x}$$

$$+ i\beta_\alpha \Lambda_n'(\beta_\alpha)\hat{y}] - \frac{W(Z_{sn}^\alpha)}{k_\parallel} \Lambda_n(\beta_\alpha)\hat{z} \Bigg] \underline{\underline{A}}_\alpha^*$$

$$- \frac{\beta_\alpha \Omega_\alpha^2}{k_\perp \omega_o} \Bigg[\sum_n \frac{1}{k_\perp (\omega_s - n\Omega_\alpha)} \underline{\underline{\Pi}}(\beta_\alpha, Z_{sn}^\alpha; n) [1 - W(Z_{sn}^\alpha)] - \frac{Z_{so}^{\alpha\,2}}{k_\perp \omega_s} \hat{z}\hat{z} \Bigg] [\underline{k} \cdot \underline{\underline{A}}_\alpha^*]$$

$$- \frac{\beta_\alpha \Omega_\alpha^2}{k_\perp \omega_o} \Bigg[\sum_n \frac{1}{k_\perp (\omega_\ell + n\Omega_\alpha)} \underline{\underline{\Pi}}(\beta_\alpha, Z_{\ell n}^\alpha; n) [1 - W(Z_{\ell n}^\alpha)]$$

$$- \frac{Z_{\ell o}^{\alpha\,2}}{k_\perp \omega_\ell} \hat{z}\hat{z} \Bigg] [\underline{k} \cdot \underline{\underline{A}}_\alpha^*] \Bigg\} \cdot (\underline{E}_1^+ + \underline{E}_2^+) \qquad (3.39)$$

where

$$Z^{\alpha}_{\ell n} = -\frac{\omega_{\ell} + n\Omega_{\alpha}}{k_{\|}(T_{\alpha}/m_{\alpha})^{\frac{1}{2}}} \quad , \quad Z^{\alpha}_{sn} = \frac{\omega_{s} - n\Omega_{\alpha}}{k_{\|}(T_{\alpha}/m_{\alpha})^{\frac{1}{2}}} \quad , \quad \beta_{\alpha} = k_{\perp}^{2} T_{\alpha}/m_{\alpha}\Omega_{\alpha}^{2} \tag{3.40}$$

whence the induced polarizations are obtained as

$$\delta\underline{P}_{s}^{-}(\underline{k},t) = \frac{i}{\omega_{s}}\,\delta\underline{J}_{s}^{-}(\underline{k},t) \quad \delta\underline{E}_{\ell}^{+}(\underline{k},t) \cdot \left(\frac{\partial\,\underline{\underline{\alpha}}}{\partial\,\delta\underline{E}_{\ell}^{+}}\right) \cdot \underline{E}^{-} \tag{3.41}$$

$$\delta\underline{P}_{\ell}^{+}(\underline{k},t) = -\frac{i}{\omega_{\ell}}\,\delta\underline{J}_{\ell}^{+} \quad ,t) = \delta\underline{E}_{s}^{-}(\underline{k},t) \cdot \left(\frac{\partial\,\underline{\underline{\alpha}}}{\partial\,\delta\underline{E}_{s}^{-}}\right) \cdot \underline{E}^{+} \tag{3.42}$$

where

$$\underline{E}^{-} = \underline{E}_{1}^{-} + \underline{E}_{2}^{-} \quad \text{and} \quad \underline{E}^{+} = \underline{E}_{1}^{+} + \underline{E}_{2}^{+}$$

V-4. DETAILED ANALYSIS OF THRESHOLD POWER AND INITIAL GROWTH RATE

1. Conditions and Properties of the Instabilities Occurring on the Basis of a General Form of the Coupled Mode Equations

In the following paragraph we will show that the coupled wave equations (2.20) and (2.21) derived in Section II can be reduced to the following scalar form similar to those introduced by Nishikawa[11]:

$$\left[\frac{d^2}{dt^2} + 2\Gamma_s \frac{d}{dt} + \omega_s^2\right] X = i\lambda Y E^-(t) \tag{4.1}$$

$$\left[\frac{d^2}{dt^2} + 2\Gamma_\ell \frac{d}{dt} + \omega_\ell^2\right] Y = -i\mu X E^+(t) \tag{4.2}$$

where for simplicity, we treat only the case with

$$\lambda\mu = \text{real} > 0$$

Taking the Fourier transform of (4.1) and (4.2), we obtain

$$\left[\omega^2 - \omega_s^2 + 2i\Gamma_s\omega\right] X(\omega) = \lambda E_o Y(\omega-\omega_o) \tag{4.3}$$

$$\left[(\omega-\omega_o)^2 - \omega_\ell^2 + 2i\Gamma_\ell(\omega-\omega_o)\right] Y(\omega-\omega_o) = \mu E_o X(\omega) \tag{4.4}$$

where

$$X(t),\ Y(t) = \int_{-\infty}^{+\infty} \frac{d\omega}{2\pi}\, e^{-i\omega t}\, X(\omega),\ Y(\omega).$$

Setting the determinant of the coefficient matrix equal to zero, the dispersion relations which determine the frequency and damping (or growing) of the waves under consideration are obtained, namely,

$$\left[\omega^2-\omega_s^2+2i\Gamma_s\omega\right]\left[(\omega-\omega_o)^2-\omega_\ell^2+2i\Gamma_\ell(\omega-\omega_o)\right]-\lambda\mu E_o^2=0 \qquad (4.5)$$

If the solution of (4.5) is written in the form

$$\omega = x + iy \qquad (4.6)$$

then x and (-y) are the frequency and damping rates, respectively, of the new normal mode with parametric coupling effect. It becomes unstable if

$$y > 0 \qquad (4.7)$$

Considering first the threshold case in which $y = 0$, $E_o = E_c$ and (4.5) can be separated into two equations

$$\Gamma_s x\left[(x-\omega_o)^2-\omega_\ell^2\right]+\Gamma_\ell(x-\omega_o)(x^2-\omega_s^2)=0 \qquad (4.8)$$

$$(x^2-\omega_s^2)\left[(x-\omega_o)^2-\omega_\ell^2\right]-4\Gamma_s\Gamma_\ell x(x-\omega_o)-\lambda\mu E_c^2=0 \qquad (4.9)$$

Since Γ_s and Γ_ℓ are arbitrary, the threshold intensity of the pump field and the frequencies of X and Y are given by

$$x = \omega_s \qquad (4.10)$$

$$x-\omega_o = -\omega_\ell \qquad (4.11)$$

$$E_c^2 = \frac{4\Gamma_s\Gamma_\ell\omega_s\omega_\ell}{\lambda\mu} \qquad (4.12)$$

Thus under the condition of frequency match, there is no frequency shift of X and Y at the threshold.

With the pump field $E_o > E_c$, we no longer can set $y = 0$. Substituting (4.6) in (4.5) and separating the real and imaginary parts, we obtain

$$(x^2-y^2-\omega_s^2-2\Gamma_s y)\left[(x-\omega_o)^2 - \omega_\ell^2-2\Gamma_\ell y\right] - 4x(x-\omega_o)(y+\Gamma_s)(y+\Gamma_\ell)$$

$$- \lambda\mu E_o^2 = 0 \qquad (4.13)$$

$$x(y+\Gamma_s)\left[(x-\omega_o)^2 - y^2 - \omega_\ell^2 - \Gamma_\ell y\right] + (x-\omega_o)(y+\Gamma_\ell)(x^2-y^2-\omega_s^2-2\Gamma_s y)$$

$$= 0 \qquad (4.14)$$

If the frequency shift is small compared with ω_s, then (4.14) can be approximated as

$$x^2-y^2-\omega_s^2-2\Gamma_s y = \frac{-2\left[\omega_\ell(x-\omega_s)+\Gamma_\ell y\right]\omega_s(y+\Gamma_s)}{\omega_\ell\,\Gamma_\ell} \approx 0 \qquad (4.15)$$

and (4.13) becomes

$$4(y+\Gamma_s)(y+\Gamma_\ell)\omega_s\,\omega_\ell \approx \lambda\mu E_o^2 \qquad (4.16)$$

After some algebraic manipulation, we find

$$y = \frac{-(\Gamma_s+\Gamma_\ell) + \sqrt{(\Gamma_\ell-\Gamma_s)^2 + \lambda\mu E_o^2/\omega_s\omega_\ell}}{2}$$

$$= \frac{-(\Gamma_s+\Gamma_\ell) + \sqrt{(\Gamma_\ell-\Gamma_s)^2 + 4\Gamma_s\Gamma_\ell E_o^2/E_c^2}}{2} \qquad (4.17)$$

$$x \approx \omega_s + \frac{y(y+2\Gamma_s)}{2\omega_s} \qquad (4.18)$$

In general Γ_ℓ is much larger than Γ_s, therefore we may express (4.17) and (4.18) in the vicinity of the threshold as

$$y \approx \Gamma_s\left[\frac{E_o^2}{E_c^2} - 1\right] \qquad (4.19)$$

$$x \approx \omega_s + \frac{\Gamma_s^2}{2\omega_s}\left[\left(\frac{E_o^2}{E_c^2}\right)^2 - 1\right] \approx \omega_s + \frac{\Gamma_s^2}{\omega_s}\left[\frac{E_o^2}{E_c^2} - 1\right] \qquad (4.20)$$

The initial exponential growth rate and the frequency shift are linearly proportional to the pump intensity. These results are, however, valid only when the frequency shift is small compared to ω_s and the pump intensity is near the threshold. These phenomena had actually been observed in Stenzel and Wong's[20] experiment in an unmagnetized plasma.

2. Parametric Decay into Longitudinal Modes (electrostatic approximation)

Thus we can write

$$\delta \underline{E}_s^-(\underline{k}, t) = -i\underline{k}\phi_s^-(\underline{k}, t) \quad \text{and} \quad \delta \underline{E}_\ell^+(\underline{k}, t) = -i\underline{k}\phi_\ell^+(\underline{k}, t) \qquad (4.21)$$

and substitute these relations in (2.20) and (2.21). We have

$$\left[\frac{d^2}{dt^2} + 2\Gamma_s \frac{d}{dt} + \omega_s^2(\underline{k})\right]\phi_s^-(\underline{k}, t) = \frac{M\omega_s^4(\underline{k})}{n_o e^2 k^2}\,\underline{k}\cdot\left[\frac{\partial(\underline{k}\cdot\underline{\underline{\alpha}})}{\partial\delta\underline{E}_\ell^+}\right]\cdot\underline{E}^-\phi_\ell^+(\underline{k}, t)$$

$$+\frac{M\omega_s'^2(\underline{k})\Omega_i^2}{n_o e^2 k^2}\,\underline{k}\cdot\left\{\hat{z}\times\left[\underline{k}\cdot\left(\frac{\partial\underline{\underline{\alpha}}}{\partial\delta\underline{E}_\ell^+}\right)\right]\cdot\underline{E}^-\right\}\phi_\ell^+(\underline{k}, t) \qquad (4.22)$$

$$\left[\frac{d^2}{dt^2} + 2\Gamma_\ell \frac{d}{dt} + \omega_\ell^2(\underline{k})\right]\phi_\ell^+(\underline{k}, t) = \frac{m\omega_\ell^4(\underline{k})}{n_o e^2 k^2}\,\underline{k}\cdot\left[\frac{\partial(\underline{k}\cdot\underline{\underline{\alpha}})}{\partial\delta\underline{E}_s^-}\right]\cdot\underline{E}^+\phi_s^-(\underline{k}, t)$$

$$+\frac{m\omega_\ell'^2(\underline{k})\Omega_e^2}{n_o e^2 k^2}\,\underline{k}\cdot\left\{\hat{z}\times\left[\underline{k}\cdot\left(\frac{\partial\underline{\underline{\alpha}}}{\partial\delta\underline{E}_s^-}\right)\right]\cdot\underline{E}^+\right\}\phi_s^-(\underline{k}, t) \qquad (4.23)$$

(a) When the pump wave is the ordinary mode and the decay waves are ion acoustic mode and electron plasma mode

Let $\underline{E}(t) = 2E_2 \cos \omega_o t \, \hat{z}$ (i.e., $\underline{E}_1 = 0$)

and

$$\underline{k} = k\hat{z} \quad (\text{i.e., } k_{\parallel} = k,\ k_{\perp} = 0,\ \beta_\alpha = 0) \tag{4.24}$$

and the substitution of (4.24) into (4.22) and (4.23) will yield

$$\left[\frac{d^2}{dt^2} + 2\Gamma_s \frac{d}{dt} + \omega_s^2(\underline{k})\right] \phi_s^-(\underline{k}, t) = \frac{iM\omega_s^4}{n_o e^2 k} \sum_\alpha \frac{n_\alpha e_\alpha^3}{m_\alpha T_\alpha \omega_o^2} \left\{ W\left(-\frac{\omega_\ell}{k\sqrt{T_\alpha/m_\alpha}}\right) \right.$$

$$\left. - W\left(\frac{\omega_s}{k\sqrt{T_\alpha/m_\alpha}}\right) \right\} E_2^- \phi_\ell^+(\underline{k}, t) \tag{4.25}$$

$$\left[\frac{d^2}{dt^2} + 2\Gamma_\ell \frac{d}{dt} + \omega_\ell^2(\underline{k})\right] \phi_\ell^+(\underline{k}, t) = \frac{im\omega_\ell^4}{n_o e^2 k} \sum_\alpha \frac{n_\alpha e_\alpha^3}{m_\alpha T_\alpha \omega_o^2} \left\{ W\left(\frac{\omega_s}{k\sqrt{T_\alpha/m_A}}\right) \right.$$

$$\left. - W\left(-\frac{\omega_\ell}{k\sqrt{T_\alpha/m_\alpha}}\right) \right\} E_2^+ \phi_s^-(\underline{k}, t) \tag{4.26}$$

Since the decay modes we are considering are in the frequency domains such that

$$\sqrt{T_i/M} \ll \omega_s/k \ll \sqrt{T_e/m} \ll \omega_\ell/k \tag{4.27}$$

then (4.25) and (4.26) become

$$\left[\frac{d^2}{dt^2} + 2\Gamma_s \frac{d}{dt} + \omega_s^2\right] \phi_s^-(\underline{k}, t) = i \frac{ke\omega_s^2}{m\omega_o^2} \phi_\ell^+(\underline{k}, t) E^-(t) \tag{4.28}$$

$$\left[\frac{d^2}{dt^2} + 2\Gamma_\ell \frac{d}{dt} + \omega_\ell^2\right] \phi_\ell^+(\underline{k}, t) = -i \frac{ke}{m} \frac{k_d^2}{k^2} \phi_s^-(\underline{k}, t) E^+(t) \tag{4.29}$$

where we have used relations

$$\omega_s^2 = k^2 T_e / M, \qquad \omega_\ell^2 \approx \omega_{pe}^2 = \frac{4\pi n_o e^2}{m} \approx \omega_o^2 \quad \text{and} \quad k_d^2 = \frac{4\pi n_o e^2}{T_e} \tag{4.30}$$

Equations (4.28) and (4.29) had been obtained by Nishikawa[11], who worked with a hydrodynamic model. If we take the Fourier transform of (4.28) and (4.29), the results would be the same as DuBois and Goldman[10], Nishikawa[11], Lee and Su[12], and Jackson's[13] conclusions.

Therefore, the threshold field is given by

$$\frac{E_{th}}{8\sqrt{\pi n_o T_e}} = \sqrt{\frac{\Gamma_s \Gamma_\ell}{\omega_s \omega_\ell}} \tag{4.31}$$

where $E_{th} = 2E_2$.

(b) When the pump field is extraordinary mode ($\underline{E} \perp \underline{B}_o$) and $|\Omega_e| >> \omega_{pe}$.

In this case we may write

$$\underline{E} = 2E_o(\hat{x} \cos\omega_o t - \hat{y} \sin\omega_o t) \quad \text{(i.e., } \underline{E}_2 = \hat{x} E_o, \ \underline{E}_1 = -E_o \hat{y}) \tag{4.32}$$

and

$$\underline{k} = k_\perp \hat{x} + k_\parallel \hat{z}$$

Substituting (4.32) in (4.22) and (4.23), we obtain

$$\left[\frac{d^2}{dt^2} + 2\Gamma_s \frac{d}{dt} + \omega_s^2\right] \phi_s^-(\underline{k}, t) = \frac{iM\omega_s^4}{n_o e^2 k^2} (k_\perp \delta P_{s1}^- + k_\parallel \delta P_{s3}^-) + \frac{iM\omega_s'^2 \Omega_i^2}{n_o e^2 k^2} k_\perp \delta P_{s1}^- \tag{4.33}$$

$$\left[\frac{d^2}{dt^2} + 2\Gamma_\ell \frac{d}{dt} + \omega_\ell^2\right]\phi_\ell^+(\underline{k},t) = \frac{im\omega_\ell^4}{n_o e^2 k^2}(k_\perp \delta P_{\ell 1}^+ + k_\parallel \delta P_{\ell 3}^+)$$

$$+ \frac{im\omega'^2_\ell \Omega_e^2}{n_o e^2 k^2} k_\perp \delta P_{\ell 1}^+ \qquad (4.34)$$

where

$$\delta P_{s1}^- = \frac{1}{\omega_s}\sum_\alpha \frac{n_\alpha e_\alpha^3 \omega_o (1+\frac{\Omega_\alpha}{\omega_o})}{m_\alpha T_\alpha(\omega_o^2-\Omega_\alpha^2)} \sum_n \left\{\frac{n\Omega_\alpha \Lambda_n(\beta_\alpha)}{(\omega_\ell + n\Omega_\alpha)}(1+\frac{n\Omega_\alpha}{\omega_o})\left[1 - W(Z_{\ell n}^\alpha)\right]\right.$$

$$+ \frac{n^2\Omega_\alpha^2 \Lambda_n(\beta_\alpha)}{\omega_o(\omega_s - n\Omega_\alpha)}\left[1 - W(Z_{sn}^\alpha)\right] + W(Z_{\ell n}^\alpha)\Lambda_n(\beta_\alpha) + \frac{n\Omega_\alpha \Lambda_n(\beta_\alpha)}{\omega_o}\left[W(Z_{\ell n}^\alpha)\right.$$

$$\left.\left. - W(Z_{sn}^\alpha)\right]\right\}\phi_\ell^+(\underline{k},t)E_o e^{-i\omega_o t} \qquad (4.35)$$

$$\delta P_{s3}^- = \frac{1}{\omega_s}\sum_n \frac{n_\alpha e_\alpha^3 \omega_o (1+\frac{\Omega_\alpha}{\omega_o}}{m_\alpha T_\alpha(\omega_o^2-\Omega_\alpha^2)} \sum_n -\frac{k_\perp}{k_\parallel}\left\{\frac{\Lambda_n(\beta_\alpha)}{\omega_o}\left[\omega_\ell W(Z_{\ell n}^\alpha)\right.\right.$$

$$\left.\left. + \omega_s W(Z_{sn}^\alpha)\right]\right\}\phi_\ell^+(\underline{k},t)E_o e^{-i\omega_o t} \qquad (4.36)$$

$$\delta P_{\ell 1}^+ = -\frac{1}{\omega_\ell}\sum_\alpha\left\{\frac{n_\alpha e_\alpha^3 \omega_o (1+\frac{\Omega_\alpha}{\omega_o})}{m_\alpha T_\alpha(\omega_o^2-\Omega_\alpha^2)} \sum_n \frac{n\Omega_\alpha \Lambda_n(\beta_\alpha)}{(\omega_s - n\Omega_\alpha)}(1-\frac{n\Omega_\alpha}{\omega_o})\left[1 - W(Z_{sn}^\alpha)\right]\right.$$

$$- \frac{n^2\Omega_\alpha^2 \Lambda_n(\beta_\alpha)}{\omega_o(\omega_\ell + n\Omega_\alpha)}\left[1 - W(Z_{\ell n}^\alpha)\right] - W(Z_{sn}^\alpha)\Lambda_n(\beta_\alpha)$$

$$\left. - \frac{n\Omega_\alpha \Lambda_n(\beta_\alpha)}{\omega_o}\left[W(Z_{\ell n}^\alpha) - W(Z_{sn}^\alpha)\right]\right\}\phi_s^-(\underline{k},t)E_o e^{i\omega_o t} \qquad (4.37)$$

$$\delta P^{+}_{\ell 3} = \frac{1}{\omega_\ell} \sum_\alpha \frac{n_\alpha e_\alpha^2 \omega_o (1 + \frac{\Omega_\alpha}{\omega_o})}{m_\alpha T_\alpha (\omega_o^2 - \Omega_\alpha^2)} \sum_n - \frac{k_\perp}{k_{||}} \left\{ \frac{\Lambda_n(\beta_\alpha)}{\omega_o} \left[\omega_\ell W(Z^\alpha_{\ell n}) \right.\right.$$

$$\left.\left. + \omega_s W(Z^\alpha_{sn}) \right] \right\} \phi^{-}_s (\underline{k}, t) E_o e^{i\omega_o t} \qquad (4.38)$$

(i) Decay waves are electrostatic ion cyclotron wave (ion acoustic wave) and upper-hybrid wave

Thus, we may assume $\sqrt{\frac{m}{M}} << k_{||}/k_\perp << 1$ such that $W(Z^\alpha_{\ell n}) \approx 0$, and $W(Z^i_{sn}) \approx 0$ for all n and $W(Z^e_{sn}) \approx 0$ for $n \neq 0$, $W(Z^e_{so})\Lambda_o(\beta_o) \approx 1$.

With these approximations, equations (4.35)-(4.38) may be reduced to

$$\delta P^{-}_{s1} = \frac{n_o e^3}{2\omega_\ell^2 m T_e} \frac{k_\perp^2}{k_d^2}$$

$$\delta P^{-}_{s3} \approx \frac{n_o e^3}{2\omega_\ell^2 m T_e} \frac{k_\perp}{k_{||}}$$

$$\delta P^{+}_{\ell 1} \approx - \frac{n_o e^3}{2 m T_e \omega_\ell^2} (1 + k_\perp^2 / k_d^2) \qquad (4.39)$$

$$\delta P^{+}_{\ell 3} \approx 0$$

and (4.33) and (4.34) become

$$\left[\frac{d^2}{dt^2} + 2\Gamma_s \frac{d}{dt} + \omega_s^2 \right] \phi^{-}_s (\underline{k}, t) = \frac{iMe\omega_s^4}{2km T_e \omega_\ell^2} (1 + k_\perp^2/k_d^2) E_o e^{-i\omega_o t} \phi^{+}_\ell (\underline{k}, t) \qquad (4.40)$$

$$\left[\frac{d^2}{dt^2} + 2\Gamma_\ell \frac{d}{dt} + \omega_\ell^2 \right] \phi^{+}_\ell (\underline{k}, t) = \frac{-ie\omega_\ell^2 (1 + k_\perp^2/k_d^2)}{kT_e} E_o e^{i\omega_o t} \phi^{-}_s (\underline{k}, t) \qquad (4.41)$$

Therefore, the threshold field can be calculated as

$$\frac{E_{th}}{8\sqrt{\pi n_o T_e}} = \sqrt{\frac{\Gamma_s \Gamma_\ell}{\omega_s \omega_\ell}}\ \frac{\omega_\ell}{\omega_{pe}} \tag{4.42}$$

where $E_{th} = (2E_o)_{th}$, $\omega_s^2 = \Omega_i^2 + \frac{k_\perp^2 T_e/M}{1+k_\perp^2/k_d^2} \approx \frac{k_\perp^2 T_e/M}{1+k_\perp^2/k_d^2}$ and $k_\perp^2/k_d^2 \approx 1$. This had been obtained by Porkolab[21].

(ii) Decay waves are lower hybrid and upper hybrid waves

In this case $k_\parallel/k_\perp << \sqrt{\frac{m}{M}}$, therefore $W(Z_n) = 0$ for all n.

Since $\omega_o = \frac{|\Omega_e|}{2} + \sqrt{(\frac{\Omega_e}{2})^2 + \omega_{pe}^2} \approx |\Omega_e| + \frac{\omega_{pe}^2}{|\Omega_e|} = \omega_\ell + \omega_s$, and

$$\beta_e = k_\perp^2 T_e/m\Omega_e^2 = \frac{k_\perp^2}{k_d^2}\ \frac{\omega_{pe}^2}{\Omega_e^2} \geq 1.,\quad \omega_\ell \approx |\Omega_e| + \frac{\omega_{pe}^2}{|\Omega_e|}\Lambda_1(\beta_e) \approx |\Omega_e|$$

$$\Rightarrow\ \omega_{pe}^2 \approx |\Omega_e|\,\omega_s$$

and $\omega_\ell \approx |\Omega_e| + \omega_s \Lambda_1(\beta_e)$; $k_\perp^2 \approx k_d^2\ \frac{|\Omega_e|}{\omega_s}$.

With these approximations, equations (4.35)- (4.38) become

$$\begin{aligned}
\delta P_{s1}^- &= \frac{n_o e^3}{m T_e \omega_{pe}^2}\ \phi_\ell^+(\underline{k},t)\ E_o e^{-i\omega_o t} \\
\delta P_{s3}^- &= 0 \\
\delta P_{\ell 1}^+ &= -\frac{n_o e^3}{m T_e \omega_{pe}^2}\ \phi_s^-(\underline{k},t) E_o e^{i\omega_o t} \\
\delta P_{\ell 3}^+ &= 0
\end{aligned} \tag{4.43}$$

and (4.33) and (4.34) become

$$\left[\frac{d^2}{dt^2} + 2\Gamma_s \frac{d}{dt} + \omega_s^2\right] \phi_s^-(\underline{k},t) = \frac{iMe\omega_s^4}{kmT_e\omega_{pe}^2} \phi_\ell^+(\underline{k},t)E_o e^{-i\omega_o t} \qquad (4.44)$$

$$\left[\frac{d^2}{dt^2} + 2\Gamma_\ell \frac{d}{dt} + \omega_\ell^2\right] \phi_\ell^+(\underline{k},t) = -\frac{2ie\omega_\ell^4}{T_e\omega_{pe}^2 k} \phi_s^-(\underline{k},t)E_o e^{i\omega_o t} \qquad (4.45)$$

Therefore; the threshold field can be calculated as

$$\frac{E_{th}}{8\sqrt{\pi n_o T_e}} = \sqrt{\frac{\Gamma_s\Gamma_\ell}{\omega_s\omega_\ell}} \frac{\omega_{pe}}{\sqrt{2\omega_s|\Omega_e|}} \qquad (4.46)$$

which also agrees with Porkolab's[21] result.

where $E_{th} = (2E_o)_{th}$, $\omega_s^2 = |\Omega_e\Omega_i| \left[\frac{\omega_{pe}^2 + |\Omega_e\Omega_i|}{\omega_{pe}^2 + \Omega_e^2}\right] \approx \omega_{pi}^2$

(c) For a forced linearly polarized pump field with upper hybrid and lower hybrid waves as decay waves

In this case we write $\underline{E} = 2E_o \cos\omega_o t\,\hat{x}$ (i.e. $\underline{E}_2 = \hat{x}E_o$; $\underline{E}_1 = 0$) and $\underline{k} = k_\perp \hat{x} + k_\parallel \hat{z}$ $\left(k_\parallel/k_\perp << \sqrt{\frac{m}{M}}\right)$

Since $\omega_o^2 \approx \Omega_e^2 + \omega_{pe}^2$, $\beta_e = k_\perp^2 T_e/m\Omega_e^2 \approx \omega_{pe}^2/\Omega_e^2 << 1$ and $\omega_s \approx \omega_{pi}$.
With these approximations; equations (4.33) and (4.34) become

$$\left[\frac{d^2}{dt^2} + 2\Gamma_s \frac{d}{dt} + \omega_s^2\right] \phi_s^-(\underline{k},t) = \frac{iMe\omega_s^4}{mT_e k\omega_{pe}^2} \phi_\ell^+(\underline{k},t)E_o e^{-i\omega_o t} \qquad (4.47)$$

$$\left[\frac{d^2}{dt^2} + 2\Gamma_\ell \frac{d}{dt} + \omega_\ell^2\right] \phi_\ell^+(\underline{k},t) = \frac{-2ie\omega_\ell^4}{\omega_{pe}^2 T_e k} \phi_s^-(\underline{k},t)E_o e^{i\omega_o t} \qquad (4.48)$$

Therefore, the threshold field is given as

$$\frac{E_{th}}{8\sqrt{\pi n_o T_e}} = \sqrt{\frac{\Gamma_\ell \Gamma_s}{\omega_s \omega_\ell}} \quad \frac{\omega_{pe}}{\sqrt{2}\,\omega_\ell} \tag{4.49}$$

3. Parametric Decay into Electrostatic Ion Cyclotron Wave and Harmonics of Electron Cyclotron Wave (Hybrid Mode) in a Uniform Magneto Plasma

For the harmonics of electron cyclotron modes, $|\underline{k}|$ is small ($|\underline{k}| \ll k_d$) such that $\beta_e \ll 1$, and $W(Z^e_{\ell n}) \approx 0$ for all n.

Since the electrostatic ion cyclotron mode is longitudinal wave, we may assume $\delta \underline{E}_s^-(\underline{k},t) = -i\underline{k}\phi_s^-(\underline{k},t)$, where $\underline{k} = k_\perp \hat{x} + k_{||} \hat{z}$ with $\sqrt{\frac{m}{M}} \ll |k_{||}/k_\perp| \ll 1$. Therefore, $W(Z^e_{sn}) \approx 0$ for $n \neq 0$ and $W(Z^e_{so})\Lambda_o(\beta_e) \approx 1$.

Because the nonlinear coupling due to electrons of the plasma is much stronger than due to ions; therefore we may neglect the ion terms of equations (3.41) and (3.42). The resulting components of the induced polarizations can be simplified to

$$\underline{k} \cdot \delta \underline{P}_s^-(\underline{k},t) = -\frac{i}{\omega} \frac{n_o e^3 \omega_o}{mT_e(\omega_o^2 - \Omega_e^2)} \delta \underline{E}_\ell^+ \cdot \left\{ -\frac{\beta_e \omega_\ell^2 \omega_s}{k_\perp \omega_o (\omega_\ell^2 - \Omega_e^2)} \hat{x} \right.$$

$$\left. + \frac{i\beta_e \Omega_e^3 \omega_s}{k_\perp \omega_o \omega_\ell (\omega_\ell^2 - \Omega_e^2)} \hat{y} - \frac{\omega_s}{k_{||} \omega_o} \hat{z} \right\} \left[\underline{k} \cdot \underline{\underline{A}}_e \cdot \underline{E}^- \right] \tag{4.50}$$

$$k_\perp \delta P_{s1}^-(\underline{k},t) = -\frac{i}{\omega_s} \frac{n_o e^3 \omega_o}{mT_e(\omega_o^2 - \Omega_e^2)} \delta \underline{E}_\ell^+ \cdot \left\{ \frac{-\beta_e \omega_s \omega_\ell^2}{k_\perp \omega_o (\omega_\ell^2 - \Omega_e^2)} \hat{x} \right.$$

$$\left. + \left[\frac{-i\omega_s \beta_e (\omega_\ell^2 - \Omega_e^2 - \omega_\ell \Omega_e)}{k_\perp \omega_o (\omega_\ell^2 - \Omega_e^2)} - \frac{i\beta_e \Omega_e}{k_\perp \omega_o} \right] \hat{y} \right\} \left[k_\perp \hat{x} \cdot \underline{\underline{A}}_e \cdot \underline{E}^- \right] \tag{4.51}$$

$$\delta P^{+}_{\ell 1}(\underline{k}, t) = \frac{1}{\omega_\ell} \frac{n_o e^3 \omega_o}{mT_e(\omega_o^2 - \Omega_e^2)} \phi_s^{-}(\underline{k}, t)\, \underline{k} \cdot \left\{ \frac{-\beta_e \omega_\ell^3}{k_\perp \omega_o (\omega_\ell^2 - \Omega_e^2)} \hat{x} + \frac{i\beta_e \Omega_e \omega_\ell^2}{k_\perp \omega_o (\omega_\ell^2 - \Omega_e^2)} \hat{y} - \frac{1}{k_\parallel} \hat{z} \right\} \left[\hat{x} \cdot \underline{\underline{A}}_e^{*} \cdot \underline{E}^{+} \right] \tag{4.52}$$

$$\delta P^{+}_{\ell 2}(\underline{k}, t) = \frac{1}{\omega_\ell} \frac{n_o e^3 \omega_o}{mT_e(\omega_o^2 - \Omega_e^2)} \phi_s^{-}(\underline{k}, t)\, \underline{k} \cdot \left\{ \frac{-i\beta_e \Omega_e \omega_\ell^2}{k_\perp \omega_o (\omega_\ell^2 - \Omega_e^2)} \hat{x} - \frac{\beta_e \Omega_e^2 \omega_\ell}{k_\perp \omega_o (\omega_\ell^2 - \Omega_e^2)} \hat{y} - i \frac{\Omega_e}{k_\parallel \omega_o} \hat{z} \right\} \left[\hat{x} \cdot \underline{\underline{A}}_e^{*} \cdot \underline{E}^{+} \right] \tag{4.53}$$

$$\delta P^{+}_{\ell 3}(\underline{k}, t) = \frac{-1}{\omega_\ell} \frac{n_o e^3 \omega_o}{mT_e(\omega_o^2 - \Omega_e^2)} \phi_s^{-}(\underline{k}, t) \left[\hat{z} \cdot \underline{\underline{A}}_e^{*} \cdot \underline{E}^{+} \right] \tag{4.54}$$

and the coupled mode equations are given by equations (4. 33) and (2. 21). From (4. 52), (4. 53) and (2. 21), we obtain the relation $\delta E^{+}_{\ell 2}(\underline{k}, t) = i \frac{\Omega_e}{\omega_o} \delta E^{+}_{\ell 1}(\underline{k}, t)$, thus the dispersion relation for the L mode is given as

$$1 - \frac{k_d^2}{k^2} \sum_n \frac{(n\Omega_e)^2 \Lambda_n(\beta_e)}{\omega_\ell(\omega_\ell - n\Omega_e)} = \frac{\Omega_e}{\omega_o} \frac{\omega_{pe}^2}{\omega_\ell^2} \sum_n \frac{\omega_\ell}{\omega_\ell - n\Omega_e} n\Lambda_n'(\beta_e) \tag{4.55}$$

let $\omega_\ell = |n\Omega_e|\,(1 + \Delta_n)$ where $n \geq 2$ and substitute into (4. 55), we have

$$\Delta_n = \frac{k_d^2 (n+1) \Lambda_n}{k^2 n \left(1 - \frac{(n^2+1)\omega_{pe}^2}{n^2(n^2-1)\Omega_e^2}\right)} \tag{4.56}$$

Since the polarization of the harmonics of electron cyclotron wave can be determined from linear dielectric tensor as

$$\frac{\delta E^{+}_{\ell 3}}{\delta E^{+}_{\ell 1}} = \frac{k_{\parallel}}{k_{\perp}} \frac{1}{1 - (\frac{\omega_{\ell}}{kc})^2 (1 - \frac{\omega_{pe}^2}{\omega_{\ell}^2})} \tag{4.57}$$

thus the linearly polarized pump field can be written as

$$\underline{E} = \left[\hat{x} + \hat{z}\, k_{\parallel}/k_{\perp} \frac{\omega_o^2+\Omega_e^2}{\omega_o^2-\Omega_e^2} \frac{1}{1 - (\frac{\omega_{\ell}}{kc})^2 (1 - \frac{\omega_{pe}^2}{\omega_{\ell}^2})} \right] 2E_o \cos \omega_o t$$

Therefore, the resulting coupled mode equations are given as

$$\left[\frac{d^2}{dt^2} + 2\Gamma_s \frac{d}{dt} + \omega_s^2 \right] \phi_s^{-}(\underline{k}, t) = - \frac{M\omega_s^4 e}{k^2 m T_e (\omega_o^2-\Omega_e^2)} \left[\frac{1}{1 - (\frac{\omega_{\ell}}{kc})^2 (1 - \frac{\omega_{pe}^2}{\omega_{\ell}^2})} - \frac{|\Omega_i \Omega_e|}{\omega_s \omega_o} \right] \delta E^{+}_{\ell 1}(\underline{k}, t) E_o e^{-i\omega_o t} \tag{4.58}$$

$$\left[\frac{d^2}{dt^2} + 2\Gamma_{\ell} \frac{d}{dt} + \omega_{\ell}^2 \right] \delta E^{+}_{\ell 1}(\underline{k}, t) = - \frac{\omega_{\ell}^2 (\omega_{\ell}^2+\Omega_e^2) e}{T_e (\omega_o^2-\Omega_e^2)} \phi_s^{-} E_o e^{i\omega_o t} \tag{4.59}$$

and the threshold field can be calculated as

$$\frac{E_{th}}{8\sqrt{\pi n_o T_e}} = (\frac{\Gamma_s \Gamma_{\ell}}{\omega_s \omega_{\ell}})^{1/2} \frac{\omega_o^2-\Omega_e^2}{(\omega_{\ell}^2+\Omega_e^2)^{1/2} \omega_{pe}} \left[\frac{1}{1 - (\frac{\omega_{\ell}}{kc})^2 (1 - \frac{\omega_{pe}^2}{\omega_{\ell}^2})} - \frac{|\Omega_i \Omega_e|}{\omega_s \omega_o} \right]^{-1/2} \tag{4.60}$$

4. Comparison Between Theory and Experiments

a. In the case of parametric decay into electrostatic ion cyclotron wave and second harmonics of electron cyclotron wave in a uniform magneto plasma. (My experiment)

With the aid of (4.60), the value of parameters can be found from Table 2, the threshold field E_{th} is calculated as

$$E_{th} = 13.7 \text{ volts/cm}$$

Near the microwave horn, the pump field is almost uniformly distributed on the cross-section of the chamber, hence the theoretically predicted threshold pump power may be calculated as

$$\text{Threshold pump power} \approx \frac{E_{th}^2}{8\pi} \times \pi r^2 \times c \approx 44 \text{ watts}$$

where $r = 7.5$ cm is the radius of the chamber.

The threshold pump power, experimentally determined, is about 47.1 watts as shown in Figure 10. This value is very close to the theoretically predicted value, and the extra 3 watts is believed to be used to sustain the plasma.

b. In the case of parametric decay into lower hybrid wave at upper hybrid resonance with a linearly polarized pump. (S. Hiroe and H. Ikegami's[22] experiment.)

$T_e = 4$ eV $\quad T_i = 300^\circ$K $\quad N = 3.4$ m torr

$\omega_s = 2\pi \times 3.5 \times 10^4 \text{ sec}^{-1} \quad \omega_\ell = 2\pi \times 4.1 \times 10^9 \text{ sec}^{-1} = \omega_o$

$B_o = 1350$ Gauss $\quad \Omega_i = 2\pi \times 1.05 \times 10^4 \text{ sec}^{-1} \quad \Omega_e = 2\pi \times 3.85 \times 10^9 \text{ sec}^{-1}$

$$\omega_{pe} = 2\pi \times 1.4 \times 10^{9} \text{sec}^{-1}, \quad \omega_{pi} = 2\pi \times 2.48 \times 10^{6} \text{sec}^{-1}, \quad n_o = 2.42 \times 10^{10} \text{cm}^{-3}$$

$$\Gamma_\ell = \frac{\nu_{en}}{2} = 3.5 \times 10^{7} \text{sec}^{-1} \qquad \Gamma_s = \frac{\nu_{in}}{2} = \frac{1}{2}\sqrt{\frac{m_e}{m_i}\frac{T_i}{T_e}}\,\nu_{en} = 0.5 \times 10^{4} \text{sec}^{-1}$$

$$m_e = 0.91 \times 10^{-27} \text{g} \qquad m_i = 200 \times 1.67 \times 10^{-24} \text{g}$$

From (4.49), the electric field associated with the threshold power can be calculated and the result is

$$E_{th} = 2.25 \text{ V/cm}$$

and the experimentally measured threshold field is about 2 V/cm.

V-5. DESCRIPTION OF EXPERIMENT AND RESULTS

Although the theories[9-13] and experiments[20, 23, 24] of parametric coupling between longitudinal electron plasma waves and ion acoustic waves in an unmagnetized plasma have been treated extensively by various authors, only recently did experiments[2, 5, 7, 22] in magnetized plasma report on the decay instability. Porkolab and his colleagues have done a series of experimental studies of plasma heating due to the parametric decay instability of plasma waves in a magnetic field and a high-frequency electric field. These decay waves have relatively short wavelengths and broad spectra such that quasi-electrostatic modes may be assumed and an anomalous heating process can be achieved. In our experiment, we have a relatively small sized plasma beam. Working on the slab model, the excited waves are of standing wave type with well defined boundary conditions. Therefore, the frequency spectra of the unstable waves are sharply spiked. The object of the present work is to study both experimentally and theoretically the threshold and saturation of the parametric decay instability of the second harmonic of the electron cyclotron wave and ion acoustic wave.

1. Experimental Apparatus and Procedure

The experiment is performed in a hollow-cathode-arc-discharge (HCD) plasma source[25], 15 cm in diameter and a vacuum chamber 2m in length, as shown in Figure 1. The 2m long stainless steel vacuum chamber is separated into two sections, a source region and a drift region, by a baffle. In order to get a highly ionized and confined argon plasma beam in the drift region, the magnetic field in the source region is a mirror field, hence it is hard to get a totally quiescent plasma. In

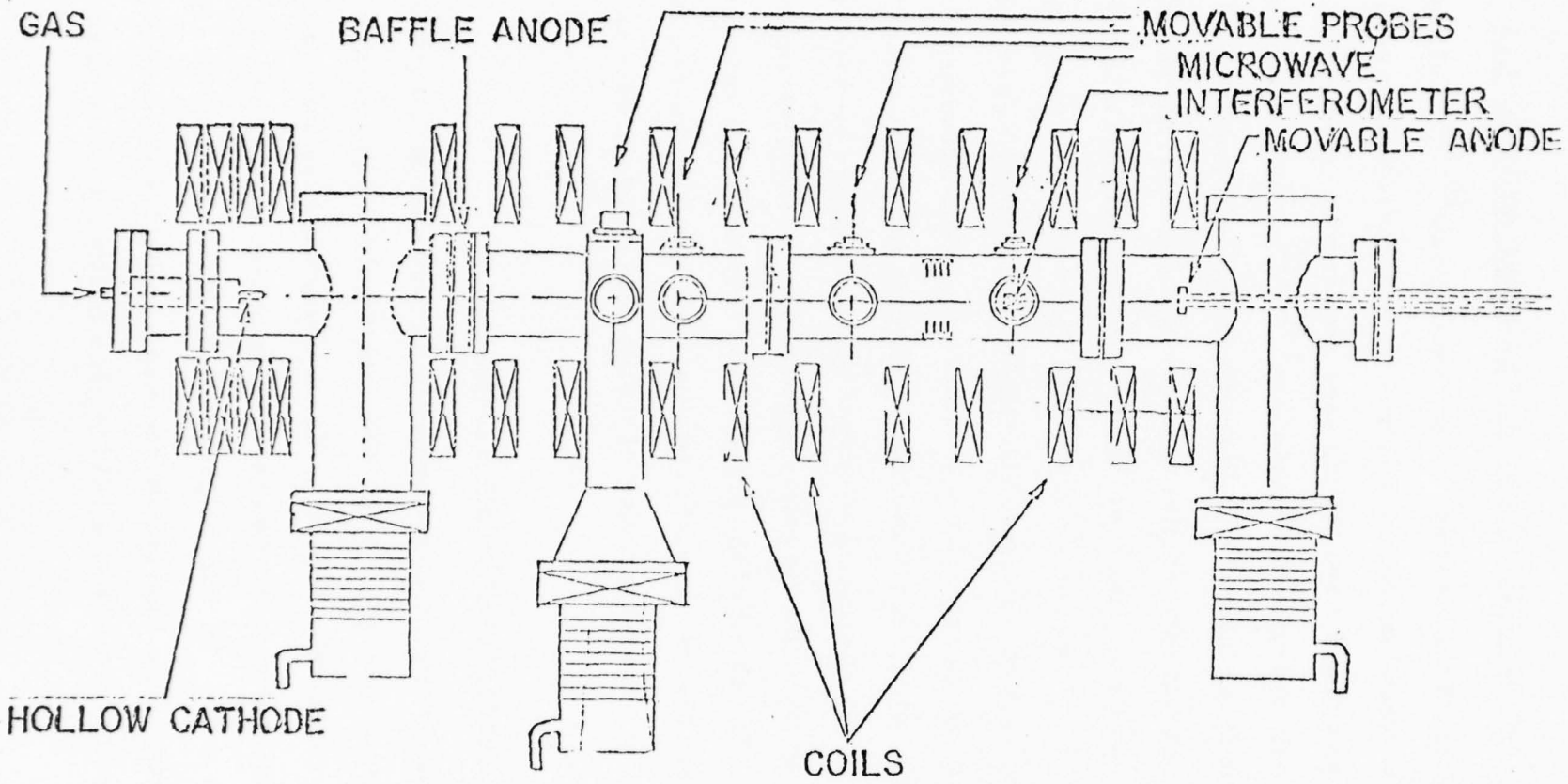

FIGURE 1: SCHEMATIC DIAGRAM OF PINY HCD SYSTEM

our experiment a new procedure is introduced to create an ultrastable microwave sustained plasma. An antenna horn is mounted on the anode and to send the high power microwave (150-200 watts) into the HCD plasma beam. Increasing the drift magnetic field and background gas pressure to a suitably high range (1.5 KG-2KG, 1 μ - 1.5μ of mercury pressure), we can then shut off the source plasma completely by setting the cathode gas flow and baffle current to zero. Yet the plasma still exists in the drift region sustained by the input microwave. This plasma is very quiescent and well confined in a beam. Adjusting the experimental parameters (such as drift magnetic field, drift gas pressure, microwave power, etc.) to proper values to achieve optimum operating conditions, we obtain a spectrum as in Figure 3, showing the instability and its harmonics due to parametric excitation.

A simplified block diagram of the experimental apparatus is shown in Figure 2. A frequency stabilized Klystron unit, operated in x-band is used as the microwave source. For the measurements of the growth and decay times of the excited waves, a fast PIN diode switch having 20 nanosecond rise and fall times is used to modulate the microwave signal which is fed into a Klystron amplifier, capable of 1K watts cw output at the frequency of 9.23 GHz. Between the PIN diode and the source two variable attenuators are used to adjust the output levels.

Microwave power is transmitted through waveguide into the plasma by means of a horn. Since the EM wave in the waveguide is TE_{10} mode, the electric field in the chamber is linearly polarized in the direction perpendicular to the uniform magnetic field and almost uniformly distributed at the cross-section of the chamber near the horn. The diagnostic devices employed in this experiment include axially and radially movable Langmuir probes.

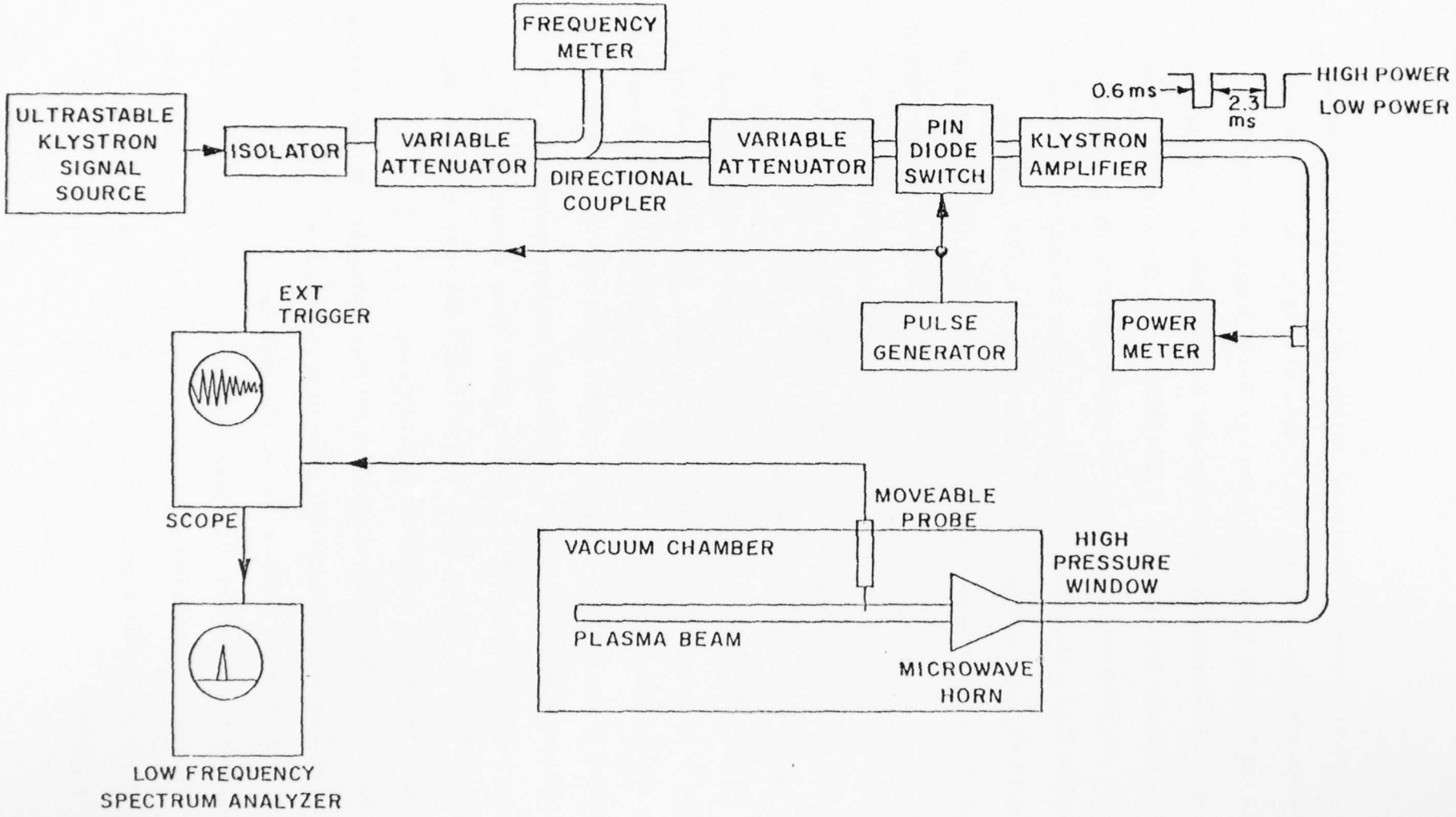

FIGURE 2: SIMPLIFIED BLOCK DIAGRAM OF EXPERIMENTAL APPARATUS

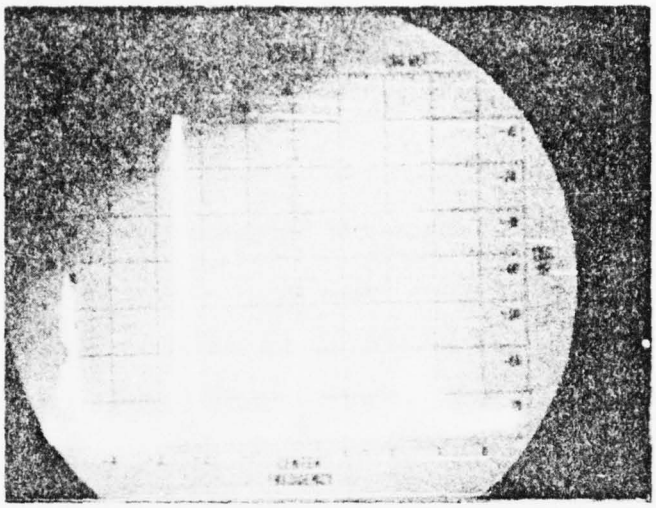

FIGURE 3: FREQUENCY SPECTRUM OF ELECTROSTATIC ION CYCLOTRON WAVE
First Peak is the Zero Reference, Center Frequency = $\omega_s/2\pi$ = = 228 KHz, P = 1.2μ, f_o = 9.23 GHz, P_1 = 173 W (cw), Linear Vertical Scale, 90 KHz/Division Horizontal Scale

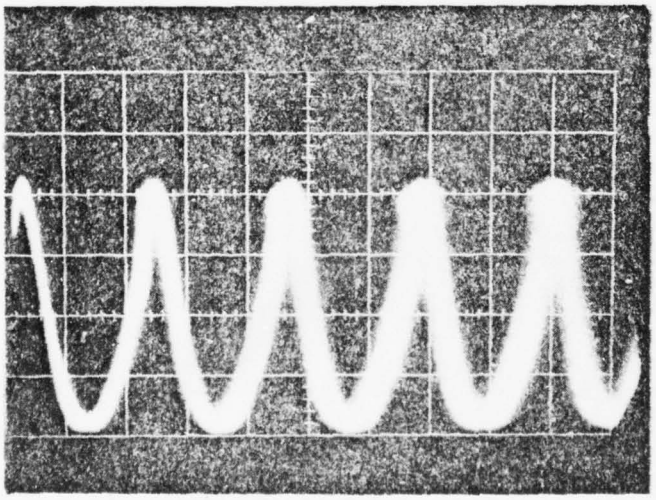

FIGURE 4: TIME DOMAIN BEHAVIOR OF ELECTROSTATIC ION CYCLOTRON WAVE
P = 1.2μ, f_o = 9.23 GHz, P_1 = 173 W (cw), Horizontal Scale = 2μs/cm, Vertical Scale = .5 V/cm

In order to parametrically excite the electrostatic ion cyclotron waves efficiently, the external dc magnetic field is suitably adjusted such that the frequency of the pump field is near or just above the harmonic of electron cyclotron frequency. We find that in the HCD device, the plasma is very unstable due to the existence of various types of low frequency unstable modes which are suspected to be: resistive drift, ion acoustic, and electrostatic ion cyclotron instabilities. It is believed that the energy source responsible for the onset of these instabilities must come from the excess of the free energy contained in the plasma not at thermodynamic equilibrium. In this regard, we find the possible deviations from equilibrium occurring in the velocity space are due to the mirror field in the source region, and not to the configuration space. This conclusion follows from the fact that all the low frequency unstable modes disappear after the source plasma is turned off completely.

Strongly enhanced signals at the acoustic wave frequencies are observed only when the pump power exceeds a threhold level. This is the characteristic of parametric excitation. With the background gas pressure readjusted to about 1.2 μ, the electrostatic ion cyclotron wave becomes most coherent in time domain as seen on a scope (Figure 4), or becomes sharpest in the frequency domain as seen on a frequency spectrum analyzer (Figure 3).

2. Measurement of Growth and Decay Times of Electrostatic Ion Cyclotron Waves

The growth and decay times of parametrically excited electrostatic ion cyclotron waves are measured as a function of microwave pump power by modulating the pump as illustrated in Figure 5. During time T_1, the power is at level $P_1 > P_{th}$ (threshold power) such that the

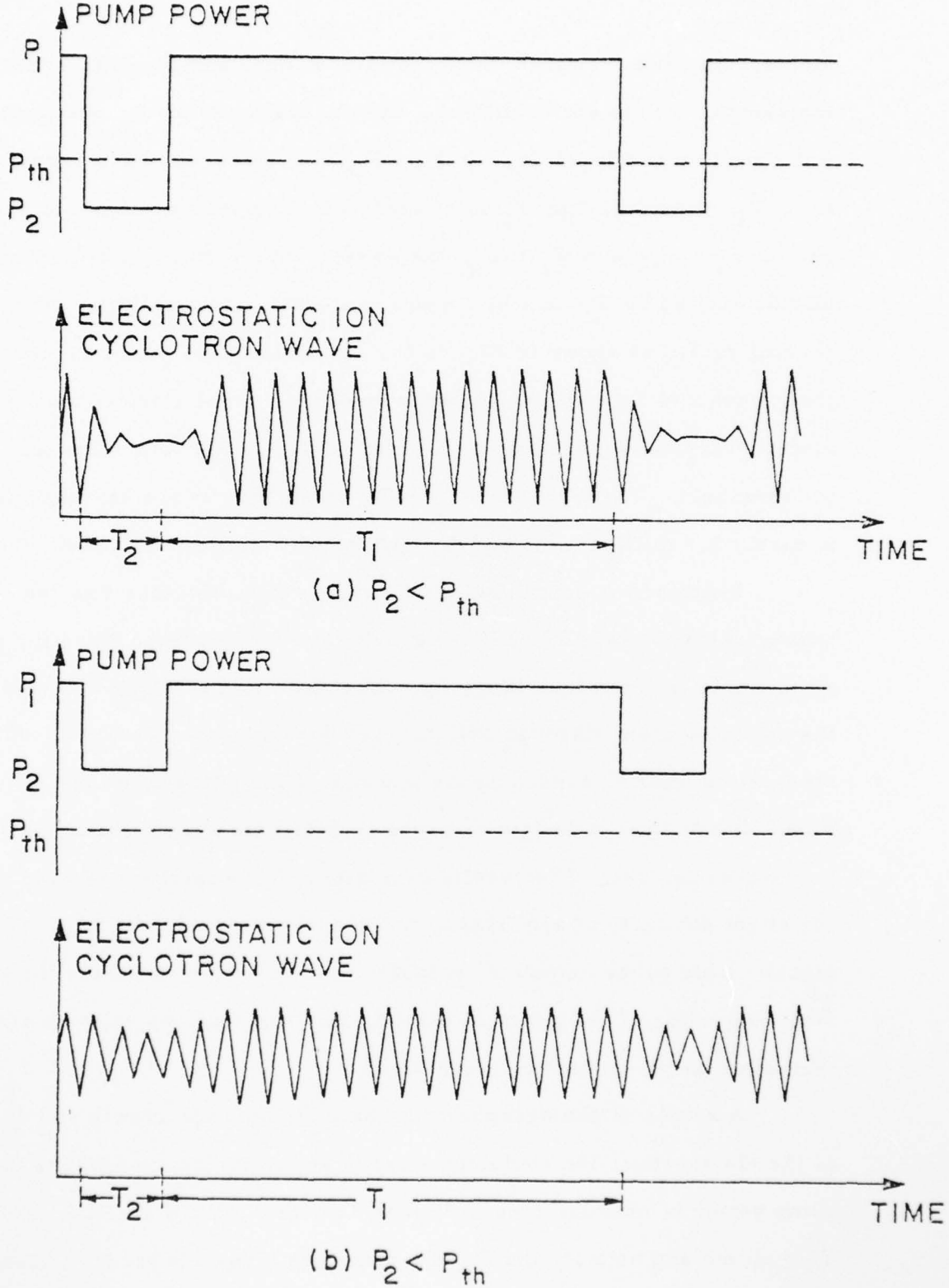

FIGURE 5: GROWTH AND DECAY OF ELECTROSTATIC ION CYCLOTRON WAVES AS A FUNCTION OF PUMP POWER

electrostatic ion cyclotron wave grows to a finite amplitude as shown in the sketch. At the end of time T_1 and the beginning of T_2, the power is switched to a new level P_2. If $P_2 < P_{th}$, the wave decays to zero during time T_2, providing that T_2 is of sufficient duration, as shown in Figure 5a. If $P_2 > P_{th}$ and $P_1 > P_2$, the wave decays during T_2 from the amplitude excited by P_1 to a new nonzero steady state amplitude corresponding to P_2 as shown in Figure 5b. Modulating the power as described, the growth and decay times, and the amplitude of the electrostatic ion cyclotron wave, are measured as a function of P_2, for both below and above the threshold. The total time $T_1 + T_2$ of the microwave signal is approximately 2.3 milliseconds and T_1 is typically 75% of this period.

Photographs containing many traces of the electrostatic ion cyclotron waves are used to obtain the growth and decay time. Since the plasma beam is isolated by a large vacuum chamber, the signal detected by the optical system (through optical fiber bundles to the photomultiplier tube) is too weak to overcome the inherent noise of the photomultiplier tube. Due to this, a Langmuir probe to detect the electrostatic ion cyclotron waves is used. The results thus obtained are fairly good even with the slight difficulty of synchronizing the excited signal with the modulating signal. This probe detection technique is also used to measure the steady state amplitude of the potential oscillation, thus enabling us to obtain information on the saturation mechanism.

A series of photographs containing the average growth and decay of the electrostatic ion cyclotron wave is shown in Figure 6 where the pump power is modulated as in Figure 5b with T_1 = 1.7 ms and T_2 = .6 ms and both P_1 and P_2 are above the threshold level. First, P_1 is set to a level such that the instability is most coherent with the

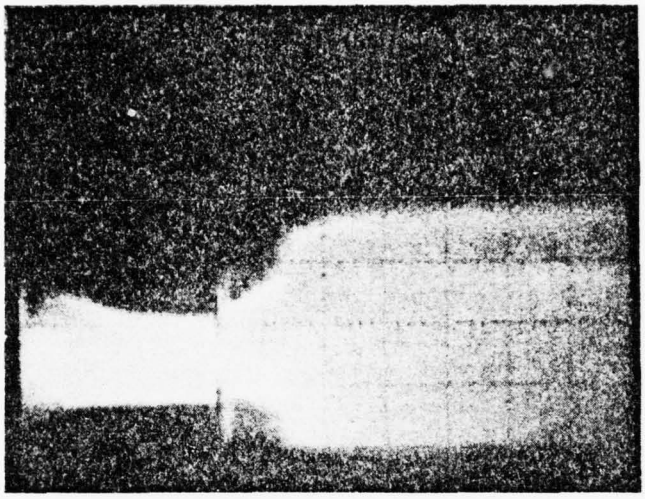

(a) P_2 = 83 W, P_1 = 173 W

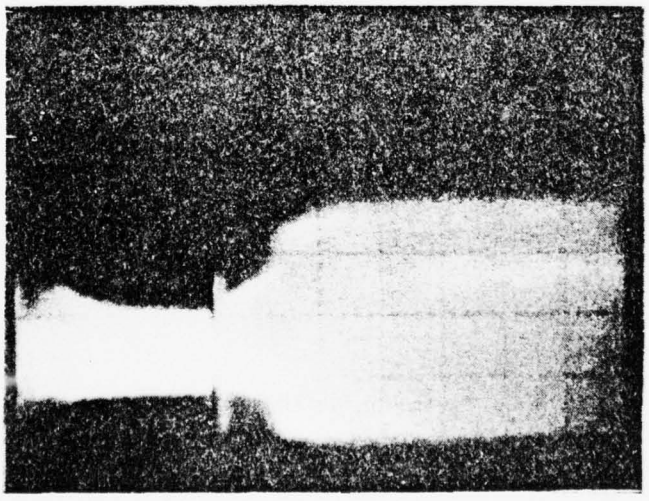

(b) P_2 = 75.5 W, P_1 = 173 W

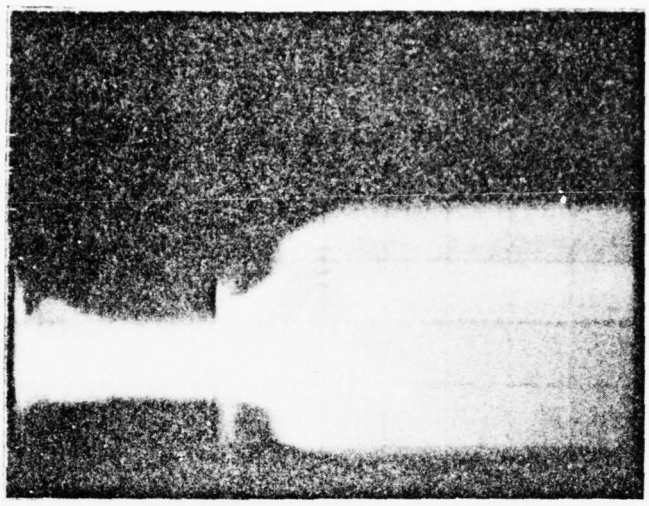

(c) P_2 = 65.5 W, P_1 = 173 W

FIGURE 6: DECAY AND GROWTH OF ELECTROSTATIC ION CYCLOTRON WAVE FROM ONE STEADY STATE AMPLITUDE INTO ANOTHER

P = 1.2μ, f_o = 9.23 GHz, Horizontal Scale = .2 ms/cm

T_2 = .6 ms, T_1 = 1.7 ms

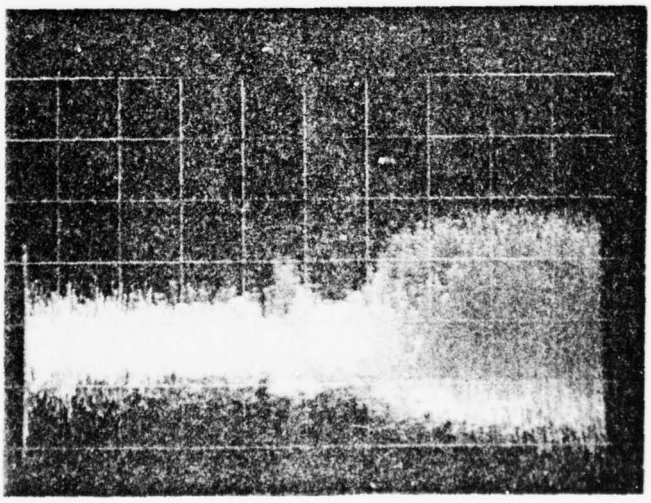

FIGURE 7: PHOTOGRAPH SHOWS THAT THERE IS A TRANSITION PERIOD BEFORE WAVE REALLY STARTS TO GROW

lowest possible neutral gas pressure. We then progressively increase the voltage amplitude of the modulating signal (which is applied to the PIN diode switch) to lower the P_2 level, and the series of photographs are taken with the scope trace triggered to start when the power is switched to P_2 level. The initial decay rate of the instability, when power is switched from P_1 to P_2, is difficult to be calculated because of its strong dependence on the initial amplitude of the instability; therefore, the average decay rate as shown in Figure 8 is calculated by averaging over the e-folding time, i. e., the time it takes for the amplitude decreases to 1/e of its initial value. Figure 6 also shows the existence of a transient before the wave starts to grow. This may be explained by noting that during both T_1 and T_2 of the growth experiments, the electron-neutral collision frequency is much larger than the average decay rate of the electrostatic ion cyclotron wave shown in the Figure 8. During T_2 the electron temperature of the plasma is lowered because of decrease in pump power, and at the end of T_2, the electron temperature rises back quickly to its original level, but it takes finite time for the frequency of the instability to switch back. A typical multiple trace photograph shown in Figure 7 clearly displays this kind of delay phenomenon. Nevertheless, the linear relation between the initial growth rate y and P_2 is clearly demonstrated in Figure 9. The curve in Figure 8 shows that as P_2 progressively decreases, (as noted in the series of photographs) the decay rate increases. Eventually P_2 reaches a power level such that it takes the wave the period T_2 to decay to zero as shown in Figure 10, and this corresponds to the threshold power.

Decreasing T_2 and increasing the total period $T_1 + T_2$ (i. e., decreasing the modulation frequency) of the microwave signal, it is possible

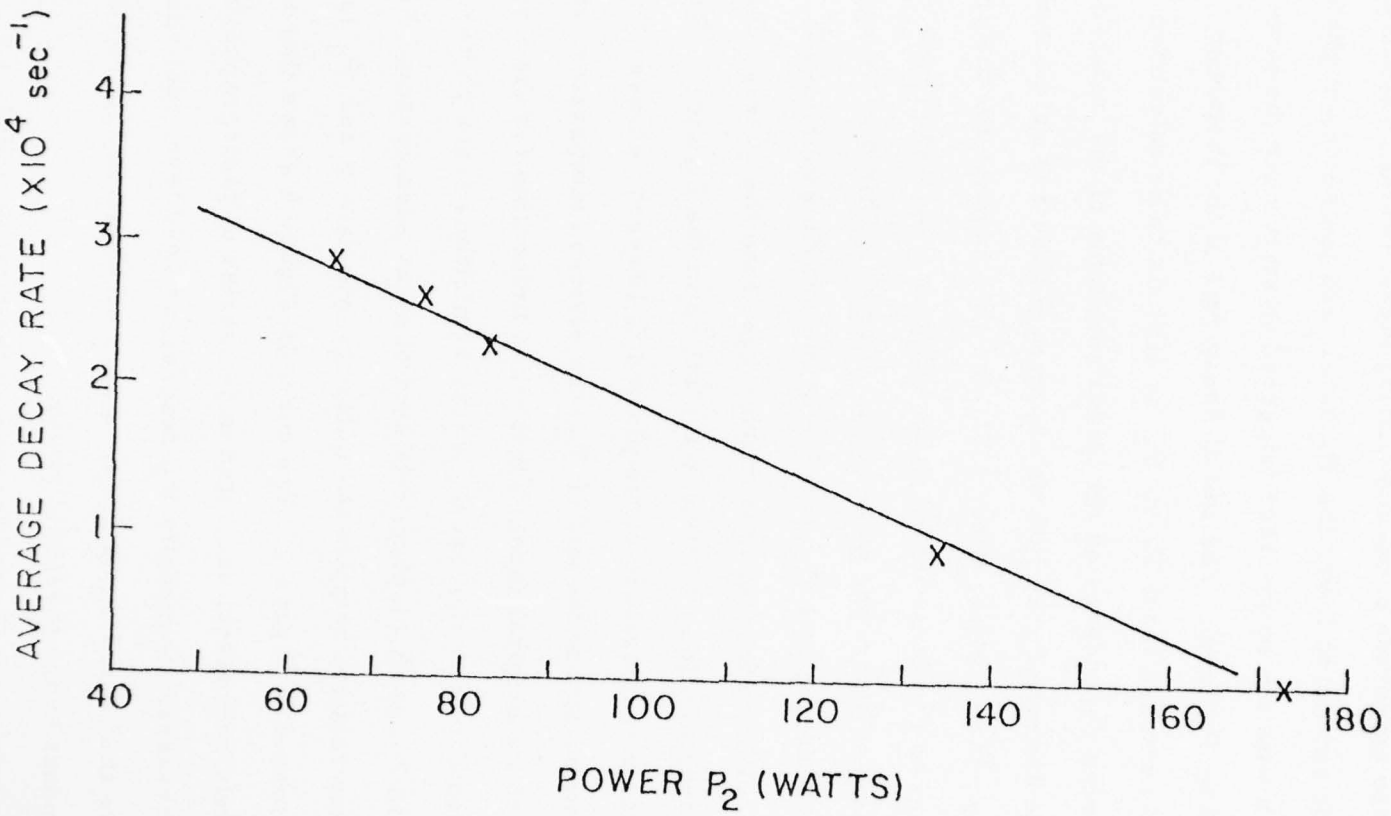

FIGURE 8: AVERAGE DECAY RATE OF ELECTROSTATIC ION CYCLOTRON WAVE AS A FUNCTION OF POWER P_2 WITH P_1 = 173 W FIXED P = 1.2 μ f_o = 9.23 GHz.

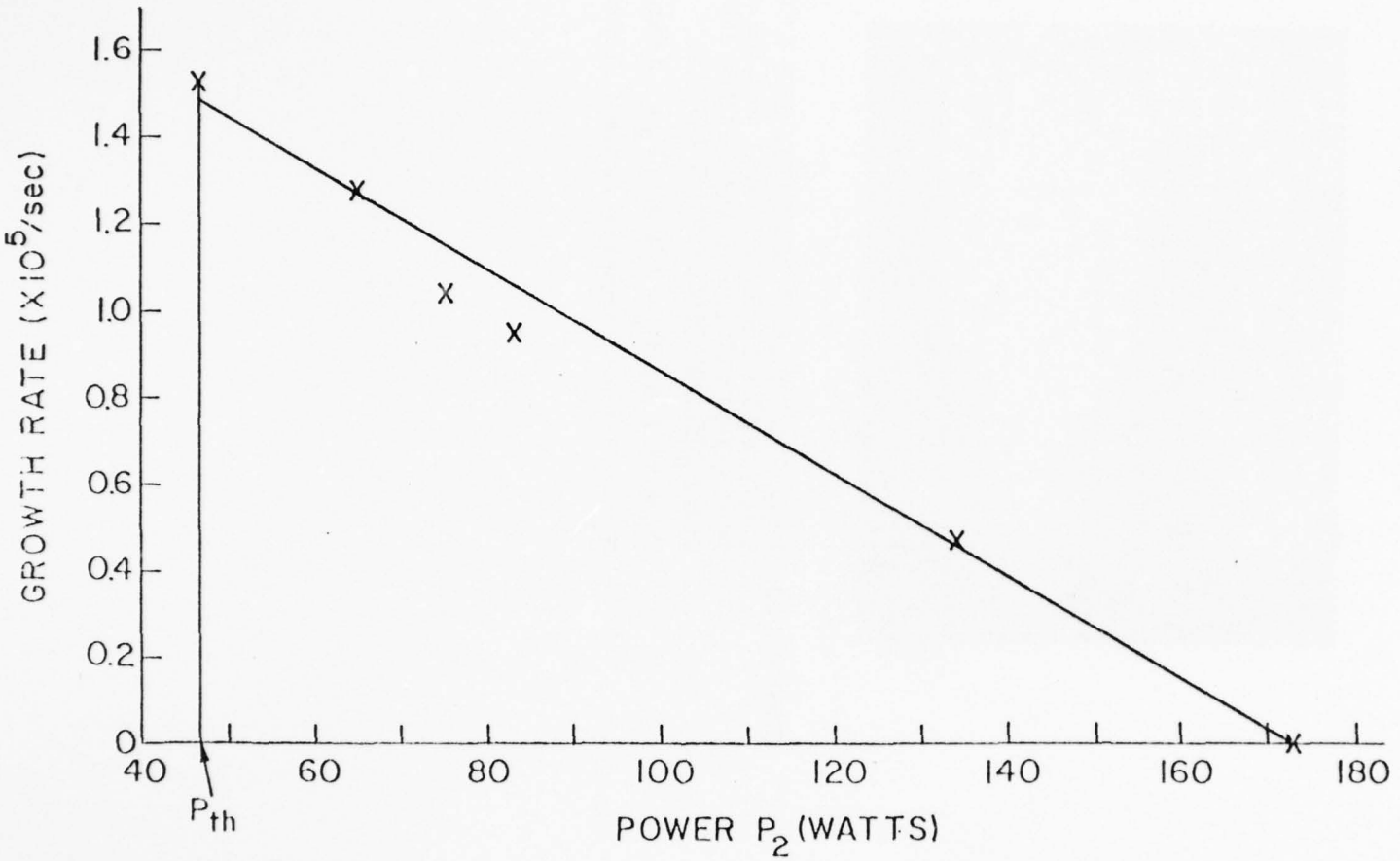

FIGURE 9: INITIAL GROWTH RATE OF ELECTROSTATIC ION CYCLOTRON WAVE FROM ONE STEADY STATE AMPLITUDE TO ANOTHER AS A FUNCTION OF POWER P_2: P_1 = 173 W, P = 1.2 μ f_o = 9.23 GHz

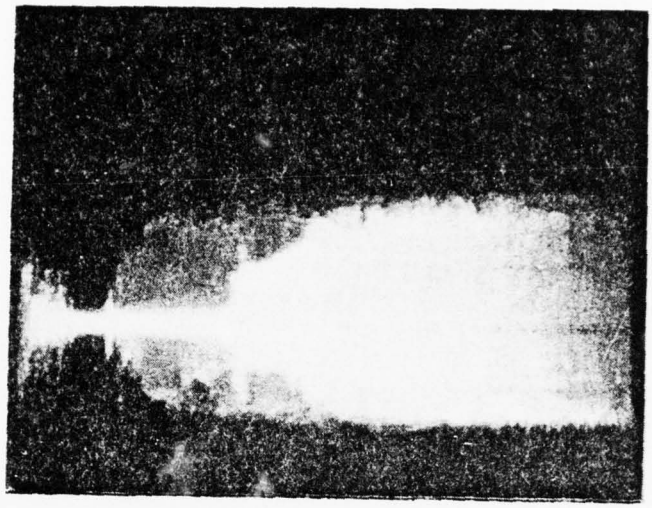

FIGURE 10: DECAY OF ELECTROSTATIC ION CYCLOTRON WAVE FROM STEADY STATE AMPLITUDE INTO NOISE FOR PUMP POWER JUST BELOW THRESHOLD LEVEL

P_2 = 47.1 W, P_1 = 141 W, T_2 = .2 ms, T_1 = 2.1 ms, Horizontal Scale = .1 ms/cm

to lower the power level P_2 to almost zero. Single and multiple traces photographs shown in Figure 11 display the growth (and decay) of the electrostatic ion cyclotron wave as power P_2 is varied from 0 watt to 173 watts. Only a portion of the total period is shown in the photograph. The wave starts to grow only with the pump power exceeding the threshold level, and it becomes an eigenmode of the collisional plasma. During the initial buildup of the potential oscillation, the energy density arising from spontaneous emission of the background plasma is comparable to the energy density produced by the parametric interaction. Therefore, to determine the initial growth rate we must calculate the growth time only after the wave has a small finite amplitude. This value is also shown in Figure 9, and is consistent with the theoretical calculation from equation (4.17).

There are two kinds of damping in our system. Linear or natural damping occurs when the pump is below the threshold level. Once the threshold level is exceeded, the amplitude of the instability would theoretically grow to infinity. However, due to the nonlinear damping, the wave always reaches a saturated state. Therefore, the nonlinear damping would exactly balance the initial growth rate of the wave at that particular power level. If the pump power is suddenly reduced to zero as in the case in Figure 11b, its initial decay rate must be equal to the sum of the linear damping rate and the initial growth rate of Figure 11a. Hence we have a linear damping rate of about $0.6 \times 10^5 \text{ sec}^{-1}$ for the electrostatic ion cyclotron waves; this value is consistent with the value calculated from the tail of the decay diagram. From this value, we can conclude that the linear damping mechanism is due to ion-neutral collisions with the ion temperature of about 0.6 eV. This value of ion temperature

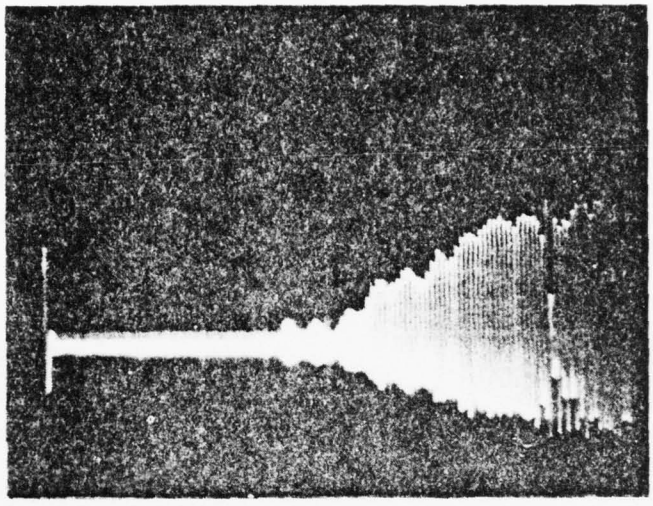

(a) SINGLE-SHOT PHOTOGRAPH
P_2 = 0 W, P_1 = 173 W, P = 1.2 μ,
Horizontal Scale = 50 μs/cm

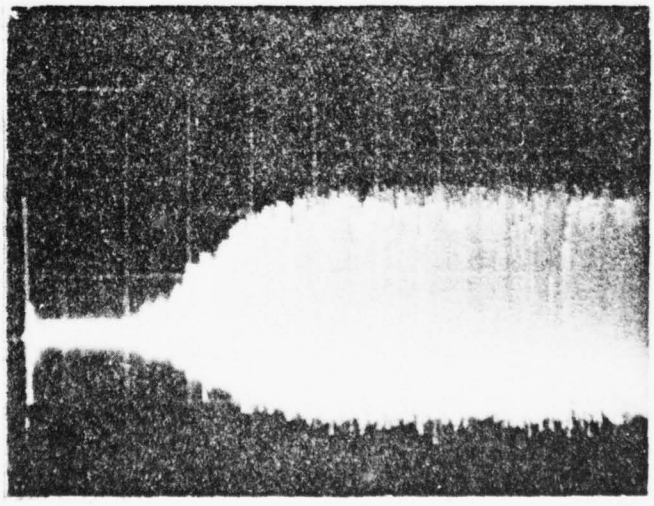

(b) MULTIPLE-TRACE PHOTOGRAPH
P_2 = 0 W, P_1 = 173 W, P = 1.2 μ
Horizontal Scale = .1 ms/cm

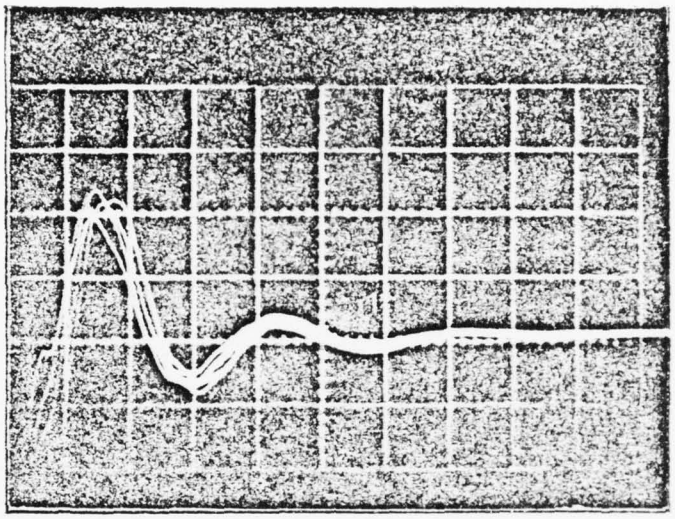

(c) MULTIPLE-TRACE PHOTOGRAPH
P_1 = 173 W, P_2 = 0 W, P = 1.2 μ
Horizontal Scale = 2 μs/cm

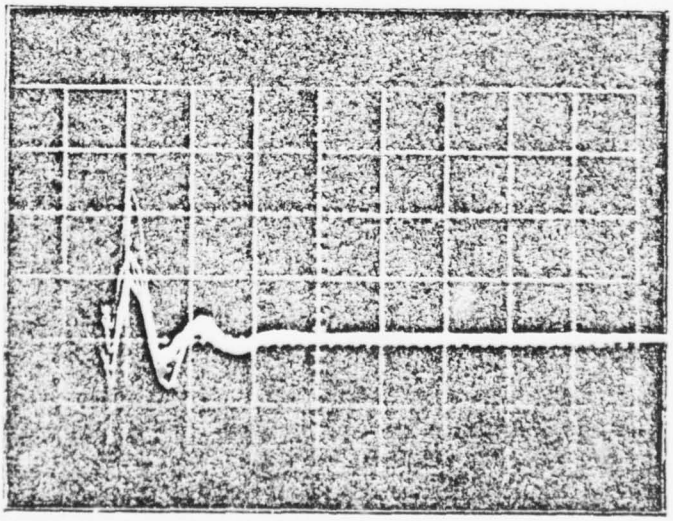

(d) P_1 = 173 W, P_2 = 0 W, P = 1.2 μ
Horizontal Scale = 5 μs/cm

FIGURE 11: GROWTH AND DECAY OF ELECTROSTATIC ION CYCLOTRON WAVE FOR P_1 = 173 W AND P_2 = 0 W

has been verified experimentally in Kristal's[26] thesis by using a Fabry-Perot interferrometer.

3. Frequency of Electrostatic Ion Cyclotron Wave as a Function of Pump Power

The frequency shift of the electrostatic ion cyclotron wave due to pump power has also been investigated. These experiments are conducted with cw microwave excitation, and the frequency is measured on the low frequency spectrum analyzer.

Electrostatic ion cyclotron frequency is shown as a function of power in Figure 12 for a fixed pressure. As shown in Table 1, the frequency shift is linearly proportional to the change of electron temperature with some discrepancy. This can be explained from the linear parametric theory, which indicates a frequency shift due to finite growth rate. After substituting all the known parameters into equation (4. 20), this discrepancy becomes more evident. However, with a minor correction, the linear relationship between the frequency shift and electron temperature change is clearly shown in Figure 13.

Electron density with the presence of the pump wave is also measured by using the probe technique. As shown in Figure 14 the electron density at the center of the plasma column decreases as the instability increases. But the pump power increases over some level, the ionization rate may cover the enhanced diffusion rate, causing the density to increase again.

4. Summary of Experimental Parameters

Table 2 summarizes the basic experimental parameters. The values given are for a magnetic field of 1. 64 kilograms and for a pressure of 1. 2 μ

AD-A071 017 POLYTECHNIC INST OF NEW YORK FARMINGDALE DEPT OF ELE--ETC F/G 20/9
STUDIES ON THE INTERACTIONS BETWEEN ELECTROMAGNETIC FIELDS AND --ETC(U)
APR 79 B R CHEO, E E KUNHARDT, S P KUO AFOSR-74-2668

UNCLASSIFIED POLY-EE-79-053 AFOSR-TR-79-0752 NL

4 OF 4
AD A071017

END
DATE FILMED
8 -79
DDC

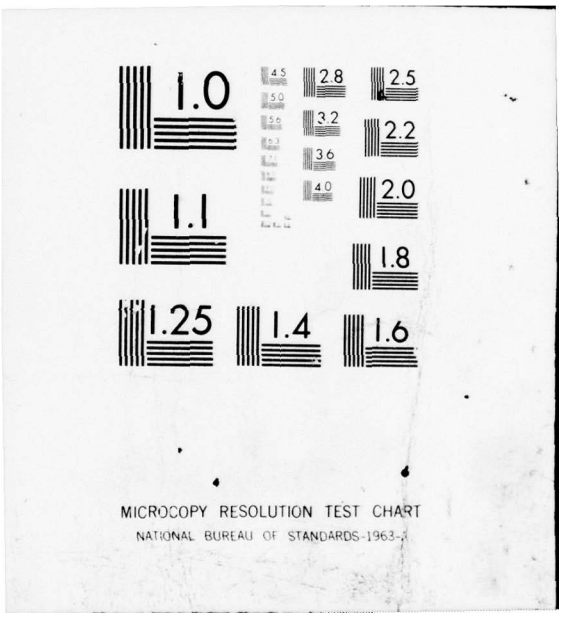
1.0
1.1
1.25
1.4
1.6
1.8
2.0
2.2
2.5
2.8
3.2
3.6
4.0
4.5
5.0
5.6
MICROCOPY RESOLUTION TEST CHART
NATIONAL BUREAU OF STANDARDS-1963-A

TABLE 1 -- EXPERIMENTAL AND THEORETICAL DATA IN SEVERAL PUMP POWER LEVELS								
Pump Power P_1 (watts)	104.5	132.6	144.6	161	193	237	305	498
Frequency of electrostatic ion cyclotron wave f_s' ($\times 10^3$ Hz)		217.4	220.3	226	232.6	243.9	253.2	285.7
Frequency shift with respect to the frequency of 132.6 watts $\Delta f_s'$ ($\times 10^3$ Hz)			2.9	8.6	15.2	26.5	35.8	68.3
Electron temperature T_e (eV)	5.58	5.85	6	6.35	6.63	7.13	7.13	7.9
Frequency shift due to electron temperature increase $\Delta f_1 = \frac{k^2 \Delta T_e}{8\pi^2 f_s M_i 10^3}$ ($\times 10^3$ Hz)			2.49	8.3	12.87	21.17	21.17	34.03
Frequency shift due to finite initial growth rate $\Delta f_2 = \frac{\Gamma_s^2}{8\pi^2 \times 10^3 f_s}\left[\left(\frac{E_o^2}{E_c^2}\right)^2 - 1\right]$ ($\times 10^3$ Hz)		1.9	2.32	3.11	4.39	6.83	11.6	31.75
$\Delta f_1 + \Delta f_2 - 1.9$ ($\times 10^3$ Hz)			2.91	9.35	15.36	26.1	30.9	63.9
plasma density $n_e = n_i = n_o$ ($\times 10^{12}/cm^3$)	.88	.82	.77	.79	.80	.80	.82	.87

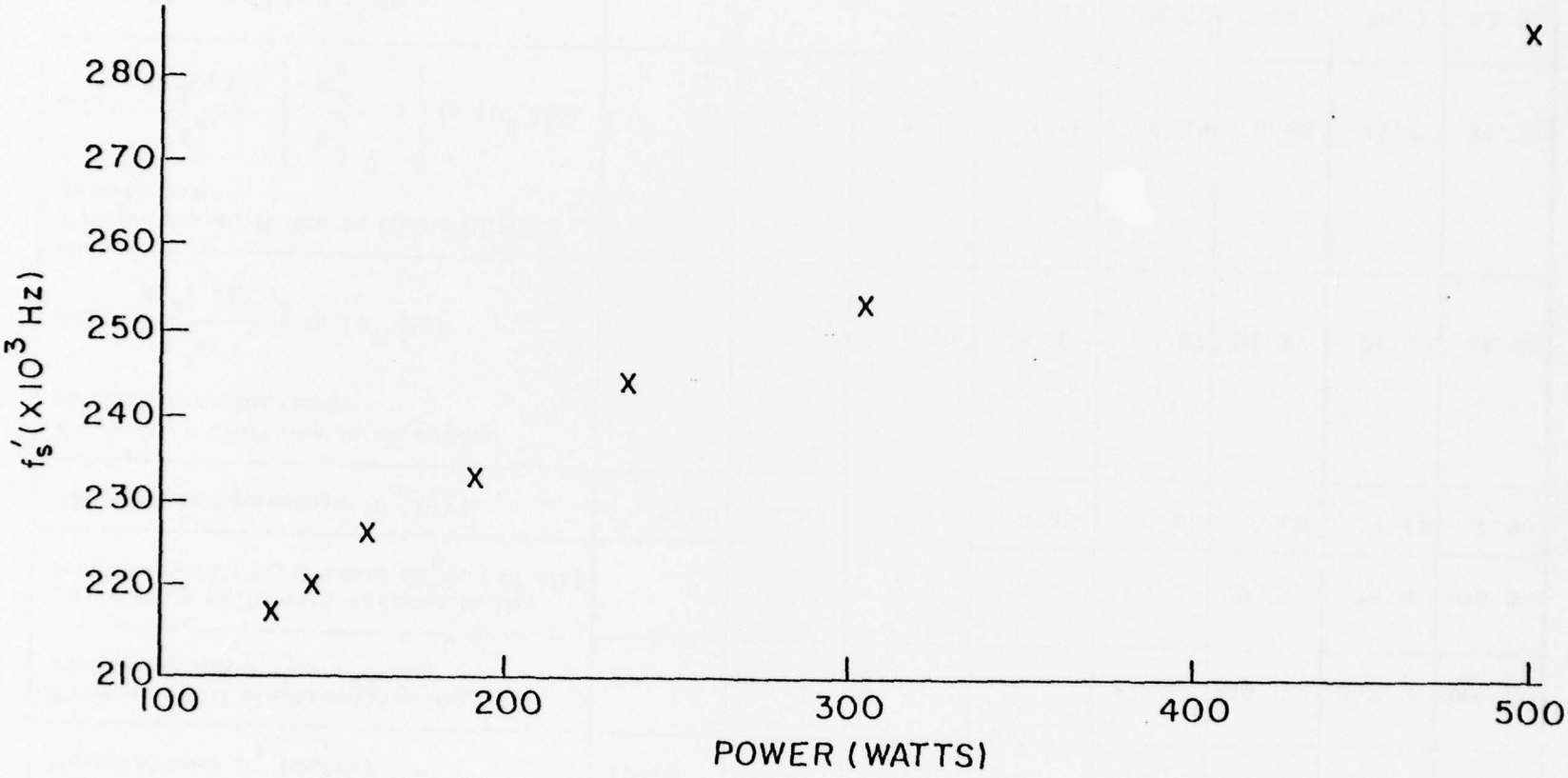

FIGURE 12: FREQUENCY OF ELECTROSTATIC ION CYCLOTRON WAVE AS A FUNCTION OF PUMP POWER

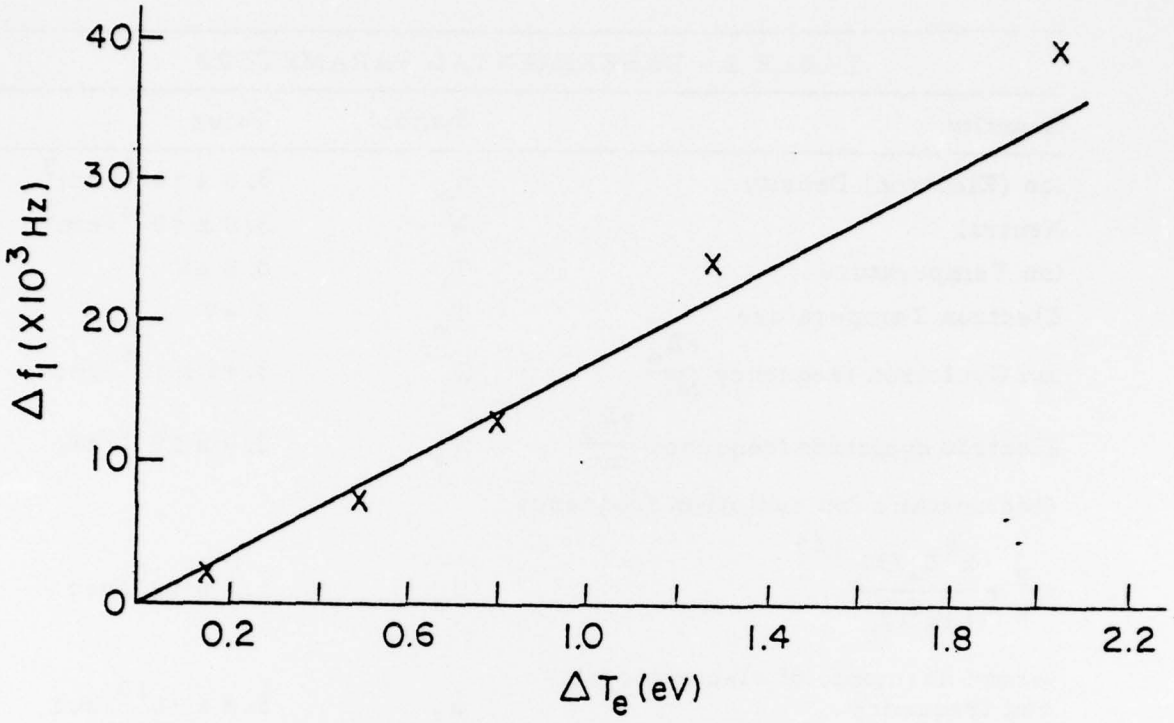

FIGURE 13: MEASURED ELECTROSTATIC ION CYCLOTRON FREQUENCY SHIFT AS A FUNCTION OF ELECTRON TEMPERATURE CHANGE

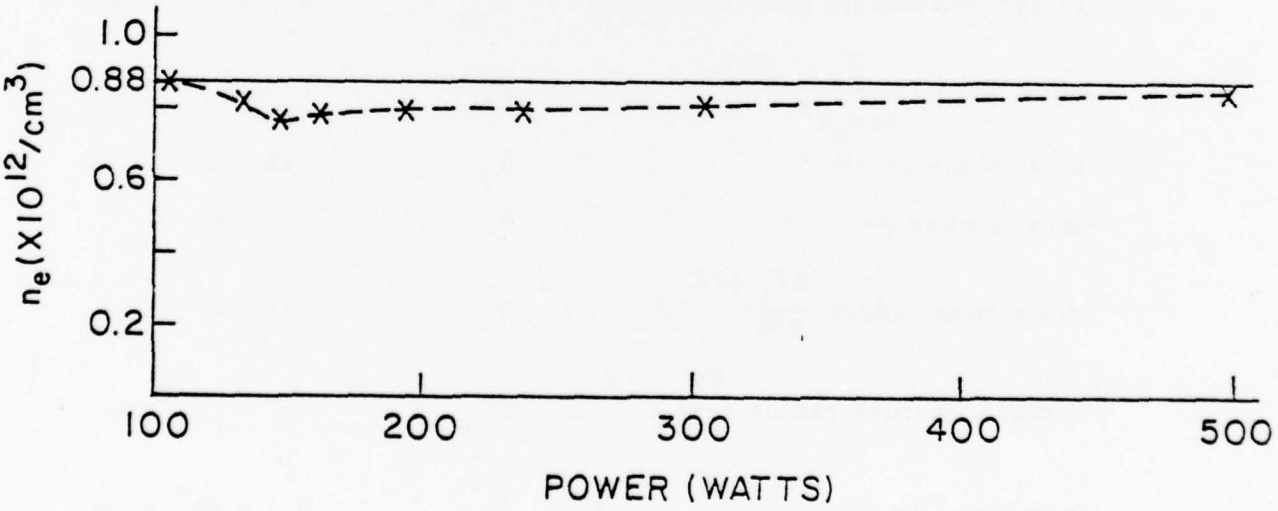

FIGURE 14: PLASMA DENSITY AS A FUNCTION OF PUMP POWER

TABLE 2 - EXPERIMENTAL PARAMETERS

Quantity	Symbol	Value
Ion (Electron) Density	n_o	$8.8 \times 10^{11}/cm^3$
Neutral	N	$3.9 \times 10^{13}/cm^3$
Ion Temperature	T_i	0.6 eV
Electron Temperature	T_e	6 eV
Ion Cyclotron frequency $\frac{eB_o}{Mc}$	Ω_i	3.95×10^5/sec
Electron cyclotron frequency $\frac{eB_o}{mc}$	Ω_e	2.9×10^{10}/sec
Electrostatic Ion cyclotron frequency $\Omega_i^2 + \frac{k^2 T_e/M}{1+k^2\lambda_D^2})^{1/2}$	ω_s	1.3×10^6/sec
Second harmonic of electron cyclotron frequency	ω_ℓ	5.8×10^{10}/sec
Pump frequency	ω_o	5.8×10^{10}/sec
Ion-neutral collision frequency	$\nu_{in} = 2\Gamma_s$	1.2×10^5/sec
Electron-neutral collision frequency	$\nu_{en} = 2\Gamma_\ell$	5.2×10^6/sec
Ion plasma frequency $(\frac{4\pi n_o e^2}{M})^{1/2}$	ω_{pi}	1.95×10^8/sec
Electron plasma frequency $(\frac{4\pi n_o e^2}{m})^{1/2}$	ω_{pe}	5.3×10^{10}/sec
Debye length $(\frac{T_e}{4\pi n_o e^2})^{1/2}$	λ_D	1.94×10^{-3} cm
Radial scale length	λ_r	.48 cm
Wave number $\frac{\pi}{\lambda_r}$	k	3.3/cm
Ion Larmor radius $(\frac{8T_i}{\pi M})^{1/2}/\Omega_i$	r_{Li}	.48 cm
Electron Larmor radius $(\frac{8T_e}{\pi m})^{1/2}/\Omega_e$	r_{Le}	$.57 \times 10^{-2}$ cm
Ion thermal speed $(\frac{3T_i}{M})^{1/2}$	V_{Ti}	2.1×10^5 cm/sec
Electron thermal speed $(\frac{3T_e}{m})^{1/2}$	V_{Te}	1.8×10^8 cm/sec
Ion mass	M	6.68×10^{-23} gram
Electron mass	m	0.91×10^{-27} gram

Note that ν_{in} includes charge transfer, which accounts for about half of the total collision rate. A cross-section of 1.3×10^{-14} cm^2 is used in the calculations.

5. Evidence of Parametric Excitation of Electrostatic Ion Cyclotron Wave

Experimental evidence and data are presented here to show that the electrostatic ion cyclotron waves are indeed parametrically excited by the microwave pump. It is found that:

a. The polarization of the excited low frequency wave is in the direction perpendicular to the dc magnetic field.

b. It is a standing wave.

c. The excited low frequency wave is the electrostatic ion cyclotron wave.

d. The excited waves start to grow only when the microwave pump reaches threshold power.

e. Its growth and decay rates follow the theoretical linear dependence with power as predicted by parametric theories.

a. First the axially movable probe is calibrated with respect to the radially movable one. Then both probes are used to measure the field strength of the wave at the same point but in two different polarizations. We find that the axial field is much smaller than the field component in the direction transverse to the dc magentic field.

b. Using the radially movable probe to measure the amplitude of the transverse field as a function of the radial position, the amplitude is found to be maximum at the center and reduces to zero just outside the plasma beam. Hence we conclude this excited mode is of standing wave type, and its wave number may be calculated from the diameter of the plasma beam.

c. To support the contention that the excited low frequency wave is electrostatic ion cyclotron wave, we note that the observed frequency is almost independent of the plasma density and dc magnetic field; therefore the possibility of exciting lower hybrid wave or harmonics of ion cyclotron wave is excluded. We also note that the observed electrostatic ion cyclotron frequency matches the one determined by the linear dispersion relation with known wavenumber, electron temperature, ion mass and dc magnetic field. Since the linear dispersion relation of the electrostatic ion cyclotron wave is

$$\omega^2 = \Omega_i^2 + k^2 \frac{T_e}{M_i} \Big/ 1 + k^2 \lambda_D^2$$

the frequency shift due to the change of electron temperature may be expressed as

$$\Delta f = \frac{k^2}{4\pi\omega M_i} \Delta T_e$$

This linear relationship has been shown in Figure 13.

d. Multiple trace photographs shown in Figure 6 and Figure 10 display both decay and growth phenomena of the electrostatic ion cyclotron wave. Decay waves have finite steady state amplitude only for pump powers above a threshold.

e. Possibly the most convincing evidence of parametric excitation of the electrostatic ion cyclotron wave lies in the main theme of this effort, i. e., the growth and decay rates of the excited ion acoustic waves are linearly related to pump power as shown in Figures 8 and 9.

6. Simplified Theoretical Explanation

The linear parametric theory derived in the preceding chapter gives us a consistent prediction of threshold power and initial growth rate. Since it does not include the saturation effects, it fails to describe the growth or decay of the unstable wave from one saturated amplitude to another. Nevertheless, the result given in Eq. (4.19) leads us to propose a phenomenological model for wave growth and decay in the presence of saturation effects as the pump power is near threshold. The amplitude A of the electrostatic ion cyclotron wave may be governed phenomenologically as

$$\frac{dA}{dt} = \Gamma_s \left[\frac{E_o^2}{E_c^2} - 1 \right] A - c_3 A^{n+1} \qquad (5.1)$$

where E_o^2 is the square of the electric field in the plasma produced by the pump and E_c^2 is the square of the threshold field. Γ_s is the linear

damping rate and $c_3 A^n$ is the phenomenological nonlinear damping rate and n is an integer of unknown value which may be determined from the experimental data.

The exact solution of (5.1) for $n > 0$ is

$$A(t) = \frac{A_o e^{yt}}{\left[1 + \frac{A_o^n c_3}{y}(e^{nyt} - 1)\right]^{1/n}} \tag{5.2}$$

where $y = \Gamma_s \left[\frac{E_o^2}{E_c^2} - 1\right]$ is the linear growth (or decay) rate and $A_o = A(0)$ is the initial amplitude of the wave.

As $t \to \infty$

$$A^n(\infty) = \frac{y}{c_3} = \frac{\Gamma_s(\frac{E_o^2}{E_c^2} - 1)}{c_3} > 0 \quad \text{for} \quad y > 0 \tag{5.3}$$

and

$$A(\infty) = 0 \qquad \text{for} \quad y < 0 \tag{5.4}$$

Hence the value of n can be experimentally determined by plotting the n^{th} power of the steady state amplitude of the electrostatic ion cyclotron wave as a function of pump power for $y > 0$ as shown in Figure 15. With $n = 2$, this graph becomes linear, and is in agreement with the prediction of (5.3). Setting $n = 2$ in (5.2) and (5.3), we obtain

$$A(t) = \frac{A_o e^{yt}}{\left[1 + \frac{A_o^2 c_3}{y}(e^{2yt} - 1)\right]^{1/2}} \tag{5.5}$$

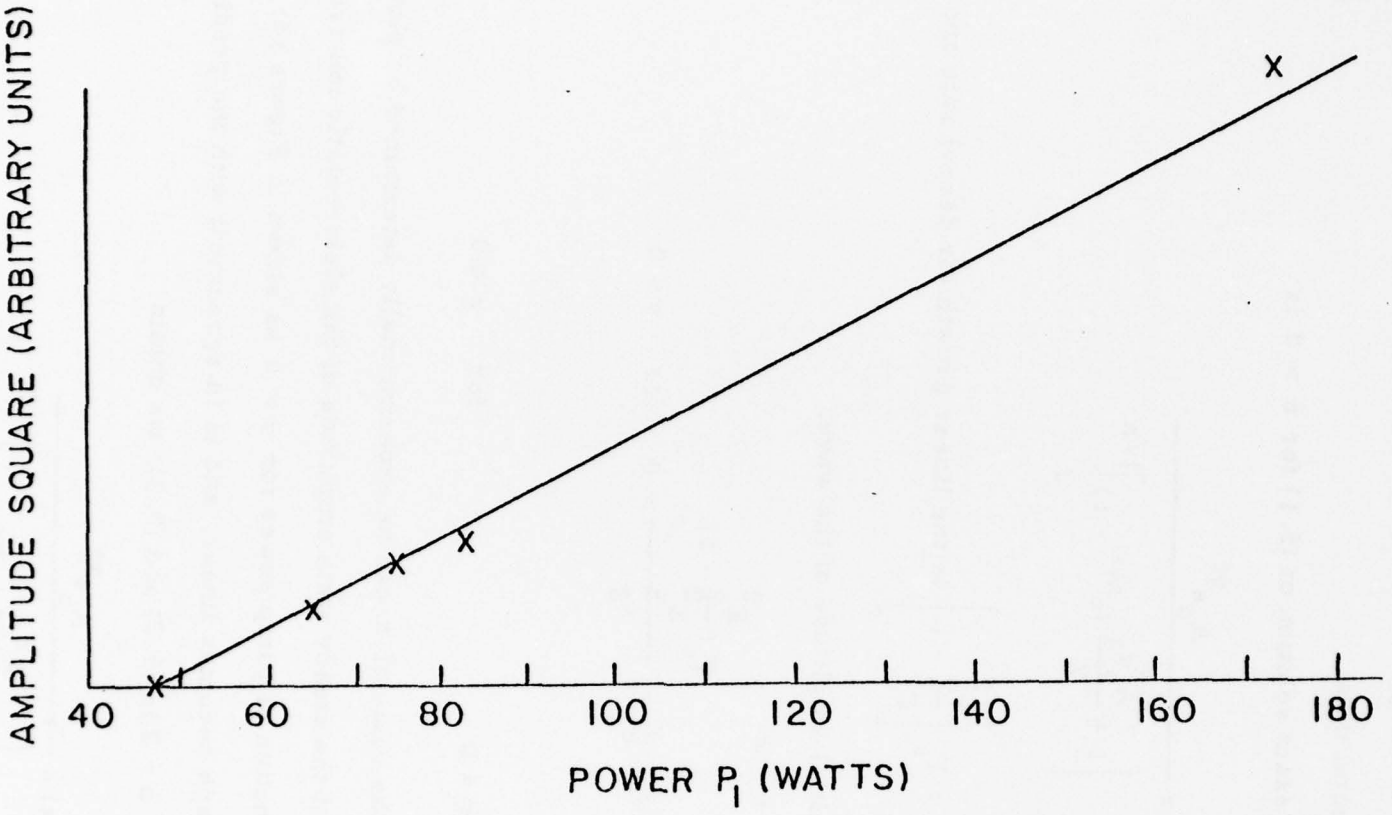

FIGURE 15: SQUARE OF THE SATURATED AMPLITUDE OF THE ELECTROSTATIC ION CYCLOTRON WAVE AS A FUNCTION OF PUMP POWER FOR POWER ABOVE THRESHOLD.

and

$$A(\infty) = \left(\frac{y}{c_3}\right)^{1/2} = \left[\frac{\Gamma_s\left(\frac{E_o^2}{E_c^2} - 1\right)}{c_3}\right]^{1/2} \quad \text{for} \quad y > 0 \tag{5.6}$$

respectively.

Now we proceed to explain the experimental results shown in Figures 8 and 9 by using (5.1).

Assuming the pump power is switched from P_1 to P_2 (or P_2 to P_1) as in the case shown in Figure 5b, then the wave decays (or grows) from original steady state amplitude $A(0)$ to another steady state amplitude $A(\infty)$.

Rewriting Eq. (5.1) as

$$\frac{dA}{dt} = \left[\Gamma_s\left(\frac{E_1^2}{E_c^2} - 1\right) - c_3A^2\right]A = \left[\Gamma_s\left(\frac{E_1^2 - E_2^2}{E_c^2}\right) + c_3(A_o^2 - A^2)\right]A \tag{5.7}$$

for the growth case

where E_1 and E_2 are the field corresponding to P_1 and P_2 respectively, and $A_o^2 = \dfrac{\Gamma_s\left(\frac{E_2^2}{E_c^2} - 1\right)}{c_3}$ is the steady state amplitude of electrostatic ion cyclotron wave at P_2 power level, and

$$\frac{dA}{dt} = \left[\Gamma_s\left(\frac{E_2^2}{E_c^2} - 1\right) - c_3A^2\right]A = -\left[\Gamma_s\left(\frac{E_1^2 - E_2^2}{E_c^2}\right) + c_3(A^2 - A_o^2)\right]A \text{ for}$$

decay case (5.8)

where $A_o^2 = \dfrac{(\frac{E_1^2}{E_c^2} - 1)\Gamma_s}{c_3}$ is the steady state amplitude of electrostatic ion cyclotron wave at P_1 power level.

Then Eqs. (5.7) and (5.8) show that the initial growth rate (or decay rate) is linearly proportional to the power level P_2.

V-6. NONLINEAR SATURATION MECHANISM

1. Introduction

We have so far considered only linear parametric theory and a phenomenological nonlinear equation which describes the low frequency unstable wave. Since saturation phenomenon is always present in experiments, an important question must be raised in order to describe the kind of nonlinear damping mechanisms which cause the instabilities to saturate. There have been earlier attempts to describe the mechanism as due to induced scattering[27, 28], and cascading[29, 30, 31] of the side band into even lower frequency waves and resonance broadening[32]. Other possible mechanisms include pump depletion and quasi-linear effects (i.e., heating). There is no generalization to be applied, because the nonlinear effects may vary for different experimental systems. As an example, if one nonlinear damping mechanism, among other competing phenomena, becomes dominant and cause to saturate before the pump depletion, then we must rule out pump depletion due to priority, or if the unstable wave is coherent, then we must reject the mechanism due to the cascading of the sideband. Therefore, the dominance among different mechanisms depends greatly on the geometry of the individual system, and the mode-types involved. Disregarding the effect of inhomogeneity, systems may be classified into three classes:

(1) Infinite plasma

When the dimensions of the plasma is much larger than the wavelength of the instabilities, boundary conditions need not be considered. Therefore, the excited modes are traveling waves, and the spectrum may be strongly broaded. In such a case, the saturation of instabilities may be due to the pump being depleted to the threshold level. Another possibility

is the interaction of the excited large-amplitude oscillations among themselves, causing a continuous flow of energy toward the large wave number region. This oscillation energy is eventually dissipated into heat by collisional damping, or via collective effects. The threshold level of the instability is thus increased, and a nonlinear saturated state may eventually be reached.

(2) Bounded plasma with sheath

If the spectra of the excited modes are sharply defined because of the confines of the boundary, the potential oscillations of the low frequency waves may carry the ion bunch into the sheath region. Therefore, recombination of ion bunches at the sheath may be the dominant nonlinear damping mechanism in this case. Since the recombination rate is linearly proportional to the density of the ion bunch, this nonlinear damping process corresponds to the n=1 case.[24]

(3) Bounded plasma without sheath

Excited modes are of the standing wave type, producing a well defined frequency spectra. From supercritical stability theory, anomalous diffusion of the plasma due to the low frequency unstable oscillations may be one of the nonlinear damping mechanisms, which corresponds to n=2 case. Another possible mechanism is the nonlinear harmonic (or subharmonic) generation, with second harmonic generation corresponding to n= 2 case.

2. Theory

In this section the description of the nonlinear damping mechanisms for case (3), bounded plasma without sheath, will be given. The experimental results in Chapter V show that (a) a density decrease in the central portion of the plasma column coincides with an increase in amplitude of

the instability. When pump power is increased over a certain level, the ionization rate would cover the enhanced diffusion rate, causing the density to increase. (b) Harmonics of the instability are also excited. The amplitude relative to that of the fundamental is small if the pump level is low, but increases with an increase in pump power.

It should be pointed out that since the excited mode is an electrostatic ion cyclotron wave, these harmonics are still in the resonance region, and they have the same linear damping rate as that of the fundamental mode. Neglecting the nonlinear damping of the harmonics, the nonlinear damping rate of the fundamental instability due to its harmonic generation may be defined as follows

$$2\Gamma_{s1}^{N}\left|\delta E_s(\underline{k},\omega_s)\right|^2\Delta\omega_{s1} = 2\Gamma_s\{\left|\delta E_s(2\underline{k},2\omega_s)\right|^2\Delta\omega_{s2}+\left|\delta E_s(3\underline{k},3\omega_s)\right|^2\Delta\omega_{s3}+..\} \tag{6.1}$$

or

$$\Gamma_{s1}^{N} = \Gamma_s\{\frac{\Delta\omega_{s2}}{\Delta\omega_{s1}}\left|\frac{\delta E_s(2\underline{k},2\omega_s)}{\delta E_s(\underline{k},\omega_s)}\right|^2+\frac{\Delta\omega_{s3}}{\Delta\omega_{s1}}\left|\frac{\delta E_s(3\underline{k},3\omega_s)}{\delta E_s(\underline{k},\omega_s)}\right|^2+\ldots\} \tag{6.2}$$

where the left hand side of (6.1) is the effective instability energy depletion rate, and the right hand side is the damping rate of the energy of the excited harmonies in steady state. $\Delta\omega_{si}$ (i=1, 2, 3...) is the bandwidth of each spectrum. Experimental observations indicate that such an infinite series may be truncated after the third harmonic when pump power is not too strong.

Knowing that the nonlinear damping rate in steady state must equal to the initial growth rate. Γ_{s1}^{N} can be calculated from (6.2) and Figure 3,

however, this value is much smaller than the initial growth rate calculated from (4.17). We may conclude that there must exist another kind of non-linear damping mechanism which dominates in the saturation process.

It is well established that diffusion exists in a magnetically confined beam plasma, and usually pure coherent longitudinal modes does not cause an enhanced plasma loss across the magnetic field. With the plasma dimension smaller than the wavelength of the oscillation in question, magnetic field causes the charged particles to gyrate and move towards the side boundary to produce a field which causes the oscillating mode to become elliptically polarized. This induced field may cause an enhanced diffusion. While ordinary diffusion of electrons and ions across a magnetic field is caused by collisions with non-identical particles, it has been observed that certain oscillations seem to enable the plasma to acquire an enhanced diffusion rate. The behavior of a low temperature plasma is then largely governed by the diffusion processes[33] involved, but the anomalous diffusion can be visualized as a consequence of additional particle collision with the electric field of the oscillating instability. This can also be regarded as made of $\underline{E} \times \underline{B}$ drift motion of the particles, and most readily understood from the test - particle point of view. Let's write the equation of motion for a single ion moving in a wave field with the presence of a uniform magnetic field $B_o \hat{z}$ as follows:

$$\frac{d\underline{r}}{dt} = \underline{v}$$

$$M \frac{d\underline{v}}{dt} = e\left\{ \underline{E}(\underline{r}(t), t) + \frac{1}{c} \underline{v} \times B_o \right\} = e\underline{E}(\underline{r}(t), t) + M\Omega_i \underline{v}(\underline{r}(t), t) \times \hat{z} \tag{6.3}$$

and the solution of (6.3) may be expressed as

$$\underline{v}(\underline{r}(t),t) = \underline{\underline{R}}_i(t) \cdot \underline{v}(0) + \frac{e}{M}\int_0^t dt' \, \underline{\underline{R}}_i(t-t') \cdot \underline{E}(\underline{r}(t'),t')$$

$$\underline{r}(t) = r(0) + \frac{1}{\Omega_i}\underline{\underline{L}}_i(t) \cdot \underline{v}(0) + \frac{c}{B_o}\int_0^t dt' \, \underline{\underline{L}}_i(t-t') \cdot \underline{E}(\underline{r}(t'),t') \qquad (6.4)$$

where

$$\underline{\underline{R}}_i(t) = \frac{1}{\Omega_i}\frac{d}{dt}\underline{\underline{L}}_i(t) = \begin{bmatrix} \cos\Omega_i t & \sin\Omega_i t & 0 \\ -\sin\Omega_i t & \cos\Omega_i t & 0 \\ 0 & 0 & 1 \end{bmatrix} \quad \underline{\underline{L}}_i(t) = \begin{bmatrix} \sin\Omega_i t & 1-\cos\Omega_i t & 0 \\ -(1-\cos\Omega_i t) & \sin\Omega_i t & 0 \\ 0 & 0 & \Omega_i t \end{bmatrix}$$

Thus the position $\underline{R}(t)$ of the guiding center is obtained as

$$\underline{R}(t) = \underline{r}(t) - \frac{1}{\Omega_i}\hat{z} \times \underline{v}(t)$$

$$= \underline{R}_o - \frac{c}{B_o}\hat{z} \times \int_0^t dt' \underline{E}(\underline{r}(t'),t) + \hat{z}\left\{v_{\parallel}(0)t + \frac{e}{M}\int_0^t dt'' E_{\parallel}(\underline{r}_i t''),t'')\right\} \qquad (6.5)$$

and the transverse drift velocity of the guiding center is given by

$$\underline{V}_{\perp}(\underline{r}(t),t) = \frac{d\underline{R}_{\perp}(t)}{dt} = -\frac{c}{B_o}\hat{z} \times \underline{E}(\underline{r}(t),t) \qquad (6.6)$$

where

$$\underline{R}_{\perp}(t) = R_{\perp o} - \frac{c}{B_o}\hat{z} \times \int_0^t dt' \underline{E}(\underline{r}(t'),t) \qquad (6.7)$$

with the aid of Eq. (6.5), $\underline{V}_{\perp}(\underline{r}(t),t)$ may be expanded with respect to the center position $\underline{R}(t)$ as

$$\underline{V}_{\perp}(\underline{r}(t),t) = \underline{V}_{\perp}(\underline{R}(t),t) + \frac{1}{\Omega_i}\hat{z} \times \underline{v}(t) \cdot \nabla \underline{V}_{\perp}(\underline{R}(t),t) + \ldots$$

$$= -\frac{c}{B_o}\hat{z} \times \left\{\underline{E}(\underline{R}(t),t) + \frac{1}{\Omega_i}\hat{z} \times \underline{v}(t) \cdot \nabla \underline{E}(\underline{R}(t),t) + \ldots\right\} \qquad (6.8)$$

This would give the following relation immediately

$$\underline{V}_{\perp}(\underline{R}(t),t) = -\frac{c}{B_o}\hat{z}\times\underline{E}\,(\underline{R}(t),t) \tag{6.9}$$

where $\underline{R}_{\perp}(t)$ may be approximately expressed as

$$\underline{R}_{\perp}(t) = R_{\perp o} - \frac{c}{B_o}\hat{z}\times\int_o^t dt'\,\underline{E}\,(\underline{R}(t'),t') \tag{6.10}$$

therefore, in the Euler's coordinate system we have

$$\underline{V}_{\perp}(\underline{R},t) = -\frac{c}{B_o}\hat{z}\times\underline{E}\,(\underline{R},t) \tag{6.11}$$

and

$$V_x(\underline{R},t) = \frac{c}{B_o}E_y\,(\underline{R},t) \tag{6.12}$$

Due to the spatially dependent force field, there is a force difference between two different points, i.e., finite excursion of the oscillating ion brings itself into regions of different field intensity. The explicit expression for the statement above is given by

$$\frac{\partial}{\partial t}V_x(\underline{R}_2,t) - \frac{\partial}{\partial t}V_x(\underline{R}_1,t) = \delta\underline{R}\cdot\nabla\frac{\partial}{\partial t}V_x(\underline{R}_1,t) \tag{6.13}$$

where $\delta\underline{R} = \underline{R}_2 - \underline{R}_1$

now let's define a force due to the force difference

$$\frac{d}{dt}V_x^{(2)}(\underline{R}_1,t) = <\frac{\partial}{\partial t}V_x(\underline{R}_2,t) - \frac{\partial}{\partial t}V_x(\underline{R}_1,t)> = <\delta\underline{R}\cdot\nabla\frac{\partial}{\partial t}V_x(\underline{R}_1,t)> \tag{6.14}$$

where $<\ >$ is meant to ensemble average

let

$$\delta\underline{R} = -\frac{c}{B_o}\hat{z}\times\int_o^t dt'\,\underline{E}\,(\underline{R}_1,t') + \hat{z}\{v_{\parallel}(0)t + \frac{e}{M}\int_o^t dt'\int_o^{t'} dt''E_{\parallel}(\underline{R}_1,t'')\} \tag{6.15}$$

and assume

$$E_y(\underline{R}_1,t) = A_y\cos\underline{k}\cdot\underline{R}_1\sin(\omega t+\phi) \tag{6.16}$$

where $\underline{k} = k\hat{x}$ and ϕ is a random phase which is a constant during the period of two successive collisions.

Substituting (6.15) and (6.16) in eq. (6.14), yields

$$\frac{d V_x^{(2)}(\underline{R}_1, t)}{dt} = < -\frac{c^2}{B_o^2} k A_y^2 [\int_o^t dt' \cos(\underline{k}.\underline{R}_1)\sin(\omega t'+\phi)] \sin(\underline{k}.\underline{R}_1)\cos(\omega t+\phi)\omega >$$

$$= < \frac{c^2}{B_o^2} k A_y^2 \sin \underline{k}.\underline{R}_1 \cos \underline{k}.\underline{R}_1 [\cos(\omega t+\phi) - \cos\phi] \cos(\omega t+\phi) >$$

$$= \frac{c^2}{4B_o^2} k A_y^2 \sin 2\underline{k}.\underline{R}_1 (1-\cos \omega t) \qquad (6.17)$$

therefore, the maximum contribution to $V_x^{(2)}(\underline{R}_1)$ between two successive collisions is

$$V_x^{(2)}(\underline{R}_1) = \frac{c^2}{4B_o^2} k A_y^2 \sin(2\underline{k}.\underline{R}_1)\, \tau_c \qquad (6.18)$$

and with the assumption

$$\omega >> \frac{1}{\tau_c} \qquad (6.19)$$

where τ_c is the collision time.

Because of the spatial dependence of $V_x^{(2)}(\underline{R}_1)$, it will give an additional damping to $V_x(\underline{R}_1, t)$.

In fluid limit, $\underline{R}_1$ is not the initial position of the particle trajectory, it is an independent variable. Thus

$$\frac{\partial \underline{R}_1}{\partial t} = 0 \qquad (6.20)$$

since

$$\frac{\partial}{\partial t} V_x(\underline{R}_1, t) + V_x(\underline{R}_1, t).\nabla[V_x(\underline{R}_1, t) + V_x^{(2)}(\underline{R}_1)] = \frac{c}{B_o} \frac{d}{dt} E_y(\underline{R}_1, t) - \upsilon_{in} V_x(\underline{R}_1, t) \qquad (6.21)$$

This may be written as

$$\frac{\partial}{\partial t} V_x(\underline{R}_1, t) + V_x(\underline{R}_1, t) \cdot \nabla V_x(\underline{R}_1, t) = \frac{c}{B_o} \frac{d}{dt} E_y(\underline{R}_1, t) - \upsilon_{in} V_x(\underline{R}_1, t) - \frac{c^2}{2B_o^2} k^2 A_y \cos(2\underline{k} \cdot \underline{R}_1) \tau_c V_x(\underline{R}_1, t)$$

$$= \frac{c}{B_o} \frac{d}{dt} E_y(\underline{R}_1, t) - \upsilon_{eff} V_x(\underline{R}_1, t) \qquad (6.22)$$

where $\upsilon_{in} = \frac{1}{\tau_c}$,

and

$$\upsilon_{eff} = \upsilon_{in} + \frac{c^2}{2B_o^2} k^2 A_y^2 \cos(2\underline{k} \cdot \underline{R}_1) \tau_c \qquad (6.23)$$

Hence at center, where $\underline{R}_1 = 0$ and

$$\upsilon_{eff} = \upsilon_{in} + \frac{c^2}{2B_o^2} k^2 A_y^2 / \upsilon_{in} \qquad (6.24)$$

Assuming $A_y = \xi A$, where A is the amplitude of E_x and $0 \leq \xi \leq 1$, the nonlinear damping rate Γ_{s2}^N of the electrostatic ion cyclotron wave due to the anomalous diffusion becomes

$$\Gamma_{s2}^N = \frac{c^2}{4B_o^2} k^2 \xi^2 A^2 / 2\Gamma_s \qquad (6.25)$$

3. Comparison between Theory and Experimental Results

As mentioned in Chapter V, the nonlinear damping rate at steady state must equal the initial growth rate. From Figure 9 the initial growth rate $y = 1.5 \times 10^5$/sec for $P_1 = 173$ watts is obtained. The amplitude of the potential oscillation for $P_1 = 173$ watts can be found in Figure 4. Since the amplitude of the potential oscillation is the integration of the amplitude of the field oscillation, then A =1.05xk=3.5 volts/cm is found.

First let's calculate the nonlinear damping rate due to the harmonic generation. From Figure 3 and Eq. (6.2), we find

$$\Gamma_{s1}^{N} = .32\text{x}10^{5}/\text{sec} \tag{6.26}$$

with the aid of Table 2 and Eq. (6.25), we have

$$\Gamma_{s2}^{N} = 10\ \xi^{2}\text{x}10^{5}/\text{sec} \tag{6.27}$$

since

$$\Gamma_{s1}^{N} + \Gamma_{s2}^{N} = y = 1.5\text{x}10^{5}$$

we find

$$\xi = .34 \approx \frac{\Omega_i}{\omega_s} \quad .$$

V-7. CONCLUSIONS

The physical origin of mode coupling mechanism in an infinite plasma is described as electrostrictive effect. Based on this physical viewpoint, a general approach to analyze the parametric decay processes of plasma waves is presented. A set of coupled mode equations is derived by using Hamiltonian approach, and the coupling coefficients are derived from the collisionless Boltzman-Vlasov equation. The threshold for parametric amplification of an electrostatic ion cyclotron mode (longitudinal wave) and a harmonic of electron cyclotron mode (hybrid wave) in the presence of external radiation of an appropriate frequency has been found.

An experiment[34] is performed in a microwave sustained plasma. The properties of the process are in qualitative agreement with the theory. Saturation of the instability is also observed in the experiment, and the nonlinear mechanisms are found to be anomalous diffusion and harmonic generation, again, in agreement with the theoretical results.

V-8. APPENDICES

APPENDIX A: NORMALIZATION OF THE ACOUSTIC MODES

The first step in the quantization procedure is to write down the Hamiltonian density. Let's define a lattice for a homogenous medium of mass density $\rho = n_o M$, where n_o and M are respectively the ion density and mass, then attach a dressed vibrating ion to each lattice point. Let the deviation of the mth ion's position from its equilibrium position x_m be given by q_m, we are led to write for the acoustic modes[35]

$$H = \frac{1}{2} \sum_{m=1}^{n_o} \left[\frac{P_m^2}{M} + C_L (q_{m+1} - q_m)^2 \right] \qquad (A.1)$$

Where for the $m=n_o$ term, $q_{n_o+1} = q_1$ because of the periodic boundary conditions and $P_m = Mq_m$, $x_m = m \left(\frac{1}{n_o} \right)^{\frac{1}{3}}$ and C_L is the force constant. The first term in the brackets corresponds to the kinetic energy of the oscillating ions, the second to the potential energy associated with the Hooke's law force. We shall now proceed to rewrite H so that it has the same form as the Hamiltonian for the linear harmonic oscillator. Let us express the coordinates q_m and momenta P_m in terms of the traveling wave normal mode expansion

$$q_m^{(k)} = \left(\frac{1}{2n_o M \omega'_k} \right)^{\frac{1}{2}} (a_k e^{i\underline{k} \cdot \underline{x}_m}) \text{ and } q_m = \sum_k q_m^{(k)} \qquad (A.2)$$

$$P_m^{(k)} = M q_m^{(k)} = -i \left(\frac{M\omega'_k}{2n_o} \right)^{\frac{1}{2}} (a_k e^{i\underline{k} \cdot \underline{x}_m} - a_k^+ e^{-i\underline{k} \cdot \underline{x}_m}) \text{ and } P_m = \sum_k P_m^{(k)} \qquad (A.3)$$

where we have $\dot{a}_k = -i\omega'_k a_k \qquad \dot{a}_k^+ = i\omega'_k a_k^+$

$$\therefore \sum_{m=1}^{n_o} P_m^2 = \sum_{m=1}^{n_o} (-i) \sum_k \left(\frac{M\omega_k'}{2n_o}\right)^{\frac{1}{2}} (a_k e^{i\underline{k}\cdot\underline{x}_m} - a_k^+ e^{-i\underline{k}\cdot\underline{x}_m})(-i) \sum_{k'} \left(\frac{M\omega_{k'}'}{2n_o}\right)^{\frac{1}{2}} (a_{k'} e^{i\underline{k}'\cdot\underline{x}_m}$$

$$- a_{k'}^+ e^{-i\underline{k}'\cdot\underline{x}_m}) = -\sum_k \frac{\omega_k'}{2} (a_k a_k - a_k a_k^+ - a_k^+ a_k + a_k^+ a_k^+) \qquad (A.4)$$

and

$$\sum_{m=1}^{n_o} (q_{m+1} - q_m)^2 = \sum_k \frac{\omega_k'}{2C_L} (a_k a_k + a_k a_k^+ + a_k^+ a_k + a_k^+ a_k^+) \qquad (A.5)$$

$$\therefore H = \frac{1}{2} \sum_k \omega_k' (a_k a_k^+ + a_k^+ a_k) \qquad (A.6)$$

If a_k and a_k^+ are now defined in terms of the new variables $Q^{(k)}$ and $K^{(k)}$ as follows:

$$a_k = \left(\frac{M}{2\omega_k'}\right)^{\frac{1}{2}} (\omega_k' Q^{(k)} + i \frac{K^{(k)}}{M}) \qquad (A.7)$$

$$a_k^+ = \left(\frac{M}{2\omega_k'}\right)^{\frac{1}{2}} (\omega_k' Q^{(k)} - i \frac{K^{(k)}}{M}) \qquad (A.8)$$

then above Hamiltonian reduces to the harmonic oscillator form

$$H = \frac{1}{2} \sum_k \left[\frac{K^{(k)2}}{M} + M\omega_k'^2 Q^{(k)2}\right] . \qquad (A.9)$$

With the Hamiltonian in the form above we proceed to quantize the acoustic vibrations by postulating that the $Q^{(k)}$, $K^{(k)}$ are operators that satisfy the poisson bracket relations $\{ Q^{(k)}, K^{(k')} \} = \delta_{kk'}$.

Now let us normalize the field produced by the acoustic vibrations

$$n_o e\,\delta E = e\sum_{m=1}^{n_o}\sum_{k}\delta E^{(k)} e^{i\underline{k}\cdot\underline{x}_m} = \sum_{m=1}^{n_o}\sum_{k}\dot{P}_m^{(k)} = -\sum_{k}\sum_{m=1}^{n_o}\omega'_k\left(\frac{\omega'_k M}{2n_o}\right)^{\frac{1}{2}}\left(a_k e^{i\underline{k}\cdot\underline{x}_m} + a_k e^{-i\underline{k}\cdot\underline{x}_m}\right)$$

(A. 10)

$$\because\ e^{-i\underline{k}\cdot\underline{x}_m} = e^{-i\underline{k}\cdot\underline{x}_m - n_o} = e^{i\underline{k}\cdot\underline{x}_{n_o}-m} \quad \therefore \sum_{m=1}^{n_o} e^{i\underline{k}\cdot\underline{x}_{n_o}-m} = \sum_{m=1}^{n_o} e^{i\underline{k}\cdot\underline{x}_m}$$

$$\therefore\ e\sum_{m=1}^{n_o}\sum_{k}\delta E^{(k)} e^{i\underline{k}\cdot\underline{x}_m} = -\sum_{k}\sum_{m=1}^{n_o}\omega'_k\left(\frac{\omega'_k M}{2n_o}\right)^{\frac{1}{2}}\left(a_k + a_k^{+}\right)e^{i\underline{k}\cdot\underline{x}_m}$$

$$= -\sum_{k}\sum_{m=1}^{n_o}\omega'_k\left(\frac{\omega'_k M}{2n_o}\right)^{\frac{1}{2}}(2M\omega'_k)^{\frac{1}{2}} Q^{(k)} e^{i\underline{k}\cdot\underline{x}_m} \qquad \text{(A. 11)}$$

$$= -\sum_{k}\sum_{m=1}^{n_o}\left(\frac{1}{n_o}\right)^{\frac{1}{2}} M\omega'^{2}_k\, Q^{(k)} e^{i\underline{k}\cdot\underline{x}_m}$$

$$\therefore\ \delta E^{(k)} = -\frac{M}{e}\frac{1}{\sqrt{n_o}}\ \omega'^{2}_k\ Q^{(k)} \qquad \text{(A. 12)}$$

Where ω'_k is the resonant frequency of the medium without pump field. If the pump field presents in the medium and near threshold level or above, the resonant frequency will shift to undamped frequency ω_k, in this case we can keep the unperturbed Hamiltonian H_o as before, but change ω'_k to ω_k for the relation between $\delta E^{(k)}$ and $Q^{(k)}$.

$$\therefore\ H_o^{(k)} = \frac{1}{2}\left[\frac{\dot{K}^{(k)2}}{M} + M\omega_k^2\, Q^{(k)2}\right] \qquad \text{(A. 13)}$$

$$\delta E^{(k)} = -\frac{M}{e}\frac{1}{\sqrt{n_o}}\ \omega_k^2\ Q^{(k)} \qquad \text{(A. 14)}$$

It is easy to be generalized to three - dimensional case

$$\therefore\ H_o^{(k)} = \frac{1}{2} \Sigma_\sigma \left[\frac{K_\sigma^{(k)^2}}{M} + M\, \omega_k'^2\, Q_\sigma^{(k)^2} \right] \tag{A.15}$$

$$\delta \underline{E}^{(k)} = - \frac{M}{e} \frac{1}{\sqrt{n_o}}\ \omega_k^2\, \underline{Q}^{(k)} \tag{A.16}$$

We can also generalize above procedure to an anisotropic case, for example, if there is a uniform magnetic field B_o in the z direction

$$\therefore\ H_o^{(k)} = \frac{1}{2}\ \sum_\sigma \left[\frac{K_\sigma^{(k)^2}}{M} + M\ \omega_k'^2\, Q_\sigma^{(k)^2} \right] \tag{A.17}$$

$$\delta \underline{E}^{(k)} = - \frac{M\omega_k^2}{\sqrt{n_o}e}\ \underline{Q}^{(k)} - \frac{\Omega_i}{e\sqrt{n_o}}\ \underline{K}^{(k)} \times \hat{z} \tag{A.18}$$

where we have $\{ Q_\sigma^{(k)}\ ,\ K_\beta^{(k')} \} = \delta_{kk'}\, \delta_{\sigma\beta}$ and $\Omega_i = \frac{eB_o}{Mc}$

APPENDIX B: NORMALIZATION OF THE OPTICAL MODES

Because of the big difference between the masses of electron and ion, ion cannot follow the high frequency electron oscillation, hence we can consider this kind oscillations are optical modes in which electrons and ions vibrate against one another. Let's expand the displacements of the individual electrons in terms of the normal coordinates U^k and A_k, A_k^+

$$\text{i e } \delta\gamma_i = \frac{1}{\sqrt{n_o}} \sum_k U^{(k)} e^{i\underline{k}\cdot\underline{\gamma}_i} = \sum_k \left(\frac{1}{2n_o m\Omega'_k} \right)^{\frac{1}{2}} (A_k e^{i\underline{k}\cdot\underline{\gamma}_i} + A_k^+ e^{-i\underline{k}\cdot\underline{\gamma}_i}) \qquad (B.1)$$

In terms of these normal coordinates we may write the total energy at any time

$$\mathcal{E}_{tot} = \sum_i \left[\frac{m}{2} (\delta\dot{\gamma}_i)^2 + \frac{C_1}{2} (\delta\gamma_i)^2 \right] \qquad (B.2)$$

$$\therefore \quad H = \frac{1}{2} \sum_k \Omega'_k (A_k A_k^+ + A_k^+ A_k) \qquad (B.3)$$

where we have $\dot{A}_k = -i\Omega'_k A_k$, $\dot{A}_k^+ = i\Omega'_k A_k^+$

$$\therefore \frac{1}{\sqrt{n_o}} \sum_{i=1}^{n_o} \sum_k U^{(k)} e^{i\underline{k}\cdot\underline{\gamma}_i} = \sum_k \sum_{i=1}^{n_o} \left(\frac{i}{2n_o m\Omega'_k} \right)^{\frac{1}{2}} (A_k e^{i\underline{k}\cdot\underline{\gamma}_i} + A_k^+ e^{-i\underline{k}\cdot\underline{\gamma}_i})$$

$$= \sum_k \sum_{i=1}^{n_o} \left(\frac{1}{2n_o m\Omega'_k} \right)^{\frac{1}{2}} (A_k e^{i\underline{k}\cdot\underline{\gamma}_i} + A_k^+ e^{-i\underline{k}\cdot\underline{\gamma}_{i-n}})$$

$$= \sum_k \sum_{i=1}^{n_o} \left(\frac{1}{2n_o m\Omega'_k} \right)^{\frac{1}{2}} (A_k e^{i\underline{k}\cdot\underline{\gamma}_i} + A_k^+ e^{i\underline{k}\cdot\underline{\gamma}_{n-i}}) \qquad (B.4)$$

$$= \sum_k \sum_{i=1}^{n_o} \left(\frac{1}{2n_o m\Omega'_k} \right)^{\frac{1}{2}} (A_k + A_k^+) \; e^{i\underline{k}\cdot\underline{\gamma}_i})$$

$$\Longrightarrow \quad U^{(k)} = \left(\frac{1}{2m\Omega'_k} \right)^{\frac{1}{2}} (A_k + A_k^+) \tag{B.5}$$

$$\therefore \mathcal{K}^{(k)} = m \dot{U}^{(k)} = -i \left(\frac{m\Omega'_k}{2} \right)^{\frac{1}{2}} (A_k - A_k^+) \tag{B.6}$$

$$\therefore A_k A_k^+ = \frac{m}{2\Omega'_k} \left(\Omega'^2_k U^{(k)2} - i \frac{\Omega'_k}{m} U^{(k)} \mathcal{K}^{(k)} + i \frac{\Omega'_k}{m} \mathcal{K}^{(k)} U^{(k)} + \frac{\mathcal{K}^{(k)2}}{m^2} \right)$$

$$A_k^+ A_k = \frac{m}{2\Omega'_k} \left(\Omega'^2_k U^{(k)2} + i \frac{\Omega'_k}{m} U^{(k)} \mathcal{K}^{(k)} - i \frac{\Omega'_k}{m} \mathcal{K}^{(k)} U^{(k)} + \frac{\mathcal{K}^{(k)2}}{m^2} \right)$$

$$\therefore H = \frac{1}{2} \sum_k \left[\frac{\mathcal{K}^{(k)2}}{m} + m \Omega'^2_k U^{(k)2} \right] \tag{B.7}$$

Now that we have obtained the Hamiltonian classically we may move directly to canonical operator form. Then $\mathcal{K}^{(k)}$ and $U^{(k)}$ become canonical variables satisfy the Poissan bracket relation

$$\{ U^{(k)} , \mathcal{K}^{(k')} \} = \delta_{kk'}$$

The final stage is to normalize the field produced by the optical vibrations

$$-e n_o \delta \underline{E} = -e \sum_{i=1}^{n_o} \sum_k \delta E^{(k)} e^{i\underline{k} \cdot \underline{\gamma}_i} = \sum_{i=1}^{n_o} \sum_k - m \Omega'^2_k \frac{1}{\sqrt{n_o}} U^{(k)} e^{i\underline{k} \cdot \underline{\gamma}_i}$$

$$\therefore \delta E^{(k)} = \frac{1}{\sqrt{n_o}} \frac{m\Omega'^2_k}{e} U^{(k)} \tag{B.8}$$

For the same reason, if pump field is present and near or above the threshold level

$$\therefore H_o^{(k)} = \frac{1}{2} \left[\frac{\mathcal{K}^{(k)2}}{m} + m \Omega'^2_k U^{(k)2} \right] \tag{B.9}$$

$$\delta E^{(k)} = \frac{1}{\sqrt{n_o}} \frac{m\Omega_k^2}{e} U^{(k)} \tag{B.10}$$

In three dimensional case we have

$$H_o^{(k)} = \frac{1}{2} \sum_\sigma \left[\frac{\mathcal{K}_\sigma^{(k)^2}}{m} + m \Omega_k'^2 U_\sigma^{(k)^2} \right] \tag{B.11}$$

$$\delta \underline{E}^{(k)} = \frac{1}{\sqrt{n_o}} \frac{m\Omega_k^2}{e} \underline{U}^{(k)} \tag{B.12}$$

We can also generalized above procedure to the case that there is an uniform magnetic field B_o in the $\hat{z}$ direction

$$H_o^{(k)} = \frac{1}{2} \sum_\sigma \left[\frac{\mathcal{K}_\sigma^{(k)^2}}{m} + m\Omega_k'^2 U_\sigma^{(k)^2} \right] \tag{B.13}$$

$$\delta \underline{E}^{(k)} = \frac{m\Omega_k^2}{e\sqrt{n_o}} \underline{U}^{(k)} + \frac{\Omega_e}{e\sqrt{n_o}} \underline{\mathcal{K}}^{(k)} \times \hat{z} \tag{B.14}$$

where $\Omega_e = \frac{-eB_o}{m_e c}$ $\quad \{ U_\sigma^{(k)} , \mathcal{K}_\beta^{(k')} \} = \delta_{kk'} \delta_{\sigma\beta}$

REFERENCES

1. H.E. Carlson, W.E. Gordon, and R.L. Showen, J. Geophys. Res. 77, 1242 (1972); R.B. White, C.S. Liu and M.N. Rosenbluth, Phys. Rev. Lett. 31, 520 (1973); H.W. Hendel and J.T. Flick, Phys. Rev. Lett. 31, 199 (1973).

2. B. Grek and M. Porkolab, Phys. Rev. Letters 30 (1973) 836.

3. L.A. Klein and B.R. Cheo, Technical Report 402-12, 1973, N.Y. Univ.

4. M. Porkolab , V. Arunasalam, N.C. Luhmann, Jr. and J.P.M Schmitt, PPPL Report MATT-1160 (1975) .

5. M. Okahayashi, K. Chen and M. Porkolab, Phys. Rev. Letters 31 (1973) 1113.

6. V.I. Farenik , V.V. Vlasov and A.M. Rozhkov, Zh. Pis. Red. 18 (1973) 409 . (Sov. Phys. JETP Lett. 18 (1973) 240) .

7. R.P.H. Chang and M. Porkolab , Phys. Rev. Letters 31 (1974) 1227; 31 (1973) 1241 .

8. M. Brusati , G. Cima, M. Fontanesi and E. Sindoni, Lettere al Nuovo Cimento 10 (1974) 67 .

9. V.P. Silin, Sov. Phys. JETP 21 (1965) 1127.

10. D.F. DuBois and M.V. Goldman, Phys. Rev. Letters 14 (1965) 544; Phys. Rev. 164 (1967) 207.

11. K. Nishikawa, J. Phys. Soc. Japan 24 (1968) 916, 1152.

12. Y.C. Lee and C.H. Su, Phys, Rev. 152 (1966) 129.

13. E.A. Jackson, Phys. Rev. 153 (1967) 203.

14. Y.M. Aliev, V.P. Silin and C. Watson, Sov. Phys, JETP 23 (1966) 626 .

15. T. Amano and M. Okamoto, J. Phys. Soc. Japan 26 (1969) 391.

16. M. Porkolab, Nuclear Fusion 12 (1972) 329.

17. M. Porkolab, Phys. Fluids 17 (1974) 1432.

18. R.Z. Sagdeev and A.A. Galleev, Nonlinear Plasma Theory, Chap. 1 (W.A. Benjamin, Inc. New York, 1969) .

19. S. Ichimaru, Basic Principles of Plasma Physics (W.A. Benjamin, Inc. 1973) .

20. R. Stenzel and A.Y. Wong, Phys. Rev. Letters 31 (1972) 274 .

21. M. Porkolab, Physica 82C (1976) 86-110 .

22. S. Hiroe and H. Ikegami, Phys. Rev. Letters 19 (1967) 1414 .

23. R.A. Stern and N. Tzoar, Phys. Rev. Letters 17 (1966) 903 .

24. L.A. Klein,B.Ru-Shao Cheo and R.A.Stern,J.Applied Phys., 45 (1974) 5218 .
L.A. Klein and B.R. Cheo , Technical Report 402-12, 1973 New York University .

25. K. Chung, K.C. Huang, and E. Oevi, Phys. Fluids 16 (1973) 1245.

26. R. Kristal, Ph.D. dissertation, June 1973, PINY .

27. V.V. Pustovalov and V.P. Silm, Sov. Phys. JETP 32 (1971) 1198 .

28. D.F. DuBois and M.V. Goldman, Phys. Fluids 15 (1972) 919 .

29. E. Valee, C. Oberman and F.W. Perking, Phys. Rev. Letters 28 (1972) 340.

30. J.A. Fejer and Y.Y. Kuo, Phys. Rev. Letters 29 (1972) 1667.

31. D.F. DuBois, M.V. Goldman and D. Mckinnis, Fluids 16 (1974) 2257.

32. N. Bezzerides and J. Weinstock, Phys. Rev. Letters 28 (1972) 481
J. Weinstock and N. Bezzerides, Phys. Fluids 16 (1973) 2287; Phys. Rev. Letters 32 (1974) 754 .

33. F.C. Hoh, Rev. Modern Phys. 34 (1962) 267.

34. Experimental set up has been described in detail in Polytechnic Institute of N.Y. Technical Report, No. 77-028, 1977 by Q.T. Yip and B.R. Cheo.

35. R.H. Pantell and H.E. Puthoff, Fundamentals of Quantum Electronics, Chap. 7, John Wiley and Sons, Inc.

36. W.A. Harrison, Solid State Theory, Chap. 4, International Series in Pure and Applied Physics.